Constitutive Modelling of Polymers at High Rates of Strain

Grace Owen[1,2]

March 2024

Thesis submitted to the University of Nottingham for the degree of Doctor of Philosophy

Supervisors: Dr Davide De Focatiis, Dr Stewart McWilliam

[1] *Faculty of Engineering, University of Nottingham, Nottingham NG7 2RD, UK;*
[2] *DPI, P.O. Box 902, 5600 AX Eindhoven, the Netherlands;*

Abstract

Polymers and their composites are frequently used in products exposed to impact events, such as car bumpers, safety spectacles, and transportation panels and components involved in accidents. Their behaviour during impact can vary significantly from that under slower loading conditions and is not always fully understood. The lack of appropriate simulation tools limits the optimisation of material properties and therefore of the structural design of components.

The mechanical properties of polymers are widely known to be highly dependent upon both temperature and strain rate. This is exacerbated at very high strain rates due to the onset of higher order transitions, and with the added complexity of the temperature change due to adiabatic conditions. A constitutive model that can predict the mechanical response across a very wide range of conditions is clearly desirable. The primary goal of this thesis is to develop further the Oxford Glass Rubber (OGR) model, specifically addressing the behaviour of polymers at high strain rates and under adiabatic conditions, necessary for the prediction of the response under impact. The primary focus is on amorphous polymers, but some considerations are also made concerning semi-crystalline polymers and short fibre-filled polymer composites. The aim is to produce a physically-based model that can simulate the constitutive response across a wide range of temperatures and rates with a single set of material input parameters.

This research forms part of the research programme "Impact Modelling of Polymers: high-Rate Experiments for Solid-state Simulations", in collaboration with experimentalists at the University of Oxford. Polycarbonate was selected as a candidate amorphous polymer, and extensively characterised experimentally by collaborators at the University of Oxford. Polycarbonate is different to previous polymers to which the OGR model has been applied in that it is less brittle and has a much tighter entanglement network, and thus a larger strain hardening modulus. A parameterisation approach involving the separation of a flow stress from a conformational stress was developed specifically to address this. A simple

model for the conformational part of the response was developed by introducing a rate and temperature dependence of the strain-hardening modulus.

The model was then further developed to account for specific high strain rate phenomena. The structural state, described through the fictive temperature, is allowed to evolve through ageing kinetics and rejuvenation driven by a plastic strain invariant. The broad range of timescales and temperatures necessitated the introduction of a temperature-dependent rejuvenation constant to achieve physically relevant structural states, and hence flow stresses. To capture the high strain rate behaviour, the effect of the β-transition was introduced to the model as a parallel viscoelastic process. The parameterisation process was adapted to cater for both the α- and the β-processes. Finally, a detailed assessment of adiabatic heating and the resulting temperature rise is presented, with considerations for dissipated energy, conformational energy, elastic strain energy, and the energy needed for structural change to allow predictions of temperature rises during adiabatic deformations.

These new developments allowed for broadly successful simulations of both tensile and compression tests of polycarbonate across a broad temperature $\left(-60\text{-}120\ °C\right)$ and strain rate $\left(0.001\text{-}3000\ s^{-1}\right)$ range. The experimentally measured temperature rises from adiabatic tests were accurately predicted by the simulations, more so at increasing strain rates, which are closer to adiabatic conditions. Some deviation from experimentally measured temperatures are observed at large true strains of over 0.6, and it is possible this may be due to little studied effects of strain on the specific heat capacity.

The model is applied to different chemistries and molecular weights of polycarbonate, and intrinsic material parameters are identified. An engineering continuum approach is then taken to model semi-crystalline polyamide, which presents a different mechanical response to semi-crystalline polymers previously modelled using the OGR model. This approach, although less physical, was remarkably successful across a temperature range of -60 to $+40\ °C$, below the glass transition and in the low strain rate range. Medium rates and temperatures

closer to the glass transition proved more challenging and highlight the limitations of this approach.

The constitutive model is formulated in such a way to be easily translatable to a user material within a finite element solver, allowing the simulation of more complex geometries and shapes, including inhomogeneous deformations such as neck formation during tensile testing.

Acknowledgments

I would like to take this opportunity to thank and acknowledge all the people who supported this work and myself over the last few years. Firstly, the largest thanks must go to my supervisor Davide de Foctaiis. It is rare to find a supervisor who has wisdom and kindness in equal measure. I am so grateful for your guidance, patience and advice; thank you for all the opportunities and your endless hours of support. I would like to extend my thanks to my secondary supervisor Stewart McWilliam for his encouragement and direction throughout my PhD.

This work was part of a research project with the DPI joint with the University of Oxford. I am incredible grateful for this opportunity and the funding to complete this work, but more so grateful for the community of polymer experts who supported this project, with special mention to Denka Hristova-Bogaerds. To Clive Siviour, Peihao Song, Akash Trivedi, David Chapman, Aaron Graham I would like to thank you for the excellent experimental research you produced, the fruitful discussions and partnership during the IMPRESS project.

I had the privilege of doing my PhD in the p.lab research group and would like to thank Gabriel Choong, Vinotharan Annarasa and Matthew Elsmore, for their continued belief, research support and kindness. Without you three I would never have started or finished this journey. To Matt Wadge, I thank you for funding my coffee addiction and fuelling my sanity, you were the light at the end of the tunnel. To the Composites research group and my colleagues in Wolfson and AMB, I thank you for helpful feedback in meetings and the day to day office companionship.

To Guy Lawrence, Joe Eastwood, Matt Thompson, Emma, Alec, Holly and Aleks for being the best of housemates and friends through the hardest of times. To Toto, je voudrais te remercier pour toutes ces dernières années, ton soutien qui est le pilier de mes réussites et pour avoir été tout ce temps mon plus grand soutien.

And finally, to my ever-loving and supportive family Rosemary, Paul & Alexander. I am forever grateful that you are my family, you nurtured my abilities, encouraged my research and empowered my dreams, I dedicate this work to you.

v

Contents

List of Figures

xiv

xvi

xviii

List of Tables

Abbreviations

BPA	Boyce-Parks-Argon (model)
DMA	Dynamic mechanical analysis
DSC	Differential scanning calorimetry
EGP	Eindhoven Glassy Polymer (model)
EV	Edwards-Vilgis
FEA	Finite element analysis
HT	Haward-Thackray (model)
IR	Intermolecular resistance
LSHPB	Long split Hopkinson pressure bar
MDSC	Modulated differential scanning calorimetry
MFR	Melt flow rate
OGR	Oxford Glass-Rubber
PA6	Polyamide-6
PC	Polycarbonate
PET	Polyethylene terephthalate
PETG	Polyethylene terephthalate glycol
PMMA	Polymethyl methacrylate
PP	Polypropylene
PS	Polystyrene
PVC	Polyvinyl chloride
RNR	Rubbery network resistance
SCP	Semi-crystalline polymer
SHPB	Split Hopkinson pressure bar
STZ	Shear transformation zone
TTS	Time-temperature superposition
WLF	William-Landel-Ferry

1. Introduction

1.1. Background

Polymers or 'plastics' are diverse materials that are commonly used in modern society across multiple sectors, from packaging to automotive to medical. A polymer can be defined as a long molecule contains many monomers. Engineering polymers and their composites are also utilised for products subjected to high-strain rate or impact events. This can include products such as car bumpers or bike helmets. Despite the regular use of polymers in products subjected to impact events, mechanical behaviour during impact is not fully understood, specifically the significant variations compared to slower loading conditions. This results in a lack of appropriate simulation tools for polymers under these impact conditions and thus reduced optimisation of material properties and therefore of the structural design of components.

The mechanical properties of polymers are widely known to be highly dependent upon both temperature and strain rate. This is exacerbated at very high strain rates due to the onset of higher order transitions. Additionally, there is insufficient time during high strain rates for heat to diffuse out of a material, adding the complexity of the temperature rise due to adiabatic conditions. A constitutive model that can predict the mechanical response of polymers across a very wide range of conditions is therefore clearly desirable.

Long-term, the development of such a modelling framework will increase the efficiency of the introduction of simulation tools for new parts and novel materials. This is of particular importance as novel polymers incorporating bio-inspired, recycled (and recyclable) or degradable materials are being more commonly used. These developments provide sustainable, high-performance systems for high value-added industries.

1.2. Outline

The work within this thesis presents an extension to the existing constitutive model for polymers, called the Oxford Glass Rubber (OGR) model, to high strain rates. To create such a model requires a detailed assessment of the polymeric behaviour at these higher rates. In Chapter 2 the relevant theory and literature to this thesis is introduced. The key concepts surrounding polymer deformation are considered, with special attention given to the post-yield response and large strain behaviour. A detailed assessment of existing literature and state of the art models is presented and discussed allowing the research opportunities to be identified and appropriate aims of the thesis defined.

Chapter 3 presents the OGR constitutive model with a focus on low strain rates and temperature ranges for both compression and tension tests. The parameterisation process and model are developed in the quasi-static rate range for amorphous polymers with the example of polycarbonate. Within this model novel methods are used to extract the conformational behaviour at yield for materials such as polycarbonate with tighter networks and facilitate the parameterisation of the large strain behaviour of the model. An evolution of fictive temperature through ageing kinetics and mechanical rejuvenation driven by a plastic strain invariant is implemented as a description for the structural state.

Chapter 4 presents the extension of the model and parameterisation methods to high strain rates and low temperatures. In this region, it is necessary to consider both the effect of the secondary transition and adiabatic heating. A novel temperature-dependent rejuvenation constant is introduced to the structural evolution implementation through the fictive temperature to account for effects in the extended range of conditions. With a successful mechanical response determined, the physical implementation of adiabatic heating allows for the simulation of temperature rise during plastic deformation. The temperature rise simulations are compared to experimentally obtained values, highlighting the success.

Chapter 5 uses the model developed in this thesis for different grades of polycarbonate, polypropylene and polyamide6. Initially, the effect of molecular

weight and monomers are explored for polycarbonates, with a statistical analysis performed to determine potential intrinsic parameters. The model is then used to simulate high strain deformation of polypropylene. With reference to a previous OGR model, the usability of the novel fictive temperature evolution method is tested, with the temperature-dependent rejuvenation constant, for high strain rates introduced in Chapter 4. Finally, the semi-crystalline polymer polyamide 6 is considered in a homogenous continuum manner. This engineering approach tests the success and limitations of our parameterisation method and model.

Chapter 6 provides overarching conclusions to the work presented in this thesis in additional to suggestions for future work based on the research conducted. Additional supporting work is provided within the Appendices.

2. Literature Review

2.1. Introduction

This chapter presents a review of topics relevant to this thesis: polymeric materials within constitutive modelling. Section 2.2 will introduce broad topics pertaining to polymer science, including a discussion of amorphous and semi-crystalline materials with an emphasis on polycarbonates and polyamides that form the focus of this work. The general constitutive behaviour of polymers is assessed, with a focus on fundamental aspects of a typical stress-strain curve including yield, strain softening and strain hardening behaviours. The concepts of transitions are introduced, including the critical effects of secondary transitions. Additionally, fictive temperature is discussed as a description of the structure of a polymer. In Section 2.3, a detailed review of the history of constitutive models is provided, with a summary of three branches of models that dominate the field. This section ends with an overview of the experimental methodology that is associated with the increased understanding of the polymer behaviour at high strain rates. In Section 2.3.8, the focus is modern approaches and high-strain rate models to analyse the state of the art to obtain a set of research opportunities. Lastly, within Section 2.5 the aims and objectives of this thesis are presented.

2.2. Polymers Introduction

The term polymer describes a broad group of substances that are long-chains or networks of macromolecules or multiple simpler monomers [1]. Polymers are used in an extremely wide range of sectors, such as packaging, transportation, the medical industry and sports equipment to name a few. In this work the focus will be on engineering plastics (a specific subset of polymers utilised for their improved properties over commodity plastics) used in impact conditions. A few examples of such usage include transportation panels, car bumpers, bike helmets or safety glasses. Polymer behaviour is a complicated, multi-time scale process that is rate and temperature dependent. Additionally, polymeric behaviours can vary significantly between amorphous and semi-crystalline polymers. In this first section, the nature of polymers is discussed.

2.2.1. Amorphous Polymers

There are two major groups of non-crystalline polymers, glassy polymers (e.g. polystyrene or polycarbonate) and elastomers (e.g. rubber). Amorphous polymers exhibit a lack of any long-range order in their microstructure such that the macromolecules are randomly oriented in the unstressed state. The chains of amorphous polymers interact with each other through weak van der Waals forces. Figure 2.1a shows an unoriented amorphous polymer, while Figure 2.1b illustrates the chain reorganisation in an oriented amorphous polymer.
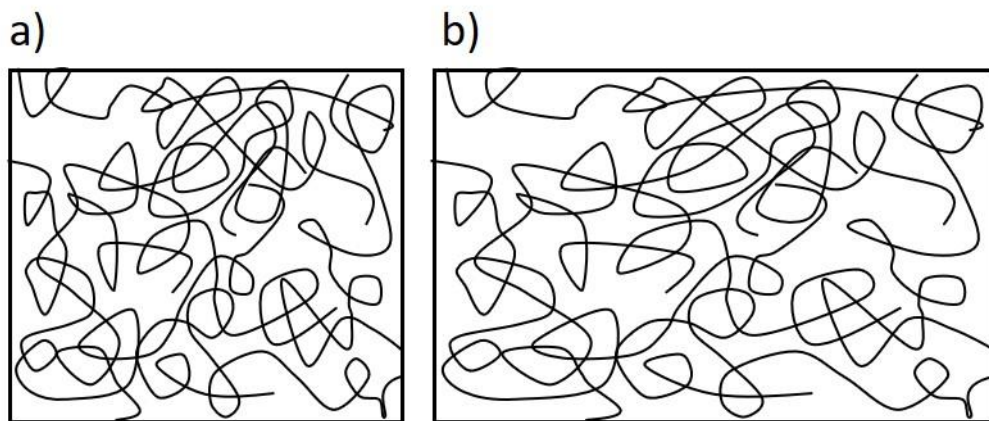
Figure 2.1: A visualisation of the chains for a typical amorphous polymers in a) an unoriented, unstressed state b) a stressed, oriented state (adapted from [2]*)*

Within this thesis the amorphous polymer chosen to characterise, and model is polycarbonate (PC). Polycarbonate is a well-research material that is often used in high strain rate components, such as safety glasses, making it the ideal candidate for this work. PC is made from aromatic polyesters and phenols, (the chemical structure is shown in Figure 2.2), and it is classified as a linear amorphous thermoplastic polymer. A linear polymer typically has long chains that are only held together by weaker van der Waals or hydrogen bonding and display no branching or cross-linking. A thermoplastic is defined as a polymer that flows as a highly viscous liquid when heated and this process is reversible [1]. PC is widely used for its diverse combination of properties: transparency, ductility, stiffness, strength, toughness and impact resistance. PC is regarded as a ductile polymer, usually failing through shear deformation over brittle failure mechanisms.
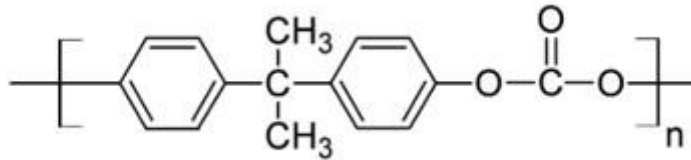
Figure 2.2: Chemical structure of polycarbonate (adapted from [3]*)*

2.2.2. Semi-crystalline Polymers

The other group of polymers to consider is semi-crystalline polymers (SCPs). SCPs contain two phases, the amorphous and the crystalline, where the latter has a regularly organised structure and exhibits long range-order. Figure 2.3 illustrates an example representation of crystalline polymers through the fringed micelle model [2][1]. In general, the crystalline phase controls the rigidity of the polymer, while the amorphous phase the ductility. Much of the literature also introduces a third phase, which is neither completely amorphous nor crystalline, called the rigid amorphous phase [4]–[6]. The properties of any SCP are highly dependent on the proportion of each of these phases. At higher temperatures, amorphous polymers become too soft for many applications, however in SCPs the crystallinity can stiffen the structure at these raised operational temperatures. Figure 2.4 shows the effect of increasing the crystallinity of a polymer on the viscoelastic modulus, highlighting the stiffening effect.

---

[1] While this is no longer considered the accurate description of the internal structure of SCPs, it provides a useful visual aid.
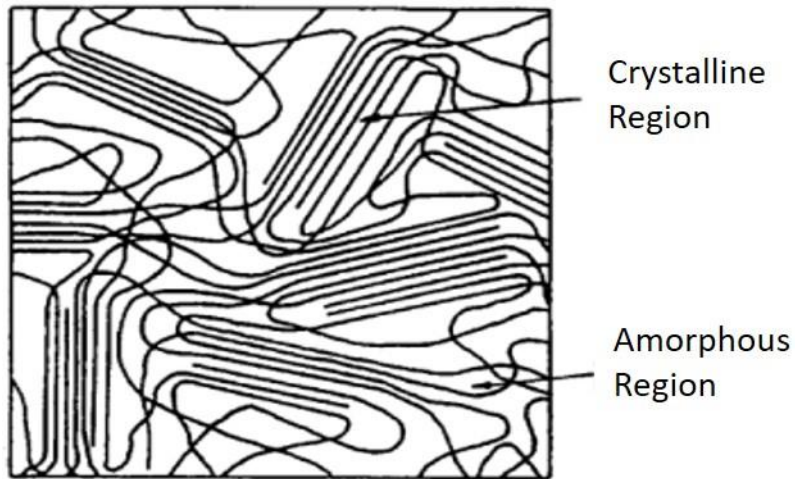
Figure 2.3: A representation of a crystalline polymer through the Fringe Micelle Model, showing the amorphous and the crystalline regions (adapted from [2])
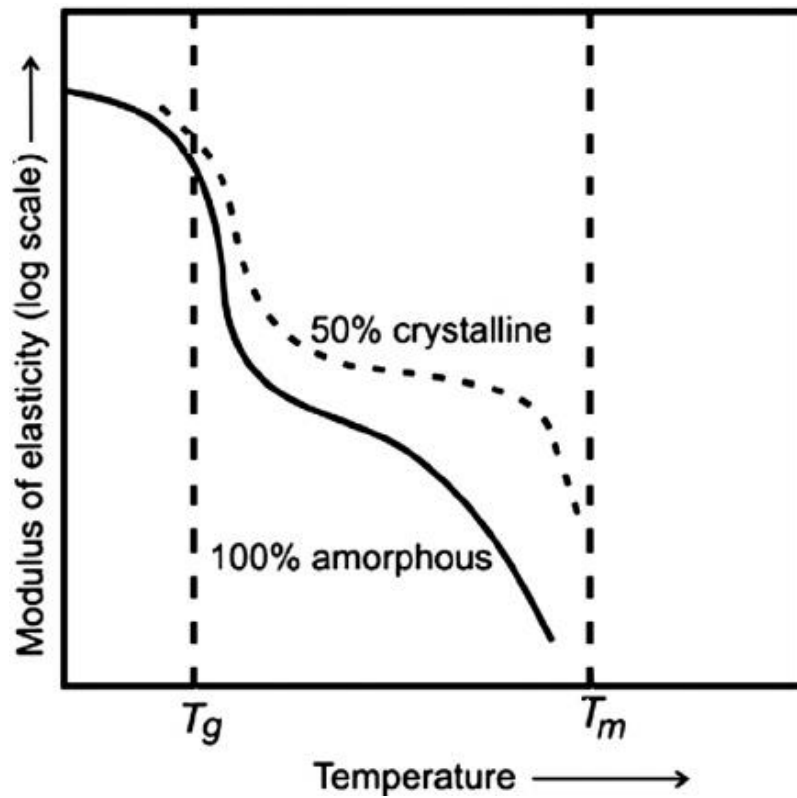
Figure 2.4: Diagram showing the influence of increased crystallinity on the elasticity modulus as a function of temperature for a generalised example for a 100% amorphous and 50% crystalline (adapted from [7])

The deformation of SCPs shares much similarity with amorphous polymers, the differences arising from the crystalline phase. At small strains, the typical elongation of the amorphous chains and the reversible swelling of lamellae is observed [8]. The region of yield tends to be wider in SCPs than amorphous

7

materials, indicating yield is occurring in both the amorphous and crystalline phases. Plastic deformation of SCPs is strongly linked to the crystalline phase, where at small strains the crystals remain intact but can distort, whilst at large strain the microstructure will begin to fail. As with amorphous materials, many SCPs exhibit strain softening and strain hardening post-yield. The exact post-yield response (i.e. shear bands, necking, stress whitening) is dependent on the material, and thus the crystallinity in question.

In some SCPs, a double yield is also observed, as shown in Figure 2.5 for nylon 101 [9], where two peaks in the stress-strain response are obtained, related to the decoupling of the amorphous and crystalline phases [10]. The literature states [9]–[11] that the first yield corresponds to the amorphous phase, while the second yield is linked to crystallographic slip mechanisms, but due to the highly linked nature of the two phases, these are dependent on each other. This double yield phenomenon is more common under low temperature or high strain rate conditions [11], or relatively low moisture materials [11].
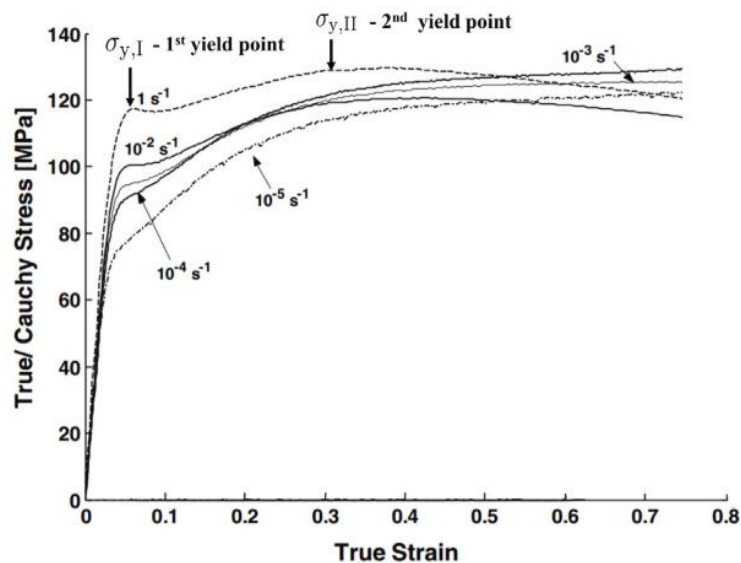
Figure 2.5: Uniaxial low strain rate compression experiments for different engineering strain rates for nylon 101 showing a double yield phenomenon labelled as the 1st yield point and the 2nd yield point. Adapted from [9], [11].

Polyamide-6 (PA6) was chosen as the semi-crystalline material to explore in this thesis. PA6 is the most widely used of the polyamide family and is often used in impact situations, hence the choice for this work. PA6 is a commonly used engineering thermoplastic due to its high operational temperature, good

processability and high abrasion resistance. However, when service temperatures are closer to room temperature, which is below its glass transition of $\sim 50\ ^{\circ}\mathrm{C}$ [12], PA6 has reduce impact strength. Additionally, moisture absorption is a major concern when working with PA6 as is it a hygroscopic material[13]. Water has been reported to act as a plasticiser [13] and as such affects the glass transition, and reduces the yield stress due to increased mobility [13]–[15].

2.2.3. Generalised Constitutive Behaviour of Polymers

The following section divides the different components of a typical mechanical response into key features. In Figure 2.6 an example mechanical response is shown, emphasising the features of a typical amorphous glassy polymer: linear elastic initial response, the initial nonlinearity into yield, strain softening and finally strain hardening [16].
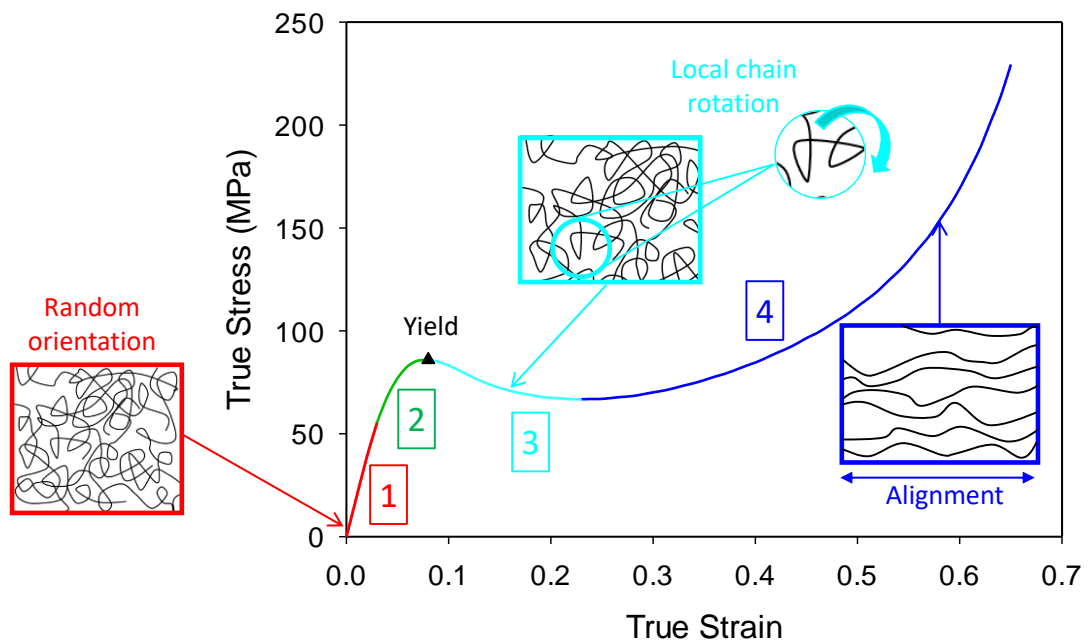
Figure 2.6: Standard stress-strain curve split into four sections, the first section is the linear elastic initial response (red), the second section is the initial nonlinearity into yield (green), next is strain softening (light blue) and finally at large strains the response shows strain hardening (blue)

Linear Viscoelastic Response

At the initial very small strains ($\leq 0.03 - 0.05$), the behaviour is categorised as linear viscoelastic, with relaxation times that depend upon temperature and

structure, shown in zone 1 of Figure 2.6. The response within this initial elastic zone is driven by intermolecular movements as chains rotate and move with limited mobility. When the stress is increased, the rise of more localised regions is observed, and the stress is now large enough to cause full chain rotation and chains can move to new positions, (zone 2 in Figure 2.6). At one point, the accumulation of localised events will pervade such that the whole sample is now experiencing plastic deformation, which is a permanent event. Yield is reached when the applied stress is great enough to overcome the intermolecular forces and this allows for large scale segmental motion to begin. The black triangle on Figure 2.6 represents the polymer yield point. The yielding of a polymeric material is dependent on strain rate, temperature and pressure [17]. As the strain increases, the behaviour becomes non-linear viscoelastic.

Post-Yield Response

Post-yield behaviour begins with strain-softening, where less true stress is required to cause further deformation, shown in the zone 3 of Figure 2.6. It is suggested that strain softening is driven by the reduction of the intermolecular barrier to chain segment rotation with plastic strain. It can be inferred from this that plastic straining induces local structural changes, which allows easier local chain segment rotation. Stress variations form due to the decreased level of stress required at this stage of the deformation; these variations lead to local strain rates that can vary largely throughout the sample being deformed. These differences result in localised plastic deformation zones, which lead to failure in some brittle polymers, such as polystyrene, where extreme localisation results in unstable growth and crazing. Crazing is a precursor to fracture for many brittle polymers, such as polystyrene, and is characterised by stabilising fibrils within micro-voids [18].

Whilst the exact origin of strain softening is debated in the literature, it is reasonable to link this behaviour with physical ageing. One important observation is the effect of ageing on the deformation behaviour, seen in Figure 2.7. As ageing of the polymer occurs, two main effects are observed; firstly, the yield stress increases and secondly, the intrinsic strain softening emerges. The effect of these two observations is seen in Figure 2.7, where the large strain behaviour is the

same for all the cases: the impact of physical ageing has been erased and the material is regarded as rejuvenated.
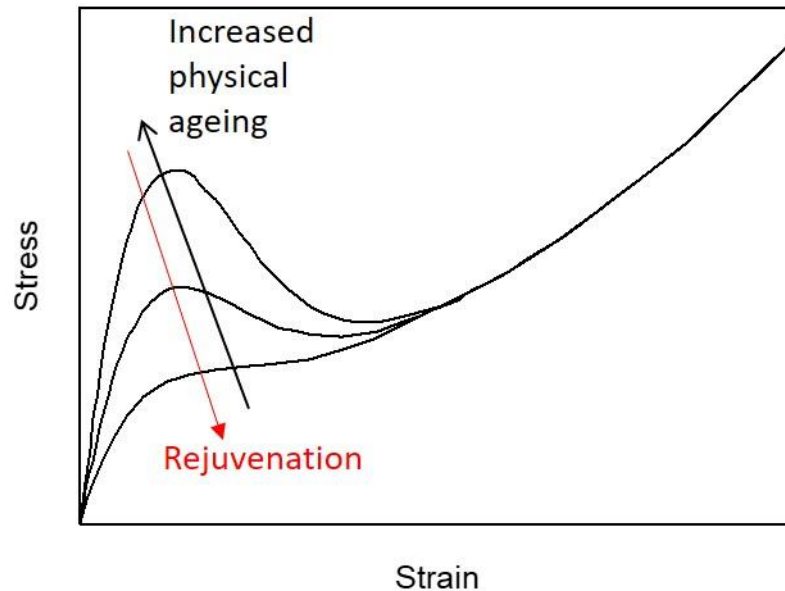
Figure 2.7: A series of stress-strain responses showing that increased physical ageing drives a greater yield response but results in the same post-yield behaviours, evidenced by the collapsing onto the same large strain curve.

With further plastic deformation, chain rotation and movement gives rise to a molecularly-oriented network where chains are generally aligned in the direction of stretch [19]. This change in network from the initially randomly isotropic and therefore disordered system to a more ordered system, results in a decrease in entropy of the polymer. It is this entropic change that relates to the concept of strain hardening. The polymer chains become both aligned and stretched, approaching the extensibility limit, resulting in strain hardening, (zone 4 of Figure 2.6): the stress increases with increasing strain. It is now established that the entropic content of strain hardening is relatively small [20], [21] and there is a developing knowledge of the physics to describe the conformational stress, discussed further in the following section.

Strain-Hardening Description

Strain-hardening is a characteristic behaviour of ductile glassy polymers at large deformations under uniaxial deformation. It has been linked to the stabilisation of polymers, preventing strain localisation, fracture and reducing wear [22]. Such

11

that, if there is a lack of strain hardening, the polymer is likely to craze, or experience a similar extremely localised drive to failure. In low molecular weight glassy polymers, segmental motion post-yield results in fracture. However, in higher molecular weight systems, the covalent chains act to reinforce, inhibiting this motion. The deformation instead permeates through the system, resulting in tougher materials.

It is possible to consider the state of these polymer systems under these high strains as rubbery solids, and thus governing theories from the study of rubbers can be utilised. The term 'entanglements' can be utilised to describe high molecular weight systems where there are 'physical knots' from entwined strands. With this interpretation, it is then necessary to discuss whether the entanglements can detangle in the timescale of the test. The mechanisms however that control this alignment are not fully understood. Some of the literature postulates that increasing entanglement or crosslink density would increase the strain hardening, while an increase in temperature would decrease it [20], [21].

Initial research on strain hardening found that upon heating a polymer glass above the glass transition, T_g, the plastic deformation could be mostly recovered [23]– [26]. These early observations imply that the entangled network remained unbroken even during plastic deformation, indicating an entropic-elastic strain hardening. The vast majority use this assumption of rubber-elastic (entropic) description of the strain hardening, as seen in the seminal work of Haward and Thackray [27]. Other models expanded on this theory, notably the three chains model [28], the eight chain model [29] and the cross-link slip-link model of Edwards and Vilgis [30], or the neo-Hookean approach of the Eindhoven Glassy Polymer model (EGP) [31], relating to the Gaussian network theory. Further details on the specifics of these models are given in the Section 2.3.

Polycarbonate has a tighter network than many other engineering polymers. This network effect triggers at large strains. In Figure 2.8, which compares the typical mechanical deformation responses for PC, polymethyl methacrylate (PMMA) and polystyrene (PS), the ensuing mechanical response is seen.
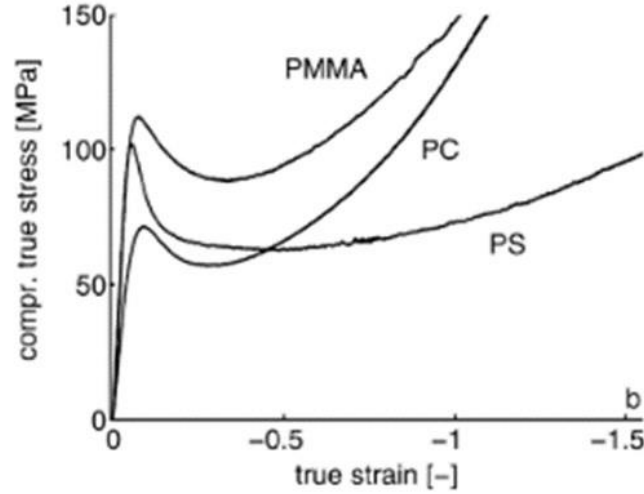
Figure 2.8: True stress against true strain compression responses for three polymers: PMMA, PS and PC, highlighting the greater stress for large deformation behaviour of PC indicative of a tight network (adapted from [32]*)*

To summarise, the deformation of polymeric materials to large strains is a complicated process that is exacerbated by test conditions such as strain rates and temperatures. The next section discusses additional concepts critical to the understanding of polymer behaviour.

2.2.4. Molecular Weight

Another consideration to polymer behaviour is the molecular weight. Molecular weight is related to the number of repeating units within a polymer chain. In polymers, it is necessary to consider the distribution, as polymerised chains are not always the same length. There are two averaging methods: weight average molecular weight M_w , and number average molecular weight, M_n , where:

$$M_w = \sum_{i=0}^{\infty} \left[\frac{N_i M_i}{\sum_{j=0}^{\infty} N_j M_j} \right] M_i \qquad (2.1)$$

$$M_n = \sum_{i=0}^{\infty} \left[\frac{N_i}{\sum_{j=0}^{\infty} N_j} \right] M_i \qquad (2.2)$$

where M, N, i is the molecular weight of the a chain, the number of chains at that molecular weight and the number of polymer molecules, respectively [33].

13

In general, low molecular weight materials exhibit lower viscosity and mechanical properties with lower transition temperatures, while high molecular weight materials show higher viscosity with increased entanglement of chains, often increasing processing difficulty. The strain at which a material reaches failure is strongly influenced by the molecular weight.

For polycarbonate, Nishitsuji et al. report that molecular weight does not affect bulk modulus or shear modulus [34], while annealing does decrease the bulk modulus and increase the shear modulus marginally. With this same work it is stated that PC will get tougher with increased molecular weight, as there is an increased contribution from slippage between entangled chains at these higher molecular weights. One study found that the impact strength of PC is observed to increase with increased molecular weight [35], which contradicts the expected behaviour. The common understanding is that within the glassy regime, only the local motions drive relaxation, and these local motions are not dependent on molecular weight. Molecular weight also affects the glass transition temperature as stated by the Flory-Fox equation [36], [37] shown in equation (2.3); T_g will increase with molecular weight.

$$T_g = T_{g\infty} - \left(K / M_n \right) \tag{2.3}$$

$$K = 2V_c \rho N_A / \alpha \tag{2.4}$$

where, $T_{g\infty}$ is the glass transition of an infinite molecular weight, M_n is the number-average molecular weight, V_c the free volume (related to chain ends), ρ the density, N_A is the Avogadro number, α is the thermal expansion coefficient.

At large strains, a decrease in molecular weight was found to only slightly influence the strain hardening behaviour of polycarbonate [38]. However, the relaxation of the network will occur more quickly when the entanglement density is decreased. One study for lower molecular weight PC had a more notable relaxation behaviour than the higher molecular weight tested [38]. The conclusion drawn from this observation is that the recorded temperature dependence on the

strain hardening modulus is resulting from the relaxation of the entanglement network, where the longest relaxation is dependent upon the molecular weight of the material.

2.2.5. Transitions

As test rates or temperatures change, polymer behaviour is affected by relaxation processes occurring in some polymer materials. This subsection expands on these transitions, with reference to discovery and origin. In some polymeric systems, multiple relaxation processes are observed. These relaxations affect both the structure and the enthalpy of a polymer and are classed as second-order transitions. The naming convention for the processes is $\alpha-, \beta-, \gamma-$,etc. in order of decreasing temperature.

These thermal transitions can be described in terms of free volume. Free volume is an intrinsic property of polymers due to inherent inefficient packing of long chains and is defined as the voids that are not containing polymer chains [39], i.e. the gaps (see Figure 2.9). The free volume of a polymer relates directly to key aspects such as ageing, viscoelasticity and impact properties [39].
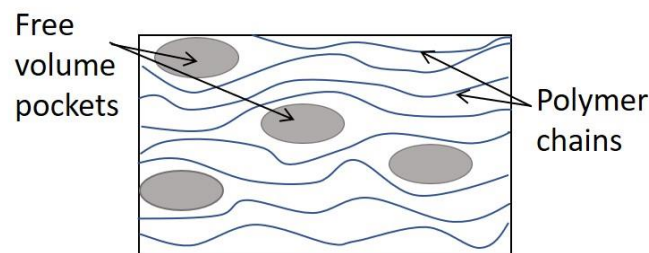
Figure 2.9: Visual representation of the concept of free volume, grey zones representing pockets of space inside a polymer where the blue lines represented individual polymer chains

The Crankshaft model, shown in Figure 2.10, is one approach to describe free volume, where a molecule is visualised as a series of jointed segments. In this model, the mobile segments are imagined to have some degree of movement, and this mobility increases as the free volume of the chain segments increases. If there is not enough free volume, then no motion is possible. At extremely low temperatures, polymer systems are considered 'frozen' or in a glassy state, where

the polymer chains are arranged randomly and have constrained mobility. Under these conditions, the polymer is typically rigid and brittle. If the temperature of the polymer is increased, thermally activated processes trigger and increased motion of the polymer chains occurs. Firstly, localised bond movement is possible, with bending or stretching, this is the $\gamma-$ transition. With further increase of the temperature and free volume, there is space for side chain movements, referred to as the β - transition. With additional heating, the most studied relaxation, the α -relaxation, is reached, commonly known as the glass transition. In this region, considerable changes in properties are observed due to large scale motions of the polymer chains. Traversing the glass transition, T_g, represents the major transition from a glassy polymer to a rubbery state and is often regarded as the end of the 'operating range' for application and forming for many polymers [40]. When in the rubbery state, polymers typically show increased flexibility. The term T_g is technically a range rather than one value (though often cited as one value), as it represents the full temperature range where vitrification occurs.

There are several factors that affect the glass transition and a brief summary is given here. Firstly, the chemical structure of the polymer, both in terms of the main chain and side groups. If there is a decreased main chain flexibility or the presence of rigid side groups the glass transition temperature will increase [41]. Molecular weight is known to affect the glass transition temperature range while chemical cross-linking will also increase the glass transition temperature. Additionally, any blends, copolymers or plasticisers are also reported to affect the transitions.
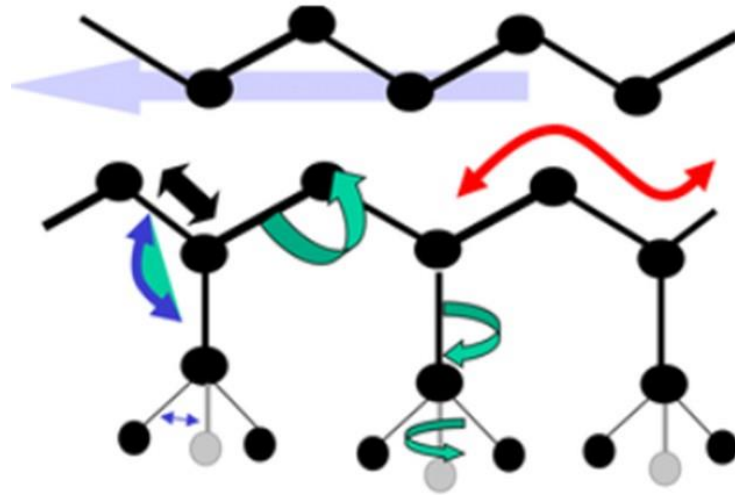
Figure 2.10: The Crankshaft Model as a visualisation of free volume, where black arrows are stretching, blue are bending, green are rotating, red are coordinated movements and lilac slippage (adapted from[42])

The $\gamma-$relaxation is the least studied in the context of the body of literature relating to constitutive modelling of polymers, and studies focus on the understanding of polymer movement. The β - transition is often regarded as the activation barrier to deformation and physical ageing. The β - transition is activated at high strain rates or low temperatures, influencing the polymer properties, notably having a significant contribution to the yield behaviour.
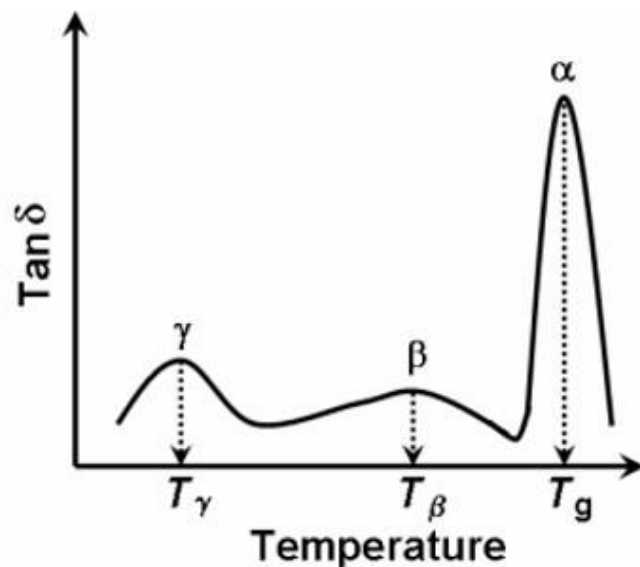
Figure 2.11: An example the loss tangent, tan δ, response showing three transitions across the temperature range, where the α-transition located at the highest temperature has the most dominant peak (adapted from [43])

17

Studies have been conducted to identify the detailed intramolecular causes corresponding to the transitions in different polymers. Some techniques used include: dielectric measurements, nuclear magnetic resonance and a comparison of relaxation characteristics in different polymeric systems with similar structures [44]. Focusing on polycarbonate as the amorphous material used in this work, the restriction of main-chain phenyl groups is reported to be the origin of the β - transition.

As the number of studies on polymer mechanical responses to varying strain rates and temperatures increased, it became clear that these transitions had a large influence on the reported behaviour. One of the first to write about this was Roetling discussing PMMA [45], [46], observing that beyond a 'transition threshold' the material experiences an increased sensitivity to strain rate. The work that followed proved this to also be true of other polymers. It became necessary to model the behaviour of these transitions in the understanding of polymeric behaviour.

Eyring and Ree-Eyring Theories

Eyring's transitional state theory hypothesises that to move between states, an energy barrier must be overcome, with no specifics concerning the molecular mechanisms involved. The generic activation process is driven by shear stress, such that an initial model for the shear strain rate at yield as a function of shear stress can be written as [19]:

$$\dot{\gamma} = \dot{\Gamma}_0 \exp\left(\frac{-\Delta G^*}{k_B T}\right) \sinh\left(\frac{\Omega_{act}\tau}{2k_B T}\right) \qquad (2.5)$$

where, $\dot{\Gamma}_0, \Delta G^*, \Omega_{act}, k_B$ are a constant with the dimensions of strain rate, the activation energy barrier, the activation volume and Boltzmann constant respectively. $\dot{\gamma}, \tau, T$ are the variables, shear strain rate, shear stress and absolute temperature, respectively. The description of plastic flow is stated by Eyring as a viscous processing that occurs at constant stress, thus rearranging equation (2.5) gives:

$$\tau = \frac{2k_B T}{\Omega_{act}} \sinh^{-1}\left[\frac{\dot{\gamma}}{\dot{\Gamma}_0}\exp\left(\frac{\Delta G^*}{k_B T}\right)\right] \tag{2.6}$$

The Ree-Eyring theory [47] is a modified Eyring theory capable of capturing yield behaviour across these transitions of the polymer through an analytical model. In the Ree-Eyring theory, the flow of the material is controlled by rate-activated processes, allowing for multiple processes to act in combination, rather than activation by a single process as with the original theory. Through this theory, it is assumed that the degrees of freedom of the polymer chains are associated with the processes. As the temperature is reduced or the rate increased, a degree of freedom of the polymer chain is limited and the corresponding process starts to contribute to the deformation resistance of the overall material. The critical assumption in the Ree-Eyring theory is that the multiple processes are additive, such that:

$$\sigma\left(\dot{\varepsilon}, T\right) = \sum_{i=\alpha, \beta} \frac{k_B T}{V_i^*} \sinh^{-1}\left(\frac{\dot{\varepsilon}}{\dot{\varepsilon}_{0,i}}\exp\left(\frac{\Delta H_i}{RT}\right)\right) \tag{2.7}$$

where, $\dot{\varepsilon}$ and T are the strain rate and temperature and $V_i^*, \dot{\varepsilon}_{0,i}, \Delta H_i, k_B, R$ are the following, respectively: the activation volume, a rate constant, the activation enthalpy, the Boltzmann's constant and the gas constant.

Roetling, Bauwens et al. and Bauwens-Crowet et al. [45], [46], [48]–[52] were the seminal works for applying the two-process Ree-Eyring theory to capture a transition in polymer yield behaviour. These examples used quasi-static rate conditions but varied the temperatures. The conclusion of these works was that the transition being observed experimentally was linked with the secondary β - transition. Many studies have since validated this hypothesis and initial work such that the Ree-Eyring theory implementation forms the basic understanding to many constitutive material models that consider multiple relaxations, as discussed in the Modelling Section 2.3.

2.2.6. Time-Temperature Superposition

Most polymers within the linear viscoelastic region obey a phenomenon called time temperature superposition (TTS). This principle allows the behaviour at two temperatures to be related through a shift in timescale. Using this principle allows the creation of a mastercurve at a selected reference temperature, the behaviour is now known for multiple decades of time. TTS can be used to estimate changes in properties of polymer materials at conditions that are experimentally unobtainable, i.e. long times or extreme temperatures. Polymeric materials that follow the TTS principle are called thermorheologically simple [53]. To use this technique requires two types of shift. The first a temperature shift (a vertical shift), b_T, of the measured behaviour with units of stress, and the second for quantities of units of time or frequency shift (horizontal shift), a_T. A mastercurve could be described by: $b_T G'(T)$ versus ωa_T. Consider the example in Figure 2.12, a plot of creep compliance results for four example temperatures are shown, through shifting on the time axis, the individual plots can be seen to combine as shown in Figure 2.12b.
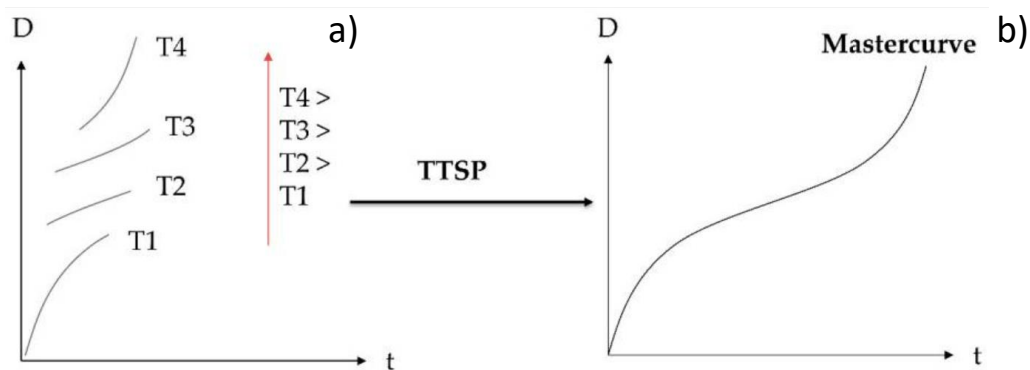
Figure 2.12: Illustration of the time-temperature superposition principle for the creep compliance (D), a) showing the original data at four temperature and b) the mastercurve created from the TTS principle . Adapted from [54]

It is interesting to also consider how a_T depends upon temperature. Firstly, for the empirical Arrhenius relationship, shown in equation (2.8),where E_a is a constant relating to activation energy for flow events. Essentially, the relaxation time relating to temperature will decrease as a result of a temperature increase, such that viscoelastic behaviours will occur more rapidly.

$$a_t(T) = \exp\left[\frac{E_a}{R}\left(\frac{1}{T} - \frac{1}{T_0}\right)\right] \qquad (2.8)$$

A second relationship is required for temperatures at and above the glass transition. The William-Landel-Ferry (WLF) equation [55] shown in equation (2.9) can be utilised for amorphous polymers above the glass transition.

$$\log(a_T) = \frac{-C_1(T - T_{\text{ref}})}{C_2 + (T - T_{\text{ref}})} \qquad (2.9)$$

where C_1, C_2 are universal constants, and T_{ref} is the reference temperature. Typically, these constants are given the values $C_1 = 17.44, C_2 = 51.6$ [55] where $T_{\text{ref}} = T_g$.

2.2.7. Fictive temperature

First introduced by Tool [56], fictive temperature, T_f, is an empirical method of describing the structure of glassy materials. It is sometimes referred to as the 'true glass-transition temperature' of an aged polymer. In a typical material, as a liquid is cooled below the liquidus, solidification occurs, and a crystal-based system with a regular structure is formed. In glassy materials, this crystallisation path is not followed, and instead as the molecular mobility decreases with decreasing temperature, the structure is 'frozen-in' to a disordered state that has a very high viscosity. To explain this concept further, consider a property of a liquid, say specific volume, shown in Figure 2.13, if the liquid is cooled suddenly from its current state there is insufficient time for crystals to form, so it does not go through crystallisation, what happens to the volume? In Figure 2.13, it is shown that the material deviates from the liquid line to form a glass. Eventually, as structural rearrangements occur in the material, it moves towards an equilibrium, the fictive temperature will tend towards the equilibrium temperature. The fictive temperature is defined as the temperature at which the glass would be in equilibrium if suddenly brought to it from its current state [57], this concept is shown in Figure 2.13.
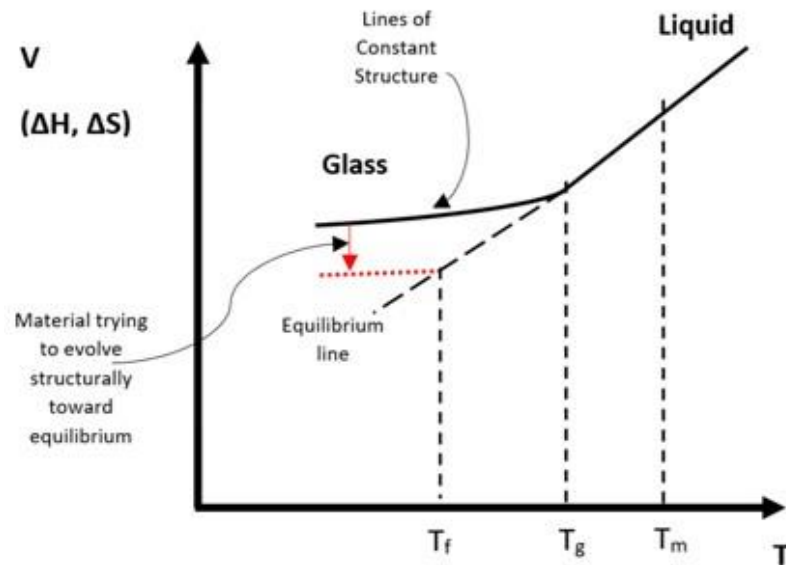
Figure 2.13: Illustration of the concept of fictive temperature, showing the deviation from the equilibrium line as the material cools, highlighting the glass transition and the fictive temperature

2.3. Modelling

The previous section introduced some of the complexities of polymeric behaviour, highlighting that the behaviour under high strain rates varies significantly from slower loading conditions. The lack of appropriate simulation tools for these complicated cases leads to the reduced efficiency of components. It is therefore clearly desirable to have a model that can capture the mechanical response of polymeric materials across a wide range of conditions. This section focuses on the different methodologies for the modelling of polymer systems under deformation. This is a very broad topic and thus only the models directly linking to the proposed research topic, constitutive models at high strain rates, are discussed.

2.3.1. Initial Models

Prior to the intensive study and implementation of constitutive models, many successful polymer models existed and the fundamentals of these are still utilised in modern models. In this subsection a brief overview of three critical early models is given, for a more detailed description the reader is advised to read the thesis of Mulliken [19]. The first glassy polymer models were extensions of Eyring's general

theory for activated rate processes [58], introduced in Section 2.2.5. By the late 1960s, Bauwens, Bauwens-Crowet and Homes were able to validate Eyring's theory against experimental data for PC and polyvinyl chloride (PVC) [48], [49]. Within these studies, the experimental yield stress values across a temperature range of $20-140\ ^\circ\mathrm{C}$ and a strain rate range of $10^{-5}-1\ s^{-1}$ were compared to the Eyring model, achieving success for PC for the whole range, but only the low strain rate regime for PVC. The Eyring equation is capable of predicting both amorphous and semi-crystalline materials, as the theory is non-specific on the origin of mechanisms required for transitions.

The second rate-dependent plastic flow model was produced by Robertson [59], focusing more on the possible mechanisms associated with yield than the Eyring model. It is theorised that shear stress on the polymer results in structural changes, and in turn the structural changes permit the new molecular arrangement related to the transitions discussed. Within this work, PMMA experimental data is compared to the theory, showing reasonable agreement, but the theory was insufficient at capturing the experimental results at low temperatures and high strain rates. This result can be explained through modern understanding of both structural change and transitional behaviour, as described in Section 2.2.5.

The third model is Argon's theory [60] which addresses the possible mechanisms for transitions. Argon postulates that intermolecular forces are the main barrier to overcome the thermally-activated motions related to plasticity, with the theory of 'stress-induced alignment of previously-kinked chains'. Argon's theory proved to be the most successful of the three in the breadth of temperatures and rate behaviour to be captured, using polyethylene terephthalate (PET) and PS experimental data. The success of these initial, predominantly yield focused, models led to studies exploring post-yield stress-strain behaviour. For this predictability, a constitutive model is required.

Viscoelastic materials are defined as exhibiting both viscous and elastic behaviour, such that a linear viscoelastic material is a combination of a purely viscous fluid and an ideally elastic solid. Firstly, addressing the purely viscous fluid, a simple

Newtonian law can be used to describe it, where the deformation is irreversible, and this is represented in a dashpot model. For an ideal elastic solid, there is known to be a linear relationship between stress and strain such that Hooke's Law can be applied, i.e. the deformation is fully reversible, and this behaviour is characterised by a spring model. The realistic behaviour of materials showing viscoelasticity that is between these two extremes can therefore be described through combining in parallel or in series these springs and dashpots. The simpler models to achieve this are the Kelvin model and the Maxwell models, shown in Figure 2.14a and Figure 2.14b. These are used as fundamental elements to build more complex models.
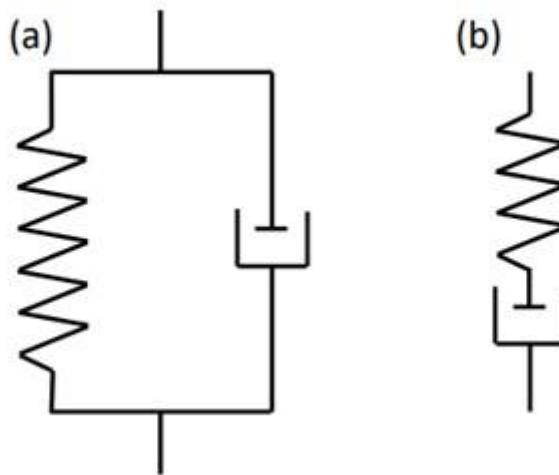
Figure 2.14: Examples of two common spring-dashpot models a) Kelvin element, b) Maxwell element

2.3.2. Constitutive Modelling

A constitutive model allows the prediction of the mechanical response of a material given a series of mathematical governing equations. In general, constitutive models can be considered in two categories, those with a phenomenological basis and those with a physics basis. Phenomenological models generally adopt known constitutive equations from other models such as for metals, then use these to fit experimental data to a constructed stress-strain relationship. Fundamentally this works to demonstrate the behaviour, as successfully seen in the literature. However, these models lack the physical understanding of the complex behaviour, especially involving pressure, rate and

temperature dependencies. The other method of physical models considers constitutive relationships through more material specific physical approaches.

Study of the constitutive modelling of polymers and their composites dates back to the 1960s, with key principles from this work still being used today. The most notable (and successful) of these initial studies is regarded to be the Haward-Thackray (HT) model for glassy polymers [27], whose work still serves as the basis for most models in this field. The HT model is a mathematical model for glassy thermoplastics that predicts stress-strain behaviour for isothermal uniaxial tension. It states that two independent contributions acting in parallel could represent the finite deformation of amorphous polymeric solids: two physically distinct resistances must be overcome to allow for large strain inelastic flow in glassy polymers. The first contribution represents the material below T_g where intermolecular resistance (IR) (segment rotation) must be overcome. The second contribution occurs once the flow has begun, representing resistance to molecular alignment and altering the configurational entropy of the material itself. The two contributions can be viewed as two free energy sinks, the first representing the IR and therefore the viscoelastic response, and the second the rubbery network resistance (RNR) and the entropic elastic response. For the viscoelastic response, the initial elastic response is represented using Hookean elasticity, described with one elastic constant, E. The temperature and rate dependent resistance to inelastic or plastic flow is represented by a single Eyring dashpot, described by Eyring kinetics [61], [62]. For the RNR, a non-linear or Langevin spring was implemented based on Gaussian chain statistics [63]. A visual representation of this is shown Figure 2.15. In Figure 2.16 the contribution from each of the three elements is considered for monotonic loading. Many groups have taken this 1D model and extended it to 3D and improved the mathematical functions that make the constitutive components but fundamentally the basic structure of the HT model remains the foundation; that the resistance to finite deformation is composed of contributions from the intermolecular forces and entropic resistance.
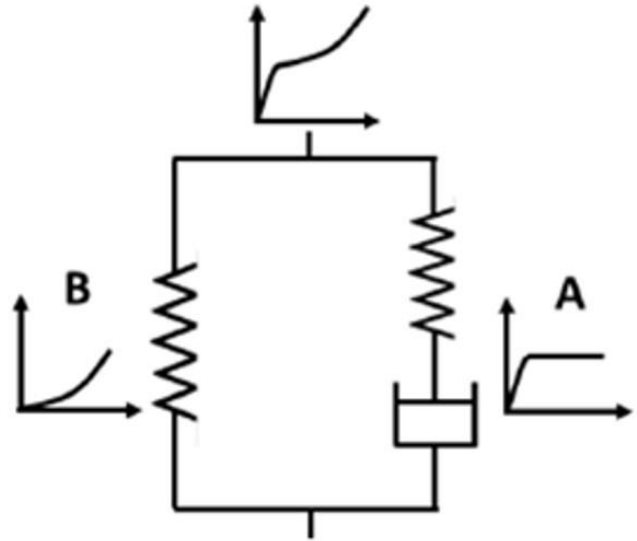
Figure 2.15: The Haward and Thackray model [27] *decomposed into the two arms, where A represents the intermolecular resistance and is composed of a spring-dashpot and B the entropic resistance represented by a spring (adapted from* [41]*)*
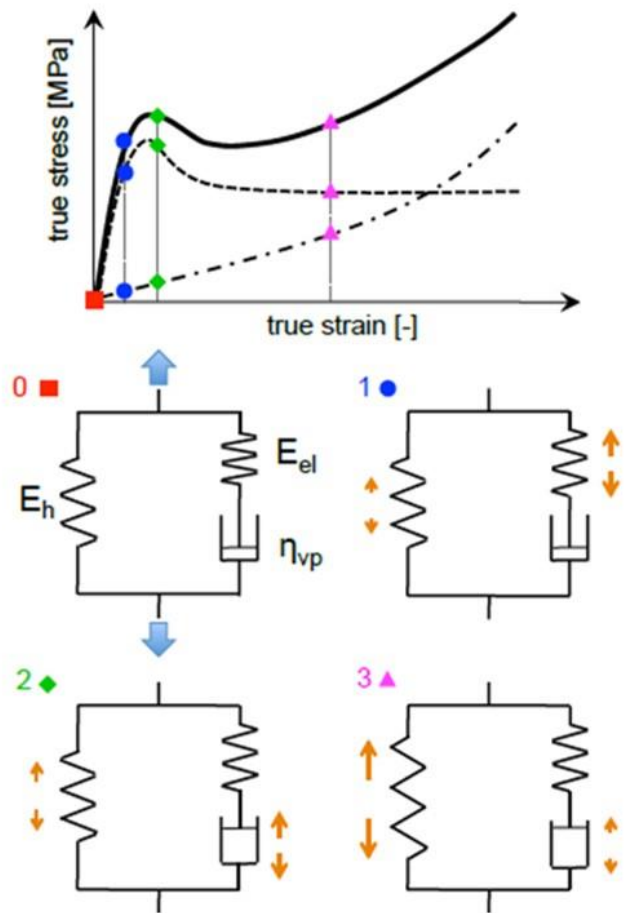
Figure 2.16: Stress decomposition of the Haward and Thackray model [27] *, highlighting the contributions of each component throughout a standard uniaxial tensile test, the size of the orange arrows indicative of the magnitude of deformation from that component (adapted from* [41]*)*

The three notable groups to extend the HT model are researchers at Oxford (OGR), Eindhoven (EGP) and MIT (BPA). As explained in more detail in the following sections the three groups have different approaches, but all three models represent a three-dimensional non-Newtonian viscoplastic flow of elastic strain-stiffening. In simple terms, the approach is a set of simultaneous equations; these are then solved numerically using a time-marching simulation which produces a prediction of the response at the given stress/strain/temperature of interest.

2.3.3. Oxford Glass-Rubber Polymer Model (OGR)

The Glass-Rubber Polymer (OGR) model produced by the Oxford group [64], built on the existing idea from the HT model that during solid-state deformation of amorphous polymers, two processes are involved, a flow process and the elastic deformation of an entangled molecular network. This first work focused only on amorphous polymers that are uncrosslinked near T_g during deformation and demonstrated that by combining in 3D a set of three different physical processes, a unified network for constitutive modelling of polymers was obtainable. The successful 3D OGR constitutive model published was able to exhibit most of the expected behaviours of an amorphous polymer near T_g. Specifically, the modelled response captured the behaviour of the glassy polymer at low temperatures/short times and the rubbery response at the higher temperatures/longer times.

One key assumption made for this model is the treatment of constant volume, as it is known to a reasonable assumption that the compressibility of materials is unaffected by plastic flow [65]. The *F*, deformation gradient, is assumed to act on both viscoelastic and hyperelastic parts. As a result, the deformation rate can be decomposed into elastic and plastic parts [66]:

$$D = D^e + D^p \tag{2.10}$$

It is worth assessing the three major weaknesses summarised from this initial OGR model, as these become the focus of the work to follow. Firstly, the relaxation of the bond stretching element is too localised with regards to the time domain. More modern models improve this by using a spectrum of relaxation times [6],

27

[67], [68] allowing a closer accuracy to experimental data. Secondly, due to large uncertainty around the topic, the modelling of the structural evolution of amorphous polymers was not attempted in this model. Modern papers have addressed this by implementing the evolution of fictive temperature in various methods [69], a concept discussed later. This inclusion of structural evolution is required as below T_g amorphous polymers undergo physical ageing, which manifests as the structure of the polymers evolving spontaneously. The third major limitation of this initial model is that it does not consider the slippage of entanglements in the implementation of the network response.

The OGR model states [69] that the conformational statistics that occur with molecular alignment at large strains are isotropic hyperelastic. One method to capture this is to use the Edwards-Vilgis (EV) free energy function [30]. Within this theory, the molecular chains are assumed to have two types of interactions, entanglements, referred to through slip-links, and rigid connections, crosslinks. The inclusion of these interactions in the model therefore allows for a highly physical implementation of the entropic network behaviour. Finite extensibility can be defined as the maximum extension that a polymer chain can reach, where the force to lead to further extension approaches infinity. Slip-links are included in the EV function through an additional concept; to simplify the behaviour the slip links are envisaged as rings that traverse the chains. Then consider that the rigid cross-links allow the slip-links to move along the polymer chains. To include the finite extensibility, a 'tube concept' is proposed, highlighted in Figure 2.17. It is considered that neighbouring chains surround one chain forming said tube. Overall, the network is therefore described by a system of tubes each containing a polymer chain [30].
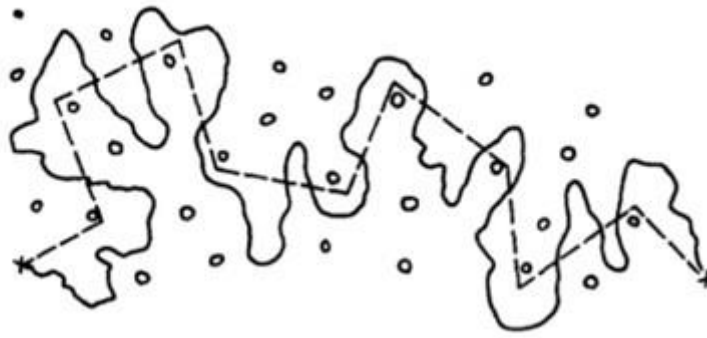
Figure 2.17: A visualisation of the tube model concept. The entanglements in the polymer are represented by a tube, where the sashed line is the centre of the tube, the solid lines are the polymer chains that has been crossed linked at the two x points, the circles represent perpendicular chains (adapted from [30]*)*

Another consideration implemented through the OGR is the non-linearity of viscoelastic behaviour [70]. This work is of particular interest as polymers exhibit a multitude of features in the non-linear regions. The findings show that a multiaxial generalisation of the well-known Eyring model presented as a spectrum could produce many of the non-linear elastic features expected. However, this model could not reproduce the strain recovery observed from unloading experimentally.

The concept of extending the model to impact conditions has also been addressed by the Oxford group [69]. This work suggested an extension that is suitable for glassy thermoset polymer resins for a wide range of strain rates. Importantly, this work included the effect of the adiabatic heating deficit, a key concern at high strain rates. This work found that at the highest strains there is a further adiabatic heating deficit to acknowledge, which was not predicted by the model. Again, the limitations of this model are the grounds for future work from the group.

To physically model the mechanical evolution of properties of polymers in a glassy state, it is critical to understand the structural evolution of glasses. To achieve this, a representation of glass structure is required. In the OGR model, the introduction of strain-induced evolution of the glassy structure is achieved through Tool's fictive temperature [56]. The fundamental assumption is that the structural state at a given scenario is represented well by this one parameter, the fictive temperature. Buckley et al. first considered this through a Macedo-Litovitz expression for viscosity, introduced in equation (2.11) [69]. Within this seminal

work, the use of equation (2.11) for the representation of structural evolution of glassy materials is justifiable if temperature terms are replaced by the fictive temperature terms, resulting in the relaxation time equation (2.12). This interpretation allows for the dependence of temperature and structure to be considered separately.

$$\mu \propto \exp\left(\frac{\Delta H}{RT} + \frac{C}{T - T_\infty}\right) \qquad (2.11)$$

$$\tau = \tau^* \exp\left(\frac{\Delta H}{RT} - \frac{\Delta H}{RT^*}\right) \exp\left(\frac{C}{T_f - T_\infty} - \frac{C}{T_f^* - T_\infty}\right) \qquad (2.12)$$

where C is the Cohen-Turnbull constant, T_∞ is the Vogel temperature, ΔH is the activation energy, T_f is the fictive temperature and T_f^* is the reference fictive temperature relating to the reference structure at reference temperature T^*. Buckley continues by assuming that previously cited rate equations for fictive time can represent the kinetics of the structural evolution [44], [56], [71], seen in equation (2.13), where the relaxation time, τ, is dependent on temperature and fictive temperature (or structure).

Considering rejuvenation in the system, the rise in fictive temperature, linked to structural change, is driven by viscoplastic deformation [69]. One question this assumption raises is which aspect of the deformation is presumed to be driving the rejuvenation. Buckley presents the viscous component of the Hencky strain, ε^v, as a reasonable measure, while for example Struik opted for the driver to be plastic work. Assuming material isotropy, the "effective viscous strain" or $\bar{\varepsilon}^v$ is utilised as a scalar measure. By taking a simple linear relationship between $\dot{T}_f$ and the rate of plastic strain, $\dot{\bar{\varepsilon}}^v$, equation (2.13) becomes equation (2.14).

$$\dot{T}_f = -\frac{T_f - T}{\tau} \qquad (2.13)$$

$$\dot{T}_f = -\frac{T_f - T}{\tau} + k\dot{\bar{\varepsilon}}^v \qquad (2.14)$$

where k is a dimensionless constant. Finally, consider that the starting condition of a system has a fictive temperature of T_{f0} at the test condition T_0. Assuming small changes in T_f, the solution to the differential equation (2.14) is equation (2.15).

$$T_f = T_{f0} + \left(\tau k \dot{\bar{\varepsilon}}^v - T_{f0} + T \right) \left[1 - \exp\left(\frac{\bar{\varepsilon}^v}{\tau \dot{\bar{\varepsilon}}^v} \right) \right] \tag{2.15}$$

In Figure 2.18, the competing physical ageing and de-ageing parts are visualised, considering an initial cooling pre-test, where ageing is viable. The fictive temperature growth is delayed compared to the stress, such that towards yield, as the fictive temperature rises, the stress will begin to drop. Considering equation (2.14), if there is no plastic strain and $T_{f0} > T$, there would be ageing whereas if $T_{f0} < T$, there would be rejuvenation of the system. At a constant rate of effective viscous strain, rejuvenation will saturate. As the structure of the system loosens, flow is easier, resulting in a plateau of all components. Within Figure 2.18 the effects of strain-hardening and the network effect are ignored for simplicity.
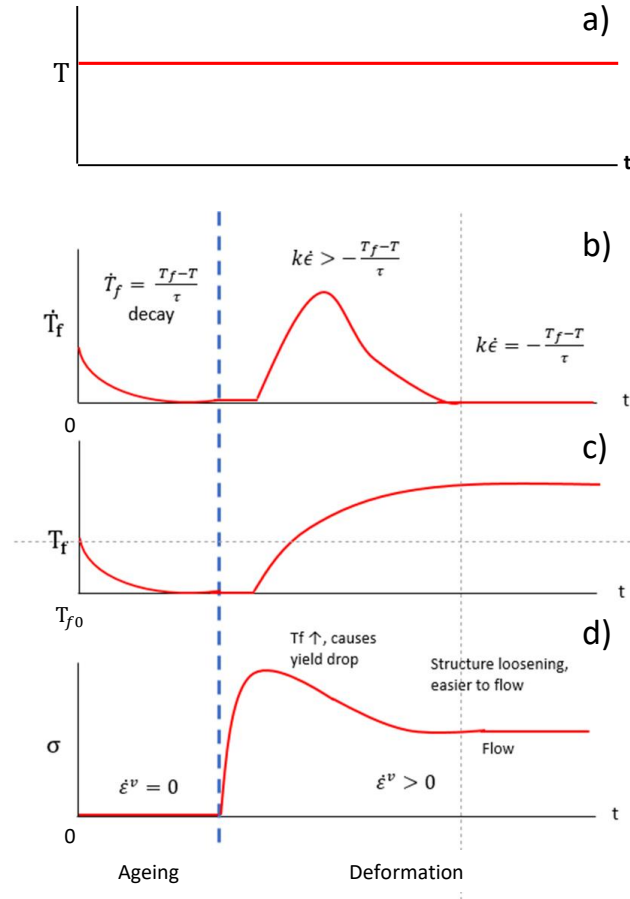
Figure 2.18: Three graphical representations of the evolution of equation (2.14) across a test, where pre-cooling is demonstrated. b) shows the changes in the rate of fictive temperature, c) the value of the fictive temperature as structural evolution is occurring and d) the stress during the test

Buckley et al. [69], demonstrated the first implementation of this structural evolution during mechanical deformation, defined by yield peak subsequent strain-softening. This was achieved through an expression connecting T_f evolution with viscoplastic strain. While much of the literature points to success in using Tool's fictive temperature as a measure, there are some limitations and caveats to discuss. Hutchinson [72] discusses that while the evolution of a single fictive temperature can accurately capture structure, other properties require alternative time-scales, such that fictive temperatures with different meanings could be applied. Perhaps the clearest example of this is discussed by Buckley [69] and applies to the OGR model. If there is a fictive temperature related to stress-relaxation, there could also be one related to enthalpy.

The evolution of fictive temperature to capture the structural evolution of glassy materials is described in equation (2.15). This is considered the full kinetics

version. However, many of the previous iterations of the OGR model [67]–[69] consider an alternative form to this, shown in equation (2.16). This version is an approximate analytical solution to equation (2.15), and it is utilised to reduce computational cost and complexity and has been proven to be successful in certain conditions. A simplification of equation (2.15) can be written as:

$$T_{\mathrm{f}} = T_{\mathrm{f}0} + \left(T_{\mathrm{f}\infty} - T_{\mathrm{f}0}\right)\left[1 - \exp\left(-\frac{\bar{\varepsilon}^{\nu}}{\varepsilon_0^{\nu}}\right)\right] \tag{2.16}$$

where, $T_{\mathrm{f}\infty}$ and ε_0^{ν} are the final fictive temperature and the strain range for the rejuvenation, respectively. In previous work these constants have been obtained by direct fitting to experimental results. The issue with the approximate analytical solution is that some key concepts are neglected. Firstly, any prior thermal history in the glassy polymer is not accounted for within equation (2.16). Secondly, any rate dependence in these two parameters, $T_{\mathrm{f}\infty}$ and ε_0^{ν}, is neglected. The current literature allowed for this simplification but if one is to extend this to a wide range of temperatures and rates, then the full kinetics are required. The literature also describes the complexities in capturing the rate and temperature dependence of fictive temperature [44], [56], [71]. Wu [67] takes equation (2.16) and extends this to a spectrum, such that $\bar{\varepsilon}^{\nu} \to \bar{\varepsilon}_j^{\nu}$. Considering that in this situation, each part of the spectrum will be experiencing a different rate of the rejuvenation process, a range of fictive temperatures will arise. However, the spectrum of fictive temperatures will then converge onto the fixed result $T_{\mathrm{f}0} + \Delta T_{\mathrm{f}}$, the final structure.

Adiabatic Heating Within the Oxford Glass-Rubber Polymer Model

Adiabatic heating is another important aspect to consider within the model. Some polymers undergo a large degree of plastic strain before failure in large strain deformations. It is known that part of the mechanical energy of this plastic deformation is dissipated, transforming into heat. At higher strain rates, there is insufficient time for this dissipation of heat, leading to adiabatic conditions. This trapped heat will lead to thermal softening within the sample, the extent of which is dependent on the temperature sensitivity of the polymer [73]. Successfully modelling these adiabatic conditions is critical to higher rate simulations. In the

OGR model the implementation was first introduced by Buckley [69]. The most physical method to encompass this is a thermo-mechanical coupling, to capture the plastic deformation leading to heating. When kinetic energy is neglected, the instantaneous power balance equation is:

$$\frac{\mathrm{d}(\rho u)}{\mathrm{d}t} = \boldsymbol{\sigma}{:}\boldsymbol{D} + \rho r - \nabla \cdot \boldsymbol{q} \tag{2.17}$$

where, $\boldsymbol{D}$ is the rate of deformation, ρ is the density, u is the specific internal energy of the system, r is the specific internal power source (this arises from structural change), and $\boldsymbol{q}$ is the heat flux. As the adiabatic limit is reached, the transfer of thermal energy out of the sample tends to zero such that $\boldsymbol{q} = 0$. Considering the internal energy, Buckley [69] proposes three outlets. Firstly, the recoverable elastic energy from bond-stretching, secondly, the unrecoverable energy that is driving structural change and finally, the remaining energy is treated as energy towards heating the polymer from viscous deformation. The specific internal power source term can be expressed as: $r = -\Delta c \dot{T}_{fh}$, where Δc is the difference in specific heat capacity traversing the glass transition. Here, T_{fh} is the enthalpy fictive temperature, where $T_{fh,0}$ would represent the structural state of the glass in enthalpic terms at the reference temperature T_0. Through neglecting any small changes in volume from temperature rise or structural changes, equation (2.17) extends to equation (2.18). This implementation has been used in the OGR model first for thermoset resins then for semi-crystalline polypropylene [69], [74].

$$\rho c \dot{T} + \boldsymbol{\sigma}^b : \boldsymbol{D}^e = \boldsymbol{\sigma} : \boldsymbol{D} - \rho \Delta c \dot{T}_{fh} \tag{2.18}$$

Sweeney and co-workers [75] presented a multiaxial loading model for large deformations, using two parallel arms; one using a single Eyring process in series with an Edwards-Vilgis network, and the second using purely an Edwards-Vilgis network. This model predicted polypropylene behaviour expected from large deformations, strain dependence and yield. Another aspect explored by the Oxford group is molecular weight variation, as this naturally plays a major part in

determining the physical properties of solid-state polymers. One paper to address this concept [67] in particular focused on the effect of the molecular length of glassy thermoplastic polymers on the three-dimensional constitutive response for cases of large-deformation. Within this work, a spectrum of relaxation times is used alongside a semiempirical representation of strain-induced structural rejuvenation. Most impressively, this work [67] looked to simplify the issues of modelling the response of glassy polymers around T_g , using the same physical mechanism for both the small strain linear viscoelasticity and the yield/flow behaviour. This work also raises an interesting discussion surrounding the use of a full relaxation spectrum. While the full spectrum allows the best prediction of yield peak, the single-mode approximation that uses a geometric mean relaxation time predicts a close fit to expected post-yield softening and is computationally much cheaper.

The OGR model was further improved through the exploration of orientation. One study extended the model for biaxial hot drawing [76], presenting developed kinetics of structural rejuvenation at low temperatures and non-linear Eyring plots, i.e. extending the capabilities across a wide time and temperature range. A similar avenue explored by the Oxford group was for polystyrene in the glassy state and the effect of prior molecular orientation on large tensile deformations [68]. Through this experimental study, a new hybrid glass-melt constitutive model is presented, by the parallel coupling of the Oxford Glass-Rubber model and the ROLIEPOLY molecularly based melt model. While successful at quantifying the expected rheology and the effect of frozen-in orientation, the model presented in did lack an element at the length-scale to address processes of sub entanglement chain orientation and intrinsic anisotropy.

More recent work using the OGR implemented two processes for SCPs over a wide range of strain rates [6], [74], [77]. This work adapts the one-process OGR model for amorphous polymers to model semi-crystalline polymers in 3D by using two relaxation processes, i.e. one associated with the amorphous region and one with the more rigid amorphous phase. Key parts of this work include: multiple viscoelastic relaxation processes, very wide strain-rate range, temperature-

dependence, adiabatic heating and structural rejuvenation. This work suggested that the two main relaxation processes, α and β, can be sufficiently associated with the yielding seen at both the low rate loading region and the impact-rate region. A visualisation of this is shown in Figure 2.19
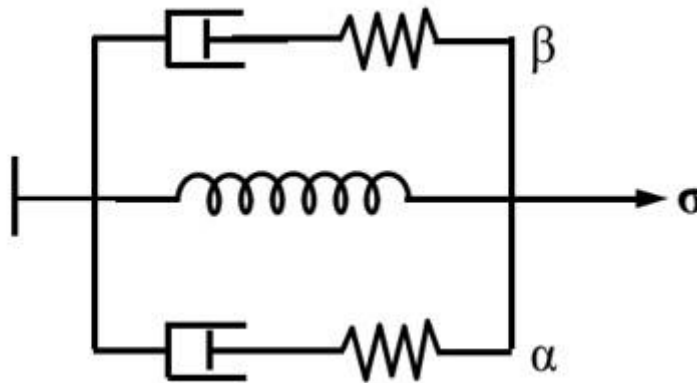
Figure 2.19: Representation of the extension to the OGR model for semi-crystalline polymers at elevated strain rates, the two viscoelastic processes being represented with an arm for the α and β relaxation, the third arm relating to the network response, (adapted from [6])

Over the years the Oxford Group have also developed a variety of successful experimental techniques surrounding this field which are discussed further in Section 2.3.7.

2.3.4. EGP Model

The Eindhoven group have a very similar approach to the OGR, called the Eindhoven Glassy Polymer (EGP) model but notably have a different focus to a large proportion of their work. The Eindhoven group have largely focused on long term deformations and failure [78]–[80] as well as moulding [81] and the impact of orientation [82], [83], but without focus on impact rates. Tervoort et al. [65] were the first studies on this branch of the model, creating a 3D implementation for nonlinear viscoelastic behaviour utilising a compressive Leonov's fluid model [84] and assessing the treatment of the Jaumann-stress rate within the elastic region [65], [85], [86]. A single Leonov model can be viewed as a Maxwell mode that has a relaxation time dependent on the equivalent stress proportional to the von Mises stress [86]. As with the OGR model, a separation of the volumetric and

isochoric parts is required. Figure 2.20 shows a single-mode Leonov model, highlighting how it corresponds to the deviatoric stress response, where Figure 2.21 shows the full EGP model representation, and how it is extended to multimode as achieved by Van Breemen [87].
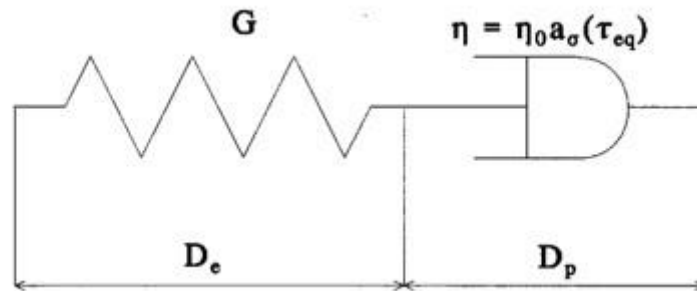
Figure 2.20: Single mode Leonov Model, demonstrating the division into elastic and plastic components (adapted from [86])
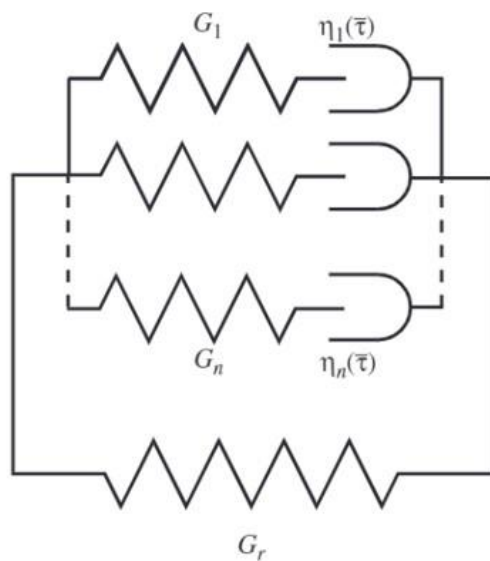
Figure 2.21: Multi-mode extension to the Eindhoven Glassy Polymer (EGP) Model, (adapted from [87])

This model was later extended to include features of strain hardening and intrinsic strain softening [65], this improved single-mode model is known as the generalized compressible Leonov model. The single-mode Leonov approach is limited in the same way as both the initial models of the OGR and the BPA, through inaccurately describing non-linear viscoelastic responses. Therefore, while the single-mode EGP was used extensively to predict deformation behaviour, an expansion to the multi-mode approach was taken [86]. This idea was developed

in future years [87], shown in Figure 2.21, to account for complex loading simulations, as with the OGR model. Govaert et al. [88] extended this model through the addition of pressure dependence, where relaxation times were utilised to describe the yielding behaviour of glassy polymers. Finally, Tervoort and Govaert [89] implemented strain hardening through a neo-Hookean rubber spring relating to Gaussian theory. Considering the EGP approach, this theory assumes that between entanglements, the polymer strands do not obtain a fully stretched conformation, such that in a uniaxial load the conformational stress could be defined as: $\sigma = G_r \left(\lambda^2 - \lambda^{-1} \right)$, where G_r, a strain hardening modulus, is equal to $N_e k_B T$, where N_e, k_B are the entanglement network density and the Boltzmann's constant respectively.

A large focus of the group was the understanding of this strain hardening[2]. The further study of strain hardening recorded some opposing observations to the initial entropy-elastic theory. Firstly, that the recorded experimental values of strain hardening are much larger than predicted values based on network density theory. Secondly, as temperature decreases, Gaussian theory predicts strain hardening to decrease whereas experimental data shows an increase [32], [89]. Thirdly, a purely elastic model will not predict the strain rate dependence that has been reported [20], [90]. Finally, the rubber-elastic interpretation is taken to be incompressible however experimental work highlights a strong dependence on hydrostatic pressure [91], [92]. Van Melick et al. [90] also researched the dependency of the entanglement network density on the strain hardening modulus and whether this implied linearity was accurate. The conclusions were that while the proportionality was conclusive, the network density should not be considered as a critical parameter to define strain hardening modulus.

One approach to handle the inconsistencies discussed previously is to introduce a viscous component to the strain hardening contribution. The impact of this is to introduce deformation dependence in the flow stress. Considering the physical meaning to this implementation, as plastic deformation occurs, chains orientate,

---

[2] This definition in polymer science is not analogous with the term from metallurgy

which has been linked to the growth of the activation barriers as the inter-chain packing changes [93]. Wendlandt [90] was one of the first to investigate this idea by adding a strain rate dependence activation volume to include deformation dependence to the Eyring flow term. The flow stress dependence on strain rate therefore increased with the deformation along with the strain hardening.

Another avenue developed from this original model was to include orientation effects by the implementation of an associated flow rule. It is based on Hill's anisotropic effective stress with the viscoplasticity arising from an Eyring model [94], initially applied to oriented polypropylene. Senden et al. [82] were then able to add this component to the EGP model. More recently this has been extended to short fibre composites modelling using an anisotropic viscoelastic-viscoplastic approach [95].

Developments following this looked at how to model behaviour for more thermorheologically complex materials and the changes this would mean for the existing compressible Leonov model. One paper accomplished this with two linear relaxation time spectra in parallel [96]. Another avenue of interest was the incorporation of an ageing kinetic term to the existing elastoviscoplastic constitutive models [31], creating a new model that successfully dealt with the post-yield response with regards to thermomechanical history. More recent developments of the EGP model include approaches around different stress-states, pre-yield nonlinearity and failure [95], [97], [98]. One of the key differences that the OGR Model has compared to the EGP model, is the introduction of fictive temperature to describe the material's structural state (4), which allows a natural production of strain-softening as fictive temperature rises, induced by the plastic strain.

2.3.5. The BPA (Boyce, Parks and Argon) Model

One of the first groups to successfully formulate a 3-D extension to the HT model was Boyce et al. [99], sometimes called the Boyce, Parks and Argon (BPA) model, first extended for large inelastic deformation of glassy polymers for PMMA. This initial BPA model came from building on existing fundamentals from Onat and co-workers and the HT model, but also included Argon's micro-mechanical model to

describe the plastic strain rate-dependence [60] over the original Eyring formulation [99]. The improvements made with this model included accounting for dependencies in material response at large deformations, namely rate, temperature and pressure. Additionally, a focus on strain-softening was presented, included through an evolution law of shear resistance. This initial model was tested over the following years for a series of materials and loading conditions, proving its success in producing accurate stress-strain data in the glassy state.

The next advancement of the BPA model was to address the implementation of the network component. Initially, it was introduced, as with the HT model, through rubber elasticity theory describing the entropic resistance, modelled by the three-chain model linked to the work of Wang and Guth [28], [100]. However, in later work, issues arose with this 3-chain model simulating different deformation states. Arruda and Boyce then introduced a new rubber elasticity model, known as the "eight-chain model". This theory states that the network could be imagined as eight non-Gaussian chains connected at a centre junction to the corners of a unit cube, shown visually in Figure 2.22, as an interpretation of the non-linear elasticity for the response of rubbers in the 3-D state of deformation [29]. This eight-chain model is particularly interesting as it accurately captures the mathematics of the co-operative nature of network deformation but requires only two more material parameters (a modulus and a limiting chain extensibility). The addition of the eight-chain model to the BPA model allowed the successful modelling of both PMMA and PC capturing the deformation state dependence on the mechanical stress-stretch response. This step is noted as critical to the increased functionality and capability of this model, whereby now regardless of the deformation mode used to obtain the parameters, any alternative mode of deformation could also be simulated. This new adaptation is referred to as the Arruda-Boyce constitutive model. Further work on rubber elasticity saw the use of a Chain Orientation Distribution Function [101], providing a comparison with three- and eight-chain models. The three models are shown in Figure 2.22. For a further comparison of rubber elasticity, readers are referred to Boyce's review [102]. At a certain distance from the extensibility limit, the Edwards-Vilgis approach of the OGR is

interchangeable with the neo-Hookean approach of the EGP and the eight-chain model. However, unlike the Edwards-Vilgis approach discussed for the OGR, the three- and eight- chain methods only account for rigid crosslinked connections between chains, which is not accurate of the whole physical picture. In fact, Sweeney established that the Edwards-Vilgis representation captures a broader range of the behaviour [103].
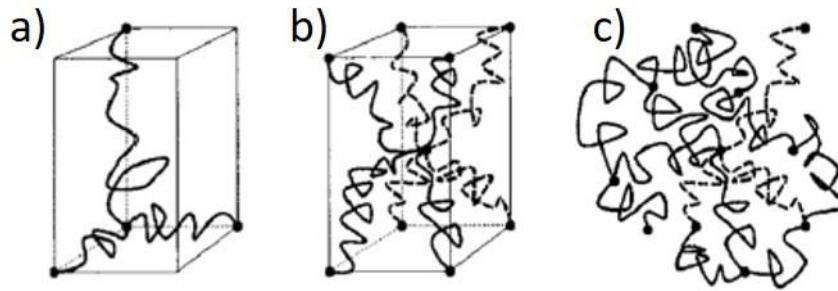
Figure 2.22: Visual representation of the a) three-chain [28], b) eight-chain [29] and c) the full network models [101] (adapted from [41])

The fundamental difference between the Boyce model and the EGP and OGR models is the approach to constant volume assumptions. In the BPA model, it is assumed that all volume change is accounted for in the an initial Hookean spring, and a constant volume is then imposed on the bottom two elements composed of a Eyring dashpot and a Langevin spring [19]. The Boyce model therefore multiplicatively decomposed the deformation gradient into plastic-elastic parts [99], $F = F^e F^p$.

Over the following years, the Arruda-Boyce constitutive model was improved further, with various parts of the simulated response being investigated. Physical ageing and thermal history were introduced into the model, followed by non-linearity of yielding and associated post-yield softening, the latter linking to the behaviour of localised shearing zones [104]. Boyce also applied the constitutive modelling to the stress-strain behaviour of poly(ethylene terephthalate) (PET) above the glass transition, considering rate and temperature dependence at these elevated temperatures, while addressing strain-induced crystallisation [105]. This was further developed, for Polyethylene terephthalate glycol (PETG), focusing on the modelling of finite strain behaviour around and through T_g [106].

As improvements were made to include temperature dependence in the model, it became necessary to capture the temperature rise as a result of large deformation and associated assumptions regarding adiabatic heating. The initial assumptions for this first inclusion saw the inelastic viscous dashpot energy being treated dissipatively while the entropic back stress is considered as stored energy [107]. The Bergstrom-Boyce model was created to increase the applicability of the Arruda-Boyce constitutive model to elastomer materials [108]. Here an alteration to the spring-dashpot combinations was required. By placing an elastic spring and dashpot in series to be in parallel with an entropic spring, the model contains the equilibrium and non-equilibrium time dependency needed to represent the response of elastomers [19].

In recent years, various groups have extended and adapted the Arruda-Boyce constitutive model to various effects. Three such examples of avenues taken are given here. First, a focus on SCPs and the challenges in comparison to amorphous polymers, specifically PET, [109] saw the extension to a two-phase model, with focus on temperatures above the transition temperature. Second, another adaptation saw the model extended to include the Raghava yield function [110] to model the pressure-dependent behaviour. The model from this study captures successfully the pressure dependency, volumetric plastic strain and strain-rate sensitivity. A third avenue is the effect of heat developed during large deformation at high strain rates, [111], and how to model the adiabatic effects. The model presented predicts the yield and post-yield behaviour of glassy polymers under these conditions. Within this more recent model, strain softening was a focus of the implementation [111], [112], through modifications to the Mulliken-Boyce pressure-dependent viscoplastic constitutive model. It is worth considering, however, that despite the success of this model it does require approximately 40 parameters in the simplest form [41].

2.3.6. Modelling of Semi-Crystalline Polymers

As with the amorphous constitutive models discussed so far, semi-crystalline polymers (SCP) constitutive models are grouped into phenomenological models and more physical, micromechanical models. The former usually involve

representative volumes of the material, while the latter consider simulating interactions on the microscale. Phenomenological models tend to contain mathematical functions for the flow stress as a function of temperature and strain rate. Holmes et al. published a comprehensive review on early SCP models [113]. The main problem arising from microscale models is the challenge of linking the microstructure theories to the constitutive response of SCPs. While initially developed for amorphous materials, the models for amorphous polymers described in Sections 2.3.3 to 2.3.5 can also reasonably describe some SCPs [114]–[116]. These models capture the key features of yield, strain softening and strain hardening, with a reasonable strain rate and temperature dependency. A few more recent semi-crystalline models are summarised in this subsection.

The Hong-Rastogi-Strobl three component model was designed specifically for the constitutive modelling of SCPs under tensile loading [117], [118]. There are three components: firstly, a relaxing stress, considering the viscous effects between phases; secondly, a crystal block stress, linking to the elastic and plastic deformation of the crystalline phase; and lastly a network stress, for the global network response of the amorphous component. Another model is the Arruda-Wang model [119] which considers the microstructural effects, alongside strain rate dependence. The basic spring-dashpot design is similar to existing amorphous models, with additional dashpots addressing the key difference for SCPs. Finally, the Sweeney-Spares and Woodhead model [75] considers multiaxial loading and any processing conditions. Shown in Figure 2.23, this model continues the two parallel arms theory, but contains one arm with an Edwards-Vilgis network in series with an Eyring dashpot and the second parallel arm containing just an Edwards-Vilgis network. This model successfully simulates yield and large strains with a strain rate dependence.
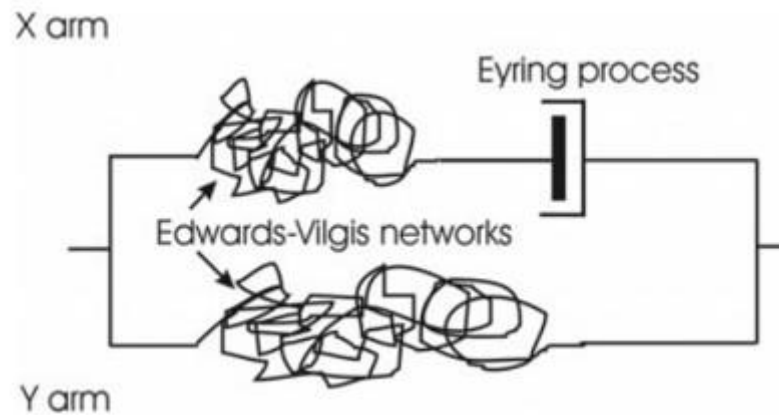
Figure 2.23: Representation of the Sweeney-Spares and Woodhead model [75] *for semi-crystalline polymers (adapted from* [75]*)*

2.3.7. Experimental Approaches

To better assess the advances to polymer constitutive modelling and improved understanding of polymeric behaviour it is necessary to understand the experimental work that underpins this. This subsection details the experimental literature surrounding the characterisation and high rate testing of polymers related to this thesis. For a full analysis of high strain rate mechanics in polymers, the reader is pointed to the review of Siviour and Jordan [17].

The seminal work in studying stress-strain behaviour over a wide range of strain rates is often considered to be Chou et al. [120], who studied the polymeric behaviour of four materials in compression. This work utilised a medium strain-rate machine and a split Hopkinson pressure bar (SHPB). The mechanical strength was recorded as a function of strain rate. The expectation was a linear relationship; however, it was reported that at high strain rates, stress increased more quickly than expected. Following this work, some authors noted the same observation in their studies [121], [122], while others [123], [124] reported some inconsistencies. As a result, there are various debates in the literature about the presence and origin of the observed nonlinearity of yield with respect to rate dependence. These inconsistencies are often linked in modern literature to the influence of secondary transitions in many polymers.
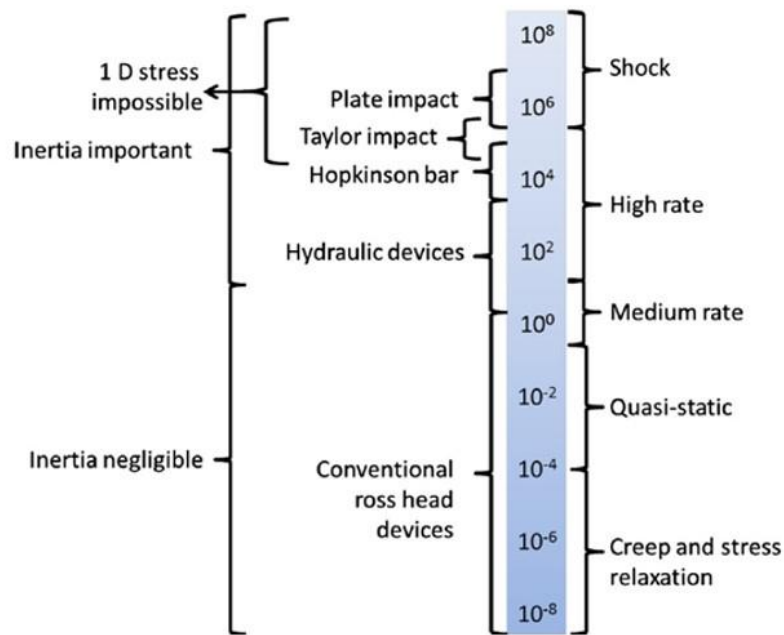
Figure 2.24: A guidance provided by [125] *for the techniques and experimental methodologies required at different strain rates, adapted from* [125]

As shown in Figure 2.24, different experimental techniques are required to obtain a wide range of strain rates. The Split-Hopkinson Bar (SHPB) is the standard characterisation test for very high strain rates. It is widely discussed in previous literature [111], [126]–[132], so only a brief description is provided in this subsection. The SHPB is used to measure high-rate performance in the range 1000 s^{-1} to $10,000\,\text{s}^{-1}$ across a wide range of materials, including for polycarbonate [111], [129]–[132]. A cylindrical specimen (which has typical lengths of 1-10 mm diameter [17]) is placed between two metal rods, with strain gauges attached. A striker rod is propelled by a gas gun and strikes the first metal rod, resulting in an incident stress wave. As the wave reaches the polymer sample, some of the wave is transmitted and some is reflected, a diagram showing the SHPB design is shown in Figure 2.25. The stress-strain response can be extracted from the measurements of these waves and the force and displacements at the interface of the sample and the metal rod. Further difficulties arise with testing soft or rubbery materials, a review of this experimental technicalities is detailed in [17].

45

Figure 2.25: A diagram showing the standard set-up of a Split Hopkinson Pressure Bar with the striker, input bar, sample position and output labelled. This set-up is utilised for high strain rate testing (adapted from[133])

Critically, while many studies have explored the high strain rate behaviour for numerous materials, the medium rate region of $1-500s^{-1}$ [133] is often excluded. This region is particularly experimentally challenging, as the frequency required is comparable to the natural frequency of the SHPB equipment. Due to these challenges, two difficult modifications are suggested: either a very long Hopkinson bar or very high acceleration actuators with high bandwidth load cells. A series of previous alterations successfully used to counter these problems include drop-weights [134]–[140], fly wheel systems [141], [142] and a very long split Hopkinson bar (LSHPB)[143]. It is essential to capture these medium rates, despite the experimental challenges, as often the polymer transitions, discussed previously, occur when traversing this region.

One avenue of modern literature is to reimagine the use of time-temperature superposition (TTS), normally applicable to modulus data, to understand rate dependence in polymers [17], [129]. An empirical formula was hypothesised in order to map the temperature dependence of yield stress values, showing a linear interdependence on temperature and strain:

$$T = T_0 + A\left(\log \dot{\varepsilon}_0 - \log \dot{\varepsilon}\right) \tag{2.19}$$

Where A defines the rate and temperature relations, where the new temperature T from the reference temperature T_0 and the new strain rate $\dot{\varepsilon}$ from reference rate $\dot{\varepsilon}_0$ are mapped. This method was tested for amorphous PC, semi-crystalline materials [144], [145] and composites with varying success [136], [146]. From this exploration of TTS methods, the use of low rate experiments to replicate high strain rate responses was then trialled. To achieve this a few considerations are required. Firstly, it is necessary to separate the dynamic loading effects from the intrinsic rate dependence seen in polymers, such as inertial effects. The second consideration is the differences in specimen heating in static and dynamic loading.

During deformation, some plastic work is converted into heat. In the low strain rate scenarios, heat has time to leave the sample, such that the system is treated as isothermal. At high rates, the heat does not have time to leave the sample, and the system is adiabatic. Kendall et al. [147] first successfully simulated high strain rate responses as low rate experiments for PVC by monitoring the temperature during the experiment. This was achieved through the replication of yield stress at lower strain rates by reducing the ambient test temperature. Then during the test, the temperature is increased to simulate the plastic work that would be converting to heat or that remaining in the sample. When utilised for PC and PMMA, this method required the proportion of the mechanical work converted to heat, the β-factor, to be varied [73], [125], [131], [147] . However, both these cases assumed that all the mechanical energy converted to heat.

2.3.8. Modern Methods & High-Rate Approaches

Within this section the state of the art is presented and the opportunities for research discussed. In more recent years, one area of focus was polymer microstructures and the implementation into constitutive models. Wang et al. and Liu et al. [148], [149] found that through dividing chains into entangled or untangled categories, a reasonable understanding of the unloading response could be achieved. Other work on microstructures related the nonlinear response to secondary bonds behaviour (dissociation, recombination) where the resulting model is referred to as the transient network model [150]. This has now been extended to include thermosets with temperature- and strain rate-dependence under different test conditions, such as both monotonic and cyclic tensile tests and stress relaxation tests [151]. Jiang and Jiang [152] concentrated on the physical and chemical entanglements in relation to deformation resistance. This microscopic understanding provided reasoning to the impact on thermal history on the yield on a macroscopic level at room temperature conditions. Jiang et al. [153] then proved the capabilities of this understanding at conditions close to glass transition.

Within this body of newer studies, failure was also significantly studied, but as this is outside the scope of this thesis, this literature will not be addressed within this

Chapter. The inclusion of some failure theories, such as the shear transformation zone (STZ), has allowed good description of structural evolution driven by deformation [154]–[156].

One other branch of modern models includes those that couple thermodynamic properties, such as Anand et al. and Ames et al. [157], [158] who modelled the unloading response with varying temperature through including a back stress. This branch of models originates from the ideas of Bouvard et al. [159], [160], who deviated from the assumptions within Haward and Thrackray's original work [27]. This alternative does not use a collection of spring and dashpots but rather utilises model understanding from other materials such as metals, using internal state variables based on the ideas of Coleman and Gurtin [161]. The three internal state variables highlighted by Bouvard et al. are: firstly, a quantity of internal strain driven by entanglement points. Secondly, a representation for strain-induced crystallisation as strain increased. Finally, a material hardening contribution from chain alignment at large strains. Molecular dynamic simulations drive the parameterisation of such models. These initial models [159], [160] were promising but showed a lack of understanding of specifics of temperature effects, reducing its usability especially approaching the glass transition. Lan et al. dealt with these weaknesses by introducing two types of entanglements: permanent entanglements and dynamic entanglements [162]. This addition did account for behaviour under varying rates and temperature, but has proven difficult to calibrate, reducing the applicability.

To capture the effects of strain rate and temperatures, Richeton et al. extended the BPA model further through the inclusion of a cooperative model with links to time-temperature superposition [163]. This work also captured the secondary transition in PMMA, allowing the extension of the temperature and rate range. The model was extended for PC by Cao et al. [164], increasing the accuracy concerning strain softening, and then most recently improvements to the yielding of PMMA [165].

2.4. Research Opportunities

This review chapter highlights the vast amount of existing literature concerning the constitutive modelling of polymers. As the models improved, it became apparent that more specific details should be the focus of work. One clear gap in the literature is models that can handle extreme ranges of temperatures and rates, and the vastly different behaviour these ranges require. The biggest shortcomings of most existing models and experimental studies of polycarbonate [111], [130], [132] is the lack of experimental data and models at medium rates $(1-500 s^{-1})$. This range is critical as it is the transition region for many polymers, including polycarbonate, and traversing the β-transition can give rise to significantly different mechanical responses. A better understanding of the onset of the β-transition stands to give us more information about high strain rates. Additionally, in this range, the transition from isothermal to adiabatic heating is expected, furthering the importance of modelling this area successfully.

It is worth considering the physicality of some models. While it is a valid avenue of work to fit many parameters to a mechanical response to create successful simulations, it is also of interest to assess the physical attributions leading to these responses and thus create a more physical-based model. Lastly, it is clear that the continued development of correctly modelling the temperature rise during deformation for adiabatic conditions is critical to understanding the behaviour and the thermal softening of polymers under impact conditions.

2.5. Aims & Objectives

The aim of this thesis is to develop further the Oxford Glass Rubber model specifically addressing the behaviour of polymers at high strain rates and under adiabatic conditions necessary for the prediction of responses under impact. To achieve this aim, the following objectives are set out.

1. Extend the Oxford Glass Rubber model to high strain rates through consideration of multiple transitions and adiabatic heating.

2. Simulate temperature rises and compare to state-of-the-art experimental measurements through a physical implementation of adiabatic heating and successful modelling of high strain rates.

3. Analyse the effects of molecular weight, polymer chemistry and semi-crystalline materials on the model and parameterisation methodology.

3. Constitutive Model and Parameterisation Method for Low-Rates

3.1. Introduction

Constitutive models are a key tool to simulate the behaviour of materials under a wide variety of conditions without the associated undertakings of experimental work. Polymeric materials provide interesting challenges to model given the rate and temperature dependency of the materials and the intrinsic non-linearities. Building upon one of the current literature constitutive models, the Oxford Glass-Rubber Model (OGR), this chapter focuses on the low strain rates and temperature range associated with the α-process. Polycarbonate is selected as an amorphous material to study this model development, with special interest paid to the differences occurring from its tight network.

Within this chapter, the basics of the constitutive model underlying this thesis are detailed. The constitutive model represents the physical processes understood to be occurring in the large strain deformation of amorphous polymers and is an extension of the Oxford Glass-Rubber Model (OGR) first presented by Buckley and Jones [64]. Fundamentally, this constitutive model is a set of non-linear simultaneous equations that predict the three-dimensional mechanical response in the form of a Cauchy stress tensor for a material system given the deformation gradient history.

Firstly, the origin of the model and the basic kinematics are summarised along with the fundamental equations and detailed physical understanding which support each decision. The two major free energy sinks to consider in glassy polymers are described as a bond-stretching and a conformational part. The relaxation times are given stress, structure and temperature dependence through a series of shift factors. Appropriate post-yield behaviour is implemented through

51

structural evolution driven by a fictive temperature and a plastic strain invariant, considering both the effects of ageing and mechanical rejuvenation.

Secondly, with the model for the α-process defined, Section 3.3 discusses the parameterisation process to populate this constitutive model, with special focus on alternative or novel decisions taken in this work. The parameters are kept as physical as possible to ensure the model remains physically based. A brief overview of the experimental data required for both parameterisation and comparisons for the simulations is provided.

Lastly, the initial simulation results utilising the model and parameterisation methodology presented are shown. The simulations are directly compared to the experimental results for varying strains rates, $0.001, 0.01, 0.1\, s^{-1}$, and temperatures, -20 to 120 °C. The success of the whole response is compared to experimental results alongside the expected trends in the yield stress data.

3.2. Constitutive Model

3.2.1. Origin

The basis of the model comes from the Haward and Thrackray (HT) model [27] which stated that two independent free energy sinks could represent the finite deformation of amorphous polymeric solids; the first representing the intermolecular resistance and therefore the viscoelastic response, and the second the rubbery network resistance and the entropic elastic response. The former is referred to as the bond-stretching contribution and the latter the conformational contribution. A visual description of this is given in Figure 2.15. The model presented in this thesis combines the Oxford Glass-Rubber model [64] with new ideas surrounding: structural evolution and flow mechanics, the role of secondary transitions and contributions to adiabatic heating.

3.2.2. Basic Kinematics

To frame the model, the following kinematic definitions are required, adapted from Buckley et al [69], where all bar terms, i.e. $\bar{x}$, represent deviatoric (shape-changing) terms. A polymer deforming as a continuum that occupies an initial space of $\mathfrak{R}_0$ displaces to $\mathfrak{R}$, a diagrammatic description is shown in Figure 3.1. A material point X in $\mathfrak{R}_0$ would displace to position x in $\mathfrak{R}$, with respect to the Euclidean reference frame. The deformation gradient tensor, $F(X)$, can be defined as:

$$F(X) = \frac{dx}{dX} \tag{3.1}$$
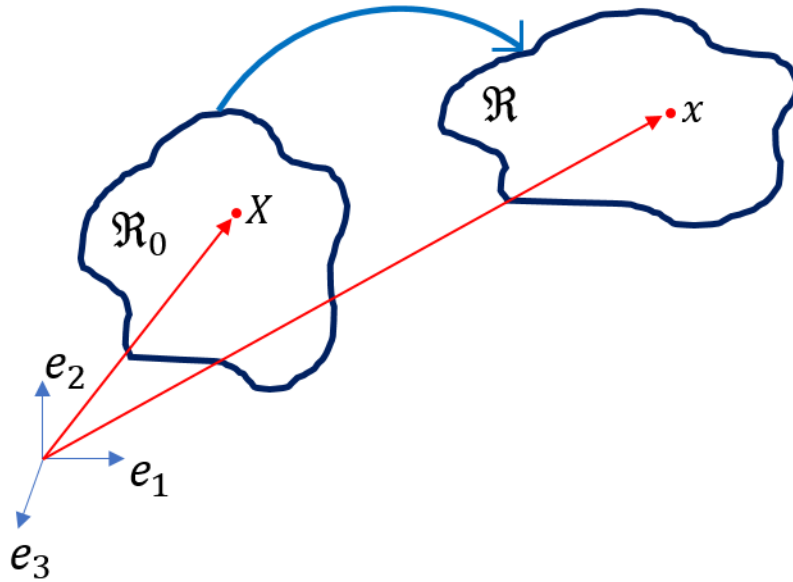
Figure 3.1: Diagrammatic description of polymer deformation in a Euclidean reference frame

The deformation gradient, F, can be separated into a volume change and a shape change (deviatoric) part through the volume ratio, J, such that:

$$J = \det F, \bar{F} = J^{-1/3} F \tag{3.2}$$

$\bar{F}$ can be decomposed into corresponding rotational R and deviatoric left stretch tensors, $\bar{V}$:

$$\bar{F} = \bar{V}R \tag{3.3}$$

The deviatoric components of the left Cauchy-Green tensor $\bar{B}$ and the velocity gradient $\bar{L}$ can be defined:

$$\bar{B} = \bar{F}\bar{F}^{T}, \bar{L} = \dot{\bar{F}}\bar{F}^{-1} \tag{3.4}$$

From these components, the spin, W, and the deviatoric rate of deformation tensors, $\bar{D}$, are defined as:

$$W = \frac{1}{2}\left(\bar{L}\text{-}\bar{L}^{T}\right) \tag{3.5}$$

$$\bar{D} = \frac{1}{2}\left(\bar{L}\text{+}\bar{L}^{T}\right) \tag{3.6}$$

The Cauchy stress tensor at any instant can also be divided into a hydrostatic, σ_{m} and a deviatoric part, S:

$$\sigma = S + \sigma_{m}\mathbf{I} \tag{3.7}$$

3.2.3. Model Description

This constitutive model simulates the material response to a deformation gradient tensor, F (defined above) in terms of the Cauchy Stress, σ [68]. As described in Section 3.2.1, the fundamental assumption for this constitutive model is that the two free energy sinks (the bond-stretching and conformational contributions), describing glassy polymers during deformation, are additive. Therefore the stress, S, defined in equation (3.7) is described as the sum of the bond stretching stress, S^{b}, and conformational stress parts, S^{c}, shown in equation (3.9). The fully Cauchy stress is given in equation (3.9).

$$S = S^{b} + S^{c} \tag{3.8}$$

$$\sigma = S^{b} + S^{c} + \sigma_{m}I \tag{3.9}$$

Such that:

$$\sigma_m = \frac{1}{3} tr\boldsymbol{\sigma} = K \ln J \qquad (3.10)$$

where K is the bulk modulus. This definition of $\boldsymbol{\sigma}_m$ therefore neglects time dependence within the hydrostatic response.

A visual interpretation of the model presented is provided in Figure 3.2. The bond-stretching arm consists of a Hookean spring and a non-linear dashpot (viscoplastic flow). The conformational arm is represented by a non-linear hyperelastic spring.
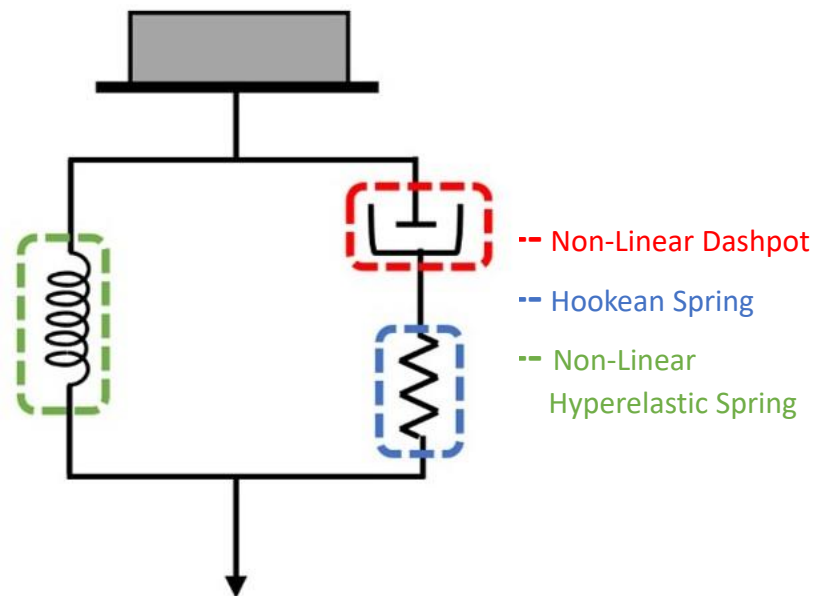
Figure 3.2: Schematic illustration of the Oxford Glass Rubber Model version used within this thesis showing two arms, one pertaining to the bond-stretching behaviour and the second the conformational, network response

3.2.4. Bond-Stretching Stress

One of the two free energy sinks to consider is associated with the intermolecular resistance, referred to as the bond-stretching contribution. The OGR model [69], discussed in detail in Chapter 2, states that bond-stretching could be relaxed by flow events on a molecular level described through Eyring rate kinetics with a stress-dependent viscosity [69]. Therefore, the deviatoric rate of deformation, $\bar{\boldsymbol{D}}$, is considered the sum of a linear elastic bond stretching contribution, and a contribution of irreversible viscous flow of molecular segments:

$$\bar{\boldsymbol{D}} = \bar{\boldsymbol{D}}^e + \bar{\boldsymbol{D}}^v \tag{3.8}$$

These assumptions of linear elasticity and a flow rule for both the elastic and viscous parts yield the following non-linear viscoelastic differential equation:

$$\bar{\boldsymbol{D}} = \frac{\hat{\boldsymbol{S}}^b}{2G^b} + \frac{\boldsymbol{S}^b}{\mu} \tag{3.9}$$

where G^b is the bond stretching component of the shear modulus, $\hat{\boldsymbol{S}}^b$ is an objective rate of $\boldsymbol{S}^b$ and the viscosity, μ, is a complicated function as a result of using Eyring theory and so is defined as:

$$\mu = 2G^b \tau \tag{3.10}$$

where τ is the glassy relaxation time.

The rate of change of the deviatoric Cauchy stress, $\dot{\boldsymbol{S}}^b$, can be defined in equation (3.14) through the objective rate of the deviatoric bond-stretch stress, $\hat{\boldsymbol{S}}^b$.

$$\hat{\boldsymbol{S}}^b = \dot{\boldsymbol{S}}^b - \boldsymbol{W}\boldsymbol{S}^b + \boldsymbol{S}^b\boldsymbol{W} \tag{3.11}$$

where $\boldsymbol{W}$ is the spin tensor defined in equation (3.5), and further details are provided in Appendix A.2. Yield Equation Origin.

The glassy relaxation time, τ, in equation (3.10) can be related to the linear viscoelastic relaxation of an unstressed reference state, τ_0^*, at a temperature T^* and a structure defined through T_f^*, the Tool's fictive temperature [56]. Fictive temperature is the temperature where the material would have the same structure in equilibrium, this concept of fictive temperature is described in further detail in Section 2.2.7. Temperature, structure and stress can all act to shift this glassy relaxation time from an unstressed reference state through a set of shift factors:

$$\tau = a_T a_s a_\sigma \tau_0^* \tag{3.12}$$

where, a_T, a_s and a_σ are the shift factors for temperature, structure and stress respectively.

Addressing each of these three shift factors individually, firstly the temperature shift factor, a_T. The temperature dependence on the relaxation time is formulated through the Arrhenius equation, which relates temperature dependence with energy of activation:

$$a_T = \exp\left[\frac{\Delta H}{R}\left(\frac{1}{T} - \frac{1}{T^*}\right)\right] \tag{3.13}$$

Where, ΔH is the activation energy, R is the universal gas constant and T^* is the reference temperature.

The second shift factor to introduce is the Macedo-Litovitz structural dependence shift factor, using the fictive temperature as a description of the structural state:

$$a_s = \exp\left(\frac{C}{T_f - T_\infty} - \frac{C}{T_f^* - T_\infty}\right) \tag{3.14}$$

Where, C is the Cohen Turnbull constant, T_f is the fictive temperature and T_f^* is the reference fictive temperature . T_∞ is the Vogel temperature, sometimes called the ideal glass transition temperature, it is the temperature at which all motions are considered frozen for that material system. Under these conditions it can be deemed that $\tau_j \to \infty$.

Finally, the stress shift factor, which includes both the mean stress and the octahedral shear stress contributions. This stress factor is introduced through Eyring rate kinetics, such that:

$$a_\sigma = \frac{V_s \tau_{oct}^b}{2RT} \frac{\exp\left(-\frac{V_p \sigma_m}{RT}\right)}{\sinh\left(\frac{V_s \tau_{oct}^b}{2RT}\right)} \tag{3.15}$$

$$\tau_{oct} = \sqrt{\frac{1}{3} S^b : S^b} \qquad (3.16)$$

where V_s, V_p are the shear and pressure activation volumes and τ_{oct}^b is the octahedral shear stress.

In previous OGR models [67], [68], the single relaxation time interpretation from equations (3.9) and (3.10) was developed into a multimode discrete spectrum for the relaxation times, such that:

$$S^b = \sum_{j=1}^{M} v_j S_j^b, \sum_{j=1}^{M} v_j = 1 \qquad (3.17)$$

$$\bar{D} = \frac{\hat{S}_j^b}{2G_j^b} + \frac{S_j^b}{\mu_j} \qquad (3.18)$$

The version of the above equations detailed in this subsection for the multimode case is presented in the Appendix A.1. Multi-Mode Version, however the single relaxation time approach is taken in this work to reduce computational time.

3.2.5. Conformational Stress

The second free energy sink to consider is that of the conformational entropy due to preferred molecular alignment within the network. To account for this conformational stress component, an isotropic hyper-elasticity approach is taken, as with the OGR Model before [64], to account for the entropic elasticity between entanglements during stretch. From this description, a scalar free energy density function $A^c(\bar{F})$ exists. The principal stresses are obtained from the differentiation of this free energy density function:

$$S_i^c = \bar{\lambda}_i \frac{\partial A^c}{\partial \bar{\lambda}_i} - p \quad \text{for } i = 1, 2, 3 \qquad (3.19)$$

$$\text{where} \quad \bar{\lambda}_i = \text{eig}\left(\bar{V} = R^T \bar{F}\right) \quad \text{and} \quad \text{tr} S^c = 0 \qquad (3.20)$$

$\bar{\lambda}_i$ is the eigenvalue of $\bar{V}$ and p is the pressure resulting from $\det \bar{V} = 1$, because the material is assumed to be incompressible with regards to $\bar{V}$. This unknown pressure can be found from $\text{tr} S^c = 0$.

Within this work the physically based Edwards-Vilgis free energy function [30] is utilised. This EV strain energy function was originally designed for crosslinked elastomers and is defined as:

$$A = A_c + A_s \tag{3.21}$$

$$A_s = \frac{1}{2} N_s kT \left\{ \sum_{i=1}^{3} \left\{ \frac{\lambda_i^2 \left(1-\alpha^2\right)\left(1+\eta\right)}{\left(1-\alpha^2 \sum \lambda_i^2\right)\left(1+\eta\lambda_i^2\right)} + \ln\left(1+\eta\lambda_i^2\right) \right\} + \ln\left(1-\alpha^2 \sum_{i=1}^{3} \lambda_i^2\right) \right\} \tag{3.22}$$

$$A_c = \frac{1}{2} N_c kT \left\{ \frac{\sum_{i=1}^{3} \lambda_i^2 \left(1-\alpha^2\right)}{1-\alpha^2 \sum_{i=1}^{3} \lambda_i^2} + \ln\left(1-\alpha^2 \sum_{i=1}^{3} \lambda_i^2\right) \right\} \tag{3.23}$$

where A_c is the strain energy due to cross-links and A_s is due to slip-links. N_c is the density of cross-links, N_s is the density of slip-links, α is a measure of the inextensibility, η is a measure for the slippage, λ is the stretch and k_B is the Boltzmann's constant. To utilise this format for polymers with no physical crosslinks the assumption is that $\eta = 0$, thus entanglements can be treated as crosslinks (in these regimes sliplinks will not move). The following simplified form of the Edwards-Vilgis strain energy function is used, where $N_c = 0$:

$$A^c = \frac{N_s k_B T}{2} \left[\frac{\left(1-\alpha^2\right)}{1-\alpha^2 \sum_{i=1}^{3} \bar{\lambda}_i^2} \sum_{i=1}^{3} \bar{\lambda}_i^2 + \ln\left(1-\alpha^2 \sum_{i=1}^{3} \bar{\lambda}_i^2\right) \right] \tag{3.24}$$

where N_s is the density of entanglements and α is a measure of finite extensibility. The parameter α relates to the number (n) of Kuhn segments that are between crosslinks, as defined by Edwards and Vilgis [30] as: $\alpha = n^{-1/2}$.

3.2.6. Structural Change

The post-yield response is characterised by strain softening, associated with a drop in stress after the point of yield. To simulate this post-yield response, an understanding and implementation of structural evolution is required. The inclusion of structural change within this model is achieved through evolving the fictive temperature, T_f. The evolution of structure is described as part physical ageing and part mechanical rejuvenation (or de-ageing) driven by a plastic strain invariant, the balance between these two counter-acting parts controls the response. The increase in fictive temperature due to plastic deformation (or rejuvenation) is cited as the primary source of the strain-softening, i.e. the defined yield-drop, in the post-yield mechanical response. Conversely, if plastic strain is no longer acting on the system, T_f falls and the system is ageing.

As discussed within Chapter 2, an empirical expression of fictive temperature and viscous strain has been used to capture structural evolution in previous implementations of the OGR, shown in equation (2.15). The limitation with this interpretation is the fitting and use of two material constants, ΔT_f and ε_0^v as these constants lack rate dependence which reduces the usability of this model. Considering these factors, within this model, the full evolution equation discussed by Buckley[69] is preferable to implement for the benefits of the full kinetics:

$$T_f = T_{f0} + (\tau k \dot{\bar{\varepsilon}}^v - T_{f0} + T)\left[1 - \exp\left(-\frac{\bar{\varepsilon}^v}{\tau_s \dot{\bar{\varepsilon}}^v}\right)\right]$$

(3.25)

In utilising the relaxation time within equation (3.25), it is necessary to make some assumptions. Firstly, it is assumed that the reference relaxation time, τ_0^*, is the same value as in equation (3.12), and that they refer to the same definition. Secondly, it is assumed that it has an unchanged dependence upon temperature and structure, such that: $\tau_s = a_s a_T \tau_0^*$. Here it is more appropriate to use the structural relaxation time, τ_s, over the mechanical relaxation time defined in

equation (3.12). The dimensionless constant κ is used in the full implementation shown in equation (3.25), sometimes referred to as the rejuvenation parameter, and at this stage it is to be obtained from fitting to experimental data for different materials. The measure of deformation used here to drive rejuvenation is taken to be the invariant of the viscous component of Hencky strain, $\bar{\varepsilon}^{v}$.

3.3. Parameterisation

The following section discusses the parameterisation methods used to populate the model. All experimental data unless otherwise stated is provided by the University of Oxford experimental team. The full experimental work has been published [133] but an overview of the experimental data required for the parameterisation process is reproduced here. The parameterisation can be achieved from a series of experimental results, optimised to be the least number of parameters whilst remaining physically based. The basis of this work follows the parameterisation of the OGR model [69] discussed earlier in this work, with extra explanation given for where new ideas have been implemented. Polycarbonate was selected as a candidate amorphous polymer for this work and is the focus of the majority of the methodology and results provided. Within this section, each parameter and the method of obtaining it is introduced. The full table of parameters for this material is presented at the end of this section in Table 3-1.

3.3.1. Polycarbonate Material Information

Within this chapter only one polycarbonate will be parameterised, LEXAN™ RESIN 103R. This glassy thermoplastic has a $T_g = 145\,°C$, a low melt flow rate (MFR) of 6 (at $300\,°C/\,1.2\,\text{kg}$) and a molecular weight of $32441\,\text{g/mol}$ [133]. Notable features of polycarbonates include high impact resistance and ductility and a tight network which results in a large strain hardening modulus.

3.3.2. Experimental Overview

To fully parameterise the model, a series of experimental data is required, with the intention of reducing the volume of experimental work where possible. It is desirable to have parameters with highly physical origins, to allow for the design

of a physically-based model. In this subsection, a brief overview of the experimental work is provided, a detailed version is given by Song [133].

Differential scanning calorimetry (DSC) was conducted to obtain the glass transition temperature (T_g) using a TA Instruments Q2000, the result of which is shown in Figure 3.3a and the temperature profile required for annealing shown in Figure 3.3b. For the first heating, the sample was raised from $110-180\ °C$ at $2\ °C/min$, the cooling was the same rate to return to the initial temperature, the reheat was the same heating rate back to $180\ °C$. These temperatures were chosen to be $\pm\ 30\ °C$ the estimated temperature of interest. The second heating curve is used to obtain the glass transition to reduce the effect of manufacturing history. Modulated differential scanning calorimetry (MDSC) was also performed to obtain the specific heat capacity as a function of temperature without the noise of transitional regions.
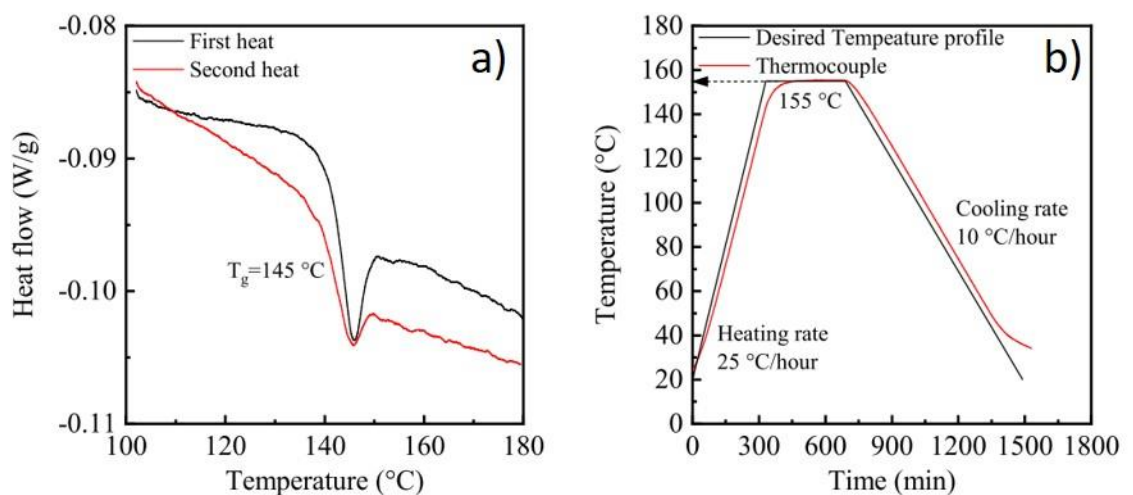
Figure 3.3: a) Heat-cool-reheat DSC for polycarbonate b) temperature profile for annealing, adapted from
[133]

For the dynamic mechanical analysis (DMA), two methods were conducted, a three-point bend and a single cantilever beam using a Thermal Analysis Q800. Figure 3.4 shows the temperature sweep results for the storage and the loss modulus for both techniques. For a full comparison explaining the experimental differences between these two results the reader is pointed to Song's study (107). For the purpose of this work, the DMA is utilised for the value of the transitional temperatures and to form a linear viscoelastic shear relaxation spectrum.
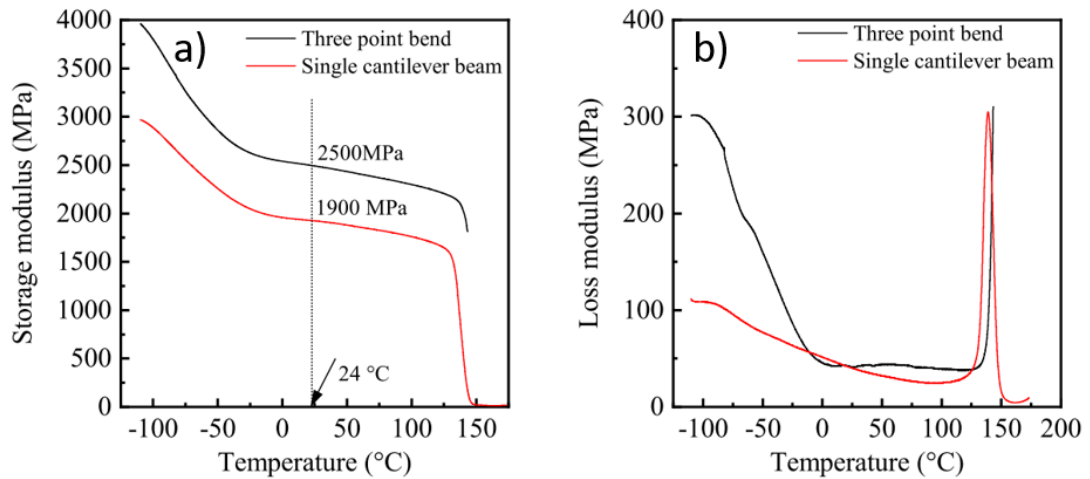
Figure 3.4: DMA temperature sweep results, adapted from [133]*, a) storage modulus versus temperature, b) loss modulus versus temperature*

Both compressive and tensile tests were performed, but the vast majority of data used to parameterise and validate the model and simulations was compressive. For the varying strain rate compressive tests, four types of tests were performed, as highlighted in Figure 3.5 which shows the experimental yield stress results across the strain rate range. The quasi-static varying temperature and the lowest varying strain rate isothermal experiments were conducted on a Universal testing machine (Instron 5980 with a 100kN load cell), with an environmental chamber for temperature control. The medium strain rates were characterised on a hydraulic machine. For the high strain rates, it is necessary to consider two categories, 400-700 s^{-1} and 1000-5000 s^{-1}. The 400-700 s^{-1} range requires a long-split Hopkinson pressure bar (LSHPB) with longer input and output bars. The 1000-5000 s^{-1} rate range can be achieved from the standard SHPB setup.

Figure 3.6 shows typical experimental stress-strain responses for varying temperature and varying strain rate. Despite the variation in width and sharpness of the yield across the large range of strain rates and temperatures (as shown in Figure 3.6), the experimental yield stress is taken to be the peak of the true-stress values. The same universal test machine was used to perform tensile tests, using an annealed dogbone sample, the dimensions of which are shown in Figure 3.7.
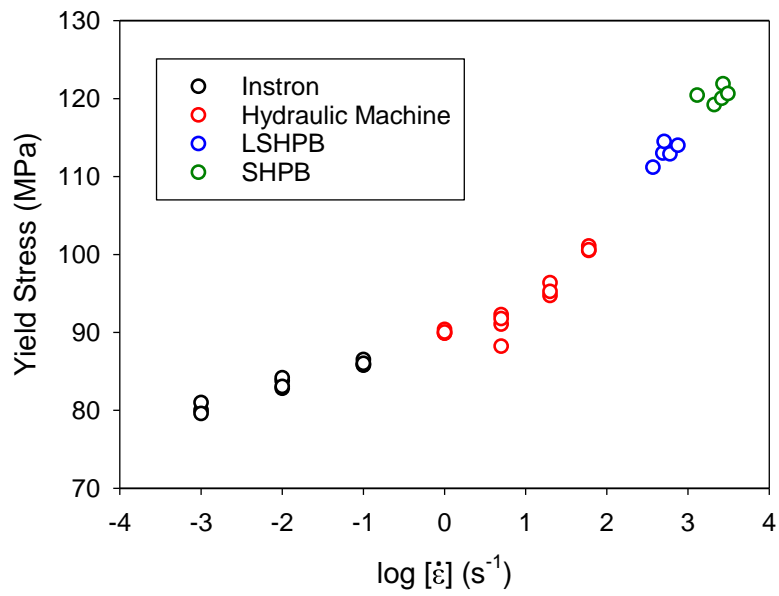
Figure 3.5: Experimental yield stress results (107) across a range of strain rates highlighting the four different methods used to obtain this data; screw-driven machine, hydraulic machine, long split-Hopkinson pressure bar and a standard split-Hopkinson pressure bar
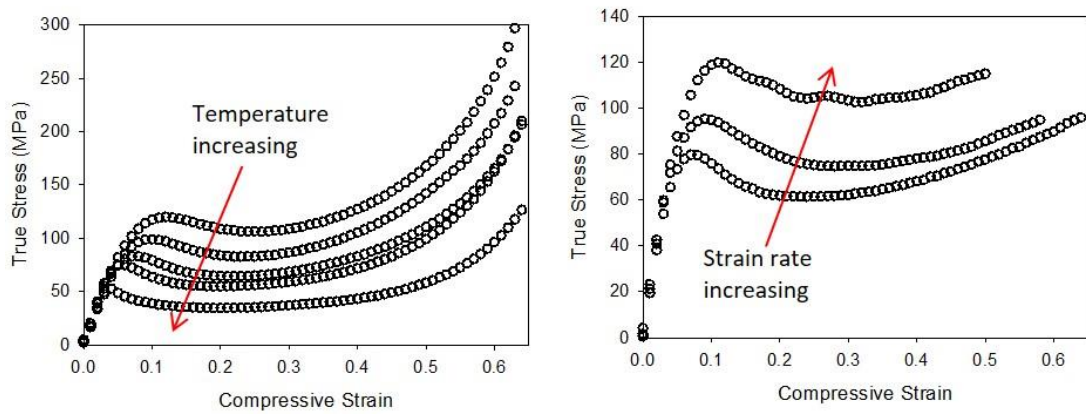
Figure 3.6: Experimental results for a) varying temperatures -60, -20, 20, 60, 120 °C b) varying strain rates for a low strain rate (0.001 s⁻¹), medium rate (1 s⁻¹) and high strain rate (3000 s⁻¹)

64
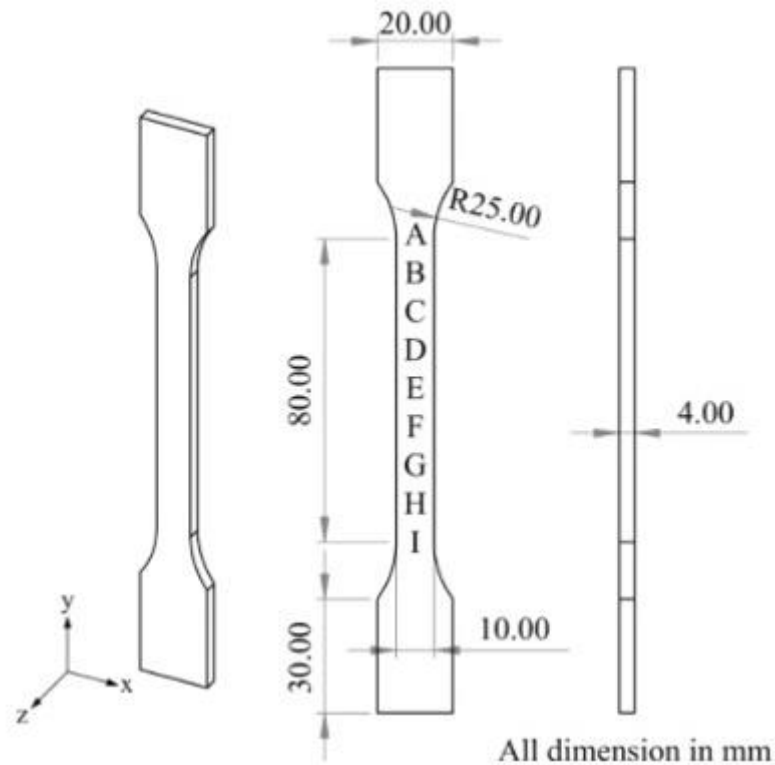
Figure 3.7: Dogbone sample dimensions used for uniaxial tensile testing, adapted from [166]

3.3.3. Initial Setup for Parameterisation

It is easiest to parameterise the model in order of the behaviour during deformation, such that the first set of parameters are those that are needed to fulfil the model sections related to the linear elasticity and initial nonlinearity approaching yield, and finally yield. For these steps, three sets of mechanical deformation experimental data are required. Firstly, varying strain rate data in compression at constant temperature, secondly varying temperatures also in compression at constant strain rate and finally DMA data.

To fully capture the yield behaviour of the material, the yield stresses of the experimental data should be extracted. Within this work it was found that a critical pre-analysis step is needed at this stage. Some polymers have tighter networks, resulting in a larger strain hardening modulus. The major consequence of this feature for parameterisation of polycarbonate is that, at yield, the component of stress attributed to conformation is larger than for materials previously modelled. Following this observation, the initial step of this parameterisation process is to

65

determine the bond-stretching yield stress, $\sigma_{y,b}$ from the experimental yield stress data, to account for the strain hardening stress contribution within the total yield stress, assuming the decomposition detailed in Figure 3.8. Adding this separation to the parameterisation process allows for a wider variety of materials to be successfully modelled.
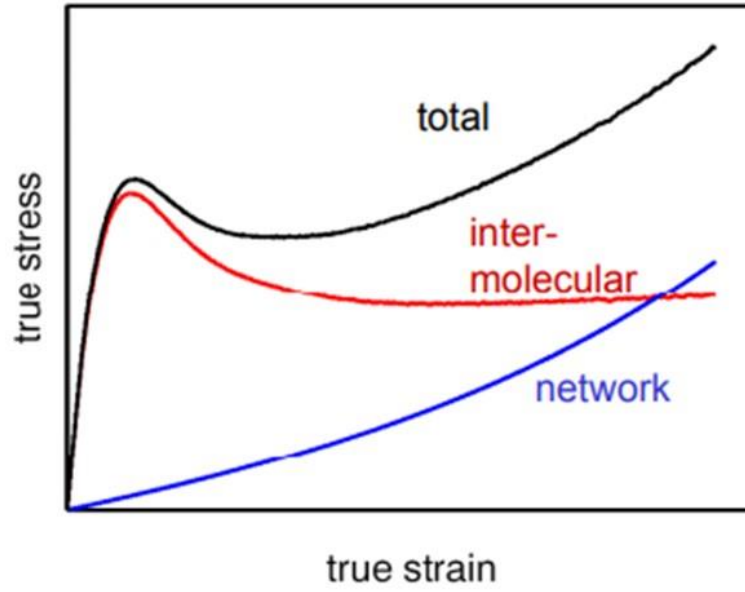
Figure 3.8: Visualisation of the deformation response for a glassy polymer decomposed into the two contributing responses, the inter-molecular resistance and the network resistance, adapted from [41]

To capture the strain hardening components of the mechanical response, an Edwards-Vilgis function with a constant flow stress was fitted to the large strain section of the experimental stress-strain response such that two parameters (N_s, α) and two stresses (the flow stress and the conformational stress at the yield strain) are extracted. The flow stress can be taken as a constant value as these tests are at a constant true strain rate. Effectively, at a constant true strain rate, after yield:

$$\sigma = \sigma_c + \sigma_{flow} \text{ where } \sigma_c = \text{fn}(N_s, \alpha, \lambda) \tag{3.26}$$
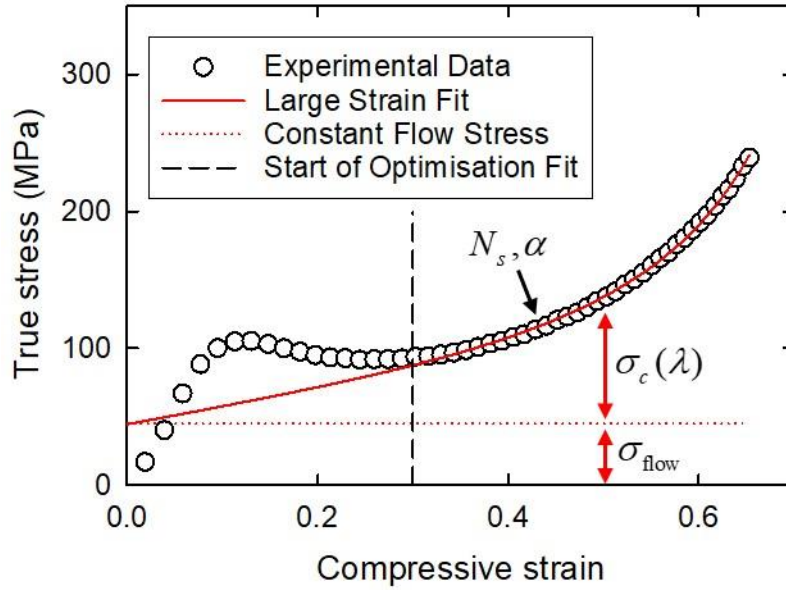
Figure 3.9: Example of fitting an Edwards-Vilgis function with constant flow to a true stress-strain curve for polycarbonate where the fit begins at yield strain of 0.3

The fit was optimised for a compressive strain > 0.3, as this is taken to be far enough from the yield strain to be able to discount yield effects. An example of this fitting process for a standard polycarbonate mechanical response is shown in Figure 3.9 for the isothermal conditions $\dot{\varepsilon} = 0.01 \text{ s}^{-1}$ and $T = -40\,^\circ\text{C}$. The fit was found to be very successful across the temperature range, $-20-120\,^\circ\text{C}$, and the isothermal strain rates $0.001 - 0.1\,\text{s}^{-1}$. This novel method allows the conformational stresses extracted from this fit to be subtracted from the total experimental yield stress to give the bond-stretching yield stress, $\sigma_{y,b}$. This method is discussed further within Section 3.3.10.

3.3.4. Activation Volume Ratio

With the bond-stretching yield stress isolated, the parameters relating to the bond-stretching equations can be determined. There are two fundamental assumptions to discuss that allow the use of equation (3.30), which is provided by Wu [67] as a yield stress Eyring equation to be applied to experimental yield stress data; the full formulation of this is given in the Appendix

A.2. Yield Equation Origin and the paper cited. Firstly, it is possible to neglect any change in fictive temperature, this is because the yield strains are small (as validated by the experimental data). Secondly, in this work it is possible to discount conformational effects at the point of yield because the contribution has now been extracted. It is therefore possible to state that, at yield, where the rate of change of bond-stretching stress is zero, $\dot{S}_j^b = 0$:

$$\frac{V_s \tau_{oct}}{2RT} + \frac{V_p \sigma_m}{RT} = \ln d_{oct} + \ln \tau_{0,j} + \ln\left(\frac{2G^b V_s}{RT}\right) \tag{3.27}$$

It is then necessary to adapt this equation for the experimental data being analysed, in this case uniaxial compression tests. It known that at yield the octahedral shear stress and the mean stress can be defined as: $\tau_{oct} = \left(\sqrt{2}/3\right)\sigma_y$ and $\sigma_m = -\sigma_y/3$. It then follows that equation (3.27) can be written as:

$$\sigma_y = \frac{6RT}{\sqrt{2}V_s \pm 2V_p}\left[\ln\left|\frac{\dot{\lambda}}{\lambda}\right| + \ln\langle\tau_0\rangle + \ln\left(\frac{\sqrt{2}G^b V_s}{RT}\right)\right] \tag{3.28}$$

where, the $\pm$ indicates the cases for tension $(+)$ or compression $(-)$.

This formulation can be used to extract the apparent activation volume, V_p/V_s because the experimental tensile and compressive yield stresses for comparable strain rates $(0.001, 0.01, 0.1 \text{ s}^{-1})$ at $22\ ^{\circ}\text{C}$ are known. The tensile and compressive yield stresses from equation (3.28) can be expressed as:

$$\sigma_{y,T} = A\left[\dot{\varepsilon} + B\right], \sigma_{y,C} = C\left[\dot{\varepsilon} + B\right] \tag{3.29}$$

where $A = 6RT/\left(\sqrt{2}V_s + 2V_p\right)$ and $C = 6RT/\left(\sqrt{2}V_s - 2V_p\right)$ for the two cases. B is an expression of the remaining constants from equation (3.28).
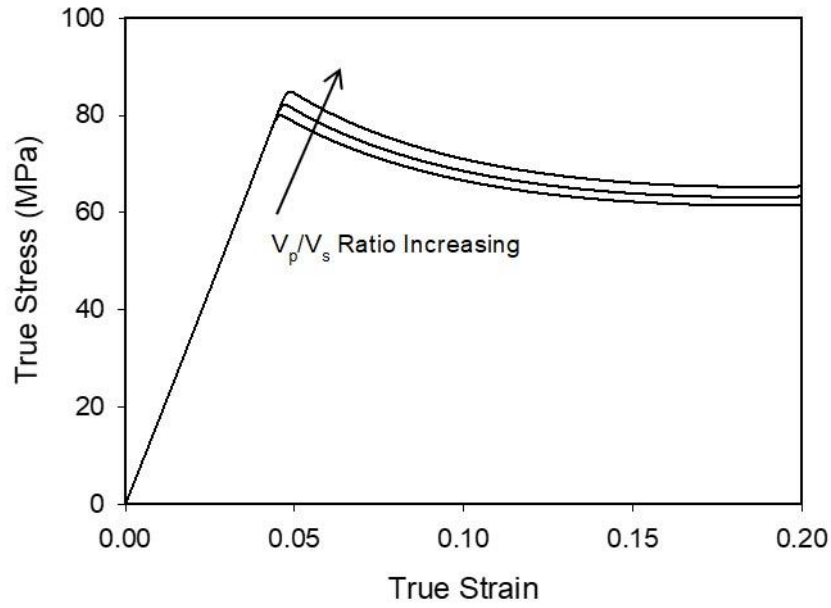
Figure 3.10: Influence of increasing the apparent activation ratio (V_p/V_s) on the yield stress on a standard quasi-static room temperature uniaxial compression test, increasing the ratio increases the yield stress

Bauwens-Crowet [167] present results for a similar ratio between the compression and tension data using the constant μ, shown in equation (3.33). In their work the μ for polycarbonate is given in the range: $0.05 - 0.075$. The value for V_p/V_s from this work is given as 0.033, given that $\mu = 2(V_p/V_s)$, this value fits within the literature range for polycarbonate.

$$\frac{|\sigma_c|}{\sigma_t} = \frac{\sqrt{2} + \mu}{\sqrt{2} - \mu} = \frac{\sqrt{2} + 2\left(V_p/V_s\right)}{\sqrt{2} - 2\left(V_p/V_s\right)} \tag{3.30}$$

3.3.5. Activation Volumes

With the apparent ratio, V_p/V_s, found, the values of the individual activation volumes are determined. This will introduce the nonlinearity of strain rate and pressure dependence to the model's yield process through the stress shift factor, a_σ. An understanding of these three parameters allows for both tensile and compressive simulations to be conducted by the same model. V_s is obtained from

69

the compression varying strain rate experimental results using the manipulation of the Eyring rate kinetics equation given in equation (3.28). For tests conducted at a constant temperature, $22\ ^\circ\mathrm{C}$, at yield a plot of $\sigma_y/T\ vs\ \ln(\dot{\varepsilon})$ will yield a linear regression as seen in Figure 3.11, such that V_s can be found in equation (3.28). The contribution of V_p is then calculated through the apparent ratio V_p/V_s found for this set of polycarbonate data, through comparing tensile and compressive yield stresses, as shown in the previous step. For this parameter extraction, it is required to use low strain rate data, to best capture the dominant behaviour of the material at these smaller strain rates.
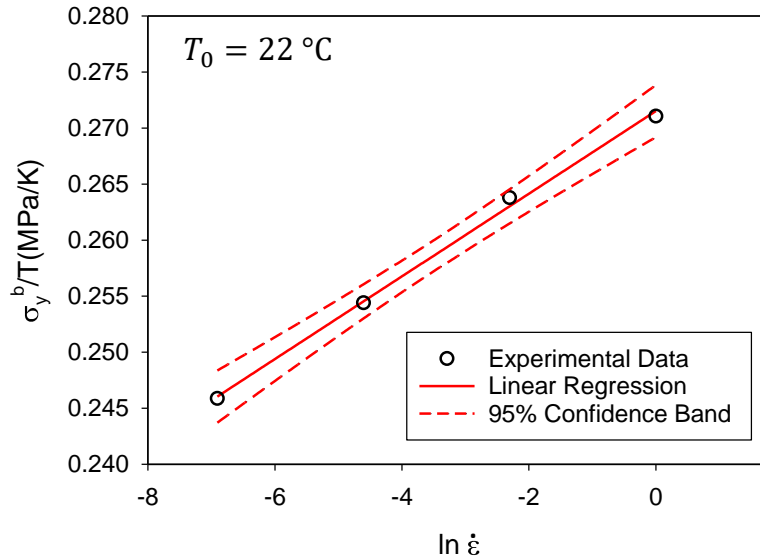
Figure 3.11: An Eyring plot for compression polycarbonate tests at 22°C, showing a linear regression (red solid line) and 95% confidence bands (dashed lines)

$$V_s = \frac{const}{m}\ ,\ \text{where}$$

$$const = \frac{6R}{\sqrt{2}-2(V_p/V_s)} \tag{3.31}$$

Where m is the gradient of the linear regression of Figure 3.11 and the constant stated can be found from the existing value of the apparent activation ratio in order to find V_s.

3.3.6. Relaxation Time

Equation (3.28) can be rearranged again to consider the reference relaxation time, τ_0^*. The intercept, c, of the same Eyring plot with gradient, m, shown in Figure 3.11 for the varying strain rates will give the mean reference relaxation time at the reference temperature of the experimental tests, $22\ °C$, seen in equation (3.35).

$$\tau_0^* = \frac{RT}{\sqrt{2}G^b V_s}\exp\left(\frac{c}{m}\right)$$

(3.32)

3.3.7. Activation Enthalpy

The next step is to add a temperature dependence into the model, related to the temperature shift factor, a_T. The temperature dependence is introduced through the activation enthalpy, ΔH, which can be obtained from temperature dependent experimental yield stress data at constant compression rate under assumed isothermal conditions. As with the varying strain rate yield stress data, it is important to isolate only the bond-stretching stresses to ensure accurate parameters are used to populate the model. Referring back to the shift factors introduced in Section 3.2.4, substituting the shift factor equations into equation (3.28), for cases with the same structure, a linear fit with a gradient equal to $\Delta H/R$ can be found from a plot of $\sigma_y/T + A\ln T$ versus $1/T$, shown in Figure 3.12, where $A = 6R/(\sqrt{2}V_s - 2V_p)$ [67].
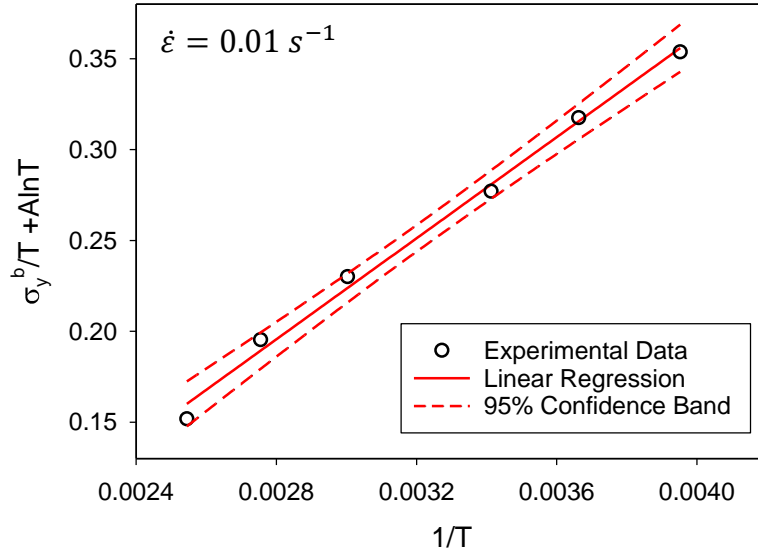
Figure 3.12: Linear fit for varying temperature isothermal tests with constant strain rate to find the activation enthalpy, showing a linear regression (red solid line) and 95% confidence bands (dashed lines)

3.3.8. Structural Evolution Parameters

Further nonlinearity enters the model through the evolution of the fictive temperature (linked to plastic strain), as structural evolution of the polymer system is considered [67]. These parameters for non-linearity are presented through the structural shift factor, a_s, equation (3.14). The three parameters to find are the Cohen-Turnbull constant, C, the Vogel temperature, T_∞, and the fictive temperature, T_f^*. To achieve this is it necessary to consider the temperature dependence of relaxation times above the glass transition. This is required as above the glass transition (i.e. $T_f = T$) the structure is always in equilibrium, and therefore equation (3.36) can be assumed:

$$\frac{\tau_0}{\tau_0^*} = a_T a_s = \exp\left[\frac{\Delta H_0}{R}\left(\frac{1}{T} - \frac{1}{T^*} \right) + \frac{C}{T - T_\infty} - \frac{C}{T^* - T_\infty} \right] \qquad (3.33)$$

Considering next the case where below T_g, the material has departed from structural equilibrium, such that the previous assumption of $T_{f0} = T$ is no longer

72

valid and equation (3.33) becomes equation (3.37). This behaviour is shown visually in Figure 3.13a for polystyrene from a previous OGR model implementation [67] and in Figure 3.13b for this study on polycarbonate.

$$\frac{\tau_0}{\tau_0^*} = a_T a_s = \exp\left[\frac{\Delta H_0}{R}\left(\frac{1}{T} - \frac{1}{T^*}\right) + \frac{C}{T_{f0} - T_\infty} - \frac{C}{T_f^* - T_\infty}\right] \tag{3.34}$$

The three parameters can now be found through the optimisation of the model parameters using the shift factors obtained from the shifted experimental DMA data shown in Figure 3.13b using equation (3.33). To achieve the mastercurve shown in Figure 3.13b, it is necessary to use time temperature superposition on the linear viscoelastic data. Time temperature superposition allows for the relation of viscoelastic material responses at different temperatures to one reference temperature if a shift in the time domain is also applied.
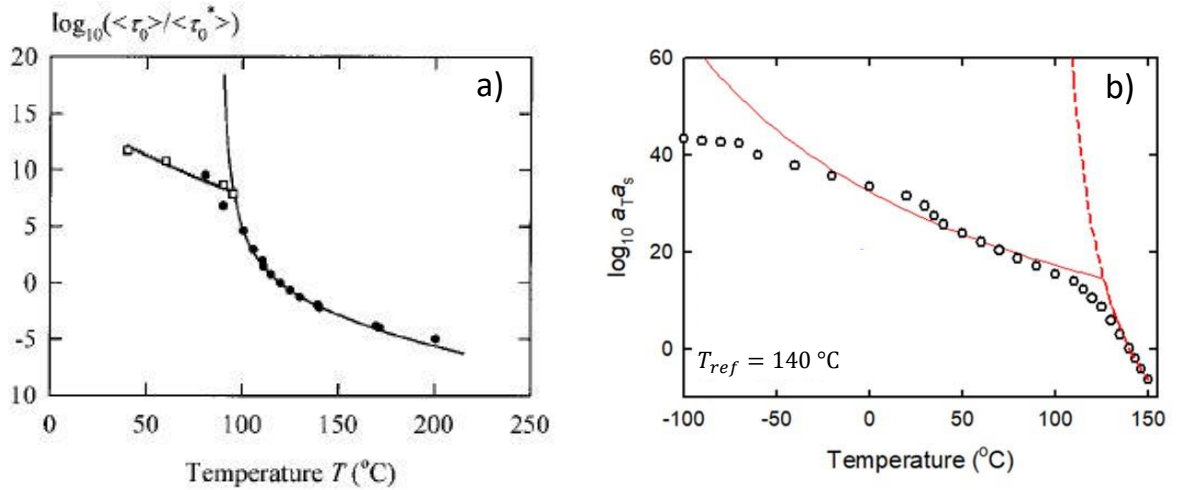
Figure 3.13: Optimisation of DMA data in both equilibrium and non-equilibrium states a) for PP (adapted from [67]) b) PC from this work at a reference temperature of 140°C

Equation (3.25) presents the fictive temperature evolution linked to structural change evolution. k is considered a dimensionless parameter linked to that rejuvenation process. It is found through an optimisation fit with experimental data. It is assumed that given the varying post-yield behaviour of different polymers that perhaps this value is different for each polymer system being modelled.

In previous versions of the OGR, Okereke is able to use the initial fictive temperature to be the temperature of the tests, while Buckley uses the glass transition temperature. Wu highlights a follow-up step to is to obtain a fictive temperature value, with an optimisation of equation (3.34).

3.3.9. Bond-Stretching Shear Modulus

The next parameter to extract is the bond-stretching shear modulus, G^b, in equation (3.9). This parameter directly affects the steepness of the curve of the pre-yield mechanical response, as shown in Figure 3.14. To find the bond-stretching shear modulus, it is first necessary to obtain the linear viscoelastic shear relaxation spectrum. This is achieved through utilising the real and imaginary parts of the complex shear modulus, G^*: the storage and loss modulus, G', G'', acquired during small strain DMA testing. The storage modulus represents the stiffness and is related to elastic behaviour and the capacity of the polymer to store energy. In contrast, the loss modulus is related to dissipated energy and thus to the viscous behaviour of the polymer. Another common value to obtain from this experimental data is the $\tan \delta$ which is the ratio of the loss and storage modulus, G'' / G', this represents the damping of the material and so is a measure of the energy dissipation.
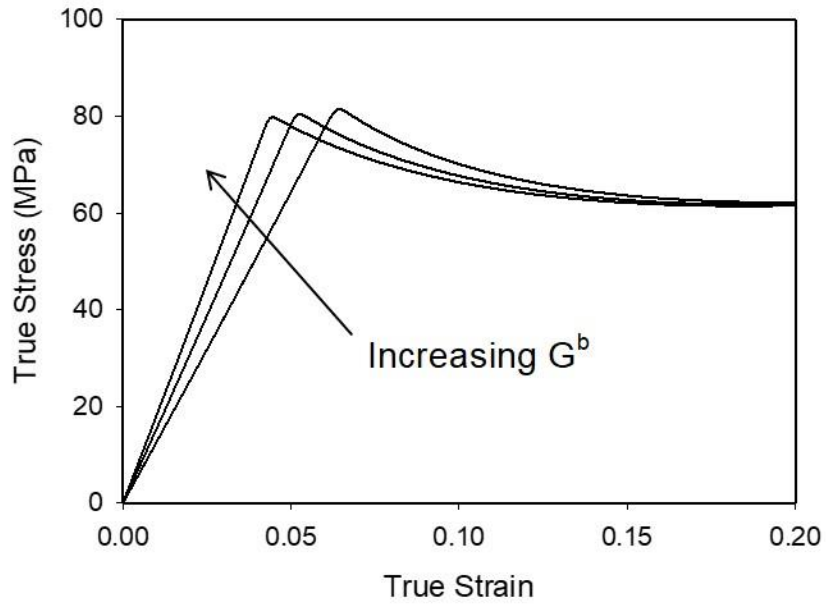
Figure 3.14: Influence in the bond-stretching shear modulus on the pre-yield mechanical response demonstrated on a true stress-true strain graph for polycarbonate at a quasi-static room temperature test condition, an increased modulus increases the steepness of the pre-yield response

The DMA tests were conducted across a temperature range of -110 °C-140 °C in 2 °C steps and traversing five frequencies in the range of 0.1-10 Hz. Depending on the specific DMA test conducted, the results may yield E^* or G^*. If a shear test has been conducted, then the shear modulus is applicable, G^*. If tensile or bending tests have been performed, then the elastic modulus, E^*, is obtained. It is therefore necessary in this scenario, where the tests were in the latter category, to convert the experimental results acquired from E^* to G^*. The conversion is assumed to be as follows through elastic relationship equations:

$$E^* = E' + iE'', G^* = \frac{E^*}{3 - \left(\dfrac{E^*}{3K}\right)}, G^* = G' + iG'', \tan\delta = \frac{G''}{G'} \tag{3.35}$$

Alternative methods were considered for this conversion and are discussed in Appendix A.3. Alternative Conversion of Shear to Elastic Modulus. This conversion then raises the question: what value of bulk modulus, K, should be used? Bulk modulus is defined as a measure to the resistance to changes in volume when deformed compressively. It would be incorrect to relate the relations in equation (3.35) through Poisson's ratio, i.e. $G = E/2(1+v)$, as Poisson's ratio is known to

75

be a viscoelastic property and will vary across a test for polymeric materials with strain rate and temperature as well as strain. It is more physically reasonable to assume that the bulk modulus does not vary. Such that the bulk modulus can be found from:

$$E = 3K\left(1-2\mu\right), E = \frac{9KG}{\left(3K+G\right)} \tag{3.36}$$

With the complex shear modulus, G^*, found from the initial E^* values, the linear viscoelastic shear relaxation spectrum is determined by employing time-temperature superposition through the pre-established shift factors. The mastercurve plot obtained from the above methodology is given in Figure 3.15. The storage modulus, $G^{'}$, curve shows a clear plateau in the response which is the value for the bond-stretching shear modulus, G^b.
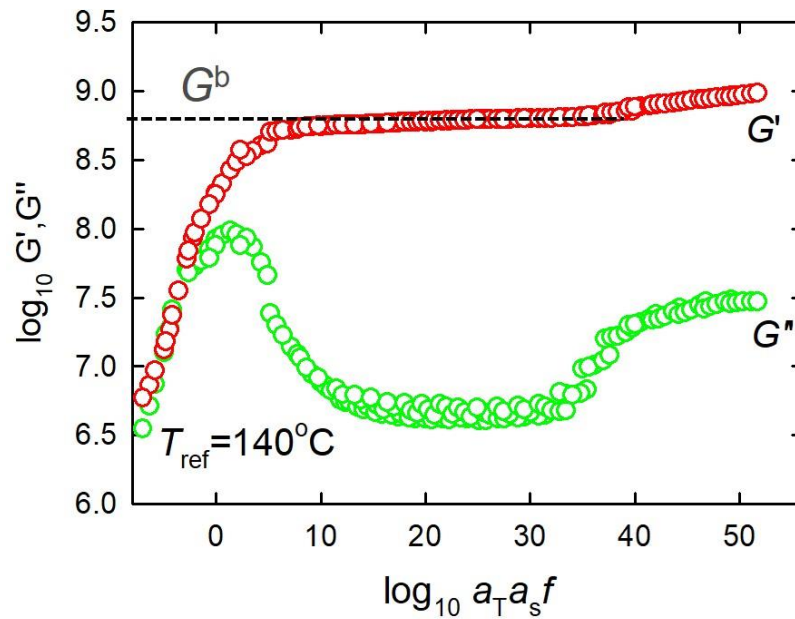
Figure 3.15: Linear viscoelastic shear relaxation spectrum of polyconate showing components G' and G" at a refence temperature of 140°C, the plateau of G' represents the bond-stretching shear modulus

3.3.10.   Conformational Parameters

With the parameters for the bond-stretching components found, the next stage is the parameterisation of the conformational part. The two parameters in equation (3.24) to be obtained are: α, the finite extensibility factor and N_s, the density of

entanglements. Previous versions of the OGR Model found the latter through relating the molecular weight between entanglements, the density and the Avogadro's number, such that: $N_s = \rho N_A / M_e$. However, as alluded to by Wu [67], there should be an adjustment for this with varying temperatures or varying molecular weights, if the stress contribution from the conformational part is considerable. It is of course known in polycarbonate that the conformational part is a major feature of the response, and, in this case, a wide temperature range is studied, therefore a new method is required.

One alternative method to parameterise the conformational part is to consider instead a strain hardening modulus, G_r, such that an equivalent hardening stress could be determined from this modulus and a relation to the draw ratio, λ [31], [89], [90]. Previous methods extracted this strain hardening modulus through first plotting the true stress versus the specific strain measure, $\lambda^2 - \lambda^{-1}$, as shown for representative experimental data in Figure 3.16. If a linear relationship between true stress and $\lambda^2 - \lambda^{-1}$ at large strains can be found, then a neo-Hookean strain hardening response can be established, taking the gradient of this plot to be the strain hardening modulus G_r, indicated with the dotted line in Figure 3.16. However, at large strains, it becomes less apparent at which range of $\lambda^2 - \lambda^{-1}$ values to average the gradient across, as the experimental date deviates from the possible linear fit and therefore from the neo-Hookean behaviour assumption. An alternative to this method is required.
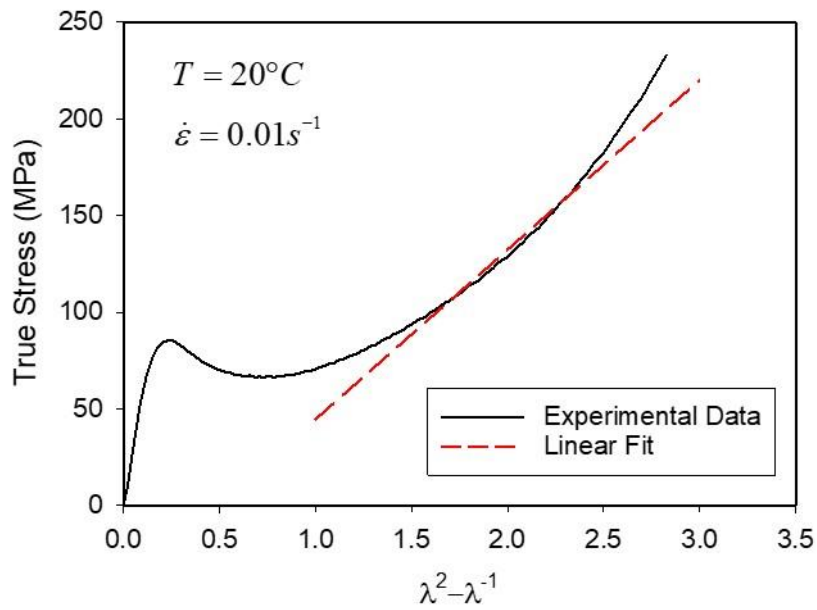
Figure 3.16: True stress versus $\lambda^2 - \lambda^{-1}$ measure for polycarbonate, highlighting the lack of linear behaviour relating to neo-Hookean behaviour. The dashed line represents a constant strain hardening modulus slope and the solid line is the experimental data for 20 °C at 0.01 s^{-1}

As introduced in Section 3.3.3, in this work a different method was adopted that is believed to not only fit this data more accurately but broadens the width of applicability of the model. An Edwards-Vilgis function with a constant flow stress is fitted to the large strain experimental stress-strain data, as shown in equation (3.26). The caveat to this optimisation, is that the test must be at constant true strain rates to allow for the constant flow stress assumption to be valid. From equation (3.26), there are two key parameters to be obtained. The density of entanglements, N_s, and the finite extensibility parameter, α. This fitting process achieved an excellent fit for low strain rates and the whole temperature range, shown Figure 3.17.
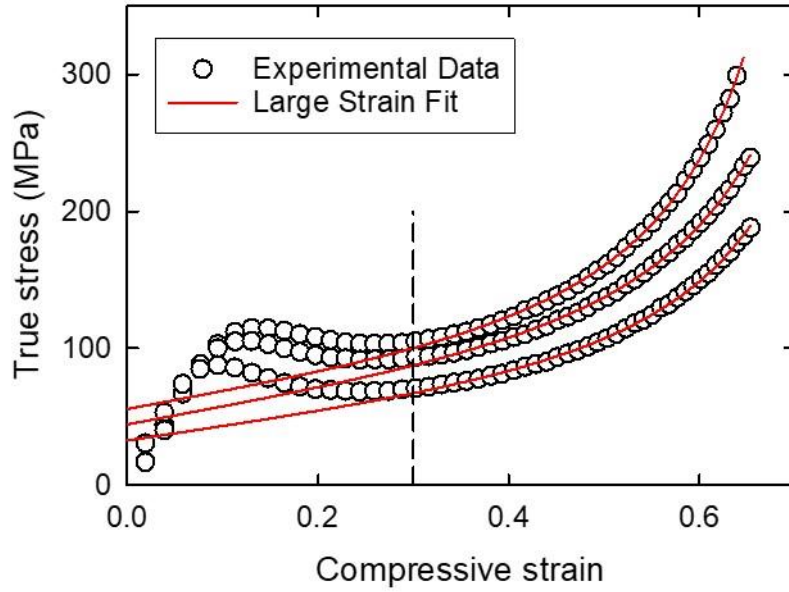
Figure 3.17: Multiple Edwards-Vilgis fits with constant flow stress optimised for multiple curves to capture the large strain, strain hardening behaviour

In conducting this study, it was found that the first parameter, α, linked to the length of chain between entanglements, varies little with rate and temperature and so can be treated as a material constant, this is shown in Figure 3.18a. This constant was therefore found to be 0.2775 ± 0.0159 by taking the average values of all valid optimisations.
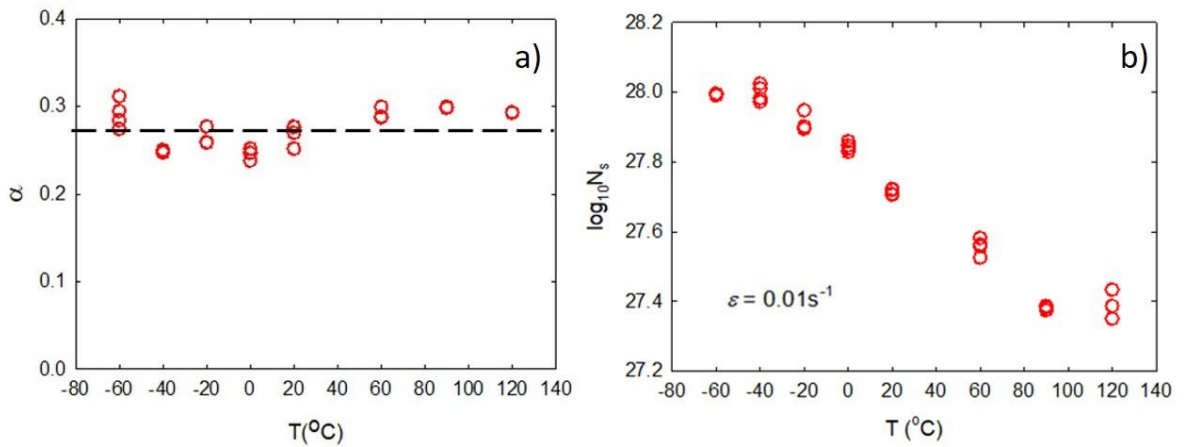
Figure 3.18: The dependence on temperature on a) α, showing no temperature dependence and b) Ns, showing a strong temperature dependence

However the second parameter, N_s, showed a temperature dependence, highlighted in Figure 3.18b, that is necessary to capture in order to simulate the physical response of the strain hardening behaviour. This dependence has been

documented previously in the literature [20]. In other versions of the OGR model [67], there was no need to account for the effects of varying temperature or rate on N_s as for previous materials, such as polystyrene, there is only a small stress contribution made by the entanglement network. To account for this rate and temperature dependence of N_s, that is observed in polycarbonate, existing shift factors can be utilised to construct a temperature dependent mastercurve for N_s, shown in Figure 3.19. An appropriate function can then be fitted to the assembled mastercurve, accounting for the temperature and rate dependencies.
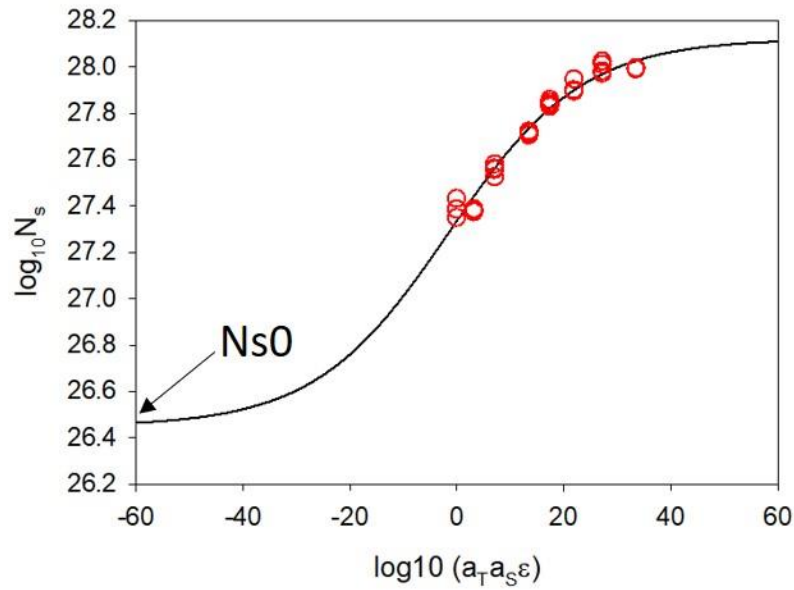
Figure 3.19: Mastercurve of N_s constructed from shift factors, showing a simple sigmoid can be fitted to this data, where the lower plateau is defined as Ns0 and can be found from entanglements dynamics theory

From Figure 3.19 the most appropriate function which can fit this data was found to be a simple sigmoid function, described in equation (3.40).

$$N_{s,0} + \frac{N_{s,\infty} - N_{s,0}}{2\left(1 + \tanh\left(n\tau_{Ns}\dot{\bar{\varepsilon}}_{Ns}\right)\right)} \qquad (3.37)$$

where, $N_{s,\infty}, n$ and τ_{Ns} are fitting constants. At sufficiently low rates or high temperatures, the network density should tend towards a lower bound, shown as the lower plateau of Figure 3.19 as $N_{s,0}$. This can be found from entanglement

dynamics [89], described in equation (3.41). This lower bound is far from all experimental data and so is not very important.

$$N_{s,0} k_B T = G_{n0} = \frac{\rho R T}{M_e}$$

(3.38)

where, G_{n0} is this initial shear modulus relating to entanglements and M_e is the entanglement molecular weight.

The fit shown in Figure 3.17 is limited to isothermal tests. For adiabatic medium to high rates the mastercurve shown in Figure 3.19 facilitates the calculation of the conformational stress at yield.

Table 3-1: Full list of parameters for polycarbonate Lexan™ Resin 103R with values and standard deviations provided alongside sources. .

Parameter	Value (±std)	Source
Bond-Stretching Terms		
T_g (°C)	145	Experimental Paper [133]
$V_{s,\alpha}$ (m^3/mol)	0.01465±0.027	Figure 3.11, Equation (3.31)
V_p / V_s	0.0327	Equation (3.29)
$\tau^*_{0,\alpha}$ (s)	4.25x10^{29}± 3.09 x10^{28}	Figure 3.11, Equation (3.32)
ΔH_α (J/mol)	2.96x10^5±5787	Figure 3.12
C (°C)	3606±261	Figure 3.13
T_∞ (°C)	91.5±5.3	Figure 3.13
$T_{f,0}$ (°C)	126.5±1.9	Figure 3.13
$G^{b,\alpha}$ (Pa)	5.8x10^8	Figure 3.15
k_0	300	This work, fit to experimental results
Conformational Terms		
α	0.272±0.0159	Figure 3.18
$N_{s,0}$	26.45	Figure 3.19, Equation (3.37)

3.4. Modelling Setup

In Figure 3.20 a flowchart is presented to explain the formulation of the above constitutive model into a usable MATLAB code. A MUMAT is created, or a MATLAB User Material model, that can successfully run the desired simulations. The MUMAT set-up described is easily transferable to FEA software, such as Abaqus, as it follows a similar formulation to that of a typical VUMAT.
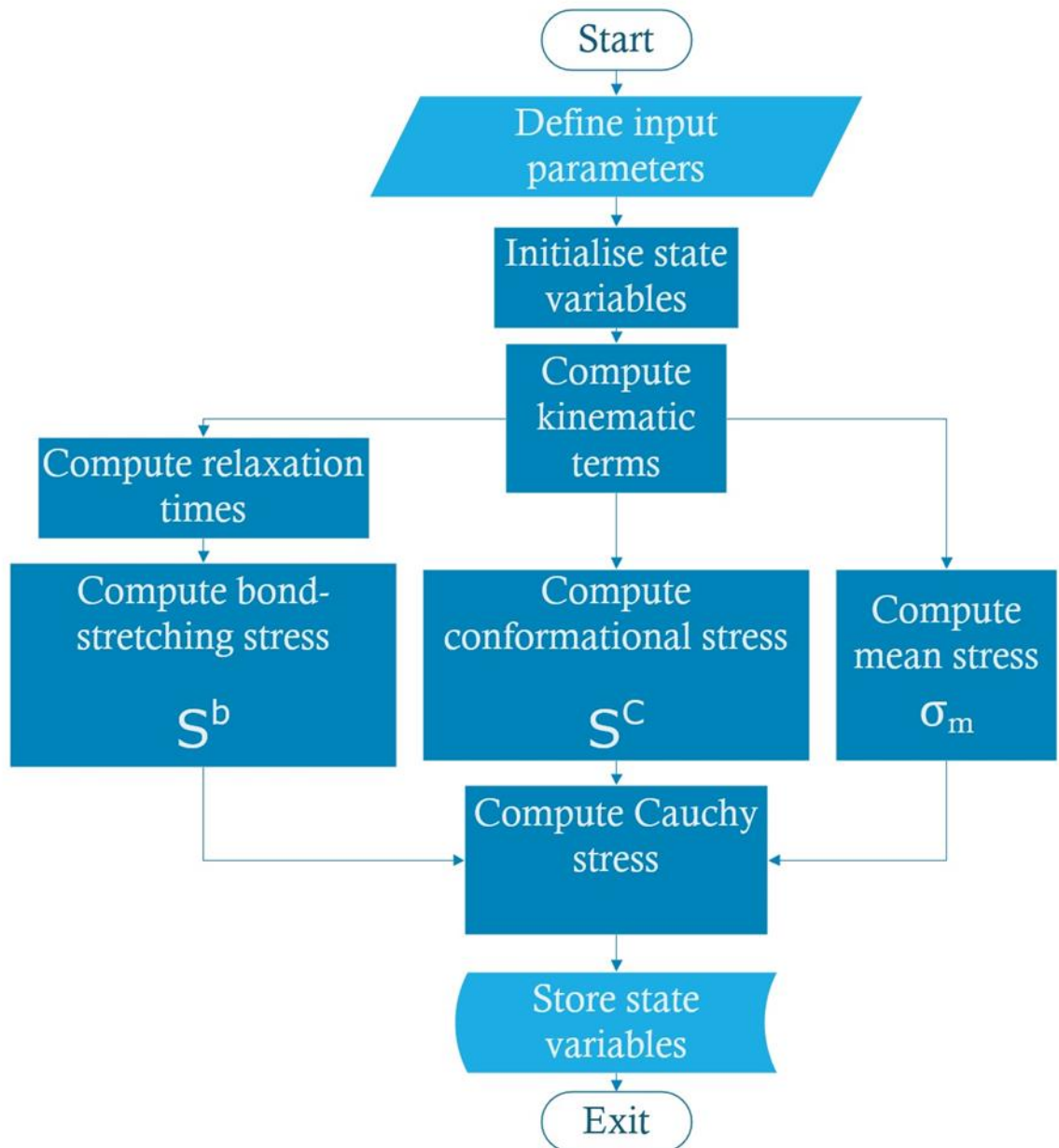
Figure 3.20: A flowchart representing the programming map for this constitutive model

3.5. Simulations

In this section the simulation results are presented for the model and parameters shown in this Chapter. The mechanical responses of the simulations are compared to experimental results and the fit across the deformation range is assessed. Varying strain rates and temperatures simulations were conducted to highlight the capabilities of the model to capture a range of test conditions. In subsection 3.5.4 a comparison of tensile and compressive simulations is provided.

3.5.1. Initial Simulation

Figure 3.21 shows the true stress versus true strain responses for an uniaxial compression test at $\dot{\varepsilon} = 0.01 \text{ s}^{-1}, T = 22 \text{ }^{\circ}\text{C}$. The full simulation is compared to the experimental results and the decomposition into the bond-stretching and conformational components are shown. These test conditions should be the most accurate to capture as no temperature or rate shift from reference conditions are required.
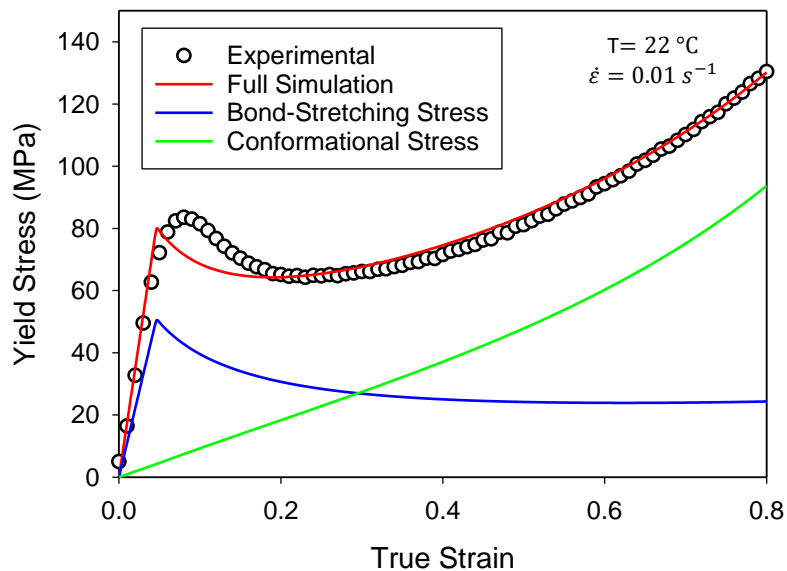
Figure 3.21: Full true stress- true strain simulated response for 0.01 s⁻¹ and 22 °C (red line) compared to the experiment results (circles) with the bond-stretching (blue line) and conformational stress (green line) contributions shown

The simulated result fits well to the experimental data, capturing all the key elements of a mechanical response of polymers discussed in Section 2.2.3. The yield stress value is $80\,\mathrm{MPa}$ compared to $83.5\,\mathrm{MPa}$ for experimental results. The yield drop driven by structural evolution due to plastic strain is captured and finally the second rise in true stress related to strain hardening at large strains is simulated. The most notable difference in the experimental and simulated results is that the model predicts an earlier and sharper yield than is seen in experimental data. This modelling artefact has been seen in the literature before. This sharpness would be reduced by the introduction of a spectrum of relaxation times, capturing a wider range of the activation barriers being overcome to cause flow in glassy polymers. Inadvertently, this may also lead to a value of yield strain closer to the experimental value. The smaller yield strain also affects the conformational stress predictions slightly. In Appendix A.5. Multi-mode Spectrum Results a 12-mode spectrum is compared to the single mode results presented in Figure 3.21. While the multi-mode case does improve the fit as expected from the literature, the difference is minimal and thus given the additional complications from high strain rates focused on in Chapter 4 it is not worth the extra computational time.

3.5.2. Varying Temperature

Having assessed the full response for the simplest condition, next the effect of temperature is evaluated, initially on the yield stress results. Figure 3.22a firstly highlights the key trend that yield stress increases with a decrease in temperature. For the standard temperature range, $-20\text{-}120\,^{\circ}\mathrm{C}$, the simulated yield stresses correspond with high accuracy to the experimental results. However, there is a slight discrepancy between the simulations and the experimental results. A more accurate measure of the success of the bond-stretching component is shown in Figure 3.22b, where just the bond-stretching yield-stresses, $\sigma_{y,b}$, are compared; this then accounts for the small error in simulated conformational yield stress originating from a smaller simulated yield strain than measured experimentally. In Figure 3.23 the full mechanical simulation response is compared to the experimental results for three temperatures $\left(20-90\,^{\circ}\mathrm{C}\right)$.
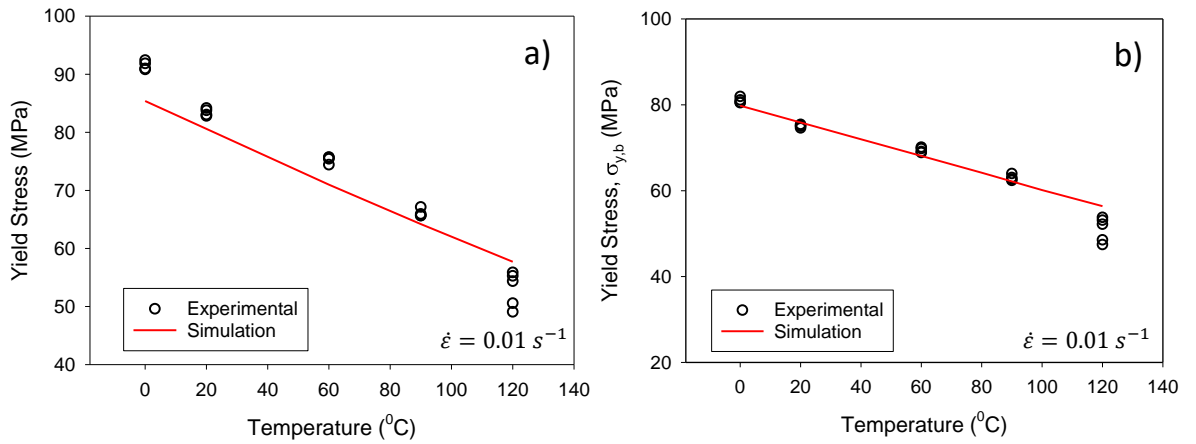
Figure 3.22: Yield stress simulation results for varying temperature isothermal tests at 0.01s⁻¹ compared to experimental results for a) the full yield stresses, b) the bond-stretching contribution of the yield stress
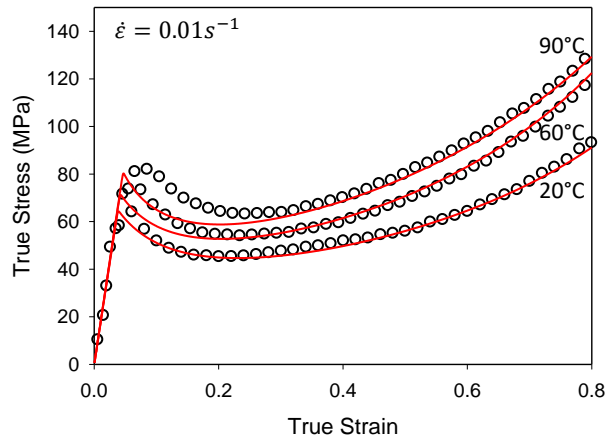
Figure 3.23: Full true stress versus true strain simulations compared to experimental results for polycarbonate at 20,60,90°C for a uniaxial compression test at 0.01s⁻¹

3.5.3. Varying Rate

The next set of results to present and analyse are the varying strain rate simulations. In Figure 3.24 the full true stress-strain curves of three quasi-static rates, $0.001, 0.01, 0.1 \text{ s}^{-1}$, under isothermal conditions with an initial test temperature of $T = 22$ °C are considered. The simulated strain rate are taken to be constant true strain rate to be the same as the experimental conditions. Assessing the full stress-strain response, the major features are again captured, seeing an equivalent yield stress, a comparable yield drop and then a strain-hardening equivalent to the experimental results. The major trend of increasing

yield stress with increasing strain rate is also achieved, shown in Figure 3.24. As with the varying temperature data, the yield strain is smaller for the simulation than the experimental value and the yield peak is sharper. As an artefact of this, the minimum of the yield-drop, driven by strain-softening behaviour, is modelled to be at a smaller strain than the experimental value, but critically the yield drops are comparable, implying that the structural evolution is being captured.
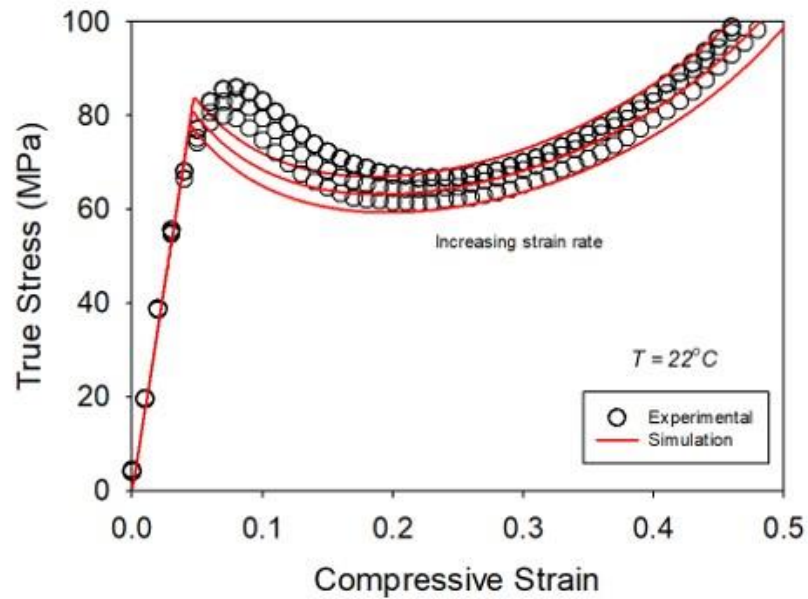
Figure 3.24: Varying strain rate results for isothermal tests 0.001, 0.01, 0.1s[-1] at an initial temperature of 22°C, simulations shown as red lines, circles representing experimental data

The parameter κ was obtained by matching the post-yield behaviour to experimental data. To highlight the effect of the parameter κ on the post-yield strain-softening of the simulated deformation, Figure 3.25 shows stress-strain responses where only k varies.
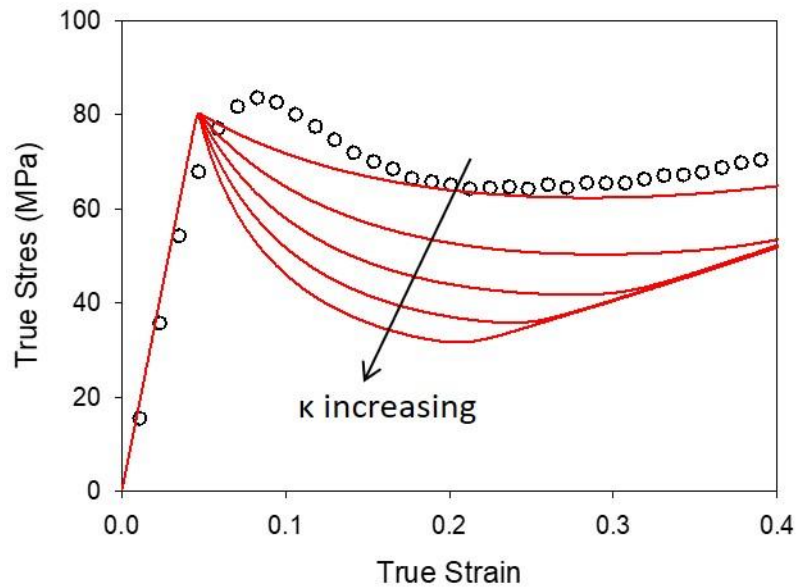
Figure 3.25: The consequence of varying the parameter k shown on the post-yield response for true stress- true strain curves at 0.01 s⁻¹ for 22 °C, increasing k increasing the effect of the de-ageing and so the yield-drop

3.5.4. Tensile Results

Another exploration of the model is to simulate tensile tests and compare to experimental results, specifically the yield stress values obtained and the nature of necking in these conditions. To make the comparison between simulation and experimental results, it is important to note strain rate will not be constant throughout the sample and so the mechanical response curve will vary in different parts of the sample, shown in Figure 3.26. The dogbone shape used to create the test samples is shown in Figure 3.7. It is observed that close to the initial localisation, there will be a very quick change in strain rate during neck formation.
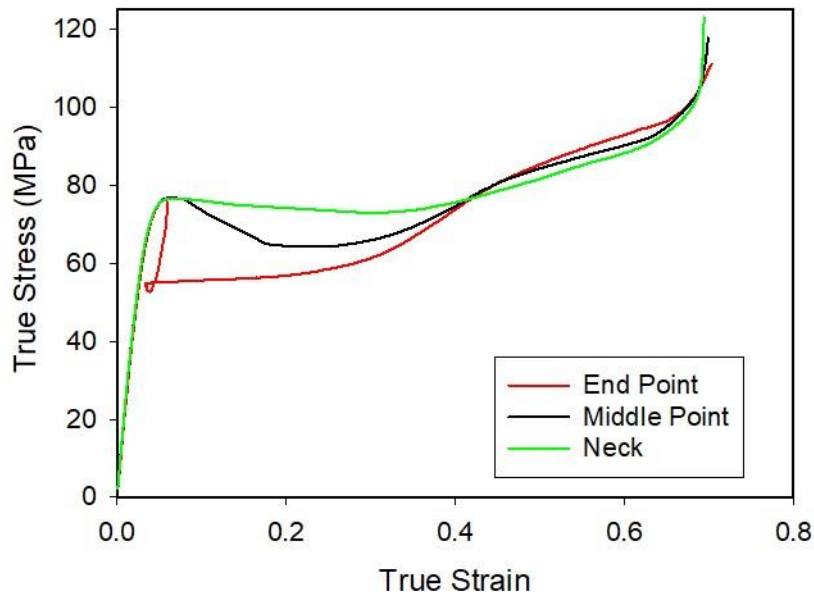
Figure 3.26: Three true stress strain curves for a tensile test highlighting the inhomogeneous deformation as local effects dominate the mechanical response

There are no modifications made to the parameters or the model for tensile simulations, only the input test conditions which change from compressive to tensile. The resulting simulations successfully predict the yield stress in tension for quasi-static tests, shown in Figure 3.27a. These yield stresses are lower than the equivalent compression results, as expected from theory. In Figure 3.27b, the full stress-strain curve is compared, critically observing the minimum flow stress relating to the neck is equivalent at $64 \, \text{MPa}$. At larger strains, the behaviour is seen to deviate from the experimental curve. There are a few possible explanations for this difference. Mainly, this is simulated isothermally, but in the sample, there will be regions of higher strain rates relating to localisation, leading to the potential of local adiabatic conditions. It is likely that the sample is between isothermal and adiabatic conditions.
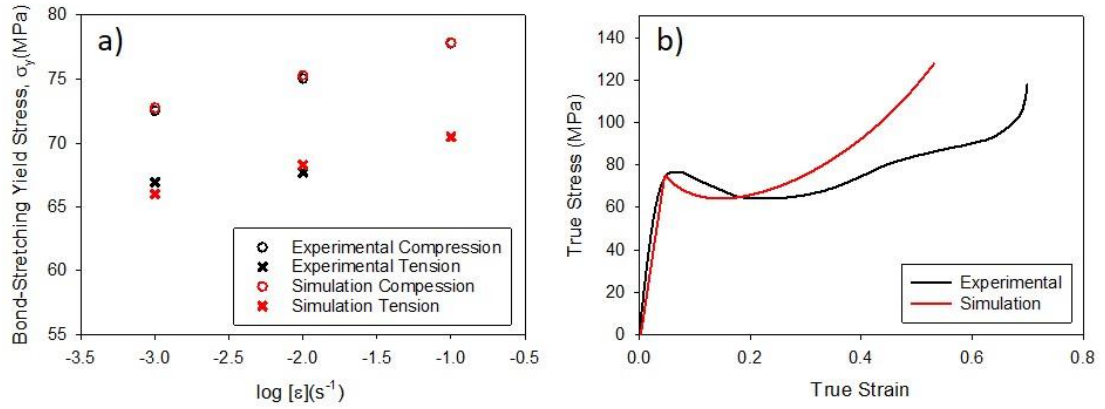
Figure 3.27: Tensile simulation results compared to experimental values a) yield stress responses, b) full true stress-strain curves considering the middle point of the sample

3.6. Conclusions

This chapter introduced a constitutive model for the deformation of amorphous polymers focusing on low strain rates and temperatures associated with the α-relaxation. The model can be divided into two significant contributions, the bond-stretching part, linked to intermolecular resistance and the conformational part, due to the rubbery network resistance. The model presented follows the framework of the Oxford Glass Rubber model. The post-yield response is considered through evolution of a fictive temperature to represent the structural evolution driven by a plastic strain invariant. The full kinetics of fictive temperature evolution are presented for the first time for polycarbonate, over the semi-empirical version used within previous versions of the OGR model.

Within the second half of this chapter, the parameterisation process required to populate this model for polycarbonate is detailed. Improvements and novel versions of parameterisation techniques have been discussed, including considerations for tight networks polymers such as polycarbonate. Conformational parameters are obtained from optimisation of experimental data through fitting an Edwards-Vilgis fit with a constant flow stress at strains far from yield, generating remarkably successful fits to experimental data. A rate and temperature of the dependence of the density of entanglements, N_s, is included,

to best capture the large conformational stresses originating in polycarbonate and the dependencies of this on test conditions.

The final section presents the initial simulation results for polycarbonate for low strain rates, using the model and parameters introduced in this Chapter. Varying rates and varying temperatures are explored and successful trends in data were captured. The model simulates the full mechanical response, including the complicated post-yield behaviour with the yield drop followed by strain-hardening. With the model and parameterisation established for strain rates and temperatures connected with the α -relaxation process, the next chapter will discuss the method and associated challenges with extending this model to high-strain rates that traverse the β - relaxation process.

Further exploration allowed the successful modelling of tensile tests. Both the yield stresses and the minimum stress associated with the neck were captured, however the intricacies of localisation of strain rate and inconsistent adiabatic heating at large strain behaviour for tensile tests resulted in deviation between simulation and experimental results at large strains.

4. Extension to High-Rate

4.1. Introduction

Chapter 3 introduced the fundamental model and parameterisation process developed for this work. Within this chapter the extension of the model to account for high rate behaviour will be carried out. Initially, an assessment of the experimental results at higher rates is conducted. There are two fundamental changes that occur as the rate range is traversed to higher strain rates, as introduced in Chapter 2. The first fundamental change is that the test environments will change from isothermal to adiabatic conditions, this is discussed in Section 4.3.1. Four energy components are considered; elastic strain energy, structural change energy, conformational energy and dissipated energy. The second change to understand and implement is the influence of the secondary transition, the $\beta-$ transition. In this chapter, the material in focus will continue to be polycarbonate, which has a $\beta-$ transition of approximately -95 °C [19].

In Section 4.4, the extension of the parameterisation process to high rates is presented. In Section 4.5, the simulation results are shown and discussed for varying temperature including the low temperatures (down to -60 °C) and then for varying rates including the high strain rates (up to 3000 s^{-1}). The resulting temperature rises for adiabatic varying strain rate tests are compared to experimental results. In Section 4.7, a discussion of the results and the novel procedures in this chapter are considered. Finally, conclusions are provided in Section 4.8.

4.2. Experimental Data Evaluation

To fully understand the effect of extending the model to high rates, an assessment is performed on the high strain rate experimental results. The experimental work was performed by Song et al [133]. This analysis allows the understanding of trends in the mechanical responses needed to capture and simulate the behaviour

of the polymer and secondly to assess which data can be used to parameterise the additional parameters required to extend the model.

Initially, the varying rate response is assessed as it is extended to medium and high strain rates. Figure 4.1 shows the yield stress responses for polycarbonate under uniaxial compression for rate $\left(0.001-3000\ \text{s}^{-1}\right)$ and temperature dependence $\left(-60\text{-}120\ °\text{C}\right)$. A universal testing machine (Instron 5980), with an environmental chamber for temperature control was used for the low strain rate experiments. The medium rate experiments were done on a hydraulic machine, a long split-Hopkinson pressure bar (LSHPB) was used for the range $400-700\ \text{s}^{-1}$ and finally the $1000-3000\ \text{s}^{-1}$ compression rate range was conducted on a standard split-Hopkinson pressure bar. As expected from literature, the dependence on strain rate changes at higher rates, and this is associated with the $\beta-$transition. It is observed that the yield stresses deviate from a linear relationship to become bilinear, shown in Figure 4.1.
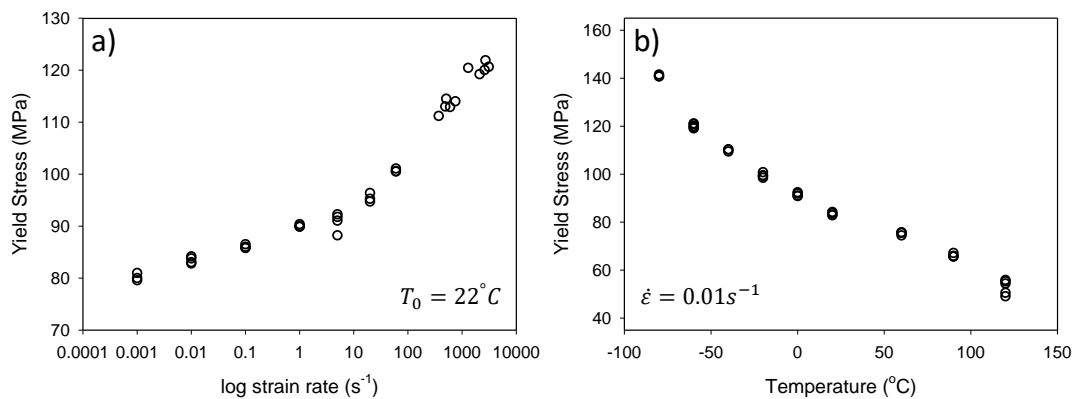
Figure 4.1: Experimental yield stress results for polycarbonate uniaxial compression tests for a) varying strain rates with an initial test temperature of 22°C and b) varying temperatures with a constant strain rate of 0.01s-1

The response of the varying temperature experimental yield stress data when extended to lower temperatures, shown in Figure 4.1b, highlights further the influence of the $\beta-$transition. In Figure 4.1b, at close to $-20\ °\text{C}$, a deviation from the α -response is seen, as the $\beta-$transition is approached. An estimation of the values for the α - and β -transitions can be observed within small strain viscoelastic experiments when the $\tan\delta$ is analysed. Figure 4.2 shows the

response of the loss tangent (tan δ) for polycarbonate as a function of temperature, where the narrower but larger peak at 145 °C is associated with the α-relaxation, or the glass transition. The broader, less well defined peak at approximately −90 °C corresponds to the β-relaxation.
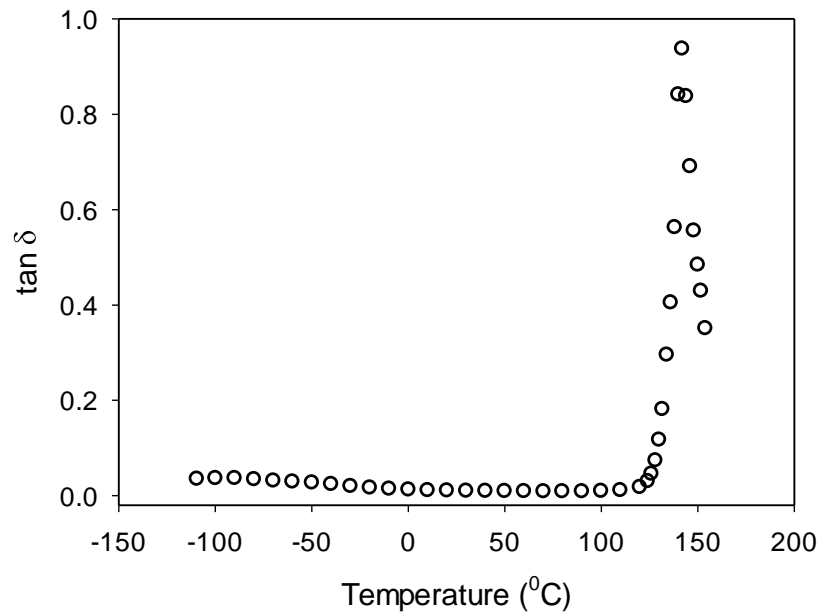
Figure 4.2: The loss tangent (tan δ) for polycarbonate as a function of temperature highlighting two peaks at the two transitions, α and β

4.3. Modelling Updates

In this section all the new developments to the model presented in Chapter 3 required to capture rates and temperatures related to the β-relaxation are introduced.

4.3.1. Adiabatic Heating

During large strain deformations, some polymers will reach large plastic strains pre-failure. While at lower strain rates the energy from plastic deformation has sufficient time to dissipate into heat, at higher strain rates the heat will be trapped, and resultant thermal softening will occur. Therefore, as the strain rate range is extended past quasi-static strain rates, the test conditions cease to be isothermal

and become adiabatic. It is possible to calculate the expected strain rate associated with transition from the thermal diffusivity of the polymer [133], [147].

$$\alpha = \frac{k}{\rho C_p} \tag{4.1}$$

$$l_t = 2\sqrt{\alpha t} \Rightarrow t = \frac{1}{\alpha}\left(\frac{l_t}{2}\right)^2 \tag{4.2}$$

$$\dot{\varepsilon} = \frac{1}{t} \tag{4.3}$$

where α is thermal diffusivity, k is thermal conductivity $\left(0.2\ \mathrm{Wm^{-1}K^{-1}}\right)$, ρ is the density $\left(1.2\ \mathrm{gcm^{-3}}\right)$ and C_p is specific heat capacity $\left(1.2\ \mathrm{Jg^{-1}K^{-1}}\right)$. Utilising these and the length of the specimen, the timescale (t) of thermal diffusion can be estimated. From equation (4.1)-(4.3) the transition is found to be $0.6\ \mathrm{s^{-1}}$.

To correctly simulate the behaviour of these polymers at higher strain rates it is essential to accurately account for adiabatic heating. One method to achieve this is to account for energy storage mechanisms that occur during deformation. A thermo-mechanical coupling is implemented within this model, as first demonstrated for the OGR model by Buckley [69], introduced in Chapter 2. The energy input from the test can be divided into the following four contributions: elastic strain energy, structural change energy, conformational energy and dissipated energy. It is expected that plastic deformation will be the main cause of heating.

Elastic Strain Energy

The first energy sink will come from the bond-stretching part of deformation. The energy is stored in the elastic strain and acts for small strains in the initial elastic region of the strain-strain response. It is equivalent to an elastic spring, compressing or releasing, and thus the energy is recoverable. For large strain deformations it is expected that this energy will be an increasingly smaller

proportion of the overall energy, but at small strain it will be the dominant contribution.

Structural Change Energy

As the polymer deforms, some energy must go towards changing the structure of the polymer. This unrecoverable energy going towards structural change should be accurately accounted for, as less energy will go towards temperature rise contributions and so the overall temperature rise will decrease. To assess the structural change energy, the change of enthalpy is considered as defined through an enthalpy fictive temperature, discussed in Chapter 2. Previous literature [69] raises the possibility of multiple fictive temperatures, representing different physical properties, e.g. structure or enthalpy. The first, $T_{f,\sigma}$, is the fictive temperature associated with the stress relaxation, and is normally referred to as the mechanical fictive temperature. As this is the main interpretation for this thesis all equations containing T_f refer to this mechanical description. The second is the fictive temperature associated with enthalpy, $T_{f,h}$. Buckley suggests [69] that it would be more appropriate to use the fictive temperature associated with enthalpy, $T_{f,h}$, to relate to the structural change energy, as discussed in Chapter 2. It has been previously suggested these two fictive temperatures are not the same value, but the exact relationship is unknown. With no access to superior knowledge it is assumed that $\varphi = 1$ in equation (4.4) such that:

$$\dot{T}_{fh} = \varphi \dot{T}_f \tag{4.4}$$

Conformational Energy

As the polymer deforms to large strains, conformational behaviour must be included. It can be considered as a non-linear entropic elastic spring that stores energy as heat, and such is recoverable energy alongside the elastic strain energy previously discussed.

Considering the input energy and subtracting the three energy sinks above, the remaining energy will be dissipated energy. This is analogous to a dashpot response, originating from viscous deformations as molecules slide past each other. This contribution will be all go towards temperature rise. Considering all four energy sinks, equation (2.18) will become the equation from the literature [69] introduced in Section 2.3.3.

The adiabatic heating itself arises from two sources, the dissipation of these flow stresses and the entropy elasticity of the entanglement network. The temperature rise under fully adiabatic conditions is presented in equation (4.6).

$$\rho c \dot{T} + \boldsymbol{\sigma}^b : \mathbf{D}^e + \dot{A}^c = \boldsymbol{\sigma} : \mathbf{D} - \rho \Delta c \dot{T}_f \tag{4.5}$$

$$\dot{T} = \frac{1}{\rho c} \left[\sigma : D - \sigma^b : D^e \right] - \frac{\varphi \Delta c \dot{T}_f}{c} \tag{4.6}$$

Adiabatic Heating Parameters

With a methodology for the implementation of adiabatic conditions presented, the next step required is the parameterisation of equation (4.6). From this equation there are three parameters needed: the density, ρ , the Δc ,which is the heat capacity difference for a relaxation process, and finally the specific heat capacity. The density can be quoted from literature [133], $\rho = 1.2\text{g cm}^{-3}$. Previously, the parameter Δc was found through an optimised fit of simulated and measured temperature rises [6], [69]. This had some success in the literature results but there is an alternative method based on experimental measurements. The remaining part of the effective heat capacity to be acquired is therefore Δc , which can be found from heat-cool-reheat differential scanning calorimetry (DSC) data, shown in Figure 4.3. Taking the second heating curve, to minimise historical artefacts, there is a clear drop in heat flow as the α - transition is traversed, confirming the T_g value as ~ 145 °C and allowing a value of Δc to be obtained.
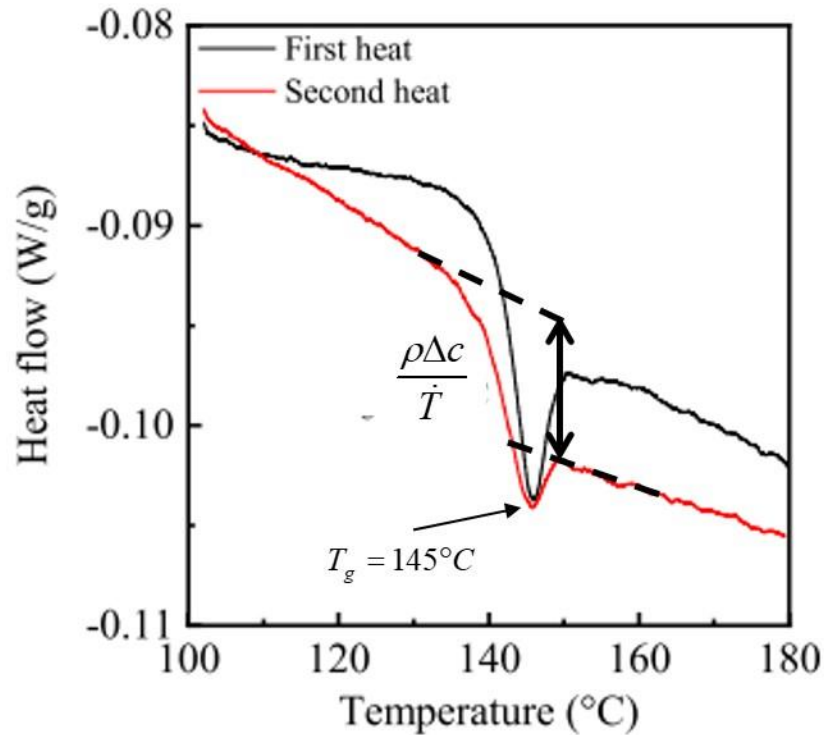
Figure 4.3: A Heat-cool-reheat DSC measurement for polycarbonate at heating rates of 2°C/min

Finally, the value of specific heat capacity, c, needs to be found. One simple method is to obtain the specific heat capacity experimentally through modulated differential scanning calorimetry (MDSC) at the test temperature, as shown in Figure 4.3. In some literature, the value of c was assumed to be a constant across temperature, strain and strain rate. Specific heat capacity is defined as the amount of heat required to increase one unit of mass by one unit in temperature. Specific heat capacity is reported to be temperature dependent [166], as the specific heat capacity refers to the internal energy of the system. During MDSC it is possible to measure specific heat capacity of polymeric materials across a temperature range, shown in Figure 4.4. From this a clear dependence on temperature is extracted: $c_p = 0.0039\text{T}+0.975$ for the range -80-140 °C. A different behaviour is observed at high temperatures close to the glass transition, $T_g = 145$ °C, but these high temperatures are not approached during the rates explored in this work, even when considering the maximum temperature rise of the highest rates.

97
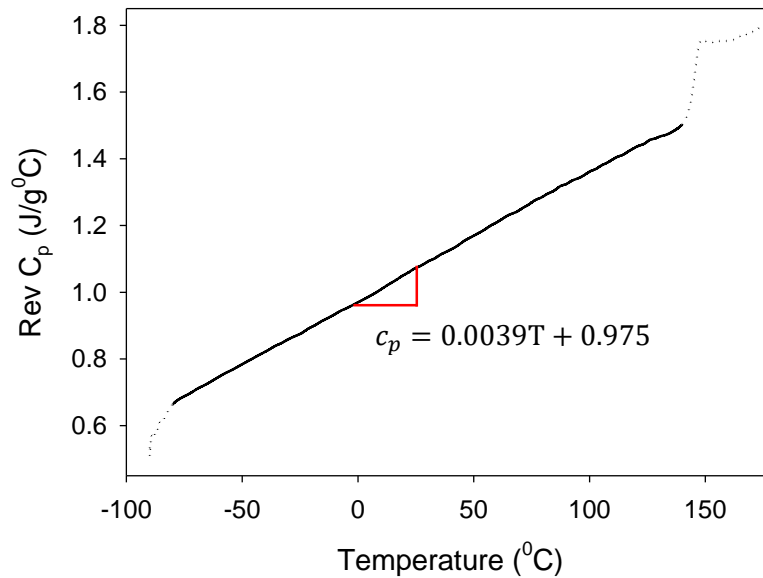
Figure 4.4: Temperature dependence of the specific heat capacity for polycarbonate using MDSC

This subsection presented the methodology and parameterisation for including adiabatic heating into the model. The addition of adiabatic heating can therefore be included with minimal additional experimental work and without the fit of parameters to adiabatic behaviour or temperature rise within the experimental data.

4.4. Updated Parameterisation Method

In Section 4.2, a series of trends were presented highlighting the change in mechanical behaviour with the extension of the strain rate and temperature ranges. This section addresses the updates required for the model and the revised parameterisation process required.

4.4.1. Initial steps

Similar to the low rate, α-relaxation, case presented in Section 3.3.3, the first step will be to isolate the bond-stretching yield stress, $\sigma_{y,b}$, from the total experimental yield stress. For the low rate cases, the optimisation for an Edwards-Vilgis function with a constant flow stress was successful enough to extract an appropriate estimation of the conformational part of the yield stress. However, this

98

optimisation is not designed for isothermal tests, as the assumptions surrounding constant flow stress will breakdown.

An alternative method is used to obtain this high rate behaviour, Firstly, it is assumed that adiabatic heating has a negligible effect at yield strain. Secondly, it is assumed that the mastercurve, detailed in 3.3.10 and Figure 3.19, can predict a value for the density of entanglements, N_s, for these medium and high strain rates. Finally, the assumption is made that the constant value for the finite extensibility factor, α, averaged for isothermal quasi-static tests $(-60-120\ \text{°C})$, is the same value at high strain rates. With the values for N_s and α found for each strain rate, the full Edwards-Vilgis energy function presented in equation (3.24) is used to obtain the experimental conformational yield stresses for these higher rates.

With the bond-stretching yield stresses separated for all the experimental data, the parameterisation process introduced in Chapter 3 can be applied to high strain rates. Figure 4.1 showed that on investigating a wider strain rate range, a single process Eyring plot is no longer sufficient to capture the yield stress data. Instead, the Ree-Eyring theory, introduced in Chapter 2, can be applied to describe the multiple relaxation processes emerging, i.e. a two process Eyring plot, highlighted in Figure 4.5.
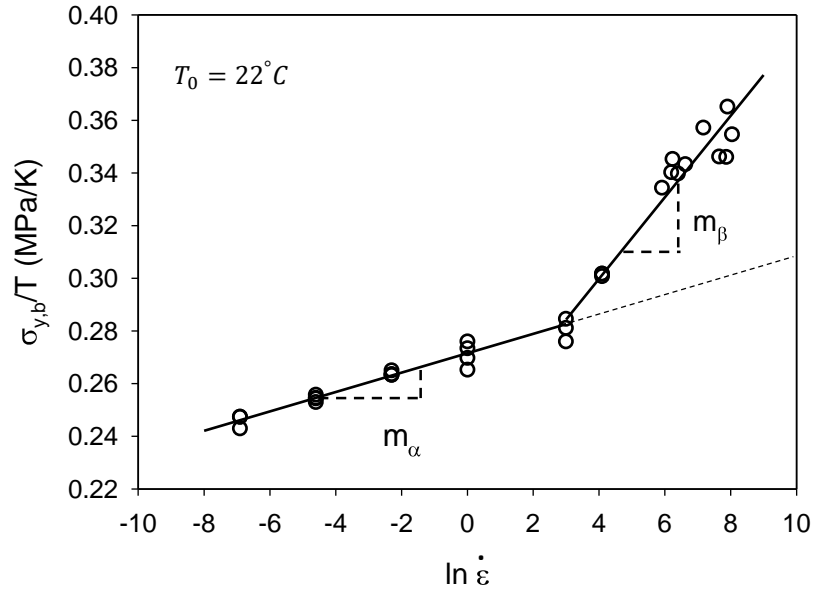
Figure 4.5: Bilinear Eyring plot for polycarbonate at an initial test temperature 22 °C, the dashed line representing the yield stress response from the α-contribution only

Within Chapter 3, an adapted Eyring yield stress equation was presented to extract yield-stress parameters from the experimental data to populate the model. In this subsection the extension of this to high rate conditions is discussed. Firstly, it is assumed that the total yield stress is additive, such that the two yield stress contributions from the two processes: $\sigma_y^b = \sigma_{y,\alpha}^b + \sigma_{y,\beta}^b$, and the bond-stretching yield equation for either process can be written as shown in equation (4.7) discussed in [67]. From this equation, it is evident that the following collection of extra parameters is needed to fulfil the second relaxation process equation; $V_{s,\beta}, V_{p,\beta}, \tau_{0,\beta}^*, G_\beta^b$. Bauwens-Crowet et al [51] make the same assumption within their work: $|\sigma_c|/T = |\sigma_{c,\alpha}|/T + |\sigma_{c,\beta}|/T$.

$$\sigma_{y,j}^b = \frac{6RT}{\sqrt{2}V_{s,j} - 2V_{p,j}} \left[\ln|\dot{\varepsilon}| + \ln\langle\tau_{0,j}\rangle + \ln\left(\frac{\sqrt{2}G_j^b V_{s,j}}{RT}\right) \right] \qquad (4.7)$$

where $j \in \{\alpha, \beta\}$.

4.4.2. Activation Volumes

The apparent activation volume for polycarbonate, found in Section 3.3.4 was obtained from low strain rate $\left(0.001 - 0.01 \text{ s}^{-1}\right)$ tensile and compressive yield stress experimental data. With a lack of sufficient evidence or data to do otherwise, it is assumed that the ratio V_p/V_s will be the same value for the high strain rates as for the lower rates. This was the same in the previous OGR model work of Okereke on polypropylene [6]. Figure 4.5 shows an updated version of the experimental yield stress plot, $\sigma_y/T \, vs \ln(\dot{\varepsilon})$, where the medium and high strain rates are shown to be captured by a second linear regression, with a gradient $m_{\alpha+\beta}$ and an intercept $c_{\alpha+\beta}$. The dashed line represents the extension to the α-relaxation plot into the high rate range, highlighting the importance of capturing both processes. Knowing that the second linear regression is the combination of yield stresses from both relaxations, $\sigma_y = \sigma_{y,\alpha} + \sigma_{y,\beta}$, the y-axis can be considered $\left(\sigma_{y,\alpha} + \sigma_{y,\beta}\right)/T$, such that the equation of the plot is given in equation (4.8).

$$\frac{\sigma_{y,\alpha} + \sigma_{y,\beta}}{T} = \left[m_\alpha x + c_\alpha\right] + \left[m_\beta x + c_\beta\right] \tag{4.8}$$

Assuming that $m_\beta = m_{\alpha+\beta} - m_\alpha$, the same method used in Section 3.3.5 is applied to utilise the second gradient to obtain the activation volume for the β-process, shown in equation (4.9). $V_{p,\beta}$ is then found from the volume ratio from equation (4.10).

$$V_{s,\beta} = \frac{const_\beta}{m_\beta} = \frac{6R/\left(\sqrt{2} - 2\dfrac{V_{p,\beta}}{V_{s,\beta}}\right)}{6R/\left(\sqrt{2}V_{s,\beta} - 2V_{p,\beta}\right)} \tag{4.9}$$

where $const_\beta = \dfrac{6R}{\sqrt{2} - 2\left(V_{p,\beta}/V_{s,\beta}\right)}$.

$$V_{p,\beta} = \frac{V_p}{V_s} \times V_{s,\beta} \qquad (4.10)$$

One decision required here is where to split the experiment yield stress data showed in Figure 4.5 into these two linear regressions. With a lack of entirely continuous data, it is not clear which of the medium rate data should fit into which of the two data ranges. Additionally, the medium rate data is a challenging region to achieve high quality experimental data. The potential change in gradients from selecting different discrete experimental data points as the end of the α-region is shown in Figure 4.6. The case using five strain rates $\left(0.001, 0.01, 0.1, 1, 5 \text{ s}^{-1}\right)$ provides a much shallower linear gradient to the three $\left(0.001, 0.01, 0.1 \text{ s}^{-1}\right)$ and four strain $\left(0.001, 0.01, 0.1, 1 \text{ s}^{-1}\right)$ rate cases.
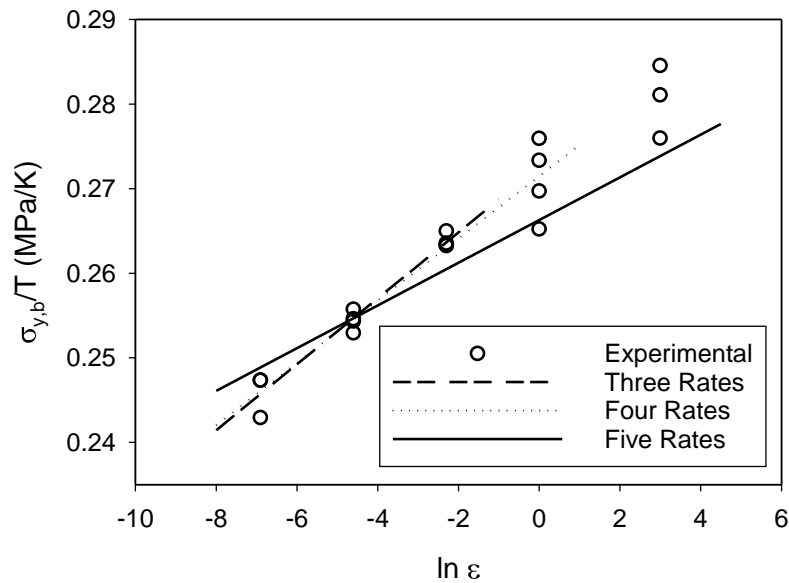
Figure 4.6: Linear fit alternatives for different data sets, the dotted line using the three lowest rates, the solid line four and the dashed line five strain rates into the medium rate region

4.4.3. Relaxation Time

This second process also requires a relevant relaxation time, $\tau_{0,\beta}^{*}$, that refers to the reference relaxation time of the β-process. The intercept of the second linear

fit, $c_{\alpha+\beta}$, is used to calculate $\tau^*_{0,\beta}$ as in equation (4.11), mirroring the method for the $\tau^*_{0,\alpha}$ value. The intercept from the second linear fit is the behaviour of both relaxations, so it necessary to subtract the α-component: $c_\beta = c_{\alpha+\beta} - c_\alpha$:

$$\tau^*_{0,\beta} = \frac{RT}{\sqrt{2}G^b V_{s,\beta}} \exp\left(\frac{c_\beta}{m_\beta}\right) \tag{4.11}$$

4.4.4. Temperature and Structural Shift Factors

In this subsection, the effect of the β-transition on low temperature results will be discussed. In Chapter 3, Figure 3.12 assumes a single linear function for the yield stresses as a function of varying temperature $(0\text{-}120\ ^\circ C)$. However, this linear fit would underpredict at the lowest temperatures, as seen by the dotted line in Figure 4.7.
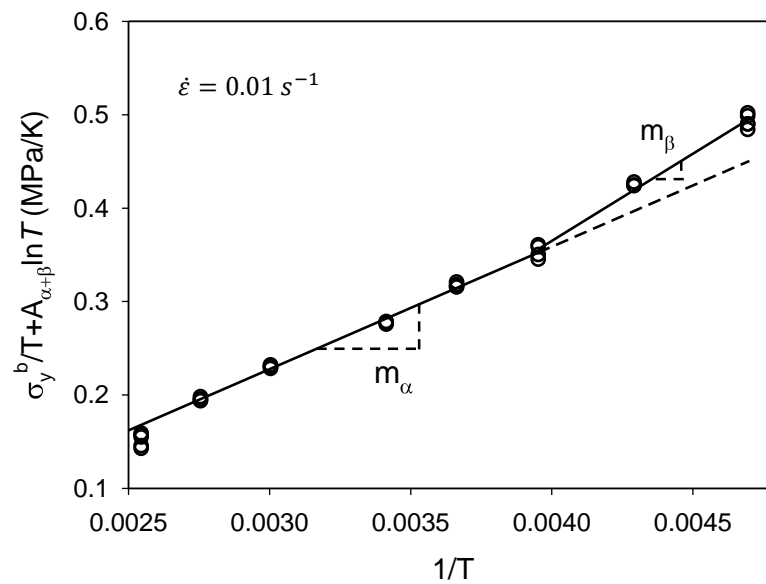
Figure 4.7: Extraction of the activation enthalpy for the bilinear case using yield stresses at varying temperature, compression tests at 0.01s-1

It would be more appropriate to account for approaching the β-transition with a bilinear approach, similar to that of the varying strain rate analysis shown in Figure 4.5. Utilising a bilinear approach introduces a different temperature shift

factor applied to the β-transition, defined in equation (4.12) where a second activation enthalpy, ΔH_β, is proposed.

$$a_{T,\beta} = \exp\left[\frac{\Delta H_\beta}{R}\left(\frac{1}{T} - \frac{1}{T^*}\right)\right]$$ (4.12)

To find a suitable starting point for the second linear regression time-temperature superposition can be utilised. In this study, there is far more strain rate data available concerning the β-transition then there is temperature data. The onset of the β-contribution is shown in Figure 4.5 to be at a rate of $\sim 20\ \text{s}^{-1}$ at a of temperature $22\ ^{\circ}\text{C}$, such that at the rate of the varying temperature tests, $0.01\ \text{s}^{-1}$, the temperature onset of the β-transition is $-23\ ^{\circ}\text{C}$. The onset of the β-transition effect is also then consistent between datasets.

Once the second linear fit from a plot of $\sigma_y^b/T + A_{\alpha+\beta}\ln T$ versus $1/T$, shown in Figure 4.7 is established, the process for obtaining the second activation enthalpy follows the same method as the α-process. The second fit represents both processes and so the α-process must be subtracted: $\Delta H_\beta = \Delta H_{\alpha+\beta} - \Delta H_\alpha$.

$$\frac{\sigma_{y,\beta}}{T} + \frac{6R}{\sqrt{2}V_{s,\beta} - 2V_{p,\beta}}\ln T = \frac{\Delta H_\beta}{R}\left(\frac{1}{T}\right) + \text{const}$$ (4.13)

There are two major difficulties when addressing the structure associated with the β-process: firstly there is limited literature on the structure of the β-component and secondly to obtain the experimental data to explore this structure is very complex. Additionally, it is important to debate the interplay of the α- and β-transitions, there is literature suggesting that the β-transition is unaffected by the α-structure [168].

Considering the test conditions used in this work $\left(-60\text{-}120\ ^{\circ}\text{C}\right)$, the β-structure is essentially in equilibrium for this temperature range, such that the structural shift factor would be: $a_{S,\beta} = 1$ and is assumed to be the same for all conditions. Defining $a_{\sigma,\beta}$ in the same manner as the $a_{\sigma,\alpha}$ from Chapter 3, shown in equation

(4.14). The above hypotheses result in equation (4.15) and equation (4.16), where $T_\beta^* = 22\,°C$.

$$a_{\sigma,\beta} = \frac{V_{s,\beta}\tau_{oct}^b}{2RT} \frac{\exp\left(-\dfrac{V_{p,\beta}\sigma_m}{RT}\right)}{\sinh\left(\dfrac{V_{s,\beta}\tau_{oct}^b}{2RT}\right)} \tag{4.14}$$

$$\tau_\alpha = \tau_\alpha^* a_{T,\alpha} a_{S,\alpha} a_{\sigma,\alpha} \tag{4.15}$$

$$\tau_\beta = \tau_\beta^* a_{T,\beta} a_{\sigma,\beta} \tag{4.16}$$

For polycarbonate, a γ-transition is observed at temperatures $\sim -192\,°C$, as shown in the work of Safari [169]) and in Figure 4.8. It is hypothesised that with a dataset such as this, a different approach may be required.
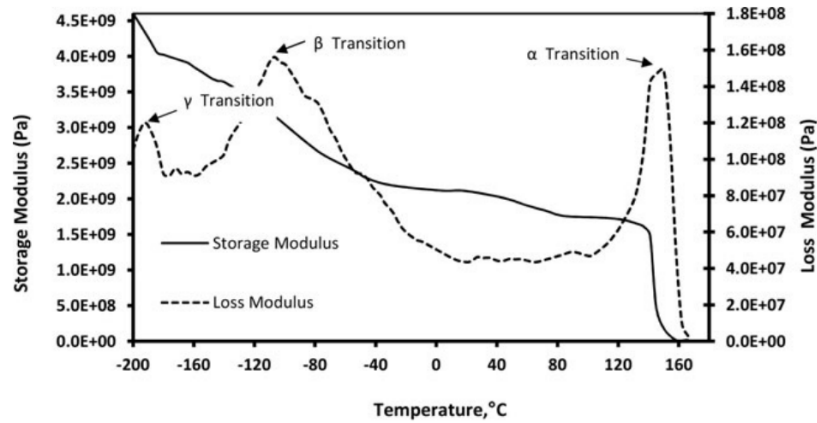
Figure 4.8: Three observed transitions (α, β and γ) for polycarbonate, adapted from [169]

4.4.5. Fictive Temperature

In Chapter 3 Section 3.2.6, a full kinetics evolution of fictive temperature was introduced as an implementation for structural evolution through equation (3.25) . The method to extend this equation to high strain rates is not evident. The first concept to explore, was whether two fictive temperatures could better represent the physical system, such that a $T_{f,\alpha}$ and a $T_{f,\beta}$ exist. However, this presents the issue, how to obtain the reference fictive temperature associated with the β-process. Assuming that a second fictive temperature exists, it is experimentally

105

very difficult to probe the behaviour below $T_{g,\beta}$. Additionally, this assumption implies that the system therefore has two measures of structure, which raises many issues, for example on the interplay between the two terms. The accompanying assumption to having two fictive temperatures, and therefore two evolution equations, is that $k_{struct,\alpha} = k_{struct,\beta}$, as was assumed in the previous GR model [6].

4.4.6. Bond-Stretching Shear Modulus

The last parameter of equation (4.7) required to be obtained for the β - process is the bond-stretching shear modulus, G_β^b. An extension to the spectrum presented in Figure 3.15 shows a secondary plateau that can be used to find a second bond stretching shear modulus, shown in Figure 4.9. Once again, this is the combination of both processes, so the bond-stretching shear modulus for the β - process is defined as:

$$G_\beta^b = G_{\alpha+\beta}^b - G_\alpha^b \qquad (4.17)$$
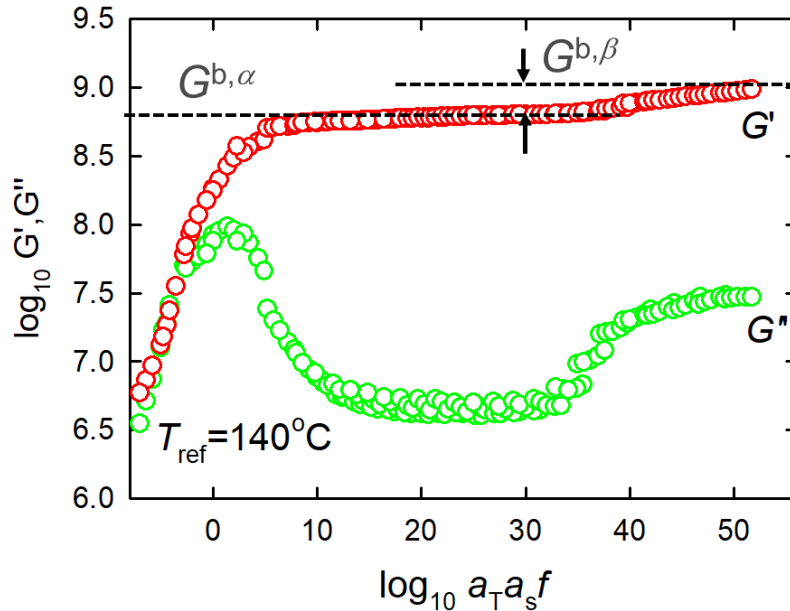
Figure 4.9: Extended linear viscoelastic shear relaxation spectrum of polycarbonate highlighting a bond-stretching shear modulus for both the α and β contributions

A previous attempt to model high rate behaviour using the OGR model for polypropylene (PP) assumed that $G_\alpha^b = G_\beta^b$ [6]. Within the temperature range used in this previous work, this assumption was acceptable, but improving this for this study was essential.

Table 4-1: Parameters for the two-process model with value and standard deviation and the sources.

	Value (± std)	Source
$V_{s,\alpha} \, (\text{m}^3/\text{mol})$	0.01465 ± 0.0027	Section 3.3.5
$V_{s,\beta} \, (\text{m}^3/\text{mol})$	0.00318 ± 0.00035	Equation (4.9)
$\tau_{0,\alpha}^* \, (\text{s})$ @ $T^* = 20\ °\text{C}$	$4.25 \times 10^{29} \pm 3.09 \times 10^{28}$	Section 3.3.6
$\tau_{0,\beta}^* \, (\text{s})$ @ $T^* = 20\ °\text{C}$	$9.33 \times 10^{-05} \pm 4.13 \times 10^{-06}$	Equation (4.11)
$T_{f,0} \, \left(°\text{C}\right)$	126.5 ± 1.9	Section 3.3.8
$\Delta H_\alpha \, (\text{J/mol})$	$2.96 \times 10^5 \pm 5787$	Section 3.3.7
$\Delta H_\beta \, (\text{J/mol})$	$4.67 \times 10^4 \pm 943$	Equation (4.13)
$C \, \left(°\text{C}\right)$	3606 ± 261	Section 3.3.8
$T_\infty \, \left(°\text{C}\right)$	91.5 ± 5.3	Section 3.3.8
$G_\beta^b \, \left(\text{Pa}\right)$	3.28×10^8	Equation (4.17)

4.5. Simulation Results

4.5.1. Compression at fixed strain rate and varying temperature

In Figure 4.1 it was shown that the lowest temperatures studied $\left(-80 \text{ to} -20 \text{ °C}\right)$ approach the β-transition, which led to a bilinear response in the yield stress results. Figure 4.10 shows the bond-stretching yield stress $\left(\sigma_y^b\right)$ simulation results compared to the experimental values for uniaxial compression tests at a constant true strain rate of 0.01 s^{-1} for varying temperatures $\left(-60 \text{ to } 120 \text{ °C}\right)$. It is seen that with the parameterisation method detailed previously, that the change in gradient at lower temperature is successfully captured and the lowest temperature yield stress simulated. As discussed in Chapter 3, the earlier yield strain results in a reduced value of total yield stress, and so the bond-stretching yield stress can be compared.
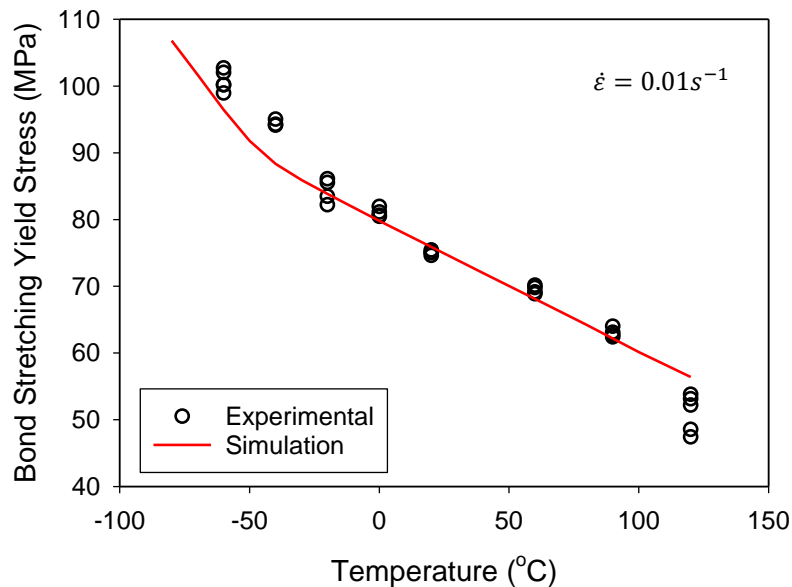
Figure 4.10: Simulation results for the bond-stretching yield stress of polycarbonate compared to experimental values for varying temperature compression tests at a strain rate of 0.01 s-1
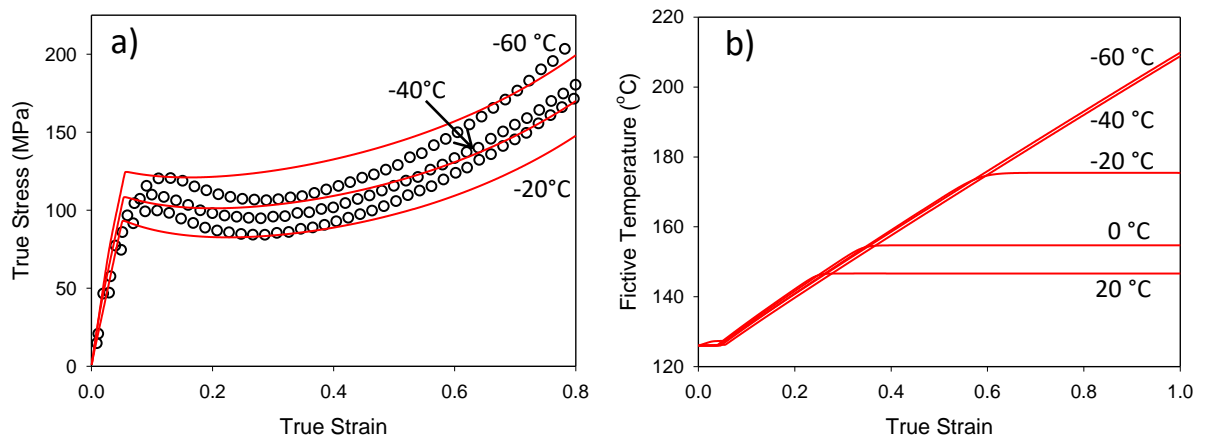
Figure 4.11: Initial polycarbonate lower temperature simulations a) the true stress true strain results for -60, -40 and -20 °C and b) the fictive temperature across true strain for -60, -40, -20, 0 and 20 °C highlighting excess evolution at low temperatures

When the full stress-strain response is assessed in Figure 4.11a, the broad behaviour is captured but the post-yield behaviour deviates from the experimental data. The deviation is linked to the inaccurate modelling of the post-yield behaviour, specifically the flow behaviour. In Figure 4.11b, the fictive temperature against stretch is presented and is seen to rise to very high values for the low temperature cases $\left(-20,-40,-60\ °\text{C}\right)$. It is expected that this parameter will evolve during the structural evolution description of post-yield behaviour, but such large values of T_f are difficult to reconcile with this physical picture. Additionally, the effect of this very large growth of fictive temperature impacts the mechanical response. The first obvious step to resolving this issue is to assess the use of the constant k, and whether fitting this to one set of experimental results makes it applicable for all temperatures and strain rates. However, changing k does not help remedy this problem, but rather shifts the issue with regards to the stress magnitude.

To address this issue, first consider what is physically occurring at this point of the deformation. It is suggested that there must reach a point where no additional plastic strain will contribute to further de-ageing, i.e. flow at constant structure is reached. If T_∞ is known to represent the ideal glass transition where all motions are treated as frozen and such is a lower boundary to T_f, it is proposed that an upper limit also exists, and thus be used to control the large growth of the fictive

109

temperature. Firstly, let T_u be the upper limit, such that equation (4.18) and (4.19) could exist and where $T_u = 160\ ^{\circ}C$. Figure 4.12 shows the results for three low temperatures $\left(-60, -40, -20\ ^{\circ}C\right)$ uniaxial compression tests at $0.01\ s^{-1}$, comparable to the results in Figure 4.11. Figure 4.12a shows the characteristic curve, with a yield drop associated with structural change followed by strain hardening. Figure 4.12b shows the fictive temperature response, plateauing at the fixed $T_u = 160\ ^{\circ}C$.

$$X = \frac{T_u - T_f}{T_u - T_\infty} \tag{4.18}$$

$$\dot{T}_f = -\frac{T_f - T}{\tau_s} + X^n k \dot{\bar{\varepsilon}}^v \tag{4.19}$$
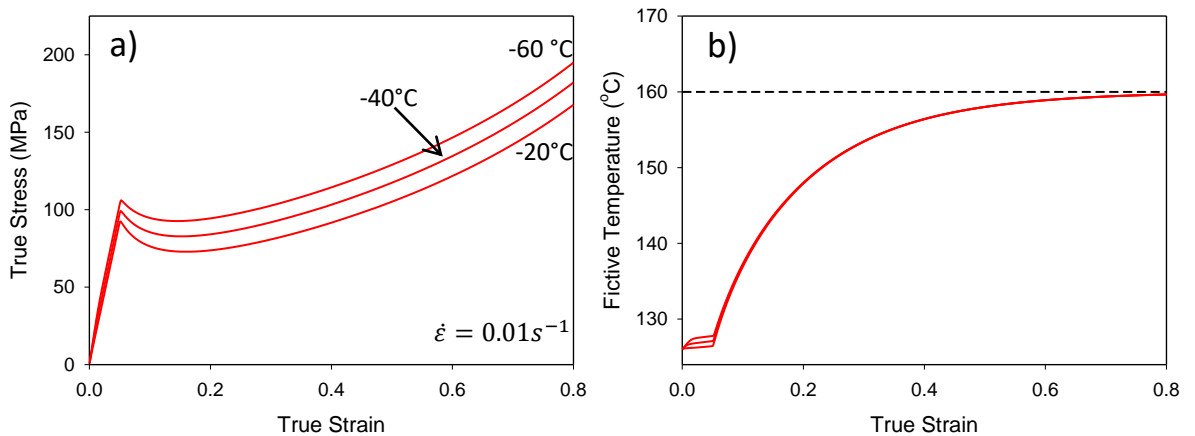
Figure 4.12: Influence of controlling the upper bound of fictive temperature for three conditions -60, -40 and -20 °C at 0.01 s^{-1} uniaxial compression a) true stress-true strain response, b) fictive temperature

It is clear from Figure 4.12 that implementing a control on the upper bound of fictive temperature response both keeps the fictive temperature at a lower, more expected value but also yields a true stress-strain response more typical of the experimental data in Figure 4.11. The next stage is to understand how an upper bound T_u value change with experimental conditions.

In Chapter 3 Section 3.3.10, a method for obtaining strain-hardening behaviour and parameters was presented, where an Edwards-Vilgis function with a constant flow stress could be fitted to isothermal experimental compression data. From this

optimisation, the values for the flow stress at yield for low strain rates and all the temperatures were extracted. The flow stress represents the structure quantified through the fictive temperature and thus it can be used it to understand how experimental quantities such as temperature and strain rate affect this structure during flow. From yield to flow the structure evolves and hence the fictive temperature will change by a certain amount.

Figure 4.13a shows the yield stress compared with the flow stress at yield for varying temperatures. The fictive temperature at the flow stress is then determined using the pre-established Eyring yield stress equation (4.7). The change in fictive temperature $\left(\Delta T_f\right)$ varying with temperature is shown in Figure 4.13b. Investigating the dependency of this flow term in Figure 4.14, a proportional relationship with flow structure, the term $T_{\mathrm{f}}-T_{\mathrm{f,flow}}$, and inverse temperature is observed.
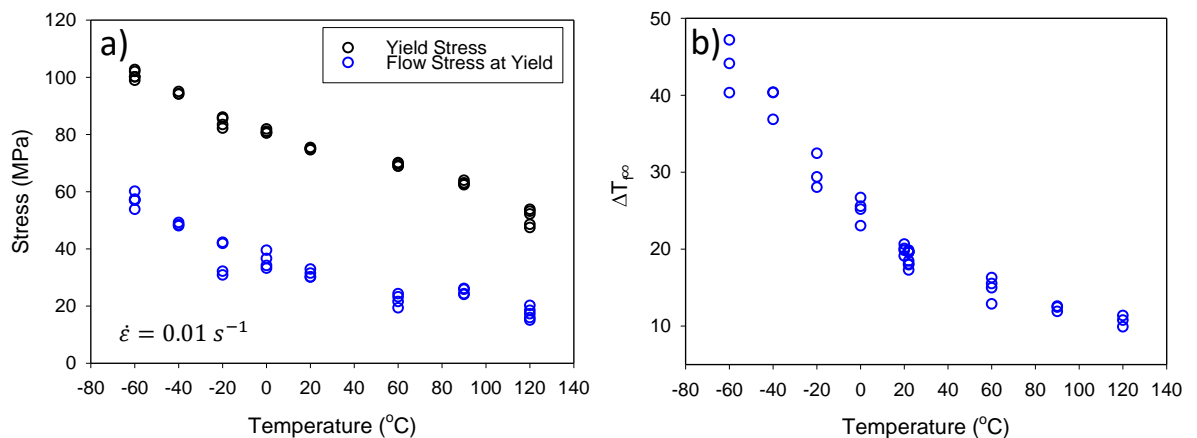
Figure 4.13: a) Extraction of flow stress at yield compared to full yield stress experimental results, b) flow structure demonstrating a dependence on inverse temperature
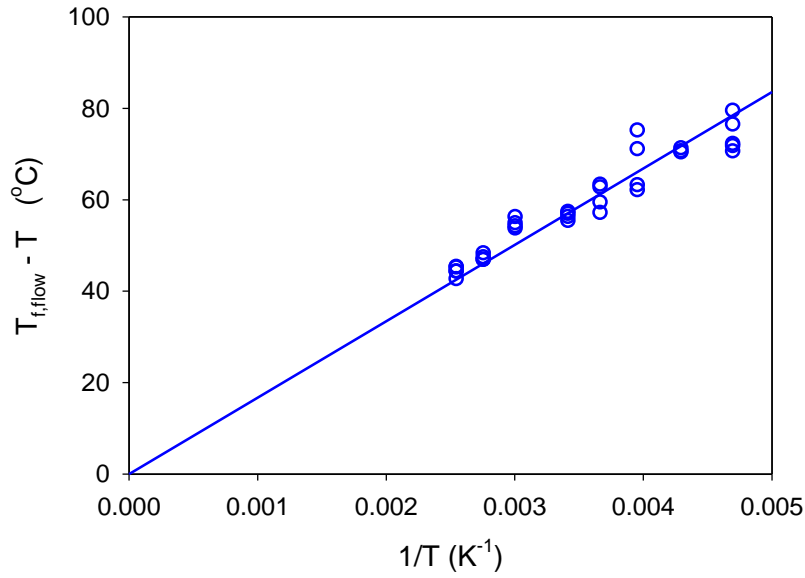
Figure 4.14: Flow structure, defined as the fictive temperature at flow minus the Vogel temperature, versus inverse temperature showing a linear relationship

$$k = k_0 \left[1 - (T_{\mathrm{f}} - T) \frac{T}{m_{flow}} \right] \qquad (4.20)$$

Using the above methodology, where k_0 is a dimensionless constant to be fitted to experimental data as in previous OGR modes and m_{flow} is the gradient of the linear regression for isothermal tests from Figure 4.13, this new interpretation of k can be applied to the model through equation (4.20) and new simulations obtained. In comparison to Figure 4.11 the evolution of fictive temperature shown in Figure 4.15 is a far more logical value. Finally, within Figure 4.16 the full simulated mechanical responses for multiple temperatures across the extensive test range are compared. This novel approach allows the post-yield behaviour to be captured for a very broad range of temperatures and rates.
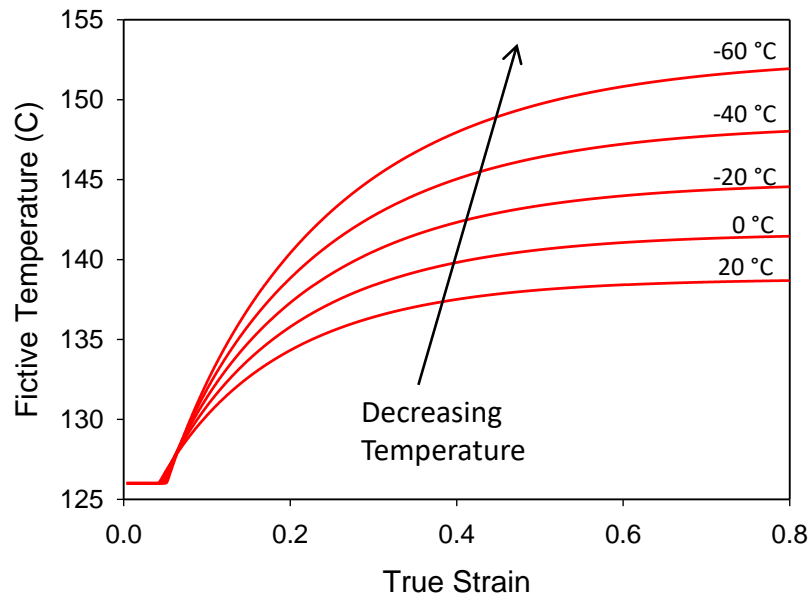
Figure 4.15: Fictive temperature evolution during deformation for varying temperatures (-60,-40, -20,0,20 °C) for the new equation of fictive temperature evolution presented in equation (4.20)

Figure 4.16 shows that the main features of the responses were successfully captured for a broad temperature range for this updated equation. The most accurate fit is for the room temperature data, which is expected given that it is in the middle of the fitting range and it is far from β-process considerations. From the experimental data, the post-yield behaviours can be seen to vary in shape. At the highest temperatures, the breadth of yield-peak is the narrowest, so the yield seems the sharpest. The drop in the yield stress is a larger percentage of the yield in the highest temperature case. The results for both Figure 4.15 and Figure 4.16 highlight that this novel method can successfully capture a yield drop of the magnitude of the experiments across a wide range.

113
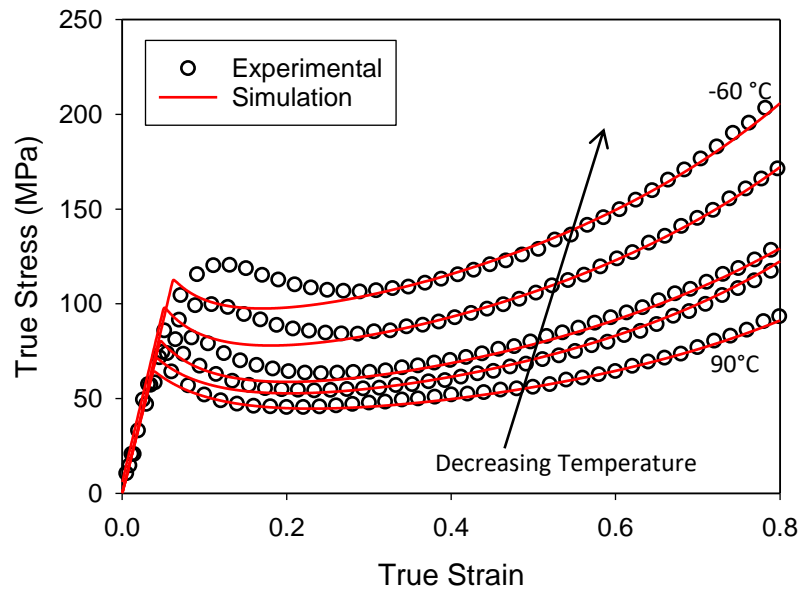
Figure 4.16: Full true stress-true strain responses for varying temperatures, -60, -20, 20, 60, 90 °C for a isothermal compression simulations and experimental results at the strain rate 0.01 s⁻¹

4.5.2. Compression Simulations at Varying Strain Rates

The next test of the model is the ability to predict the high strain rate responses. As discussed previously, there are two main factors that need to be considered for higher strain rate simulations; the effect of the secondary transition, β-transition, and the contributions from adiabatic heating. In Figure 4.17 the broad strain rate range including medium rate and high rate yield stresses are successfully simulated and compared to experimental results, showing a bilinear response. This is particularly positive as the medium and high strain rate experimental results are obtained from three different testing machines.
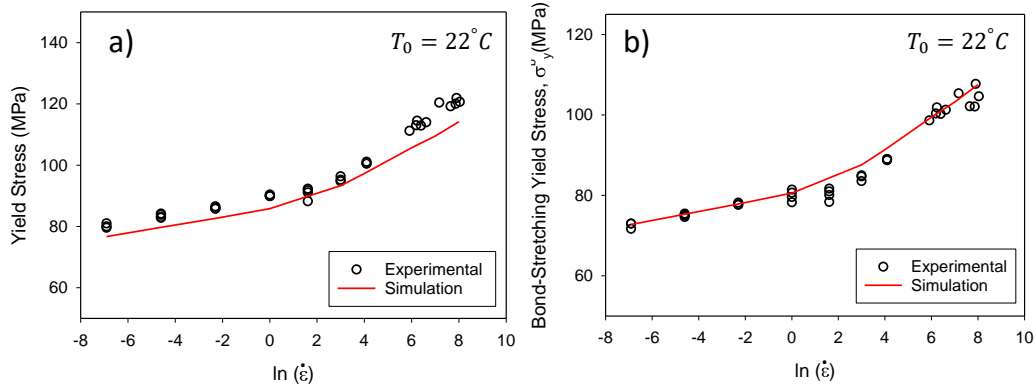
Figure 4.17: Yield stress response for medium and high strain rates a) full yield stress response, b) the bond-stretching contribution

Figure 4.18 shows the full true stress-strain response for three representative strain rates, a quasi-static test (0.001 s^{-1}), a medium rate (60 s^{-1}) and a high strain rate example (~ 2800 s^{-1}). For the latter two with simulations for both isothermal and adiabatic conditions with an initial test temperature of $T_0 = 22$ °C. All the experimental SHPB data at the highest strain rates will effectively sit on the same response. As with all the full simulations presented earlier, the yield strain is smaller and the yield peak sharper than the experimental results. As discussed in Chapter 3, this discrepancy is understood from the yield strain of the single mode. The new theory shown in equation (4.20) is proven to also capture successfully the post-yield behaviour in the high strain rate cases, as temperature is changing due to adiabatic heating. While an excessive growth of fictive temperature was observed for both the low temperatures, shown in Figure 4.11, and the high strain rates, the effect appears to be more temperature than rate dependent.
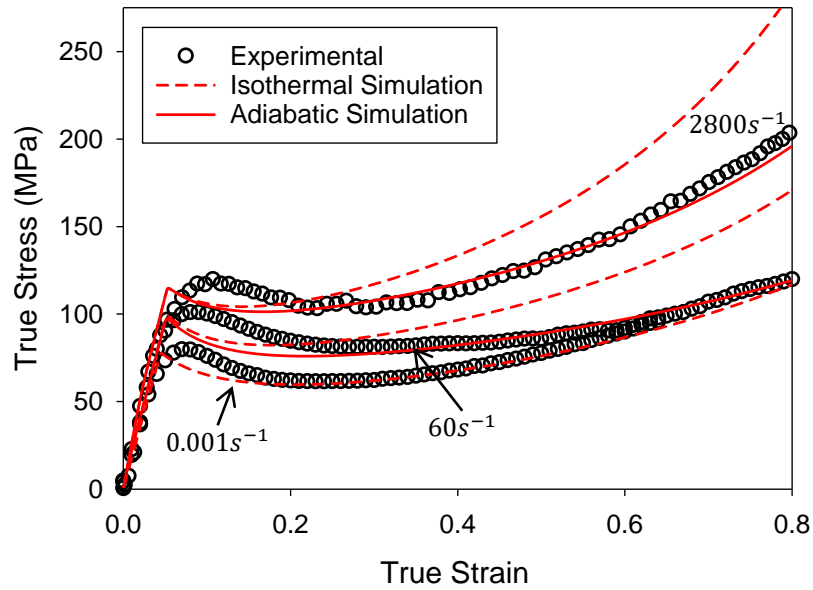
Figure 4.18: Full true stress- true strain responses for polycarbonate at an initial test temperature 22 °C and strain rates of 0.001 s⁻¹, 60 s⁻¹, 2800 s⁻¹, showing both isothermal simulations compared to experimental results and adiabatic simulations for the medium and high strain rate results

4.5.3. Temperature and Structural Shift Factors – Results and Alternative Methods

Within this chapter a new theory to the shift factors for the β-process was presented. A second activation enthalpy, to capture the low temperature results as the β-relaxation is traversed, is introduced in Section 4.4.4 . In this subsection, the results of the alternative version, where a singular activation enthalpy relating to both the α – and β – relaxation, are demonstrated.

In Figure 4.19a and Figure 4.19b the results from the assumption $\tau_\beta = \tau_\beta^* a_{T,\alpha} a_{\sigma,\beta}$, i.e. having a single activation enthalpy for temperature dependence are shown. A clear difference in simulated response, compared with the experimental results, is exhibited. Firstly, there is a very clear double yield, and secondly the magnitude of the yield stresses is much larger than observed in experimental results. Addressing this first point, the yield stress is assumed to be an additive sum of both processes, such that, $\sigma_y = \sigma_{y,\alpha} + \sigma_{y,\beta}$ is implemented. When a material

116

response is considered in such a way, it is effectively yielding twice. The first yield stress is effectively the $\sigma_{y,\alpha}$ value and captures the α-contribution. The second yield is a much larger yield stress than observed experimentally and is related to the $\sigma_{y,\beta}$, highlighting that the issue is with the β-process implementation at low temperatures.
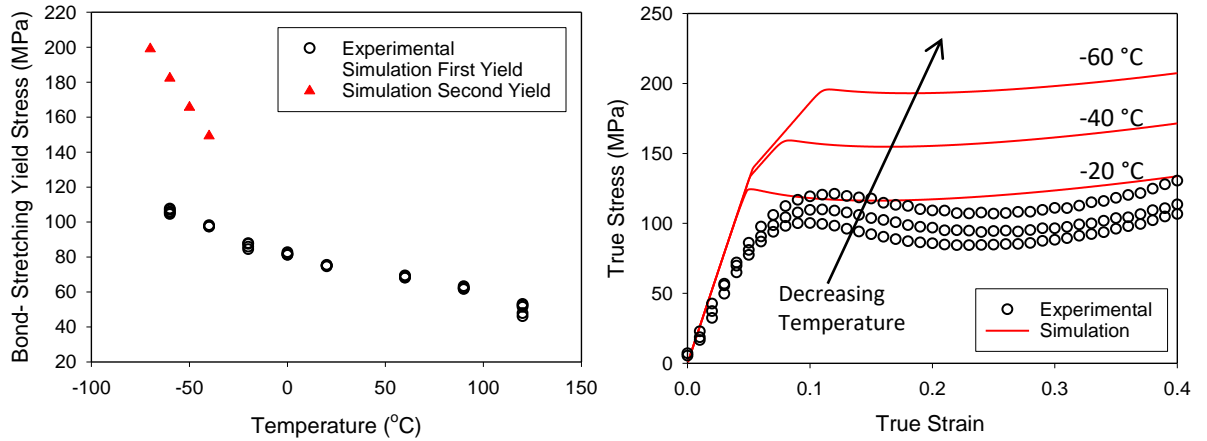
Figure 4.19: The breakdown of varying temperature simulations against experimental values for a) the bond-stretching yield stress and b) the true stress true strain response for -20,-40 and -60°C

When addressing the implementation of temperature dependence for the β-process a few alternative methods were attempted, detailed in this subsection. The main concept is to utilise the information that is known, in this case the value of τ_{β}^{*}, from the intercept c_{β} at the reference temperature of the experimental yield stress data, $22\,°C$.

One alternative method was to utilise the well-known William-Landel-Ferry (WLF) method as an alternative shift factor relating to τ_{β}^{*}, show in equation (4.21). The main benefit of this method is that there are universal values C_1, C_2 that are established $\left(C_1 = 17.44, C_2 = 51.6 \right)$ using the a reference temperature of the glass transition. This reduces the number of new parameters required for the extension to the β-process. T_r in equation (4.22) is the reference temperature, which needs defining. For this example, the most obvious value of T_r would be the β-transition. The dilemma this raises is given the breadth of the peak representing

117

$T_{g,\beta}$ shown Figure 4.20 and the range of reported values, it is difficult to choose a sensible value.

$$\tau_\beta = \tau_\beta^* a_{wlf} a_\sigma \tag{4.21}$$

$$a_{wlf} = \exp\left(\frac{-C_1(T-T_r)}{C_2+(T-T_r)}\right) \to \exp\left(\frac{-C_1(T-T_{g,\beta})}{C_2+(T-T_{g,\beta})} + \frac{-C_1(T^*-T_{g,\beta})}{C_2+(T^*-T_{g,\beta})}\right) \tag{4.22}$$
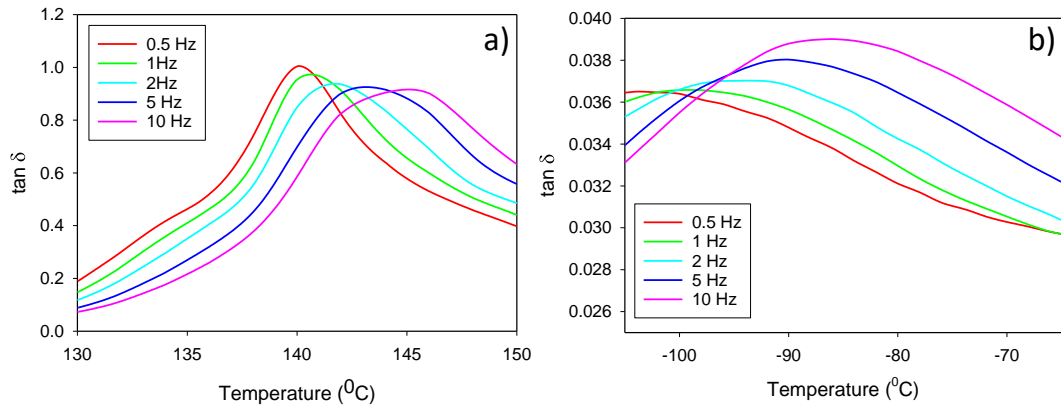
Figure 4.20: Loss tangents against temperature for polycarbonate obtained from frequency sweep DMA results using single cantilever beam for five different frequencies for a) α-relaxation b) β- relaxation

Figure 4.21 shows the resulting simulations when this theory was applied to the model. It is observed that this method does trigger the secondary behaviour required to capture low temperature data, however none of these values of $T_{g,\beta}$ portray the second gradient required.
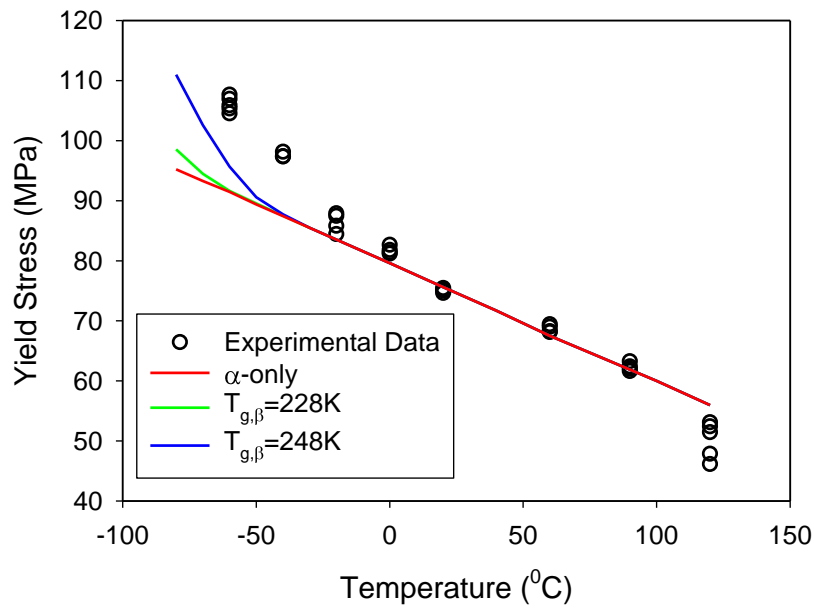
Figure 4.21: Varying temperature simulation results against experimental results for the a_{wlf} implementation of the β-shift factors

4.5.4. Temperature Rise Results

A critical aspect of successful high strain rate modelling is the implementation of adiabatic heating and the associated temperature rise when heat cannot leave the system. Firstly, the accumulated energy can be considered across the deformation of the test. Then the resulting temperature rise is compared to the experimental results.

In Section 4.3.1, the implementation for the inclusion of adiabatic heating is introduced. In this subsection the results from each energy contribution are discussed. It is possible to monitor these energies throughout the test and analyse the magnitudes of each at different strain levels. Consider a compression polycarbonate test at $22\ °C$ and a strain rate of $11\ s^{-1}$. In the small strain of $0 - 0.2$ shown in Figure 4.22a, at yield the elastic strain energy is the full contribution of the accumulated energy region shown. The elastic strain energy will drop post-yield due to the dashpot in series with the elastic spring on the bond-stretching arm of the model. Post-yield, the effect of structural change energy appears, as the material is experiencing structural evolution driven by the mechanical

rejuvenation (de-ageing). At close to $\varepsilon = 0.15$, the contribution from the conformational behaviour contribution starts to become visible. Given the previously discussed tight network of polycarbonate (Section 3.3.3) it is to be expected that this contribution starts at a relatively small strain compared with other polymers. In Figure 4.22b the distribution of energy for large strains is shown. Most notably, the dissipated energy is the dominant energy. The structural energy plateaus as the structural evolution slows post strain softening. Similar behaviour is also observed at high strain rates $\left(\sim 2800 \text{ s}^{-1} \right)$, Appendix A.4. High Strain Rate Energy Plots for Polycarbonate shows the same two true strain levels again for compression polycarbonate tests at $22°C$.
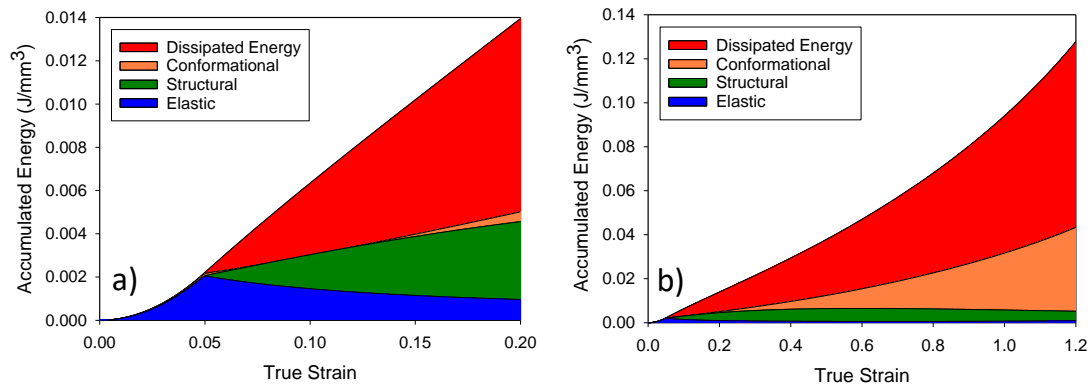
Figure 4.22: Accumulated energies during the deformation of polycarbonate in a compression test at initial test temperature 22°C and strain rate 11s⁻¹ for a) a true strain of 0- 0.2 and b) for a true strain of 0-1.2

The energy contributions allow the calculation of the temperature rise throughout the deformation. Firstly, the temperature rise for a series of strain rates are presented and compared to the experimental temperature results. Figure 4.23 presents temperature rise simulations against experimental results for three medium strain rates, $0.5, 1.5, 11 \text{ s}^{-1}$ and one high rate $\left(2800 \text{ s}^{-1} \right)$ simulating the SHPB result. As the strain rate increases, and the tests become more adiabatic, the simulated temperature rises shows an increasingly good fit to the experimental data. From our energy contribution analysis, it is known that at yield, no dissipated energy or conformational energy is accounted for (i.e. no associated temperature rise), with the full contribution going towards elastic strain energy. This is visible in the temperature rise as a delayed starting strain to the temperature rise plot in comparison to the experimental results. The high rate simulations are compared

to the mean temperature rise for seven Hopkinson bar tests obtained using a high-speed infrared camera, with an approximate strain rate of 2800 s^{-1}. The success of these temperature rises is the result of successful implementation of adiabatic heating and improvements already discussed to the mechanical response.
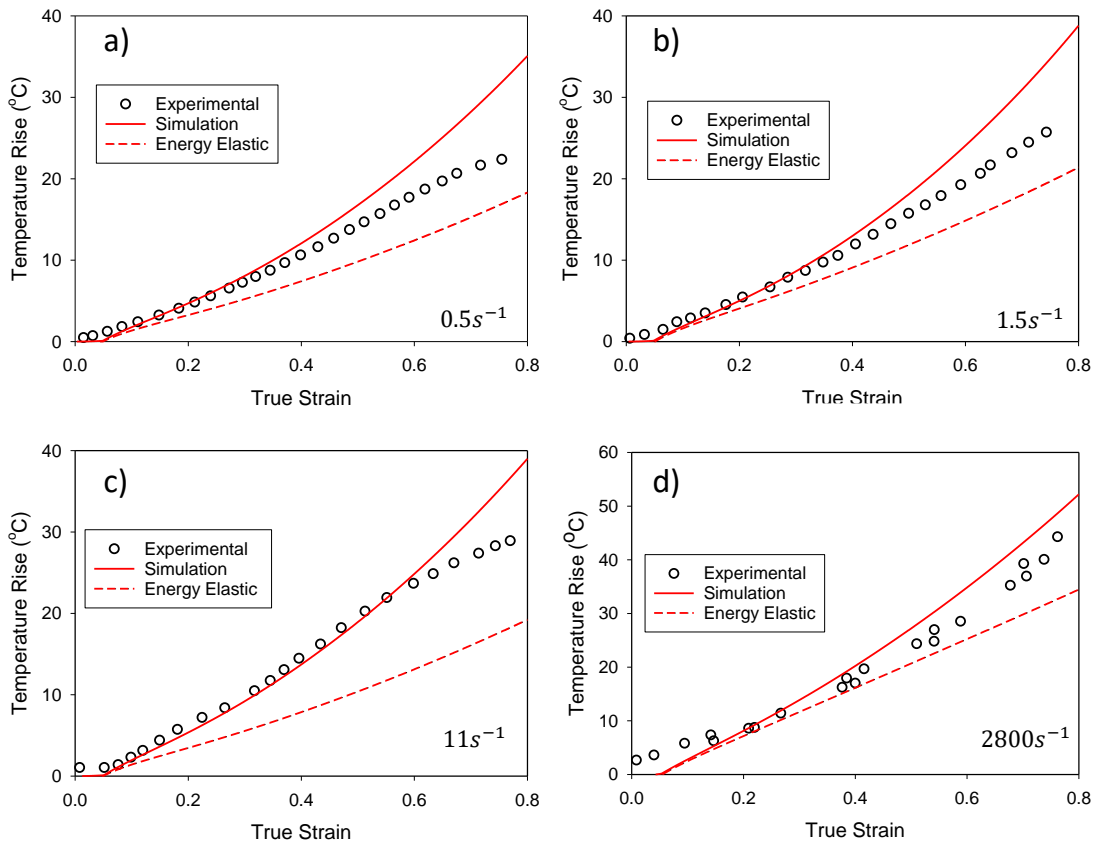
Figure 4.23: Simulated temperature rises compared to experimental results for strain rates of a) 0.5s-1 , b) 1.5s-1, c)11s-1 , d) 2800s-1

Considering three strain rates $\left(1.5, 11, 2800 \text{ s}^{-1}\right)$ at an initial temperature of 22 °C , Figure 4.24 highlights the impact of simulating with either a constant specific heat capacity (where the value is taken to be the c_p at the initial temperature of the test) versus the temperature dependent specific heat capacity described in section 4.3.1. For the mechanical response in Figure 4.24a, there is slight deviation visible on the true stress- true strain plot at and beyond the true strains of 0.8 where the constant c_p produces a lower true stress. Figure 4.24b shows the thermal response, where the deviation between the two simulations is more

evident. Here the temperature dependent c_p acts to reduce the temperature rise, with a difference visible from an earlier true strain, $\varepsilon = 0.4$. At the maximum true strain, the temperature difference is 9.2 °C for the highest strain rate, 3000 s^{-1}.
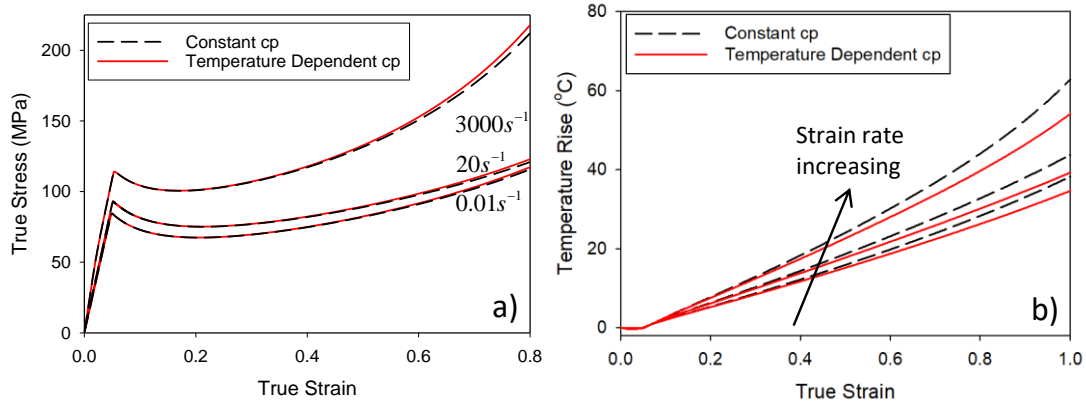
Figure 4.24: Effect of using a constant specific heat capacity value over the temperature dependent version for three strain rates ($0.01, 20, 3000s^{-1}$), a) the true stress versus true strain and b) the temperature rise

It is hypothesised that in addition to the temperature dependence highlighted, a strain dependence could be present, especially at large strain deformations. However, it is not evident how to construct an experimental methodology that explores this strain dependence.

It is clear that at high strain rates, adiabatic conditions must be implemented and at quasi-static tests an isothermal assumption is required. However, when the treatment of tests changes from isothermal to adiabatic is less clear. It is possible to consider the transition purely from the experimental results, published by the Oxford experimental team as part of the wider project. Three quasi-static compression tests in the region between isothermal and adiabatic conditions, $0.01, 0.1, 0.5$ s^{-1}, were conducted at room temperature, with an IR camera used to capture the temperature rise data, shown in Figure 4.25. The minimal rise in temperature and then plateau seen in the temperature rise of the 0.01 s^{-1} test results implies that this test is almost completely isothermal. The clear temperature rises for 0.1 and 0.5 s^{-1} indicates it is not appropriate to treat these tests isothermally. The downwards curvature at larger strains of the 0.1 s^{-1} test

seems to indicate that it is at a transitional point where neither isothermal nor adiabatic is entirely accurate.
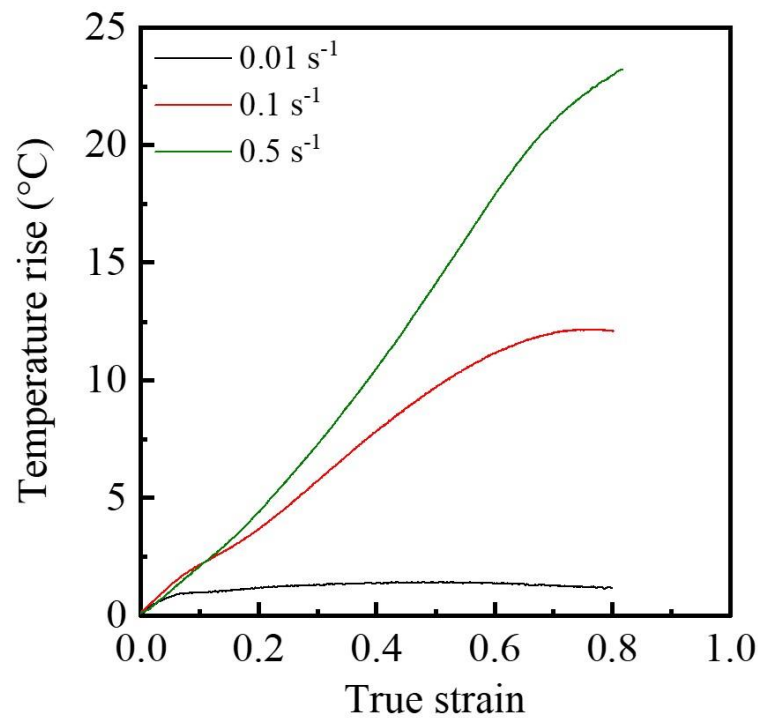
Figure 4.25: Experimental temperature rises against the true strain for three rates traversing the isothermal to adiabatic range[3]

The adiabatic heating implementation in this model is manually switched on and off and does not have a 'natural trigger' but through conducting simulations under both conditions and comparing to experimental results, an understanding of when using each is appropriate can be observed. Figure 4.26 shows two low strain rate tests, showing simulation results for both isothermal and adiabatic conditions. In Figure 4.26a, at a rate of $0.1 \, s^{-1}$, the isothermal simulation fits to the experimental data very well, whereas here an adiabatic assumption would underpredict the mechanical experimental response. Conversely, Figure 4.26b shows the simulation of a rate of $0.5 \, s^{-1}$ where the isothermal simulation vastly overpredicts the experimental stress-strain curve. This highlights from a simulation

---

[3] Work adapted from experimental results from colleagues at the University of Oxford (P. Song), to be published soon

perspective that the transition is in this strain rate region. In Section 4.3.1, the isothermal-adiabatic transition was found for theory to be 0.6 s^{-1}.
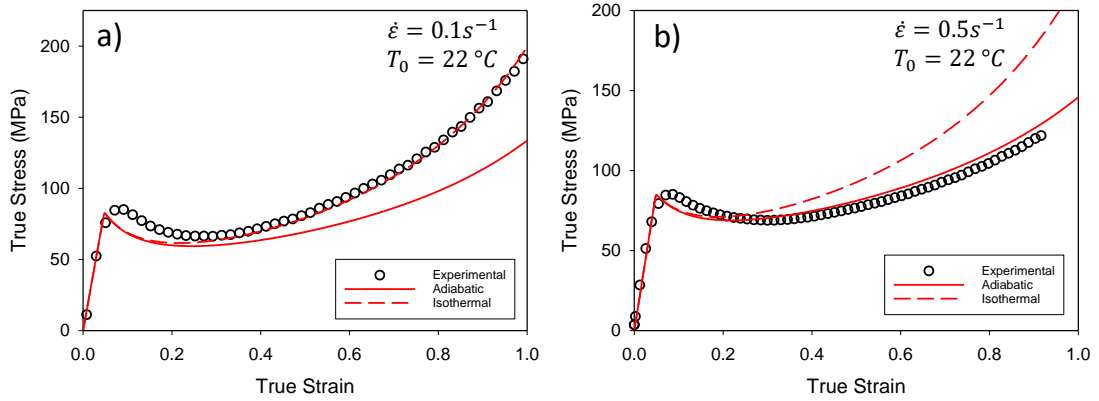
Figure 4.26: Adiabatic and isothermal simulated true stress-true strain responses, a) 0.1 s^{-1} where the isothermal conditions best fit the experimental data b) 0.5 s^{-1}where adiabatic conditions best represent the experimental response

4.6. Load-Unload Conditions

For further analysis of the model a series of load-unload simulations were performed. Load-unload simulations were performed at three rates: isothermal $\left(0.01 \text{ s}^{-1}\right)$, adiabatic $\left(0.5 \text{ s}^{-1}\right)$ and adiabatic $\left(2800 \text{ s}^{-1}\right)$.

Figure 4.27 shows the full true stress strain response for these three rates, whereas Figure 4.28 decomposes the load-unload stress-strain response into the bond-stretching and the conformational stresses. Focusing on Figure 4.28a and Figure 4.28b, at large strains a second increase in the bond-stretching stress is simulated, which is attributed to an increase in flow stress. The origin of this increase in stress is related to the hydrostatic compression at these large strains. As a result of the conformational stresses rising, relaxation times will lengthen and an increase in the previously plateaued flow stress. This attribution is verified through the isothermal case, where a reduction in conformational stress is simulated and such the secondary increase is decreased. It is observed in Figure 4.28a and Figure 4.28c that the flow stress is effectively constant in the true strain range $0.4-1.1$. In the adiabatic cases, the conformational stress plots show a different response than the isothermal, where the unload curves do not follow the load curves.

124
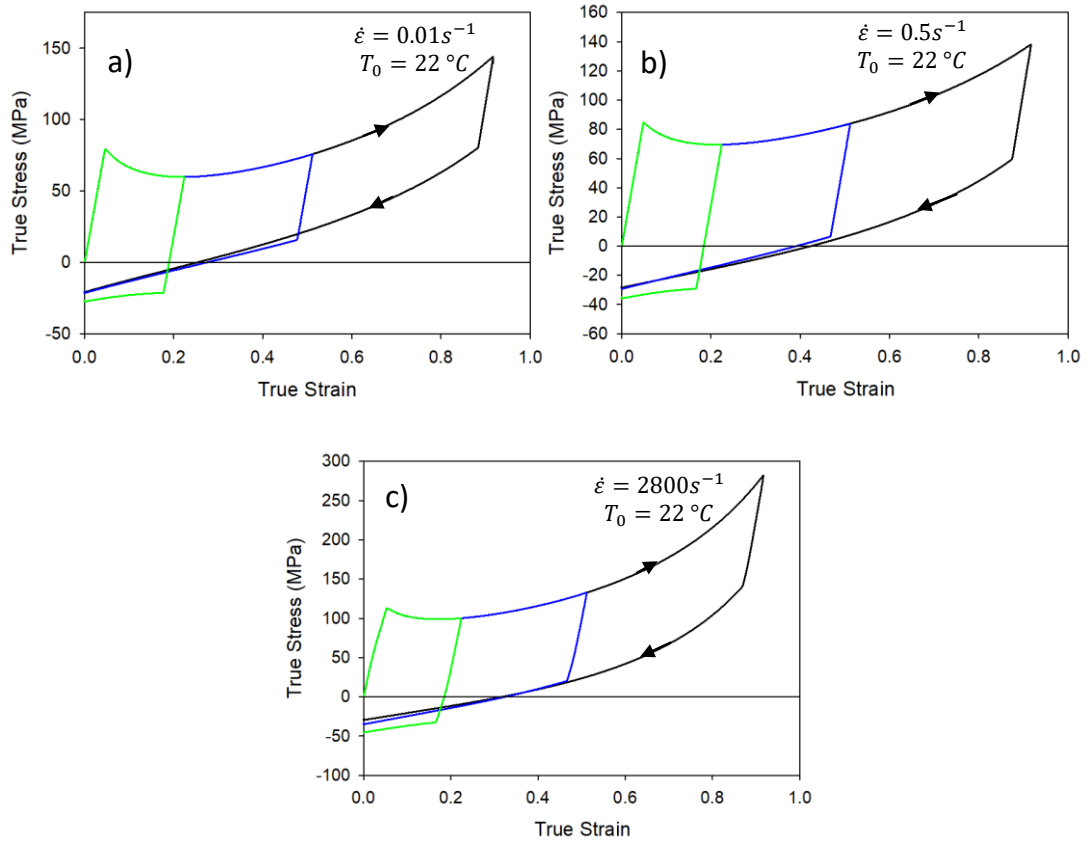
Figure 4.27: The true stress-true strain mechanical response for load-unload simulations for three strain rates a) 0.01 s⁻¹ isothermal, b) 0.5 s⁻¹ adiabatic, c) 2800 s⁻¹ adiabatic

125
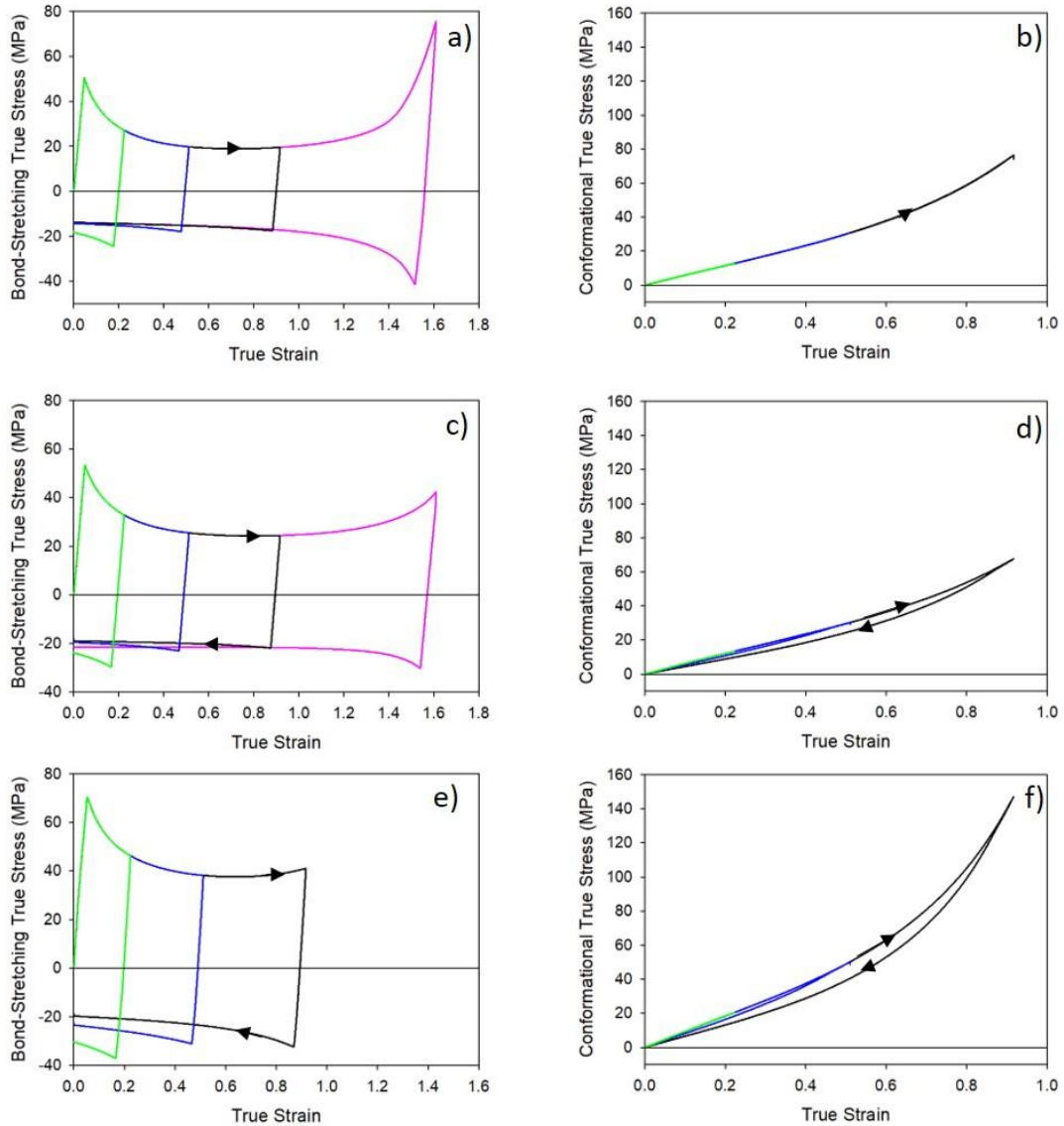
Figure 4.28: The decomposition of the stress response for three rates 0.01 s⁻¹, 0.5 s⁻¹ and 2800 s⁻¹ for a),c),e) the bond stretching stress, b),d),f) the conformational stress

In addition to the stress, the temperature and fictive temperature is extracted for the load-unload conditions, shown in Figure 4.29, where Figure 4.29a shows the temperature rise for the 0.5 s^{-1} test and Figure 4.29b is the 2800 s^{-1} simulation. Figure 4.29c is an example of the fictive temperature behaviour across the deformation for the 0.5 s^{-1} test. In the load-unload simulations to smaller strains, where the structure has not finished evolving, the fictive temperature is seen to rise during the unload step, whereas, in the cases where the structure evolution has plateaued, the fictive temperature does not increase in the unload step.

126
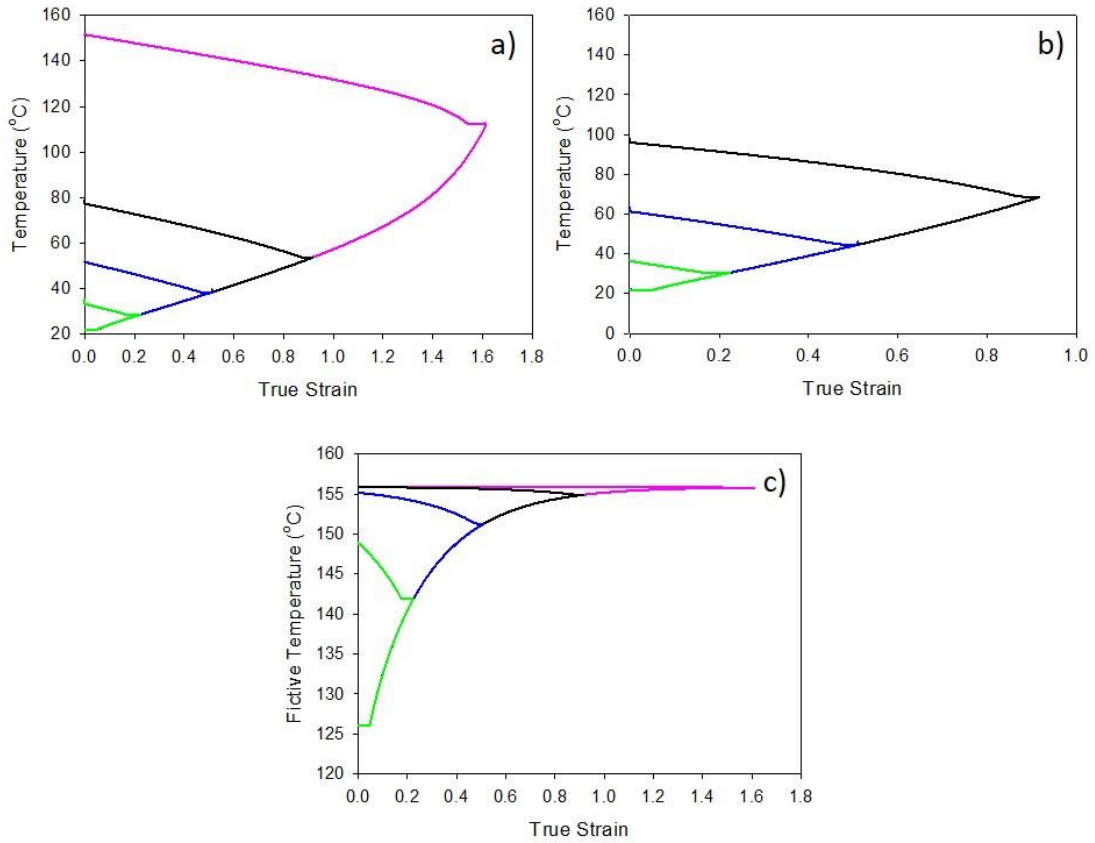
Figure 4.29: The temperature rise response for a) 0.5 s⁻¹, b) 2800 s⁻¹, and c) the fictive temperature response for a strain rate of 0.5 s⁻¹ highlighting the structural evolution influence

4.7. Discussion

The previous section presented the simulations obtained from the model presented in this thesis, with new theories and implementations detailed throughout. Within this section a deeper analysis will be performed on some of the methods and results.

4.7.1. Old Method Structural Evolution

Within the previous chapters, much focus has been given to implementing a more comprehensive structural evolution, with the use of a full kinetic version of fictive temperature evolution. In this subsection, the results from the old implementation, as stated in equation (4.23) are analysed and compared to the more comprehensive formulation.

$$T_{\mathrm{f}} = T_{\mathrm{f}0} + \left(\Delta T_{\mathrm{f}} \right) \left[1 - \exp \left(- \frac{\bar{\varepsilon}^{v}}{\varepsilon_0^{v}} \right) \right] \qquad (4.23)$$

In equation(4.23), ε_0^{v} and ΔT_{f} are taken to be material constants. The values taken to parameterise this version of the model are fitted to experimental data, as with the previous examples of this implementation [67], [68]. The main issue with this implementation is it neglects any rate or temperature dependence of the two parameters. Figure 4.30 visualises the effect of increasing ε_0^{v} and ΔT_{f} on the true stress-true strain response and the fictive temperature.
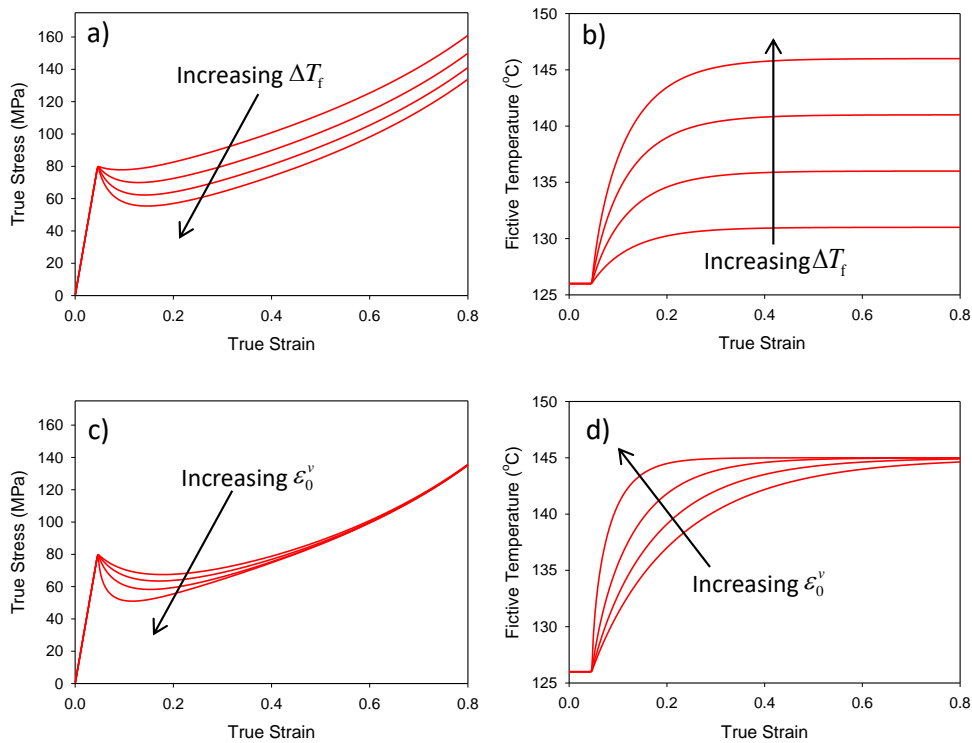
Figure 4.30: The impact of the parameters of increasing ΔTf on the a) true stress-true strain response and b) the fictive temperature, and secondly the increase of ε₀ᵛ on c) the true stress-true strain response and d) on the fictive temperature

To analyse the performance of this method across the strain rate range, constant values for this PC data were fitted at $22\ °C$ and a rate of $0.01\ \mathrm{s^{-1}}$. The old method was then implemented with these constants, and the high rate simulations conducted. It is evident from Figure 4.31, that fixed values for ε_0^{v} and ΔT_{f} from a quasi-static test optimisation do not capture the correct post-yield structural

evolution require to simulate the high strain rates or lower temperatures, with large deviations from experimental results seen for both. These results justify the use of the full kinetic version implemented in this work.
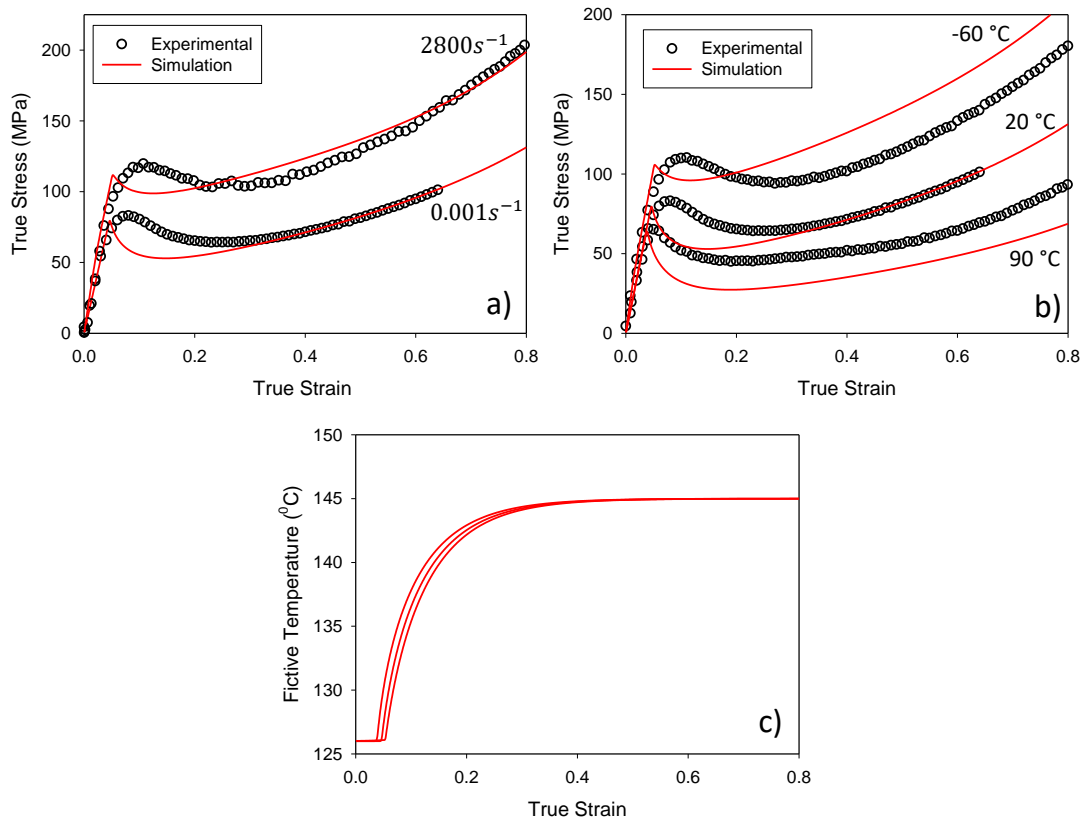
Figure 4.31: Old implementation with fixed ΔT$_f$ and ε$_0$^{v} simulations for a) varying strain rate (0.001, 3000s^{-1}), b) varying temperature (-60,20, 90°C) and c) fictive temperature

4.7.2. De-ageing at High Strain Rates

In Figure 4.17b it is observed that the model results slightly overpredicts the medium rate yield stresses and marginally underpredicts for the lower temperatures. The origin of these two performance factors are believed to be interlinked. In Figure 4.32, the simulation results for $\Delta T_f = 0$ is shown highlighting the impact this has on the yield stresses. The gradient of the yield stress versus strain rate plot for higher rate simulations now more accurately captures the full rate range (there is a slight increase to the yield stresses under this formulation). The origin for this is that the structural evolution is triggered by

the yielding of the α-process and this is at an earlier yield strain than the β-process. The result is that the simulated system is beginning to de-age before yield has been reached. This idea is supported by the performances being highly influenced by switching off the fictive temperature evolution and by the fact this scenario is only seen in the rates and temperatures impacted by the β-process.
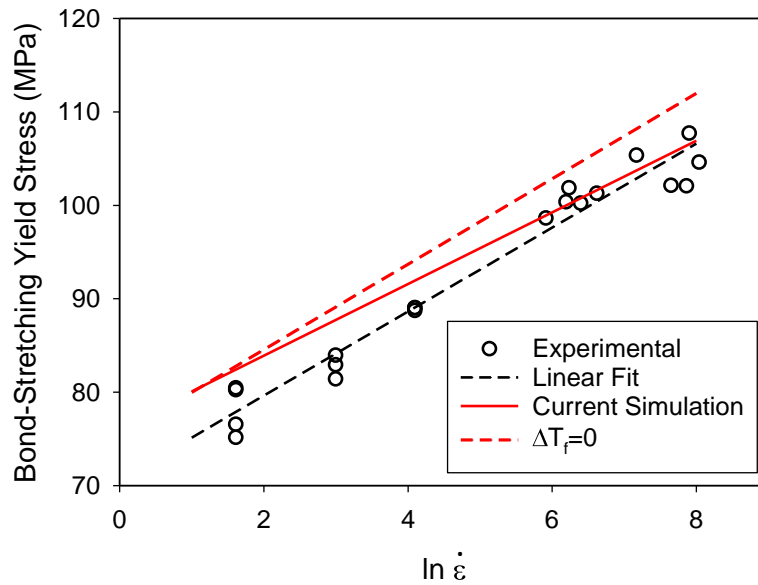
Figure 4.32: The yield stress response considered for high strain rates, showing the linear fit through the experimental data compared to the current simulation and the ΔT_f = 0 case

4.7.3. Adiabatic Heating Discussion

In Section 4.3.1, four energy contributions were discussed in detail: elastic strain, structural change, conformational and dissipated energies. Within this section the success of this interpretation of adiabatic heating is discussed. Firstly, the impact of energy towards structural evolution can be assessed. Figure 4.33a shows the effect on the mechanical response if within the adiabatic heating no structural evolution is accounted for. The mechanical response simulated overpredicts the yield-drop observed experimentally. This is to be expected as the initial energy that should be going towards structural change is in fact adding to the dissipated energy and so an increase in thermal softening or strain softening is detected. This will lead to a greater temperature rise being simulated. Figure 4.33b shows the

increase in temperature rise predicted from not accounting for structural change energy. The results in Figure 4.33 highlight the necessity to include structural change energy in the adiabatic heating considerations.
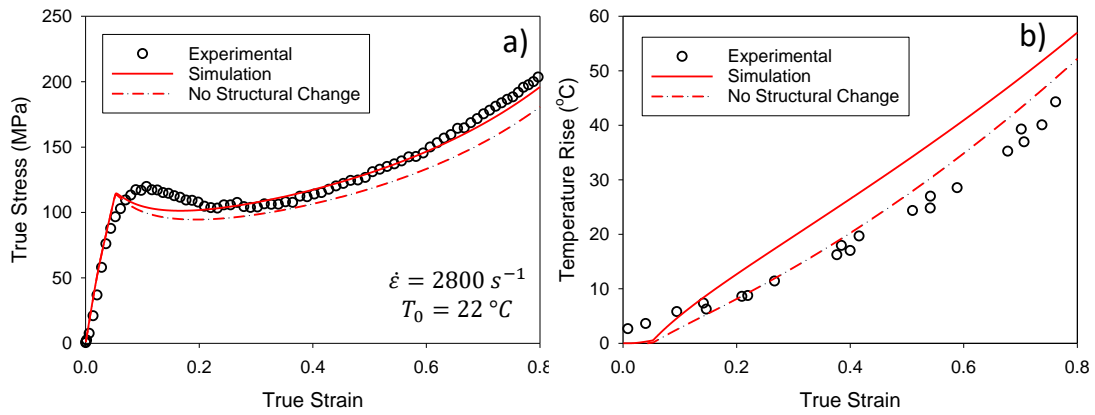
Figure 4.33: Effect of ignoring structural change energy on a) the true stress true strain response and b) the temperature rise

One avenue approached was how to account for the entropy elastic and associated heating. In this model, the conformational stress, S^c, contributes to adiabatic heating during loading as no energy is stored in inter-atomic potentials [69]. However, within the literature there are also references to the strain-stiffening that is a result of the hyperelastic back-stress being treated as energy-elastic [107].

One argument presented for the energy-elastic description is to debate whether at high rates there is time to sample all the configurations required to make the entropic elasticity claim. However, the conclusion within this work is that there is no real evidence to justify the energy-elastic treatment, as firstly it goes against well-established rubber theory and two, there is no understanding of what the time taken to sample all configurations would be. The losses of heat in experimental tests at medium rates, or an additional surface effect (as suggested in Buckley [69]) are valid reasons for the difference seen in the simulations presented within this work.

One other avenue considered was whether the conformational contribution was only part entropic. Effectively, could there be two hyperelastic springs in parallel, the first does not relax and refers to the entanglement network, the second is

considered temperature and rate dependent. Within this assumption, the second spring is treated as energy elastic and therefore does not contribute to heat generation. The effect of such an assumption is a reduced level of heating compared to assuming that all the energy is stored as heat.

4.7.4. Taylor Quinney Coefficient

One area of particular interest in the literature is the debate over the conversion of plastic work to heat, with origin work dating back to Taylor and Quinney (1934) for copper defining the Taylor Quinney coefficient (TQC). In much of the literature, it is assumed that specimen heating begins at the onset of plastic deformation, where this point can be considered either at the beginning of yield or at the yield stress [147]. If all the plastic work is converted to heat, the TQC would be 1. Many previous studies have used a constant value of TQC across strain, strain rate and temperature variations. From the energy accumulations presented in Figure 4.22, the TQC value can be calculated across the deformation from the ratio of energies shown in equation (4.24).

$$\frac{\text{Conformational+Dissipated}}{\text{Structural+Conformational+Dissipated}} \qquad (4.24)$$

Figure 4.34a and Figure 4.34b show the experimental results for the TQC value for varying temperature and varying rate. Figure 4.34c and Figure 4.34d present the simulated results.
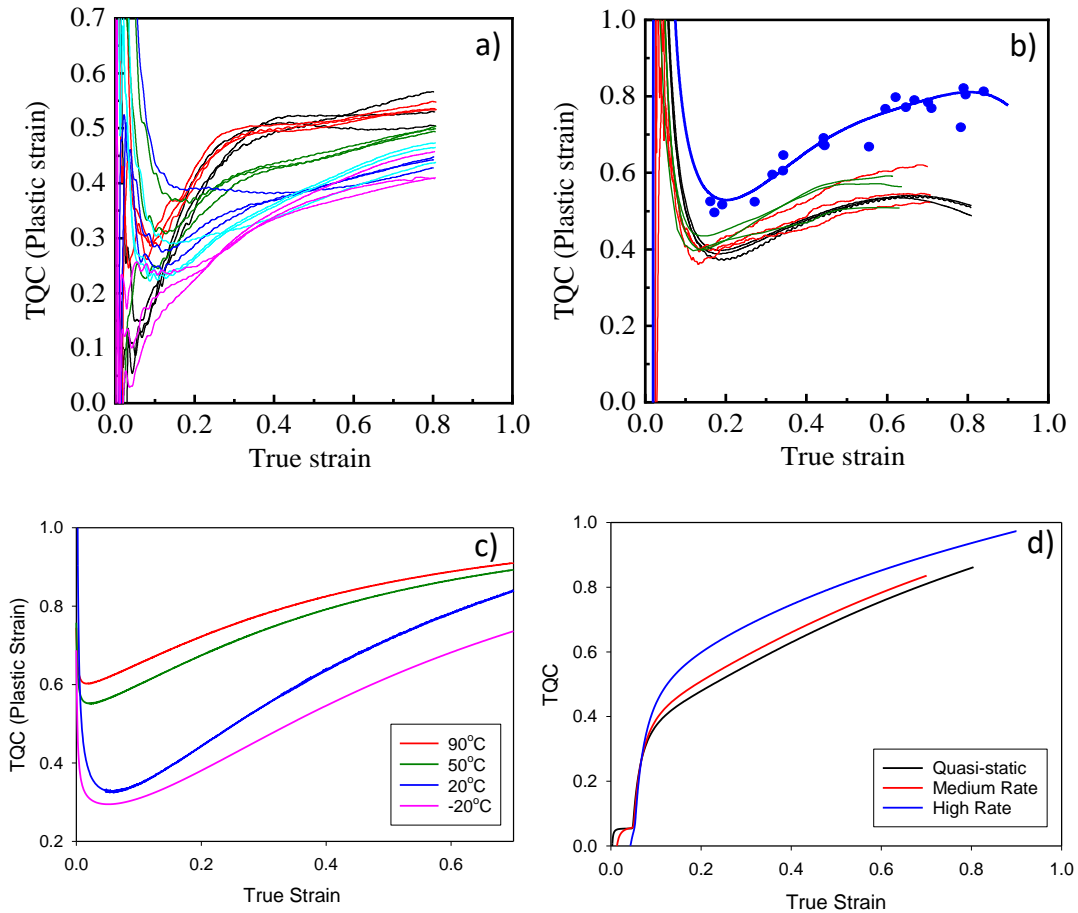
Figure 4.34: TQC response a) experimental varying temperature, b) experimental varying strain rate, c) simulation varying temperatures, d) simulation varying strain rates

Firstly, the experimental simulation results in Figure 4.34 highlight that TQC has a large dependency on strain as it does not remain constant across a strain range, nor a strain rate or temperature range, thus implying that choosing one value for a material for a range of tests will not capture the full picture. TQC increases as a function of increasing strain rate and with increasing temperature, captured both in the experimental and simulation results.

The constitutive model presented consists of a detailed breakdown of the distributions of energy, and therefore the origin of the temperature rise, is

obtained, removing the need for a TQC value, or to untangle the complexities of the strain, strain rate and temperature dependence that TQC demonstrates.

4.8. Conclusions

Within this chapter the constitutive model introduced in Chapter 3 was successfully extended to high strain rates and low temperatures. To achieve this, two main factors were considered: the effect of adiabatic heating and the influence of the β - transition. Initially, the parameterisation process is adapted to include the β -contribution. A second activation enthalpy, ΔH_β, is introduced to capture the lower temperature yield behaviour. An improved structural evolution was successfully developed to account for temperature and rate dependence, to accurately capture the post-yield response across the full rate and temperature range. These improvements to model and parameterisation process allowed high quality simulations for yield stress and full mechanical response for low temperatures and high strain rate cases. Additionally, load-unload simulations were analysed to explore the decomposition of the stresses at different rates and strain, while also providing insight to the temperature rise for adiabatic cases.

The adiabatic heating is implemented through decomposition into different energies, the elastic strain energy, the structural change energy, the conformational energy and the dissipated energy. During the parameterisation process it was observed that the specific heat capacity is temperature dependent. The Taylor Quinney Coefficient was also considered, defining the amount of plastic work converted to heat. This work established that the TQC value is strain, strain rate and temperature dependent. The energy-based method of extracting a temperature rise avoids the need for a TQC value and yields impressive predictions of temperature rises that are consistent with the observed experimental result.

A thorough physical implementation of adiabatic heating alongside an improved mechanical response through an updated modelling of the post-yield behaviour at high strain rates allowed the successful simulation of the mechanical response and temperature rises in polycarbonates at high strain rates and low temperatures.

5. Extension of the Constitutive Model to Alternative Polymers

5.1. Introduction

Within this chapter, alternative materials are investigated, parameterised and then simulated by the model presented in Chapters 3 and 4. Initially, three polycarbonates are explored to investigate the influence of molecular weight and co-monomers on the mechanical behaviour, parameterisation process and simulated mechanical response. A statistical comparison of the parameters is conducted to provide conclusions on the simplification of the parameterisation process for different grades of polycarbonate.

Following the study of the polycarbonate materials, two semi-crystalline materials are investigated. In the first instance, the model is applied to polypropylene (PP), with literature data and parameters obtained from an old version of the OGR model [6]. The aim of investigating PP is to test the improve simulated flow behaviour at high strain rates through the novel modelling methodology presented in the previous chapter in Section 4.5.1.

In Section 5.6 a second semi-crystalline material, polyamide 6 (PA6), is studied. For both PP and PA6, the material is treated as a continuum material such that the material is assumed to behave as one. The parameterisation process including obtaining the yield parameters and large strain behaviour is carried out for PA6. Stress-strain simulations for rate and temperature dependence are compared to the experimental results for yield stress and the full stress strain curves. A discussion is provided on the usability of this model and the engineering approach taken for semi-crystalline materials. Finally, in Section 5.7 conclusions are given on the process required for utilising this model for different grades of polycarbonate, polypropylene and polyamide6, with commentary on the successes and suggestions for future materials.

5.2. Polycarbonate Dataset

Table *5-1* shows material data including melt flow rate (MFR), molecular weight and glass transition for four different polycarbonates provided by Sabic®, that were characterised for this project within Song et al [133]. In Chapter 3 and 4, PC2 was studied which is a low melt flow rate (MFR) polycarbonate with a mould release agent and UV stabiliser. Within this Chapter, the differences in experimental mechanical response results due to varying molecular weight (PC3 and PC8) and the presence of co-monomers (PC4) are analysed and then simulated.

Table 5-1: Comparison of polycarbonates, adapted from [133], with code used within this work, the melt flow rate (MFR), the molecular weight and the glass transition stated.

PC (LEXAN™ RESIN)	Code[4]	MFR at 300 °C/1.2kg	Molecular weight (M_n), g/mol	T_g (°C)[5]
103R[6]	PC2	6 (Low MFR)	32441	145
500R Resin[7]	PC8	12 (Medium MFR)	25593	145
HF1110	PC3	25 (High MFR)	27401	145
HFD1014	PC4	6 (Co-monomer)	30106	130

---

[4] Nine polycarbonates were provided for this project, of which four were selected for characterisation, the codes here refer to the original material numbers.
[5] Obtained from experimental DSC measurements.
[6] This material contains a mould release agent and UV stabiliser.
[7] This polycarbonate is the pure matrix material for the SABIC composite marketed as 500R.
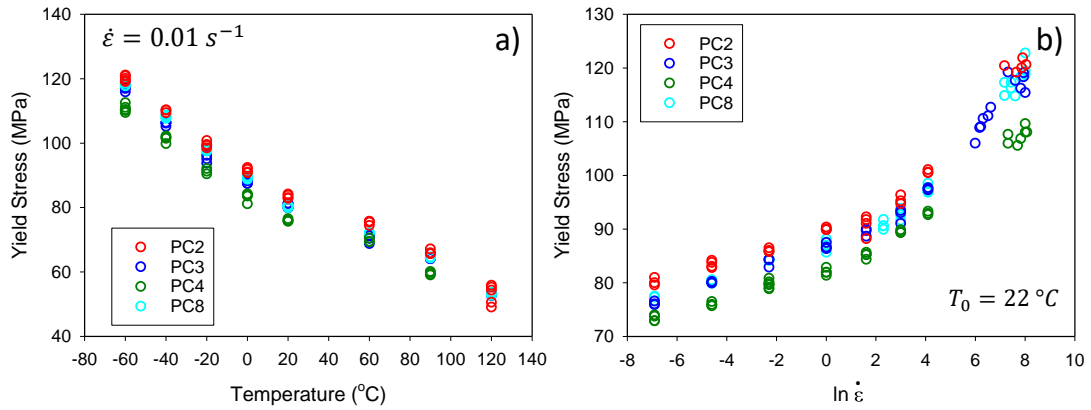
Figure 5.1: Experimental yield stress data for a) varying temperatures at a constant true strain rate of 0.01 s^{-1} and b) varying strain rates at an initial test temperature of 22 ºC

In Figure 5.1 the experimental yield stress data for the four polycarbonates introduced in Table 3-1 are shown for varying temperatures and strain rates. It is observed for all four sets of yield stresses that decreasing temperature and increasing the strain rate will increase the yield stress. In Figure 5.1, PC4 reports a lower yield stress than the other three grades across the temperature and strain rate range for both compression and tension. Additionally, looking at the change in gradients across the $\beta-$transition, PC4 exhibits different high rate behaviour to the other three polycarbonates. PC2 shows the highest yield stresses of the four materials, despite having the lowest molecular weight. Importantly, the PC2 contains mould release agent and a UV stabiliser, the effects of which are unknown. PC3 and PC8 show analogous results within Figure 5.1, which is expected as molecular weight has a negligible difference on yield response, provided it is high enough [67].

This experimental data can be utilised to study the effects of molecular weight and co-monomer behaviour on the parameterisation and modelling methodology. Through the comparison of PC3 and PC8 the impact of molecular weight is explored and through PC3 versus PC4 the influence of co-monomers.

5.3. Molecular Weight Effects

5.3.1. Material Introduction

As explored in Chapter 2, the literature predicts that the yield behaviour of the different molecular weights will be very similar, demonstrated through the comparison of PC3 and PC8 in Figure 5.1. Any deviations in mechanical behaviour as different molecular weights are tested is observed at large strains, specifically for polycarbonates due to a significant presence of the strain hardening. PC3 is also observed to be more brittle as failure occurs at a smaller strain than PC2 and PC8. This section will explore these similarities and differences further and determine which parameters that populate the model could be considered intrinsic.

Figure 5.2 shows the full true stress true strain response for three temperatures, $-60, 20, 90\,°C$, where the results of PC3 and PC8 for $-60\,°C$ and $20\,°C$ are analogous. However, in the $90\,°C$ example, the post-yield behaviour is observed to deviate between PC3 and PC8. Figure 5.3 highlights this statement through the comparison of flow structures, while Figure 5.4 shows that for higher temperatures a difference in the conformational parameter N_s is obtained. Both features contribute to the difference in the post-yield response for the $90\,°C$ example in Figure 5.2. Figure 5.5 shows the α value for both PC3 and PC8 where no temperature dependence is seen and the value is similar for both materials.
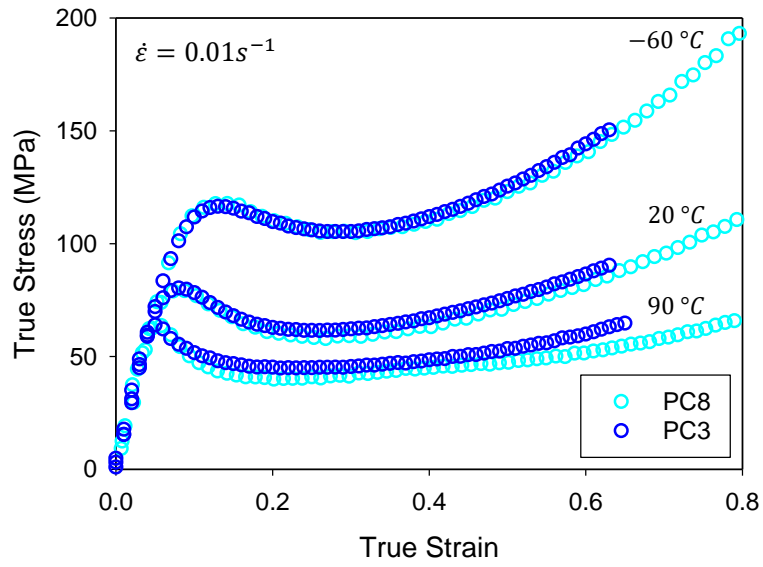
Figure 5.2: A comparison of PC3 and PC8 for varying temperatures -60, 20 and 90 ℃ at constant true strain rate test of 0.01 s⁻¹
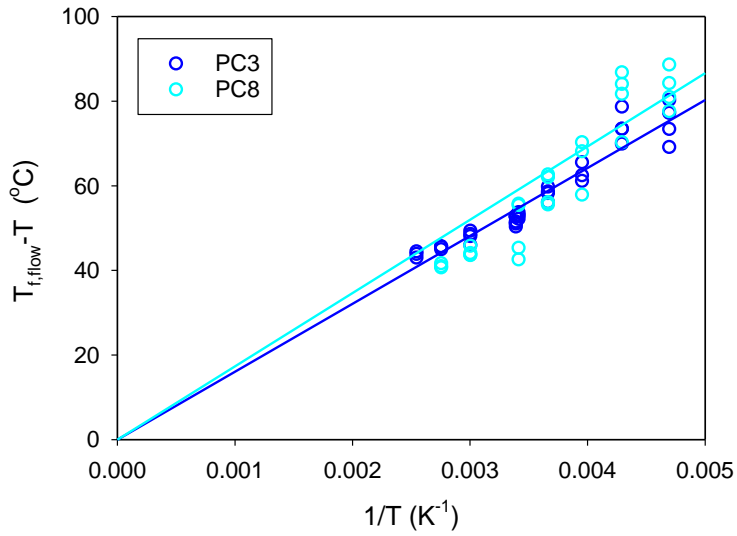
Figure 5.3: Comparison of the flow structure term ($T_{f,flow}$ -$T_∞$) for PC3 and PC8, showing proportionality with inverse temperature and slight difference in the two materials
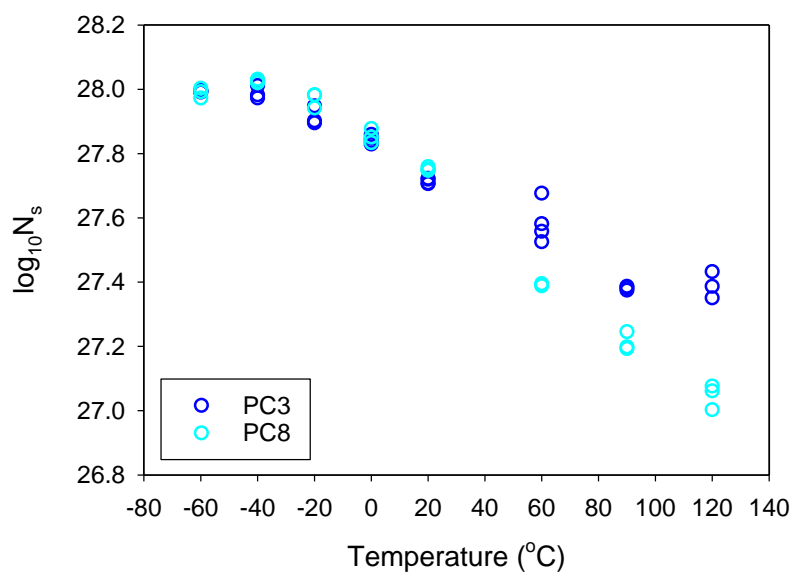
Figure 5.4: Ns temperature dependence for PC3 and PC8
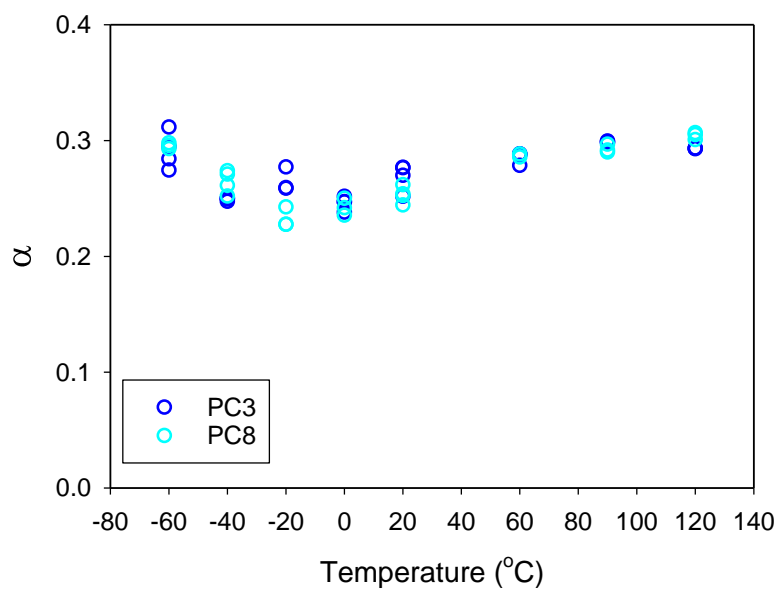
Figure 5.5: α parameter temperature dependence for PC3 and PC8

5.3.2. Molecular Weight Parameter Comparisons

To model these new materials the appropriate parameter datasets are required. One method of populating these datasets for the new polycarbonates is to recalculate all the parameters, following the methodology presented in Section 4.4. This would be the most thorough approach, but also the most time consuming and does not explore the possibility of intrinsic parameters for these materials. As the experimental results show a clear similarity between the PC3 and PC8 data,

the methodology discussed within this section is whether the parameters from PC3 could be utilised to compare simulations to both experimental datasets. The aim of this deeper analysis of the parameter process is to assess the least number of parameters required to change to successfully simulate the alternative materials.

Yield Parameters

By considering the value and standard deviation associated with each parameter, it is assessed whether the yield parameters are statistically similar. In this case, it is suggested that one value would be appropriate for both the materials considered (PC3 and PC8). However, if the parameters are found to be statistically different, then the two respective parameters for the materials will be utilised.

Firstly, the activation volumes $V_{s,\alpha}$ and $V_{s,\beta}$ for the respective α and β transitions were considered. Through the standard deviation of the linear regression fit of the experimental yield stresses shown in Figure 5.6, the resultant activation volume values are obtained with an associated standard deviation. The same process is applied to the intercept of linear fit of the experimental yield stress data to find the relaxation time, τ_0^*. Through the standard deviation of the linear regression fit of the experimental varying temperature yield stresses, the activation enthalpy, ΔH, for PC3 and PC8 are compared. All values are presented in Table 5-2.
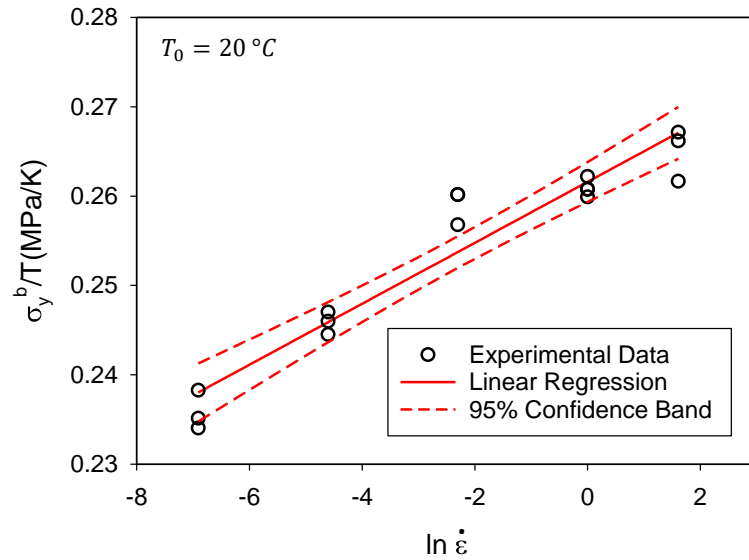
Figure 5.6: An Eyring plot for compression polycarbonate tests at 20 °C, showing a linear fit (red solid line) and two standard deviations in the gradient (dashed lines)

To examine whether these parameters for PC3 and PC8 are statistically similar, a two sample two-tailed Z-test was performed with a confidence level of 95%. For this statistical test, the z critical value is ±1.96. The method for this process is detailed in equation (5.1) where $\bar{x}$ represents the parameter value. Equation (5.2) gives the example for the $V_{s,\alpha}$ parameter while Table 5-2 presents the z value and result of the test for each parameter.

$$\text{Null Hypothesis, } H_0 : \bar{x}_1 = \bar{x}_2$$
$$\text{Alternative Hypothesis, } H_a : \bar{x}_1 \neq \bar{x}_2$$

$$z = \frac{\bar{x}_1 - \bar{x}_2}{\sqrt{\dfrac{\sigma_1^2}{n_1} + \dfrac{\sigma_2^2}{n_2}}} \tag{5.1}$$

where σ_1, σ_2 are the standard deviations of the first and second parameters being statistically compared and n_1, n_2 are the size of then dataset to reach the parameter value.

Therefore, for the $V_{s,\alpha}$ parameter:

$$z = \frac{0.00987 - 0.01057}{\sqrt{\dfrac{0.00088^2}{12} + \dfrac{0.00097^2}{12}}} = -1.85 > -1.96 \qquad (5.2)$$

This z value concludes that the null hypothesis is accepted i.e. the $V_{s,\alpha}$ parameter for PC3 and PC8 are statistically similar.

The relaxation times for PC3 and PC8 presented in Table 5-2 are not statistically similar, however this is more likely a result of the cumulation of errors through the parameterisation process, considering that the parameters are highly intertwined. The $\Delta H, V_{s,\alpha}$ and $V_{s,\alpha}$ results are all statistically similar for PC3 and PC8, allowing one value to be used to represent both materials.

Table 5-2: Comparative Yield Parameters for PC3 and PC8 with the value and standard deviation the results of the Z-test and the conclusion on statistical similarities.

	PC3 (± std)	PC8 (± std)	Z Results	Statistically Similar
$V_{s,\alpha}$ (m^3/mol)	0.00987 ± 0.00088	0.01057 ± 0.00097	-1.85	Yes
$\tau_{0,\alpha}^{*}$ (s) @ $T^{*} = 20\ °C$	1.10×10^{28} ± 9.77×10^{26}	1.86×10^{30} ± 1.710×10^{29}	-10.8	No
$T_{f,0}\ (°C)$	124.6±1.83	125.9±2.04	-	-
ΔH_{α} (J/mol)	2.8×10^{5} ± 4197	2.78×10^{5} ± 8055	0.76	Yes
$V_{s,\beta}$ (m^3/mol)	0.00313 ± 0.00039	0.00318 ± 0.00035	-0.427	Yes

The last parameter to discuss, regarding yield, is the bond-stretching shear modulus, G^b. As discussed in Section 3.3.9 and shown in Figure 3.15 the storage

modulus, G', curve will plateau at the values associated with the bond-stretching shear modulus, G^b, for both the α - and β - transitions. The value of this plateau can be found more specifically through assessing the modes associated with the linear viscoelastic spectrum. Each fitted mode has a weighted value of the total fit. These optimised modes are shown in Figure 5.8 with black squares, where the drop in these modes is representative of the α - relaxation. The dotted lines indicated the range of values associated with the α - relaxation or β - relaxation, a weighted average of the modulus in these specific ranges for the G^b value. Figure 5.7 shows every 5th datapoint for the linear viscoelastic shear relaxation spectrums for PC2, PC3 and PC8. It is observed that the largest deviation between the materials is with the β - transition region, but that PC3 and PC8 are analogous.
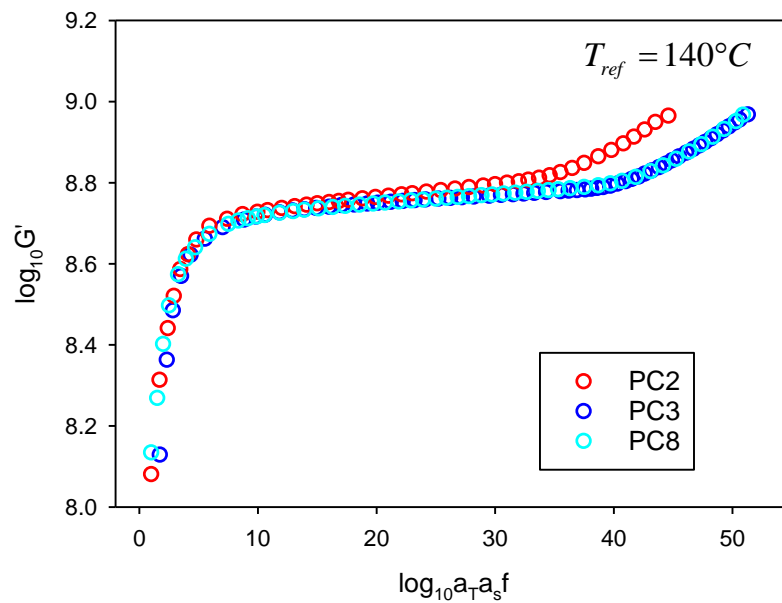
Figure 5.7: A comparison of the linear viscoelastic shear relaxation spectrums for the determination of the bon-stretching shear modulus for PC2, PC3 and PC8, polycarbonates of differing molecular weights
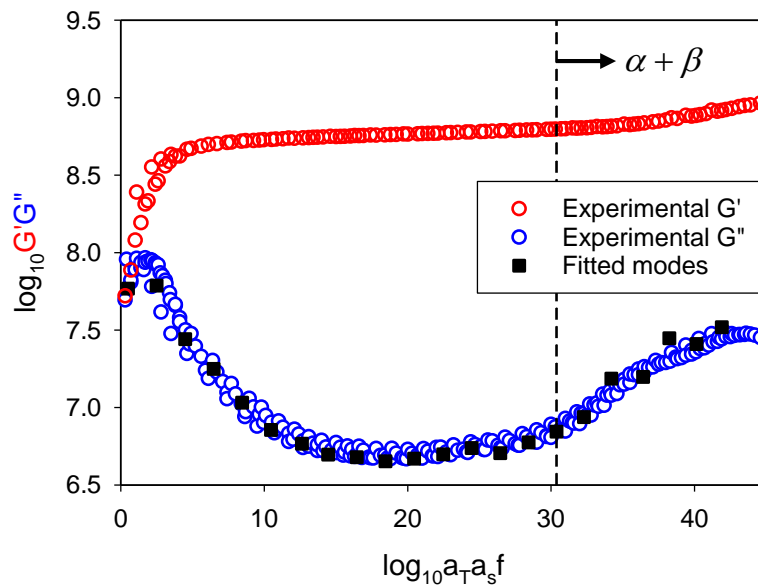
Figure 5.8: PC2 linear viscoelastic shear relaxation spectrum where black squares represent fitted modes and squares the averaging datapoints used to extract the bond stretching shear modulus

Flow Parameters

With the yield parameters established, the next parameters to consider are those needed to capture the flow behaviour. In Section 4.5.1, two parameters were introduced for the flow equation: k_0, a dimensionless constant to be fitted to experimental data, and m_{flow} which corresponds to the gradient of the linear regression for isothermal tests shown in Figure 4.13. It was assumed within Chapter 4 that the k_0 value is a constant, with no rate or temperature dependency.

A more thorough method to extract a k_0 value is to consider the drop in stress post-yield, visualised for an example of the PC2 experimental stress-strain response in Figure 5.9. The first derivative of the true stress-true strain plot is then used to find the inflection at the post-yield true stress minimum, shown in Figure 5.9b.
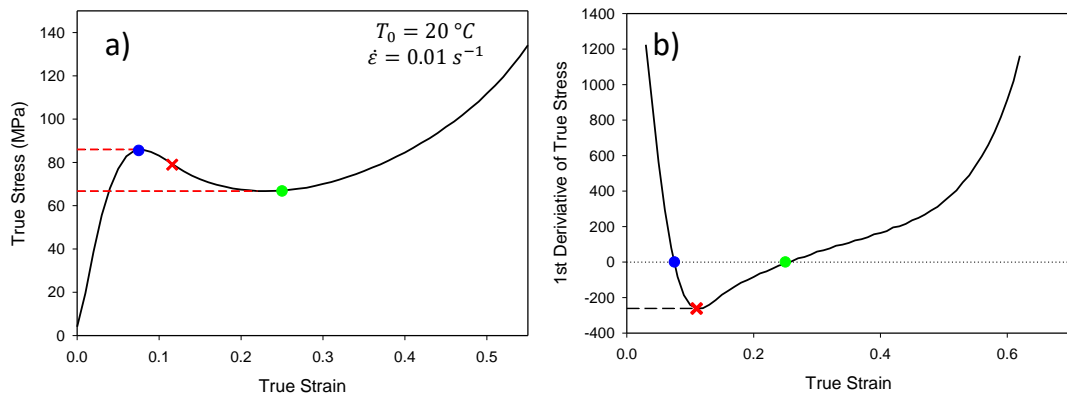
Figure 5.9: a) Full experimental true stress- true strain curve for PC2 at 20 °C and a true strain rate of 0.01 s⁻¹
b) the derivative of the plot a to find the inflection linked to the post-yield behaviour and yield drop

This process was then repeated for a series of simulation results, where different k_0 values are trialled and compared to the inflection, the results of which are presented in Figure 5.10 for 20 °C and a low strain rate of 0.01 s⁻¹. Through this method, it is clarified that the k_0 value should be approximately 300. In Figure 5.10 two materials, PC3 and PC3, are tested, showing similar results.
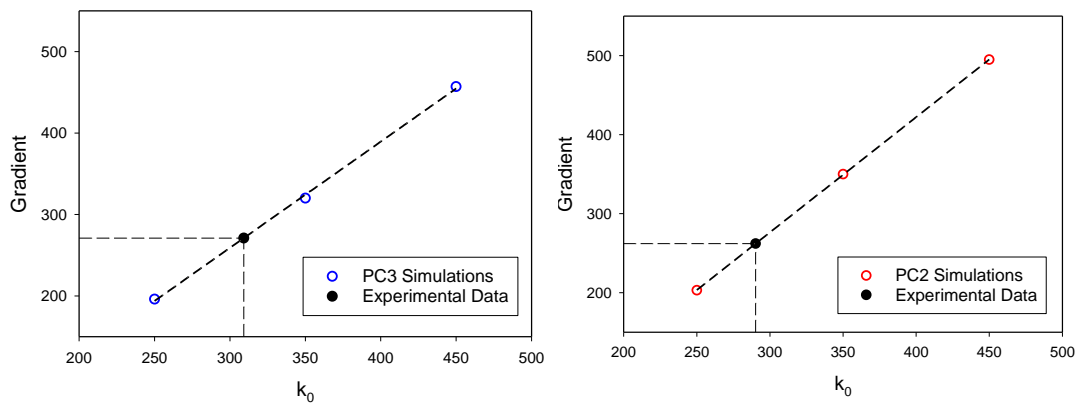
Figure 5.10: Determination of k0 for PC2 and PC3, showing similar results

Conformational Parameters

Within Section 3.3.10 it is established that two parameters are needed for the formulation of the conformational contribution, N_s, the density of entanglements and α, a measure of finite extensibility. α is taken to be a constant across temperature and rate ranges, as shown in Figure 5.11 alongside a 98% confidence

146

interval. N_s was found to not be a constant, and vary with temperature and strain rate, such that a sigmoidal function was created in Section 3.3.10, the parameters of which are adjusted with the optimisation fit to experimental data.
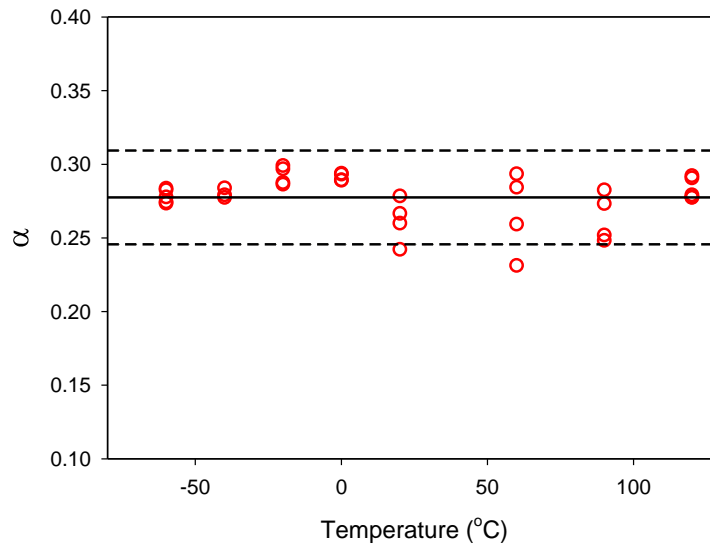
Figure 5.11: α, a measure of finite extensibility, taken to be a constant across varying temperatures and rates, shown with 98% confidence intervals

5.3.3. Results for Varying Molecular Weights

In Section 5.3.2, the appropriate datasets were found and presented in Table 5-2. Within this results section the PC3 and PC8 datasets will be used and mechanical responses simulated. Initially, in Figure 5.12 it is shown that the temperature and rate dependence of the yield stresses for both PC3 and PC8 can be captured through one dataset. The varying temperature tests are conducted at a constant true strain rate of $0.01s^{-1}$ and the varying strain rate at an initial test temperature of $22°C$. As with the PC2 case presented in Chapter 4, the yield is slightly overpredicted in the medium rate region, but the model does capture the yield stresses for the full rate and temperature range successfully.
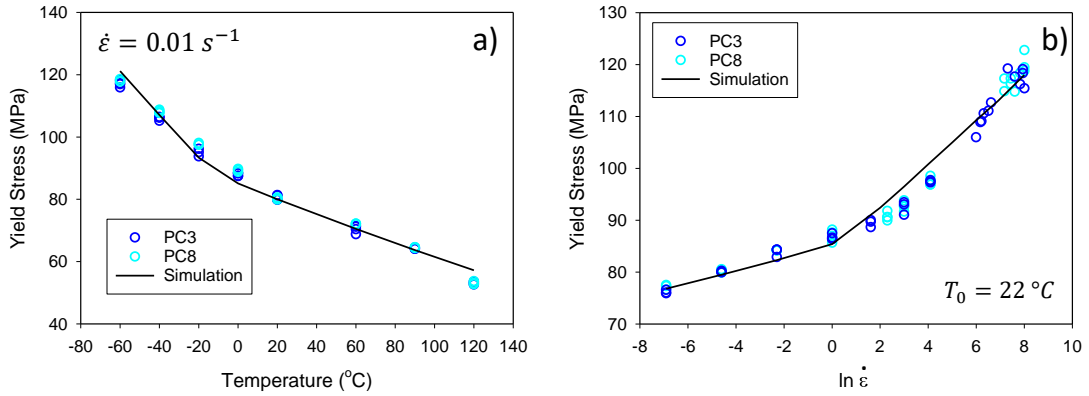
Figure 5.12: Simulation utilising PC3 parameters compared to PC3 and PC8 experimental results for a) varying temperatures at a constant true strain rate 0f 0.01s⁻¹ and b) for varying strain rates at a test temperature of 20 ᵒC

In simulating the varying temperature full responses in Figure 5.13, the subtlety of the differences between the two materials is seen and the previously discussed differences in flow behaviour are observed. In Figure 5.13a, the response for 20 °C at a constant true strain rate of 0.01 s^{-1} for both PC3 and PC8 is simulated successfully with the PC3 parameter set. In Figure 5.13b however, by acknowledging the difference in post-yield behaviour (highlighted in Figure 5.3 and Figure 5.4) and utilising both datasets two successful simulations for the 90 °C case are achieved.
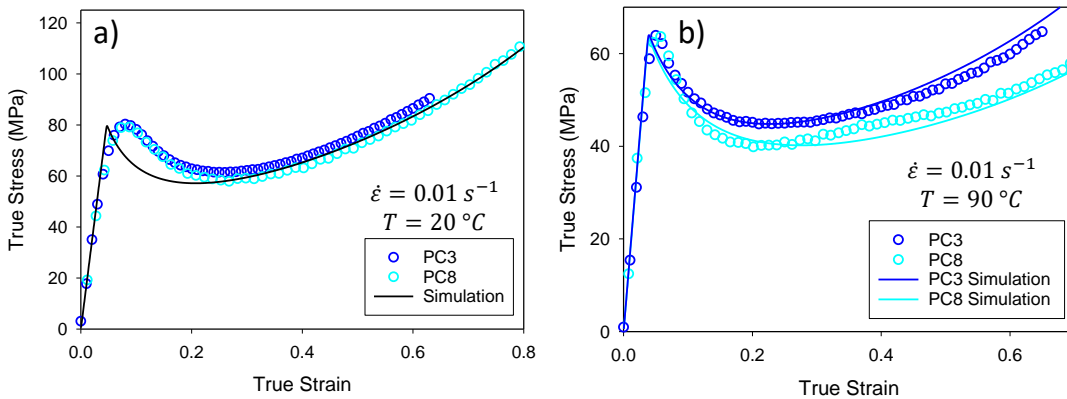
Figure 5.13: Comparison to PC3 and PC8 true stress true strain experimental results at a strain rate of 0.01s ⁻¹ for a) 20 °C using only PC3 parameters, b) 90 °C demonstrating the difference in PC3 and PC8 in higher temperature results

Finally, the quasi-static and high strain rate full mechanical responses are modelled in Figure 5.14. For both the 0.001 s^{-1} and 0.1 s^{-1} tests (in Figure 5.14a)

and for the high strain rate adiabatic simulation (in Figure 5.14b) the PC3 parameter set captures to a good degree the true stress-true strain response.
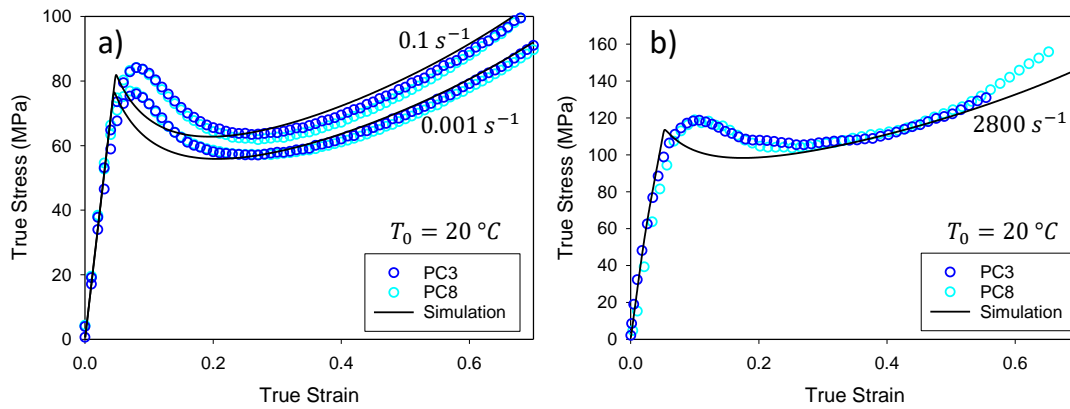
Figure 5.14: Simulation utilising PC3 parameters compared to PC3 and PC8 experimental results for a) quasi-static results 0.001 and 0.1 s⁻¹, b) for the high rate adiabatic 2800 s⁻¹ results

5.3.4. Discussion of Molecular Weight Effects

Within this section, two polycarbonates of different molecular weights, PC3 and PC8, are compared. Firstly, the parameterisation methodology and model are tested in capturing different polycarbonates. Secondly, the simplification of the parameterisation process is provided through assessing which parameters are not required to change for differing molecular weights. For the most part, the parameters associated with yield were statistically indistinguishable between the two materials, allowing an overlap of datasets. This was possible as varying molecular weight is not a significant factor to yield stress (when molecular weight is sufficiently high enough). Additionally, the materials supplied within this investigation had a relatively small difference in molecular weight $\left(25593-27401 \text{ g/mol}\right)$, observing that for more extreme cases this parameterisation test should be repeated. The severest difference in the two materials was seen in the post-yield behaviour at the higher temperatures, which is where the largest effect of differing molecular weights is observed.

From this study, the proposed recommendation for modelling a new material with differing molecular weights is that the only alteration to the parameterisation methodology is to adapt the parameters associated with post-yield behaviour, especially if higher temperatures or lower rates are of interest. For example, in the

case where only the yield stress behaviour is investigated, no changes are required.

5.4. Co-Monomer Effects

5.4.1. Co-Monomer Parameter Comparison

In Section 5.2 it was observed that PC4 reports lower yield stresses than the other three PC materials studied for both varying temperature and rate. Additionally, PC4 appears to have a less dominant $\beta-$ relaxation shown through the shallower bilinear response shown in Figure 5.1. The same set of statistical assessments introduced in Section 5.3.2 can be conducted for the co-monomer comparison of PC4 and PC3. This will provide verification that these experimental observations will result in reduced intrinsic parameters compared to the varying molecular weight case.

Table 5-3: Comparative yield parameters for PC3, PC4 and PC8 with values and standard deviations, the results of the Z-tests and the conclusion on statistical similarity.

	PC3 (± std)	PC8 (± std)	PC4 (± std)	Z Results	Statistically Similar
$V_{s,\alpha}$ (m^3/mol)	$0.00987 \pm$ 0.00088	$0.01057 \pm$ 0.00097	$0.01213 \pm$ 0.00012	-5.28	No
$\tau_{0,\alpha}^{*}$ (s)	$1.10 \times 10^{28} \pm$ 9.77×10^{26}	$1.86 \times 10^{30} \pm$ 1.71×10^{29}	1.96×10^{32} $\pm$ 1.93×10^{31}	-10.15	No
ΔH_{α} (J/mol)	$2.8 \times 10^{5} \pm$ 4197	$2.78 \times 10^{5} \pm$ 8055	$3.31 \times 10^{5} \pm$ 1.12×10^{4}	-1.45	Yes
$V_{s,\beta}$ (m^3/mol)	$0.00313 \pm$ 0.00039	$0.00318 \pm$ 0.00035	$0.00381 \pm$ 0.00039	-5.51	No

Table 5-3 presents the yield parameters for PC3, PC8 and PC4, highlighting that only the activation enthalpy of the PC4 yield parameters is statistically similar with the PC3 or PC8 materials. This implies that while the yield parameters are intrinsic for varying molecular weights, this is not the case for the co-monomer materials.

For the conformational behaviour, the value of α can be seen to be equivalent to the PC3 data, with slight deviation for the PC4 at $90\,^{\circ}\text{C}$. The temperature dependence on N_s is also present for PC4 but reporting lower values than PC3.
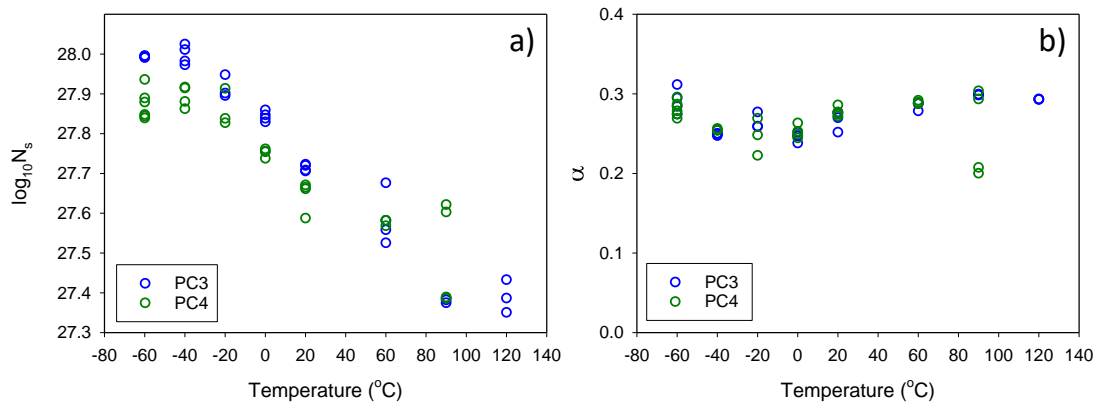
Figure 5.15: Conformational parameters for PC4 compared to PC3, the temperature dependence on a)Ns and b) α

5.4.2. Results

Initially, the yield stress responses for PC4 are plotted alongside PC3 for varying temperature and varying strain rate and compared to experimental results in Figure 5.16. In both cases the lower stresses of PC4 are successfully simulated and in Figure 5.16a the shallower gradient response of PC4 is captured.
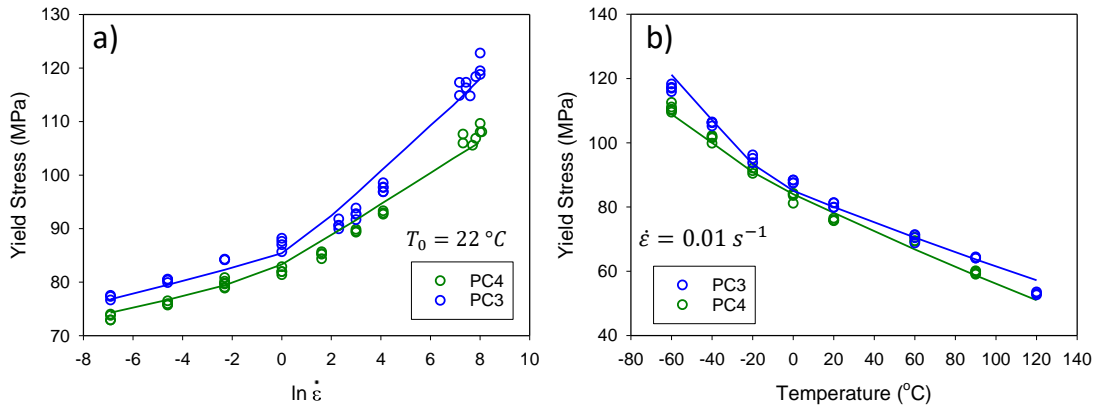
Figure 5.16: PC3 and PC4 yield stress experimental and simulated results for a) varying strain rates at an initial temperature of 20 ℃ and b) varying temperatures at a constant true strain rate of 0.01 s⁻¹

In Figure 5.17, the mechanical response for three temperatures $(-60, 20, 90 \ \text{°C})$ are shown. The general shape of the mechanical response is comparable between the two materials, with the width of the yield peak decreasing with increasing temperature.
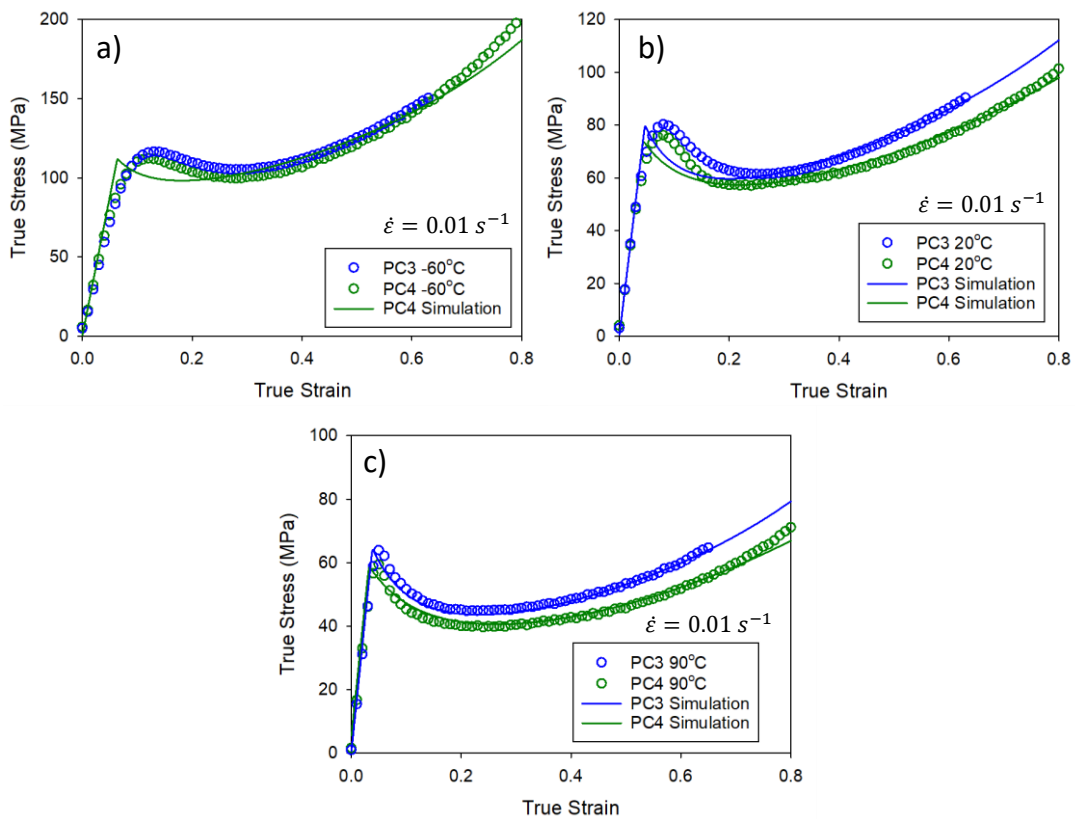
Figure 5.17: PC4 full true stress-true strain curves for a constant true strain rate of 0.01 s⁻¹ for a) -60 ℃, b) 20 ℃ c) 90 ℃

152

5.4.3. Discussion of Co-Monomer Effects

Within this subsection, the co-monomer PC4 was compared to PC3. Unlike the varying molecular weight investigation, the datasets required to populate the model for differing co-monomers are significantly different. The recommendation for this case is to repeat the full parameterisation process, though some intricacies are discussed below.

With closer inspection of the $0\ °\text{C}$ and $20\ °\text{C}$ temperature results the yield data is comparable, hypothesising that in the case of a model that is applied only in a narrow temperature and rate range, the PC3/4/8 yield parameters could be used interchangeably. However, when the operation range is extended, the differences due to the co-monomer would need to be considered, and this simplification invalid. Observing the pre-yield behaviour, it is seen to be equivalent for PC4 and PC3 (and therefore also PC8 seen in Figure 5.13 and Figure 5.14), such that the parameter that dominated this part of the response, the bond stretching shear modulus, can be taken to be the same for all polycarbonates studied.

5.5. Structural Evolution Comparison for Polypropylene

5.5.1. Introduction

In this subsection the semi-crystalline polypropylene (PP) will be modelled utilising experimental data and selected parameters from a previous OGR model by Okereke [6]. Firstly, it allows the consideration of semi-crystalline materials in the model. Secondly, it presents the opportunity to verify the new fictive temperature evolution introduced to more accurately capture post-yield flow for a wide range of temperatures and rates from Section 4.5.1. Figure 5.18 shows the mechanical stress-strain response across a wide strain rate range $\left(0.0001-11000\ \text{s}^{-1}\right)$ for experimental results and simulations for polypropylene from this previous OGR model [6]. Observing the high strain rate response, it

appears that these previous simulations had similar post-yield issues as the older adaptation of our model, results presented in Section, 4.5.1, originating from taking one value of k, the effective rejuvenation parameter, across a large temperature and rate range. Using the parameters and version of the OGR model given in this previous PP study[8], but with the new fictive temperature evolution defined in our work, is it possible to reduce the curve collapse at high strain rates shown in Figure 5.18, where curve collapse is when the curves of the stress-strain response at different strain rates come together at large strains.
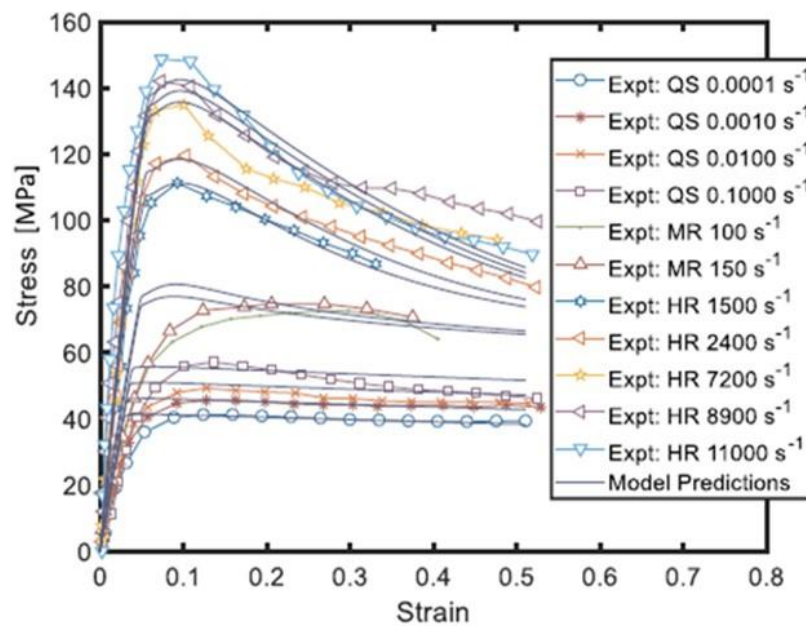
Figure 5.18: Polypropylene modelled through the OGR model, demonstrating the converging of high strain rates curves at post-yield strain, adapted from [6]

5.5.2. Modelling Approach

The model presented for polypropylene in the literature [6] contains a few differences in comparison to the model within this thesis. With a specific focus on fictive temperature evolution, the model of Okereke presents two fictive temperatures (for α and β relaxations respectively), and therefore two evolution of fictive temperature equations, where it is assumed that $k_{struct,\alpha} = k_{struct,\beta}$. The response for the low strain rates shown in Figure 5.18 are indicative of a post-

---

[8] The reference relaxation viscosities are believed to be a typo and Gb yield the results shown in the paper

yield response where $\Delta T_f = 0$, this is therefore the assumption when replicating the low strain rate simulations from Figure 5.18. For the medium rates in Figure 5.18, $100 - 1500 \text{ s}^{-1}$, the experimental data stops at an earlier strain, so no assumptions can be made on the behaviour at large strains. With these interpretations of the code used in the model of Okereke [6] assumed, Figure 5.19 shows the mechanical response and the evolution of fictive temperature for three high strain rates $100, 1000, 10000 \text{ s}^{-1}$.
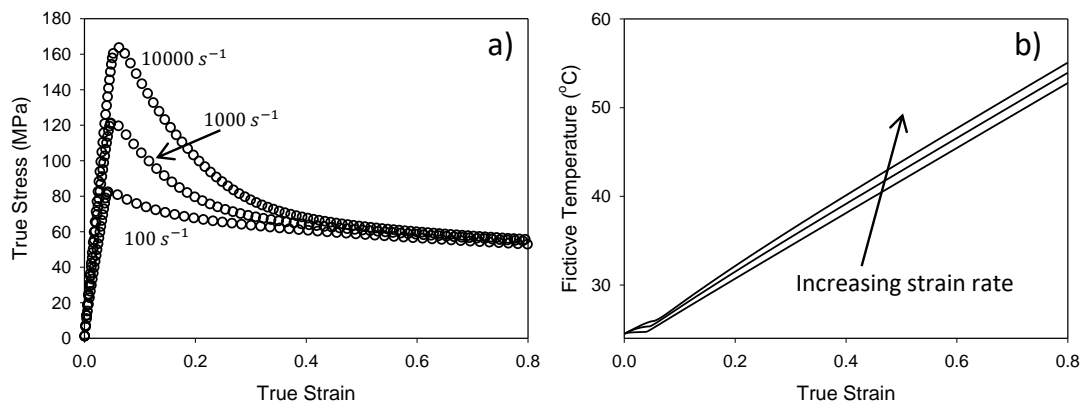
Figure 5.19: Simulations representing Figure 5.18 using the model presented in this thesis, specifically the novel approach in Section 4.5.1 for $100, 100, 1000 \text{ s}^{-1}$, a) the true stress versus true strain response and b) the fictive temperature evolution with true strain

In this case, the unrealistic evolution of the fictive temperature manifests as the collapse of the stress-strain curves in high rate tests. In Figure 5.20 the results with the new evolution of fictive temperature implemented are shown, for the rates $100, 1000, 10000 \text{ s}^{-1}$. The low rates are not shown as there is no change in fictive temperature to analyse.

Critically, the new version presented in this work for the evolution of fictive temperature across a wide range of temperatures and rates was able to improve the results for this version of the OGR and for a semi-crystalline material.

155
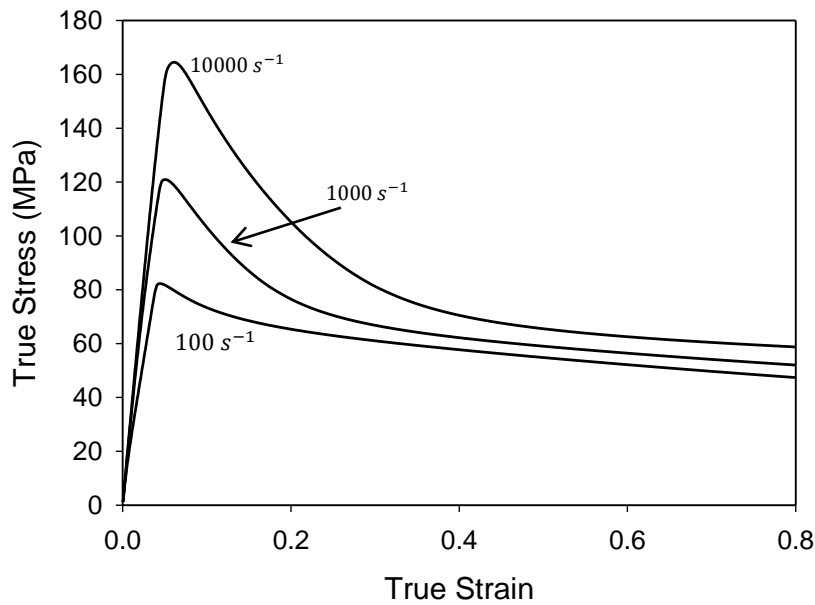
Figure 5.20: Improved results for the true stress- trues strain simulation of polypropylene at high strain rates (100,1000, 10000 s⁻¹) through our Chapter 4 methodology

5.6. Phenomenological Application to Semi-Crystalline Polymers

5.6.1. Modelling Approach

The final material explored was another semi-crystalline, polyamide. For this semi-crystalline material, the modelling approach is to treat the material as a homogeneous material, rather than to attribute separate properties to amorphous and crystalline phases. With this assumption, all parts of the material behave as one. This will allow the use of the existing model and an assessment of the limitations in this assumption.

To test the feasibility of this method, first an assessment of the mechanical experimental data is required. Figure 5.21a shows the experimental true stress-true strain response of PA6 for uniaxial compression tests at a true strain rate of $0.01 \, s^{-1}$ and varying temperature. Figure 5.21b shows varying strain rate temperature of $30 \, °C$. Most notably, for the temperature and rate ranges presented, there is no drop in the stress post-yield (post-yield softening), as was observed for polycarbonate and the high strain rate responses of polypropylene.

The lack of an easily distinguished yield requires a different definition of the yield stress, here taken to be the stress at a true strain of 0.1. The last feature to consider is the large strain behaviour and associated strain hardening, a distinct lack of curvature indicates a different large strain behaviour to that of the initial amorphous polycarbonate. At the quasi-static rates, a rise in stress is seen post-yield, demonstrating some strain hardening while at high strain rates, the large strain behaviour plateaus until failure.
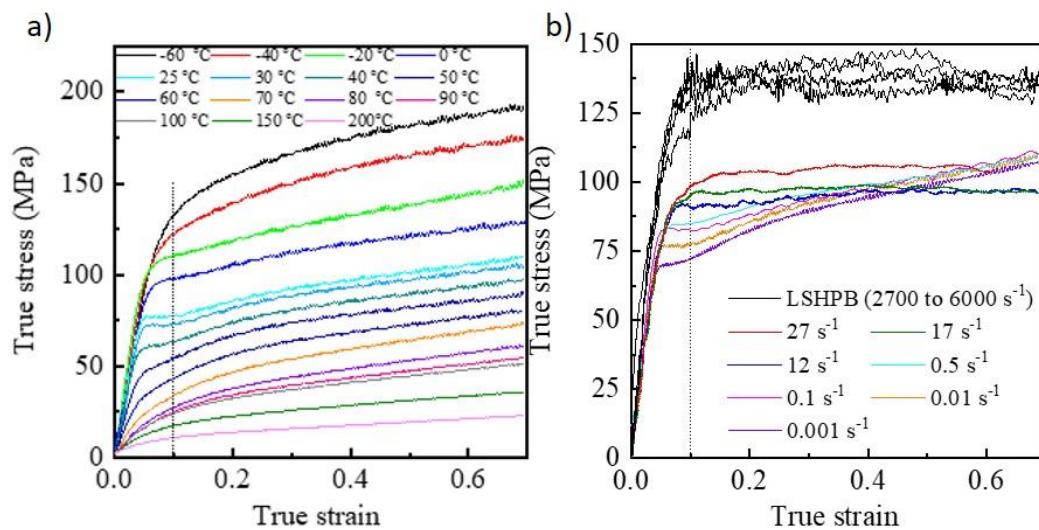
Figure 5.21: Full true stress versus true strain response for PA6 a) varying temperature results, b) varying strain rate, adapted from Song et al.[9]

5.6.2. New Parameterisation Method

With the defining mechanical response features clarified, the following section details how to approach the parameterisation of this material following a homogeneous approach. Initially, the novel method introduced in this work to separate the bond-stretching yield stress can be applied, shown in Figure 5.22, using an Edwards-Vilgis fit with a constant flow stress. From this optimisation and the quasi-static rates where some strain hardening is observed, this method successfully works for a material with vastly different behaviour to polycarbonate.

---

[9] Work adapted from experimental results from colleagues at the University of Oxford (P. Song), to be published soon
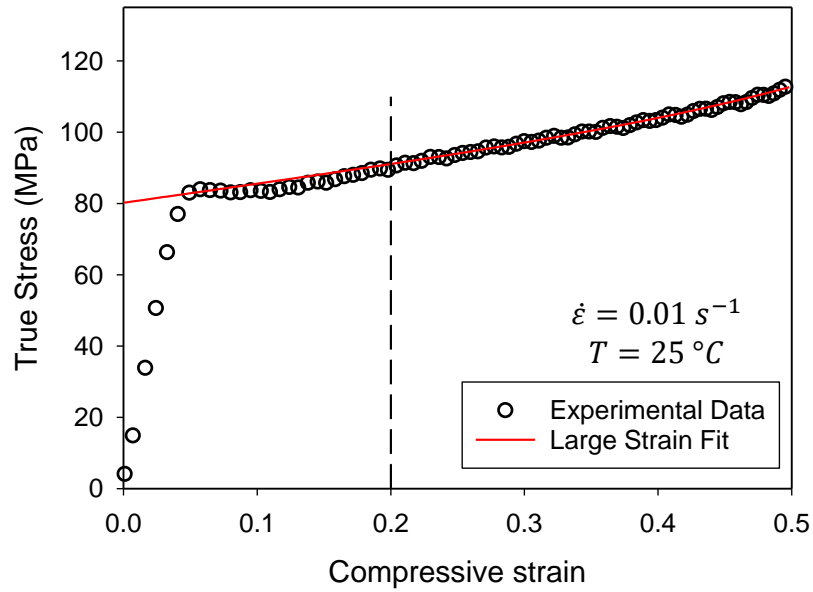
Figure 5.22: Edwards-Vilgis function with a constant flow stress for PA6 at a 0.01 s⁻¹ and 25 ᵒC, the optimisation starting from the dashed line at a strain of 0.2

To capture the yield process, Figure 5.23 shows the yield stress experimental results for fixed temperature $(25\,^{\circ}\mathrm{C})$ but varying constant true strain rates. As with the amorphous example in Chapter 4, a bilinear Eyring plot can be obtained, and the associated parameters found $(V_{s,\alpha}, V_{s,\beta}, \tau^*_{0,\alpha}, \tau^*_{0,\beta})$. Figure 5.24 shows the temperature dependency, with varying temperatures in the range of -60-$100\,^{\circ}\mathrm{C}$, and a fixed strain rate of $0.01\ \mathrm{s}^{-1}$. This temperature data range can be split into three regions, considering that the two transition temperatures are $T_g \approx 50\,^{\circ}\mathrm{C}$ and $T_\beta \approx -50\,^{\circ}\mathrm{C}$. The first region shows the linear behaviour far below the glass transition, though this temperature range approaches the β -transition temperature expected, it is not obviously detectable within the temperature yield stress data. The second shows a curvature and deviation from Arrhenius behaviour to this plot around the glass transition. The third region contains temperature far above the glass transition, an area not currently considered by the model presented in this thesis.
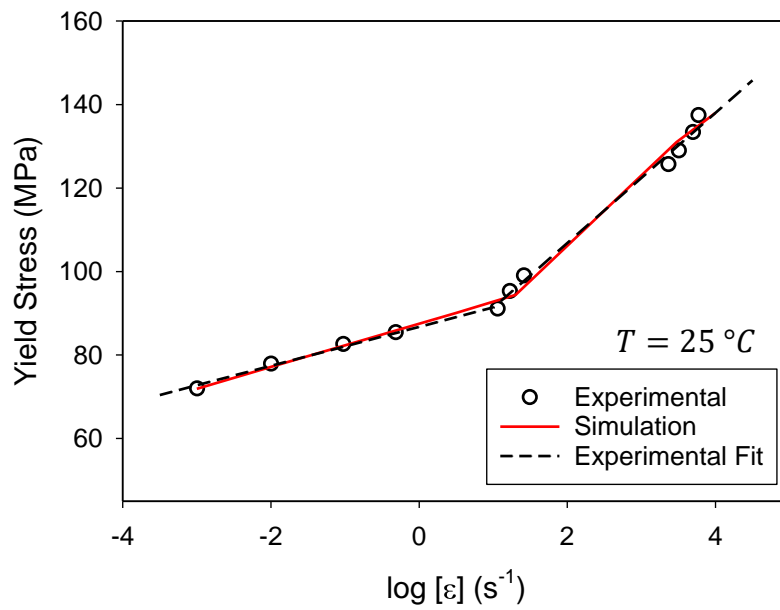
Figure 5.23: PA6 yield stress for varying strain rates with experimental results and simulated values highlighting the bilinear response
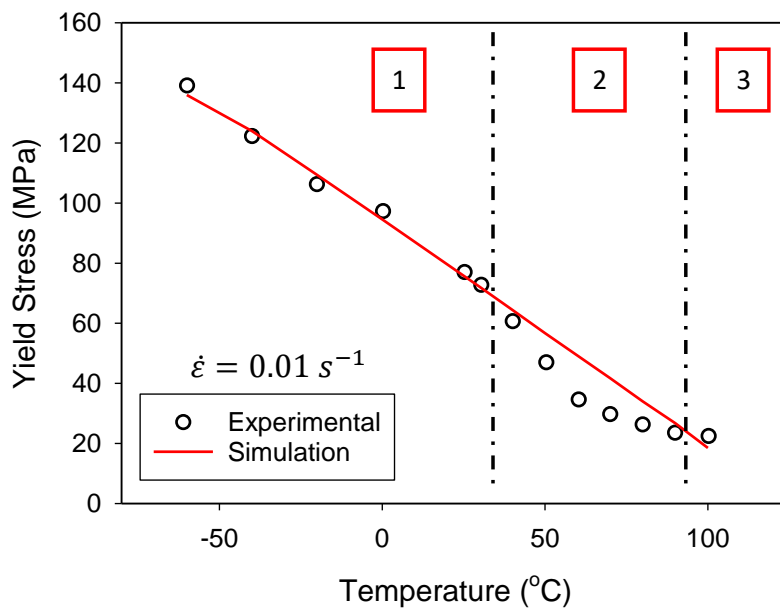
Figure 5.24: PA6 yield stresses for varying temperatures, three zones noted, 1- below Tg, 2- close to Tg, 3- far above Tg

From these three regions, the first region temperatures $\left(< 35 \,^\circ\mathrm{C}\right)$ can be utilised to follow the same process as presented in Section 4.4 to find a ΔH_α. To implement the observation of a lack of strain softening (exhibiting as no visible

drop in stress post-yield) into the model, the evolution of fictive temperature can be switched off, such that $\Delta T_{\mathrm{f}} = 0$.

Table 5-4: Full list of PA6 Parameters with the source

Bond-Stretching Terms		
$T_g\,(°C)$	50	Experimental [133]
$V_{s,\alpha}\,(\mathrm{m}^3/\mathrm{mol})$	0.0051	Section 4.4.2
$V_{p,\alpha}\,(\mathrm{m}^3/\mathrm{mol})$	0.00026	Section 4.4.2
$\tau_{0,\alpha}^{*}\,(\mathrm{s})$	3.53x10¹³	Section 4.4.3
$\Delta H\,(\mathrm{kJ/mol})$	246	Section 3.3.7
Conformational Terms		
α	0.179	Figure 5.22
$N_{s,0}$	27.62	Figure 5.22

5.6.3. Simulation of Structural Evolution and Mechanical Response

Varying Temperature

Figure 5.24 shows the yield stress results for the temperature range $-60\text{-}100\ °\mathrm{C}$ for the isothermal test with constant true strain rate $0.01\ \mathrm{s}^{-1}$. The simulations successfully fit the temperatures in region one. However, as expected, the second region that deviates from the Arrhenius behaviour is not captured by this method. The full true stress- true strain response for three temperatures $(-20, 0, 30\ °\mathrm{C})$ in this first region are shown in Figure 5.25. Post-yield the response is successfully simulated due to the $\Delta T_{\mathrm{f}} = 0$ assumption and capturing the conformational behaviour through the method shown in Figure 5.22.
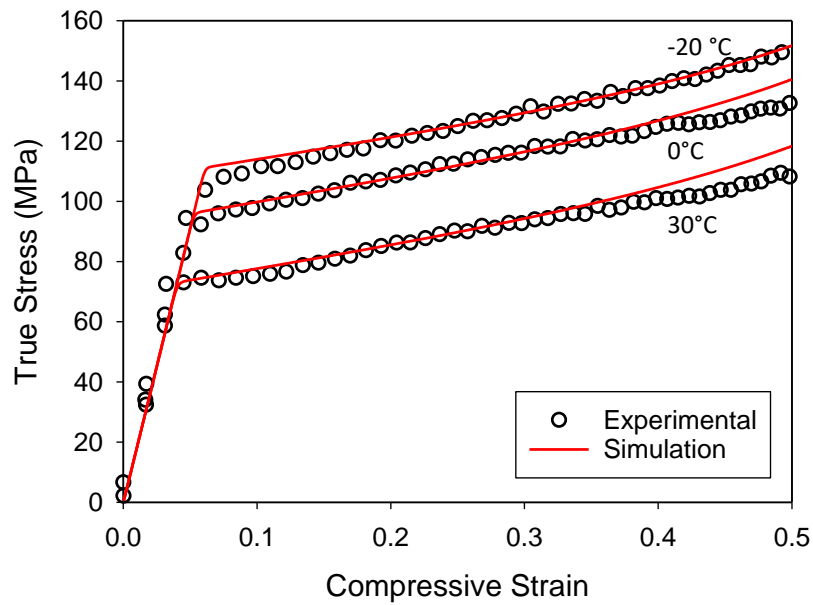
Figure 5.25: Simulated results for PA6 compared to experimental for three temperatures, -20, 0, 30 ºC

Varying Rate

The simulated yield stress results for varying strain rates and the initial temperature of 25 ℃ are compared to the experimental results in Figure 5.26. In Figure 5.26b, a true stress- true strain curve is presented for an example high strain rate ~ 3000 s^{-1}, showing both the isothermal and the adiabatic simulations.
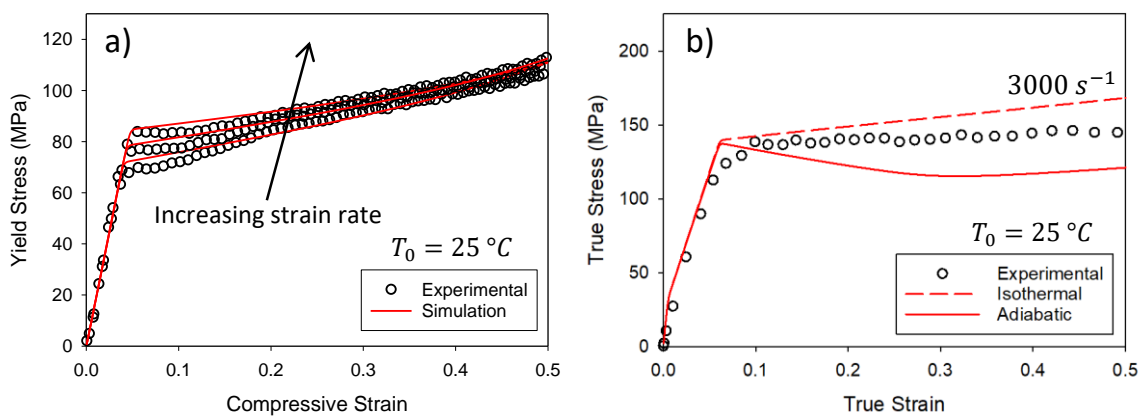
Figure 5.26: Simulations of PA6 varying strain rate tests at an initial temperature of 25 ºC for a) quasi-static rates 0.001,0.01.0.1 s^{-1} and b) a high strain rate example at 3000 s^{-1}

161

5.6.4. Discussion of PA6 Simulations

Overall there is a good level of success with this continuum, engineering approach to the simulation of polyamide 6 using the model presented in Chapters 3 and 4 despite the simplifying assumptions used. For the varying rate temperature simulations shown in Figure 5.24 a good agreement in yield stress is obtained for region one, where test temperatures are far from the glass transition for this material. The lack of a secondary activation enthalpy associated with the β - transition, ΔH_β, does not appear to affect the lowest temperature simulations, even though $T_\beta \approx -50\,^\circ\mathrm{C}$. If there was experimental data at lower temperatures it may be possible to model this additional subtle contribution to temperature dependence. As the temperatures increase into the glass transition, a decrease in yield stress experimentally is seen, and thus the simulated data overpredicts in this region. This is to be expected as there are no considerations in the model to account for the changing behaviours associated with above the glass transition in this region.

Extending the model to large strains, for the low temperatures, a good agreement with experimental data is simulated, shown in Figure 5.23. The parameterisation alterations described in Section 5.6.2, can capture the large strain response as temperature varies, as shown in Figure 5.25. In the full true stress strain plots for high strain rates, shown in Figure 5.26, less accurate simulations compared to experimental data are seen in comparison with the quasi static rates, with the adiabatic response underpredicting the large strain behaviour, specifically not capturing the plateau response seen experimentally.

However, the limitations on physical understanding for this method are considered. For a more physical model than this, more experimental data would be required, providing a more complete understanding of the crystalline structures and the interplay with the amorphous regions.

5.7. Conclusions

This chapter expands on the work presented in Chapters 3 and 4 by applying the current model to different grades of polycarbonate, polypropylene and polyamide6. Initially, the molecular weight effects of amorphous polycarbonates are explored, finding that PC3 (high MFR) and PC8 (medium MFR) have analogous yield responses. Therefore, one set of parameters adequately captures the behaviour of both materials, reducing the number of experiments and size of the parameter dataset required. In fact, for the majority of strain rates and temperatures studied, one set of parameters can capture the full mechanical response for both PC3 and PC4. The differences were observed at the higher temperatures $(\sim 90°C)$ where the flow behaviour and conformational contribution began to vary between the two materials. In this case, using the flow and conformational parameters for the respective material captures the post-yield behaviours more successfully.

The comonomer PC4 was observed to have lower yield stresses across the temperature and rate range than PC3 and PC8 and a different high strain rate behaviour, observed through the shallower bilinear response in Figure 5.1. While the PC3 data set could therefore not capture the yields of PC4, the model did successfully simulate the lower yield stresses and capture the less dominant β-contribution. The pre-yield response for all the polycarbonates is comparable and therefore the one parameter that can be used for all the materials is the bond stretching shear modulus that controls the gradient of the small strain behaviour.

The next material studied was polypropylene, not only is this a semi-crystalline material but previous OGR studies on PP exhibited difficulties modelling the post-yield flow. This could also be observed in Chapter 4 with the extension to high rates and low temperatures for polycarbonate. The novel equation presented in Section 4.5.1 was applied to the PP literature data to determine the success on controlling the flow response of alternative materials. The new equation for the evolution of fictive temperature was found to reduce the collapse of the stress-strain curves in the previous simulations of PP and control the unrealistic growth of the fictive temperature at high strain rates.

Finally polyamide 6 was parameterised and modelled through a homogeneous approach and the model presented in this thesis. While it is acknowledged that for a detailed understanding and simulation of PA6, a full implementation of the crystalline contributions and the interplay with the amorphous regions would be needed, this requires an extensive experimental data set. In this work, it was shown that the yield stress response for a wide strain rate and temperature range below the glass transition can be captured to a reasonable degree of accuracy using this homogeneous approach. Furthermore, the full mechanical response can be simulated successfully for the temperatures close to room temperature and the quasi-statics conditions. The continuum approach begins to breakdown at the high strain rates, where the plateau of stress post-yield seen experimentally is underpredicted by the adiabatic simulation.

The work in this chapter allows the model to be verified against alternative materials, extending the usability and validating the novel work within Chapter 3 and 4 surrounding conformational parameter fitting and evolution of flow. Additionally, this chapter provides recommendations on the methodology of modelling new materials.

6. Conclusions

The purpose of this thesis has been the development of the Oxford Glass Rubber (OGR) constitutive model with the purpose of capturing the behaviour of polymers at high strain rates and under adiabatic conditions. This chapter will summarise the key findings in this thesis, with Sections 6.1-6.3 detailing conclusions on the work presented and Section 6.4 recommending potential avenues for future work.

6.1. Low Rate Model

Within Chapter 3, a new version of the OGR constitutive model for amorphous polymers at low strain rates $(0.001-0.1\,\text{s}^{-1})$ and temperatures close to room temperature $(0\text{-}120\,^{\circ}\text{C})$ was presented. The first major novel development to previous OGR models was the more thorough implementation of structural evolution through the fictive temperature which evolves through ageing kinetics and rejuvenation driven by a plastic strain invariant. Although the differential equation formulation was developed in Buckley et al [69], only a solution to this equation was previously employed, thus lacking the rate and temperature dependence in the structural evolution. This new implementation was seen to capture the post-yield softening observed experimentally for polycarbonate.

The model parameterisation was improved further to consider materials such as polycarbonate with tighter networks and therefore larger strain hardening moduli. This was achieved firstly through the division of yield stress into contributions from bond-stretching and conformational parts, to allow the correct simulation of both parts. This separation is not essential in materials with looser entanglement networks, such as was employed in previous OGR models [67], [77] for polystyrene and polypropylene. This extends the usability of the model by including more materials. Conformational parameters were obtained through fitting an Edwards-Vilgis fit with a constant flow stress at strains far from yield $(\varepsilon > 0.3)$ to experimental data. A temperature dependence in the parameter, N_s, density of entanglements, was discovered and implemented to best capture the

large conformational stresses originating in polycarbonate and the dependencies of this on test conditions.

Finally, tensile simulations were presented alongside experimental data. The full stress-strain curve presented a challenge as the strain rate will not be homogeneous throughout the sample, such that the mechanical response curve will vary in different parts of the sample. The yield stresses and the minimum stress associated with the neck were successfully simulated. The model less successfully modelled these tensile tests at large strains, attributed to the challenges of localisation of strain rate and inconsistent adiabatic heating within the sample.

6.2. High Rate Model

As the model was extended to high strain rates, as presented in Chapter 4, considerations for the β - transitions and adiabatic heating were required. Initially, to address the high strain rate behaviour, the effect of the β-transition was implemented to the constitutive model as a parallel viscoelastic process. The parameterisation methodology was developed to include both the α- and the β- processes.

When simulating the structural state at this broad range of timescales and temperatures is was required to introduce a temperature-dependent rejuvenation constant to achieve physically relevant structural states, and hence flow stresses. A novel implementation of bounding of the fictive temperature was introduced to capture this structural change. This bound was implemented through dependence on difference between the fictive temperature and the Vogel temperature. Additionally, to capture the lower temperature yield behaviour, a second activation enthalpy, ΔH_β, was established through the bilinear treatment of varying temperature yield stress data. These new improvements to the model and parameterisation process produced high quality simulations for yield stress and full mechanical response for both the low temperatures and high strain rate cases, extending the usability of the model to a broad range of conditions.

A detailed assessment of adiabatic heating and the resulting temperature rise was presented, with considerations for dissipated energy, conformational energy, elastic strain energy, and the energy needed for structural change. The adiabatic heating itself arises from two sources, the dissipation of flow stresses and the entropy elasticity of the entanglement network and with this definition, accurate temperature rises during adiabatic deformations were simulated. The accuracy of the temperature rise simulations was observed to improve throughout the medium strain rate range (from 1.5 s^{-1} to 11 s^{-1}) as the conditions become increasingly adiabatic. At the highest strain rates $\left(\sim 3000 \text{ s}^{-1} \right)$, temperature rise simulations successfully captured the novel split Hopkinson bar experimental measurements for the first time.

6.3. Alternative Materials

In Chapter 5, four different grades of polycarbonate and two semi-crystalline materials (polypropylene and polyamide 6) were considered. It was found that the parameterisation method and model presented in this thesis can be extended to alternative polycarbonates, polypropylene and polyamide successfully with a few modifications discussed below.

Molecular weights effects were studied in two polycarbonates (PC3 and PC8). Within the experimental results, the yield behaviour and full mechanical responses for many of the rates and temperatures appeared similar between these two materials. Through a two sample two-tailed z-test the statistical similarity of these parameters needed to populate the model for simulations of PC3 and PC8 were tested. The conclusions verified the use of the same set of parameters for the two materials. The same statistical analysis of parameters between polycarbonates was conducted to assess co-monomer effects. For the co-monomer effects it was observed that the mechanical response and yield stresses of PC4 varied significantly. The z-test found that the parameters were statistical different such that the same parameters are not appropriate for varying co-monomers.

From these two studies on grades of polymers the recommendations are that when comparing two grades with varying molecular weights, unless considering high temperatures, it is appropriate to use the same parameters for both materials. For co-monomers, a new set of parameters are required. Further work could be conducted on grades with more extreme molecular weight differences to further these conclusions.

PP has been studied in a previous OGR model [6] where it appeared that the flow behaviour was affected by the application of fictive temperature evolution. In analysing the old model, it was found that having a single rejuvenation parameter k with no temperature and rate dependence produced a large value of fictive temperature evolution causing curve collapse in comparison to experimental results. By implementing the novel approach presented in this thesis in Section 4.5.1, where a temperature dependence was given to this rejuvenation parameter, the fictive temperature evolution was controlled in our model. This control of fictive temperature allowed for a more accurate model post-yield behaviour.

Finally, a homogenous continuum approach was taken to simulate the semi-crystalline PA6. A novel parameterisation method for extracting conformational parameters was presented in this thesis for polycarbonate where an Edwards-Vilgis function with constant flow stress was fitted to large strain data. This new approach proved to capture the large strain behaviour of PA6. The lack of strain softening observed in the model was implemented through $\Delta T_{\mathrm{f}} = 0$. Utilising the processes detailed above, the model successfully captured the yield stress response for varying strain rates and the temperature range below the glass transition using this continuum approach.

6.4. Future Work

With the key findings of this thesis presented, a few areas for further development and future research opportunities have been identified.

6.4.1. Semi-Crystalline Materials

It is acknowledged in Section 5.6 that a less physical, homogeneous approach was taken to address the semi-crystalline polymer polyamide 6 (PA6) within this work. While this engineering approach was largely successfully, further work could be done on the intricacies of the crystallinity and the interplay with the amorphous zones at high strain rates in this semi-crystalline polymer. As discussed in Chapter 2, the major challenge is linking the microstructure theories to the constitutive response. To thoroughly consider these factors a series of further experimental data would be required, including but not limited to high rate imaging, x-ray diffraction techniques to analyse crystal structure or microscopy to observe morphology.

6.4.2. Implementation to Finite Element Software

The constitutive model presented in this thesis was formulated in MATLAB to be easily translatable to a user material within a finite element solver. It would be possible to utilise a FE model to simulate more complex geometries and shapes, including inhomogeneous deformations such as neck formation during tensile testing. This would be achieved by defining a user material subroutine (VUMAT) in, for example, ABAQUS™ with a series of material constants corresponding with those presented in this thesis. Previous efforts to implement the OGR model in finite element code were presented in the works of Safari [111] for polycarbonate and Okereke [6] for polypropylene.

To implement the model from this thesis would require a few areas of focus. To obtain the conformational parameters discussed in Section 3.3.10, a sigmoidal function for N_s was presented, shown in Figure 3.19. At a zero rate this would result in an instantaneously different shear modulus, G, and therefore an immediate drop in conformational yield stress, rather than a smooth transition as would be observed experimentally. In reality, a time-based formulation is required to tend the relaxation towards a new value. This timescale is difficult to determine but it is suggested to be between the sub-entanglements and

entanglements relaxations; i.e. between the Kuhn's length and the Rouse relaxation time.

Figure 6.1a shows a deformation at 0.01 s^{-1} followed by a hold, where $\dot{\varepsilon} = 0$ s^{-1}, the stress-strain response of such a deformation test with the existing model presented this thesis is shown in Figure 6.1b, highlighting the drop in stress. Figure 6.1c the conformational stress versus time is shown, where the clear instantaneous drop is observed. The current model simulates successfully for continuous scenarios, such as impact, and so for this work this is not a concern, however this could be an area of focus for future work.
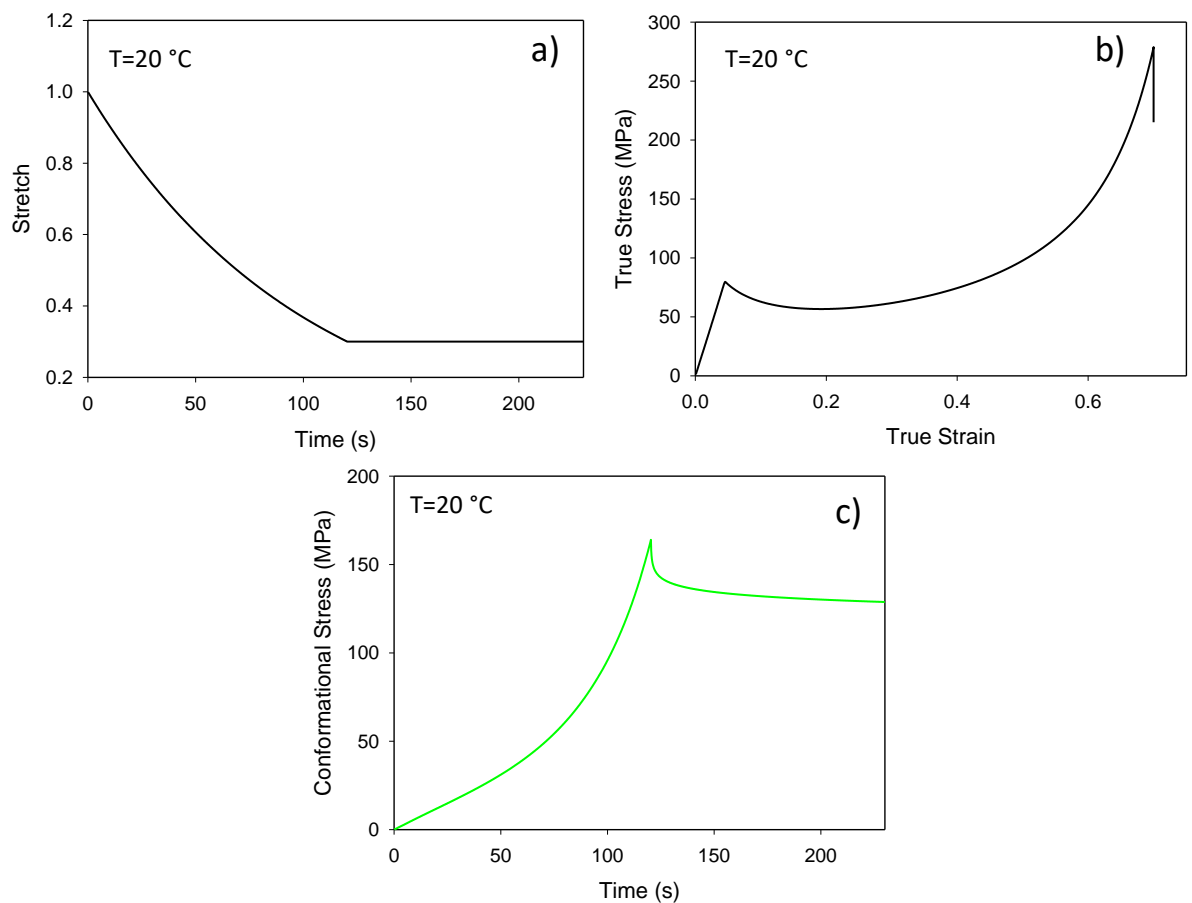
Figure 6.1: Compression test at 0.01 s^{-1}, 22 °C followed by a hold, strain rate of zero, a) compressive stretch with time showing the two parts of the test, b) full true stress versus true strain curve showing the drop in stress and c) the conformational stress with time to show the immediate drop in stress as the strain rate becomes zero

6.4.3. Extension to Ballistic Impact

In this thesis very high strain rates are addressed, a natural progression to this work would be further development of impact and ballistic conditions. When ballistic impact is considered, the very wide range of strain rates presented in this thesis are utilised but additionally failure and damage criterions are required. Additionally, multiple modes of deformation would need to be considered in further detail. For materials where brittle failure is dominant, further study of processing history and the effect of this on failure would be needed.

Bibliography

[1] C. B. Buckley, C. P., McCrum, N. G., Bucknall, *Principles of Polymer Engineering*, 2nd ed. Oxford University Press, 1997.

[2] J. Ward, I M J; Sweeney, "Structure of Polymers," in *Mechanical Properties of Solid Polymers*, 3rd ed., 2012, pp. 1–18.

[3] G. Choong, "A study of melt-compounded nanocomposites of polycarbonate and carbon nanotubes in the melt and solid states," University of Nottingham, 2014.

[4] Q. Zia, D. Mileva, and R. Androsch, "Rigid Amorphous Fraction in Isotactic Polypropylene," *Macromolecules*, vol. 41, no. 21, pp. 8095–8102, Nov. 2008, doi: 10.1021/ma801455m.

[5] B. Wunderlich, "Reversible crystallization and the rigid–amorphous phase in semicrystalline macromolecules," *Prog. Polym. Sci.*, vol. 28, no. 3, pp. 383–450, 2003, doi: https://doi.org/10.1016/S0079-6700(02)00085-0.

[6] M. I. Okereke and A. I. Akpoyomare, "Two-process constitutive model for semicrystalline polymers across a wide range of strain rates," *Polymer (Guildf).*, vol. 183, no. September, p. 121818, 2019, doi: 10.1016/j.polymer.2019.121818.

[7] W. Santos, J. Sousa, and R. Jr, "Thermal conductivity behaviour of polymers around glass transition and crystalline melting temperatures," *Polym. Test.*, vol. 32, pp. 987–994, Aug. 2013, doi: 10.1016/j.polymertesting.2013.05.007.

[8] D. Barba, A. Arias, and D. Garcia-Gonzalez, "Temperature and strain rate dependences on hardening and softening behaviours in semi-crystalline polymers: Application to PEEK," *Int. J. Solids Struct.*, vol. 182–183, pp. 205–217, 2020, doi: 10.1016/j.ijsolstr.2019.08.021.

[9] A. S. Khan and B. Farrokh, "Thermo-mechanical response of nylon 101 under uniaxial and multi-axial loadings: Part I, Experimental results over wide ranges of temperatures and strain rates," *Int. J. Plast.*, vol. 22, no. 8, pp.

1506–1529, 2006, doi: https://doi.org/10.1016/j.ijplas.2005.10.001.

[10] M. Razavi and S.-Q. Wang, "Double Yielding in Deformation of Semicrystalline Polymers," *Macromol. Chem. Phys.*, vol. 221, no. 19, p. 2000151, Oct. 2020, doi: https://doi.org/10.1002/macp.202000151.

[11] P. Hao, V. Laheri, Z. Dai, and F. A. Gilabert, "A rate-dependent constitutive model predicting the double yield phenomenon , self-heating and thermal softening in semi-crystalline polymers," *Int. J. Plast.*, vol. 153, no. January, p. 103233, 2022, doi: 10.1016/j.ijplas.2022.103233.

[12] H. Wang, H. Liu, Z. Ding, and N. Li, "Experimental and constitutive modelling studies of semicrystalline thermoplastics under solid-state stamp forming conditions," *Polymer (Guildf).*, vol. 228, no. April, p. 123939, 2021, doi: 10.1016/j.polymer.2021.123939.

[13] L. V Pastukhov, L. E. Govaert, and T. A. P. Engels, "Influence of fiber orientation , temperature and relative humidity on the long-term performance of short glass fiber reinforced polyamide 6," no. November 2020, pp. 1–19, 2021, doi: 10.1002/app.50382.

[14] T. S. Ellis, "Moisture-induced plasticization of amorphous polyamides and their blends," *J. Appl. Polym. Sci.*, vol. 36, no. 3, pp. 451–466, Jul. 1988, doi: https://doi.org/10.1002/app.1988.070360301.

[15] N. Jia, H. Fraenkel, and V. Kagan, "Effects of Moisture Conditioning Methods on Mechanical Properties of Injection Molded Nylon 6," *J. Reinf. Plast. Compos.*, vol. 23, pp. 729–737, May 2004, doi: 10.1177/0731684404030730.

[16] T. Lan *et al.*, "A physically-based constitutive model for amorphous glassy polymers in large deformations," *Eur. J. Mech. A/Solids*, no. April, p. 105015, 2023, doi: 10.1016/j.euromechsol.2023.105015.

[17] C. R. Siviour and J. L. Jordan, "High Strain Rate Mechanics of Polymers: A Review," *J. Dyn. Behav. Mater.*, vol. 2, no. 1, pp. 15–32, 2016, doi: 10.1007/s40870-016-0052-8.

[18] D. W. Van Krevelen and K. Te Nijenhuis, "Chapter 13 - Mechanical Properties of Solid Polymers," in *Properties of Polymers*, 4th ed., Amsterdam: Elsevier, 2009, pp. 383–503.

[19] A. D. Mulliken, "Mechanics of Amorphous Polymers and Polymer Nanocomposites during High Rate Deformation," Massachusetts Institute of Technology, 2006.

[20] R. S. Hoy and M. O. Robbins, "Strain Hardening of Polymer Glasses : Effect of Entanglement Density , Temperature , and Rate," *J. Polym. Sci. Part B Polym. Phys.*, vol. 44, no. 24, pp. 3487–3500, 2006, doi: 10.1002/polb.21012.

[21] R. S. Hoy and M. O. Robbins, "Strain hardening of polymer glasses: Entanglements, energetics, and plasticity," *Phys. Rev. E*, vol. 77, no. 3, p. 31801, Mar. 2008, doi: 10.1103/PhysRevE.77.031801.

[22] Y. J. Mergler and R. P. Schaake, "Relation Between Strain Hardening and Wear Resistance of Polymers," *J. Appl. Polym. Sci.*, vol. 92, no. 4, pp. 2689–2692, 2004, doi: 10.1002/app.20251.

[23] G. I. Gurevich and P. P. Kobeko, "A Study of Polymers. III. Technique of Mechanical Tests of Vulcanizates of Rubber and Plastics," *Rubber Chem. Technol.*, vol. 13, no. 4, pp. 904–917, Dec. 1940, doi: 10.5254/1.3546568.

[24] R. N. Haward, "The extension and rupture of cellulose acetate and celluloid," *Trans. Faraday Soc.*, vol. 38, no. 0, pp. 394–403, 1942, doi: 10.1039/TF9423800394.

[25] E. A. W. Hoff, "Some mechanical properties of a commercial polymethyl methacrylate," *J. Appl. Chem.*, vol. 2, no. 8, pp. 441–448, Aug. 1952, doi: 10.1002/jctb.5010020804.

[26] R. N. Haward, B. M. Murphy, and E. F. T. White, "Relationship between compressive yield and tensile behavior in glassy thermoplastics," *J. Polym. Sci. Part A-2 Polym. Phys.*, vol. 9, no. 5, pp. 801–814, May 1971, doi: 10.1002/pol.1971.160090503.

[27] R. . Haward and G. Thackray, "The Use of a Mathematical Model to Describe

Isothermal Stress-Strain Curves in Glassy Thermoplastics," *Proc R Soc L. A Math Phys Sci*, vol. 302, pp. 453–472, 1968.

[28] M. C. Wang and E. J. Guth, "Statistical theory of net- works of non-Gaussian flexible chains," *J. Chem. Phys.*, vol. 20, no. 1144, 1952.

[29] E. M. Arruda and M. C. Boyce, "A three-dimensional constitutive model for the large stretch behavior of rubber elastic materials," *J. Mech. Phys. Solids*, vol. 41, no. 2, pp. 389–412, 1993, doi: 10.1016/0022-5096(93)90013-6.

[30] S. F. Edwards and T. Vilgis, "The effects of entanglements in rubber elasticity," *Polymer (Guildf).*, vol. 27, pp. 483–492, 1986.

[31] E. T. J. Klompen, T. A. P. Engels, L. E. Govaert, and H. E. H. Meijer, "Modeling of the postyield response of glassy polymers: Influence of thermomechanical history," *Macromolecules*, vol. 38, no. 16, pp. 6997–7008, 2005, doi: 10.1021/ma050498v.

[32] H. G. H. Van Melick, L. E. Govaert, and H. E. H. Meijer, "On the origin of strain hardening in glassy polymers," *Polymer (Guildf).*, vol. 44, no. 8, pp. 2493–2502, 2003, doi: 10.1016/S0032-3861(03)00112-5.

[33] A. Shrivastava, "2 - Polymerization," in *Plastics Design Library*, William Andrew Publishing, 2018, pp. 17–48.

[34] S. Nishitsuji, Y. Watanabe, H. Ito, M. Ishikawa, and T. Inoue, "Molecular weight dependence of the physical aging of polycarbonate," *Polymer (Guildf).*, vol. 178, no. June, p. 121571, 2019, doi: 10.1016/j.polymer.2019.121571.

[35] H. Soma, S. Nishitsuji, and T. Inoue, "Molecular weight dependence in a relaxation phenomenon at glassy state: Physical aging of polycarbonate," *Polymer (Guildf).*, vol. 53, no. 4, pp. 895–896, 2012, doi: 10.1016/j.polymer.2012.01.011.

[36] T. G. Fox Jr. and P. J. Flory, "Second-Order Transition Temperatures and Related Properties of Polystyrene. I. Influence of Molecular Weight," *J. Appl. Phys.*, vol. 21, no. 6, pp. 581–591, Jun. 1950, doi: 10.1063/1.1699711.

[37] T. G. Fox and P. J. Flory, "The glass temperature and related properties of polystyrene. Influence of molecular weight," *J. Polym. Sci.*, vol. 14, no. 75, pp. 315–319, Sep. 1954, doi: 10.1002/pol.1954.120147514.

[38] L. E. Govaert and T. A. Tervoort, "Strain hardening of polycarbonate in the glassy state: Influence of temperature and molecular weight," *J. Polym. Sci. Part B Polym. Phys.*, vol. 42, no. 11 SPEC. ISS., pp. 2041–2049, 2004, doi: 10.1002/polb.20095.

[39] D. J. Hoffman, S. M. Fica-Contreras, and M. D. Fayer, "Amorphous polymer dynamics and free volume element size distributions from ultrafast IR spectroscopy," *Proc. Natl. Acad. Sci. U. S. A.*, vol. 117, no. 25, pp. 13949–13958, 2020, doi: 10.1073/pnas.2003225117.

[40] P. Hempel, "Constitutive modeling of amorphous thermoplastic polymers with special emphasis on manufacturing processes," Karlsruher Institut für Technologie (KIT), 2016.

[41] X. Morelle, "Mechanical characterization and physics-based modeling of highly-crosslinked epoxy resin," Universite catholique de Louvain, 2015.

[42] K. P. Menard and N. R. Menard, *Dynamic Mechanical Analysis in the Analysis of Polymers and Rubbers*, no. 9. 2015.

[43] S. K. Kaliappan, "Characterization of Physical Properties of Polymers Using AFM Force-Distance Curves," no. October 2007, pp. 1–113, 2007.

[44] J. M. Hutchinson, "Relaxation processes and physical aging.," in *The Physics of Glassy Polymers*, 1997, pp. 85–153.

[45] J. A. Roetling, "Yield stress behaviour of polymethylmethacrylate," *Polymer (Guildf).*, vol. 6, no. 6, pp. 311–317, 1965, doi: 10.1016/0032-3861(65)90081-9.

[46] J. A. Roetling, "Yield stress behaviour of poly(ethyl methacrylate) in the glass transition region," *Polymer (Guildf).*, vol. 6, no. 11, pp. 615–619, 1965, doi: 10.1016/0032-3861(65)90056-X.

[47] T. Ree and H. Eyring, "Theory of Non-Newtonian Flow. I. Solid Plastic

System," *J. Appl. Phys.*, vol. 26, no. 7, pp. 793–800, May 1955, doi: 10.1063/1.1722098.

[48] J. C. Bauwens, C. Bauwens-Crowet, and G. Homès, "Tensile yield-stress behavior of poly(vinyl chloride) and polycarbonate in the glass transition region," *J. Polym. Sci. Part A-2 Polym. Phys.*, vol. 7, no. 10, pp. 1745–1754, Oct. 1969, doi: 10.1002/pol.1969.160071010.

[49] C. Bauwens-Crowet, J. C. Bauwens, and G. Homès, "Tensile yield-stress behavior of glassy polymers," *J. Polym. Sci. Part A-2 Polym. Phys.*, vol. 7, no. 4, pp. 735–742, Apr. 1969, doi: 10.1002/pol.1969.160070411.

[50] J. C. Bauwens, "Relation between the compression yield stress and the mechanical loss peak of bisphenol-A-polycarbonate in the β transition range," *J. Mater. Sci.*, vol. 7, no. 5, pp. 577–584, 1972, doi: 10.1007/BF00761956.

[51] C. Bauwens-Crowet, J.-C. C. Bauwens, and G. Homès, "The temperature dependence of yield of polycarbonate in uniaxial compression and tensile tests," *J. Mater. Sci.*, vol. 7, no. 2, pp. 176–183, 1972, doi: 10.1007/BF02403504.

[52] C. Bauwens-Crowet, "The compression yield behaviour of polymethyl methacrylate over a wide range of temperatures and strain-rates," *J. Mater. Sci.*, vol. 8, no. 7, pp. 968–979, 1973, doi: 10.1007/BF00756628.

[53] W. P. Hernández, D. A. Castello, N. Roitman, and C. Magluta, "Thermorheologically simple materials: A bayesian framework for model calibration and validation," *J. Sound Vib.*, vol. 402, pp. 14–30, 2017, doi: doi.org/10.1016/j.jsv.2017.05.005.

[54] A. E. Krauklis, A. G. Akulichev, A. I. Gagani, and A. T. Echtermeyer, "Time-Temperature-Plasticization Superposition Principle: Predicting Creep of a Plasticized Epoxy.," *Polymers (Basel).*, vol. 11, no. 11, Nov. 2019, doi: 10.3390/polym11111848.

[55] J. . Williams, M.L., Landel, R.F. and Ferry, "Physical, thermal, and mechanical properties of polymers," *J. Am. Chem. Soc.*, vol. 77, pp. 3701–3707, 1955.

[56] A. . Tool, "Relation between inelastic deformability and thermal expansion of glass in its annealing range.," *Am. Ceram.*, vol. 29, pp. 240–253, 1946.

[57] N. V Priezjev, "The effect of thermal history on the atomic structure and mechanical properties of amorphous alloys," *Comput. Mater. Sci.*, vol. 174, p. 109477, 2020, doi: doi.org/10.1016/j.commatsci.2019.109477.

[58] H. Eyring, "Viscosity, Plasticity, and Diffusion as Examples of Absolute Reaction Rates," *J. Chem. Phys.*, vol. 4, no. 4, pp. 283–291, Dec. 1936, doi: 10.1063/1.1749836.

[59] R. E. Robertson, "Theory for the Plasticity of Glassy Polymers," *J. Chem. Phys.*, vol. 44, no. 10, pp. 3950–3956, May 1966, doi: 10.1063/1.1726558.

[60] A. S. Argon, "A theory for the low-temperature plastic deformation of glassy polymers," *Phil. Mag*, vol. 28, no. 39, 1973.

[61] A. Krausz and H. Eyring, "Deformation Kinetics," *Wiley-Intrescience*, 1975. .

[62] A. . Tobolsky and H. Eyring, "Mechanical Properties of Polymeric Materials," *J. Chem. Phys.*, vol. 11, pp. 125–134, 1943.

[63] L. R. G. Treloar, "The Physics of Rubber Elasticity," *Clarendon Press*, vol. 3rd Edn. 1975.

[64] C. P. Buckley and D. C. Jones, "Glass-rubber constitutive model for amorphous polymers near the glass transition," *Polymer (Guildf).*, vol. 36, no. 17, pp. 3301–3312, 1995, doi: 10.1016/0032-3861(95)99429-X.

[65] T. A. Tervoort, R. J. M. Smit, W. A. M. Brekelmans, and L. E. Govaert, "A Constitutive Equation for the Elasto-Viscoplastic Deformation of Glassy Polymers," *Mech. Time-Dependent Mater.*, vol. 1, no. 3, pp. 269–291, 1997, doi: 10.1023/A:1009720708029.

[66] J. Bonet and R. D. Wood, *Nonlinear Continuum Mechanics for Finite Element Analysis*, 2nd ed. Cambridge: Cambridge University Press, 2008.

[67] J. J. Wu and C. P. Buckley, "Plastic deformation of glassy polystyrene: A unified model of yield and the role of chain length," *J. Polym. Sci. Part B Polym. Phys.*, vol. 42, no. 11, pp. 2027–2040, Jun. 2004, doi:

10.1002/polb.20089.

[68] D. De Focatiis, J. Embery, and C. P. Buckley, "Large Deformations in Oriented Polymer Glasses: Experimental Study and a New Glass-Melt Constitutive Mo," *J. Polym. Sci. Part B Polym. Phys.*, vol. 48, no. 13, pp. 1449–1463, 2010, doi: 10.1002/polb.22028.

[69] C. P. Buckley, P. J. Dooling, J. Harding, and C. Ruiz, "Deformation of thermosetting resins at impact rates of strain. Part 2: Constitutive model with rejuvenation," *J. Mech. Phys. Solids*, vol. 52, no. 10, pp. 2355–2377, 2004, doi: 10.1016/j.jmps.2004.04.001.

[70] P. J. Dooling, C. P. Buckley, and S. Hinduja, "The onset of nonlinear viscoelasticity in multiaxial creep of glassy polymers: A constitutive model and its application to PMMA," *Polym. Eng. Sci.*, vol. 38, no. 6, pp. 892–904, 1998, doi: 10.1002/pen.10256.

[71] S. . Rekhson, "Memory effects in glass transition.," *Non-Crystalline Solids*, vol. 84, pp. 64–85, 1986.

[72] J. M. Hutchinson, "Relaxation processes and physical aging BT - The Physics of Glassy Polymers," R. N. Haward and R. J. Young, Eds. Dordrecht: Springer Netherlands, 1997, pp. 85–153.

[73] A. R. Trivedi, P. Song, and C. R. Siviour, "Experimentally simulating adiabatic behaviour: Capturing the high strain rate compressive response of polymers using low strain rate experiments with programmed temperature profiles," *Polym. Test.*, vol. 116, no. June, p. 107773, 2022, doi: 10.1016/j.polymertesting.2022.107773.

[74] M. I. Okereke, C. H. Le, and C. P. Buckley, "A new constitutive model for prediction of impact rates response of polypropylene," *EPJ Web Conf.*, vol. 26, 2012, doi: 10.1051/epjconf/20122604031.

[75] J. Sweeney, R. Spares, and M. Woodhead, "A Constitutive Model for Large Multiaxial Deformation of Solid Polypropylene at High Temperature," *Polym. Eng. Sci.*, vol. 49, no. 10, pp. 1902–1908, 2009, doi: 10.1002/pen.21426.

[76] A. C. Y. Lew and C. P. Buckley, "Improved glass-rubber constitutive model for biaxial hot drawing of amorphous poly(ethylene terephthalate)," *23rd Annu. Meet. Polym. Process. Soc. Salvador. Brazil.*, vol. 4, Pages, pp. 2294–2298, 2007.

[77] M. I. Okereke, C. P. Buckley, and C. R. Siviour, "Compression of polypropylene across a wide range of strain rates," *Mech. Time-Dependent Mater.*, vol. 16, no. 4, pp. 361–379, 2012, doi: 10.1007/s11043-012-9167-z.

[78] A. Sedighiamiri, L. E. Govaert, M. J. W. Kanters, and J. A. W. Van Dommelen, "Micromechanics of semicrystalline polymers: Yield kinetics and long-term failure," *J. Polym. Sci. Part B Polym. Phys.*, vol. 50, no. 24, pp. 1664–1679, 2012, doi: 10.1002/polb.23136.

[79] E. T. J. Klompen, T. A. P. Engels, L. C. A. Van Breemen, P. J. G. Schreurs, L. E. Govaert, and H. E. H. Meijer, "Quantitative prediction of long-term failure of polycarbonate," *Macromolecules*, vol. 38, no. 16, pp. 7009–7017, 2005, doi: 10.1021/ma0504973.

[80] R. P. M. Janssen, D. De Kanter, L. E. Govaert, and H. E. H. Meijer, "Fatigue life predictions for glassy polymers: A constitutive approach," *Macromolecules*, vol. 41, no. 7, pp. 2520–2530, 2008, doi: 10.1021/ma071273i.

[81] A. Amiri-Rad, M. Wismans, L. V. Pastukhov, L. E. Govaert, J. A. W. Van Dommelen, and J. A. W. van Dommelen, "Constitutive modeling of injection-molded short-fiber composites: Characterization and model application," *J. Appl. Polym. Sci.*, no. December 2019, pp. 1–14, 2020, doi: 10.1002/app.49248.

[82] D. J. A. Senden, G. W. M. Peters, L. E. Govaert, and J. A. W. Van Dommelen, "Anisotropic yielding of injection molded polyethylene: Experiments and modeling," *Polymer (Guildf).*, vol. 54, no. 21, pp. 5899–5908, 2013, doi: 10.1016/j.polymer.2013.08.047.

[83] M. Mirkhalaf, J. A. W. van Dommelen, L. E. Govaert, J. Furmanski, and M. G. D. Geers, "Micromechanical modeling of anisotropic behavior of oriented semicrystalline polymers," *J. Polym. Sci. Part B Polym. Phys.*, vol. 57, no. 7, pp.

378–391, 2019, doi: 10.1002/polb.24791.

[84] A. I. Leonov, "Nonequilibrium thermodynamics and rheology of viscoelastic polymer media," *Rheol. Acta*, vol. 15, pp. 85–98, 1976.

[85] T. A. Tervoort, W. A. M. Brekelmans, and L. E. Govaert, "A 3-D stress-strain relation for glassy polymers," in *9th International Conference on Deformation, Yield and Fracture of Polymers*, 1994, pp. P66-1/4.

[86] T. A. Tervoort, E. T. J. Klompen, and L. E. Govaert, "A multi-mode approach to finite, three-dimensional, nonlinear viscoelastic behavior of polymer glasses," *J. Rheol. (N. Y. N. Y).*, vol. 40, no. 5, pp. 779–797, 1996, doi: 10.1122/1.550755.

[87] L. C. A. Van Breemen, E. T. J. Klompen, L. E. Govaert, and H. E. H. Meijer, "Extending the EGP constitutive model for polymer glasses to multiple relaxation times," *Journal of the Mechanics and Physics of Solids*, vol. 59, no. 10. pp. 2191–2207, 2011, doi: 10.1016/j.jmps.2011.05.001.

[88] L. E. Govaert, P. H. M. Timmermans, and W. A. M. Brekelmans, "The Influence of Intrinsic Strain Softening on Strain Localization in Polycarbonate : Modeling and Experimental Validation," *J. Eng. Mater. Technol.*, vol. 122, no. April, pp. 177–185, 2000.

[89] T. A. Tervoort and L. E. Govaert, "Strain-hardening behavior of polycarbonate in the glassy state," *J. Rheol. (N. Y. N. Y).*, vol. 44, no. 6, pp. 1263–1277, 2000, doi: 10.1122/1.1319175.

[90] M. Wendlandt, T. A. Tervoort, and U. W. Suter, "Non-linear, rate-dependent strain-hardening behavior of polymer glasses," *Polymer (Guildf).*, vol. 46, no. 25, pp. 11786–11797, 2005, doi: 10.1016/j.polymer.2005.08.079.

[91] J. A. Sauer, "Deformation, yield and fracture of polymers at high pressure," *Polym. Eng. Sci.*, vol. 17, no. 3, pp. 150–164, Mar. 1977, doi: 10.1002/pen.760170304.

[92] W. A. Spitzig and O. Richmond, "Effect of hydrostatic pressure on the deformation behavior of polyethylene and polycarbonate in tension and in

compression," *Polym. Eng. Sci.*, vol. 19, no. 16, pp. 1129–1139, Dec. 1979, doi: 10.1002/pen.760191602.

[93]   K. Chen and K. S. Schweizer, "Suppressed Segmental Relaxation as the Origin of Strain Hardening in Polymer Glasses," *Phys. Rev. Lett.*, vol. 102, no. 3, p. 38301, Jan. 2009, doi: 10.1103/PhysRevLett.102.038301.

[94]   T. B. van Erp, C. T. Reynolds, T. Peijs, J. A. W. van Dommelen, and L. E. Govaert, "Prediction of yield and long-term failure of oriented polypropylene: Kinetics and anisotropy," *J. Polym. Sci. Part B Polym. Phys.*, vol. 47, no. 20, pp. 2026–2035, Oct. 2009, doi: 10.1002/polb.21801.

[95]   A. Amiri-Rad, L. V. Pastukhov, L. E. Govaert, and J. A. W. van Dommelen, "An anisotropic viscoelastic-viscoplastic model for short-fiber composites," *Mech. Mater.*, vol. 137, no. February, p. 103141, 2019, doi: 10.1016/j.mechmat.2019.103141.

[96]   E. T. J. Klompen and L. E. Govaert, "Nonlinear viscoelastic behaviour of thermorheologically complex materials : a modelling approach Citation," *Mech. Time-Dependent Mater. 3*, pp. 49–69, 1999, doi: 10.1023/A:1009853024441.

[97]   S. M. Mirkhalaf, F. M. Andrade Pires, and R. Simoes, "Modelling of the post yield response of amorphous polymers under different stress states," *Int. J. Plast.*, vol. 88, pp. 159–187, 2017, doi: 10.1016/j.ijplas.2016.10.008.

[98]   H. Khaleghi, A. Amiri-Rad, and M. Mashayekhi, "A thermodynamically consistent continuum damage model for time-dependent failure of thermoplastic polymers," *Int. J. Plast.*, vol. 154, no. February, p. 103278, 2022, doi: 10.1016/j.ijplas.2022.103278.

[99]   M. C. Boyce, D. M. Parks, and A. S. Argon, "Large inelastic deformation of glassy polymers. part I: rate dependent constitutive model," *Mech. Mater.*, vol. 7, no. 1, pp. 15–33, 1988, doi: 10.1016/0167-6636(88)90003-8.

[100] H. . James and E. Guth, "Theory of the Elastic Properties of Rubber," *J. Chem. Phys.*, vol. 11, pp. 455–481, 1943.

[101] P. D. Wu and E. Van Der Giessen, "On improved network models for rubber elasticity and their applications to orientation hardening in glassy polymers," *J. Mech. Phys. Solids*, vol. 41, no. 3, pp. 427–456, 1993, doi: 10.1016/0022-5096(93)90043-F.

[102] M. C. Boyce and E. M. Arruda, "Constitutive Models of Rubber Elasticity: A Review," *Rubber Chem. Technol.*, no. 73, pp. 504–523, 2000.

[103] J. Sweeney, "A comparison of three polymer network models in current use," *Comput. Theor. Polym. Sci.*, vol. 9, no. 1, pp. 27–33, 1999, doi: 10.1016/S1089-3156(98)00050-6.

[104] O. A. Hasan and M. C. Boyce, "A constitutive model for nonlinear viscoelastic viscoplastic behavior of glassy polymers," *Polym. Eng. Sci.*, vol. 35, no. 4, pp. 331–344, 1995, doi: 10.1002/pen.10587.

[105] M. C. Boyce, S. Socrate, and P. G. Llana, "Constitutive model for the finite deformation stress-strain behavior of poly(ethylene terephthalate) above the glass transition," *Polymer (Guildf).*, vol. 41, no. 6, pp. 2183–2201, 2000, doi: 10.1016/S0032-3861(99)00406-1.

[106] R. B. Dupaix and M. C. Boyce, "Constitutive modeling of the finite strain behavior of amorphous polymers in and above the glass transition," *Mech. Mater.*, vol. 39, no. 1, pp. 39–52, 2007, doi: 10.1016/j.mechmat.2006.02.006.

[107] E. M. Arruda, M. C. Boyce, and R. Jayachandran, "Effects of strain rate, temperature and thermomechanical coupling on the finite strain deformation of glassy polymers," *Mech. Mater.*, vol. 19, no. 2–3, pp. 193–212, 1995, doi: 10.1016/0167-6636(94)00034-E.

[108] J. S. Bergström and M. C. Boyce, "Constitutive modeling of the large strain time-dependent behavior of elastomers," *J. Mech. Phys. Solids*, vol. 46, no. 5, pp. 931–954, 1998, doi: 10.1016/S0022-5096(97)00075-6.

[109] A. Makradi, S. Ahzi, R. V. Gregory, and D. D. Edie, "A two-phase self-consistent model for the deformation and phase transformation behavior of polymers above the glass transition temperature: Application to PET," *Int. J. Plast.*, vol. 21, no. 4, pp. 741–758, 2005, doi: 10.1016/j.ijplas.2004.04.012.

[110] M. Polanco-Loria, A. H. Clausen, T. Berstad, and O. S. Hopperstad, "Constitutive model for thermoplastics with structural applications," *Int. J. Impact Eng.*, vol. 37, no. 12, pp. 1207–1219, 2010, doi: 10.1016/j.ijimpeng.2010.06.006.

[111] K. H. Safari, J. Zamani, R. M. Guedes, and F. J. Ferreira, "The effect of heat developed during high strain rate deformation on the constitutive modeling of amorphous polymers," *Mech. Time-Dependent Mater.*, vol. 20, no. 1, pp. 45–64, 2016, doi: 10.1007/s11043-015-9283-7.

[112] A. G. Varghese and R. C. Batra, "Constitutive equations for thermomechanical deformations of glassy polymers," *Int. J. Solids Struct.*, vol. 46, no. 22–23, pp. 4079–4094, 2009, doi: 10.1016/j.ijsolstr.2009.08.006.

[113] D. W. Holmes, J. G. Loughran, and H. Suehrcke, "Constitutive model for large strain deformation of semicrystalline polymers," *Mech. Time-Dependent Mater.*, vol. 10, no. 4, pp. 281–313, 2006, doi: 10.1007/s11043-007-9023-8.

[114] L. Anand and M. E. Gurtin, "A theory of amorphous solids undergoing large deformations, with application to polymeric glasses," *Int. J. Solids Struct.*, vol. 40, no. 6, pp. 1465–1487, 2003, doi: 10.1016/S0020-7683(02)00651-0.

[115] A. D. Mulliken and M. C. Boyce, "Polycarbonate and a polycarbonate-POSS nanocomposite at high rates of deformation," *J. Eng. Mater. Technol. Trans. ASME*, vol. 128, no. 4, pp. 543–550, 2006, doi: 10.1115/1.2345446.

[116] V. Srivastava, S. A. Chester, N. M. Ames, and L. Anand, "A thermo-mechanically-coupled large-deformation theory for amorphous polymers in a temperature range which spans their glass transition," *Int. J. Plast.*, vol. 26, no. 8, pp. 1138–1182, 2010, doi: 10.1016/j.ijplas.2010.01.004.

[117] K. Hong, A. Rastogi, and G. Strobl, "Model treatment of tensile deformation of semicrystalline polymers: Static elastic moduli and creep parameters derived for a sample of polyethylene," *Macromolecules*, vol. 37, no. 26, pp. 10174–10179, 2004, doi: 10.1021/ma049172x.

[118] K. Hong, A. Rastogi, and G. Strobl, "A model treating tensile deformation of

semicrystalline polymers: Quasi-static stress-strain relationship and viscous stress determined for a sample of polyethylene," *Macromolecules*, vol. 37, no. 26, pp. 10165–10173, 2004, doi: 10.1021/ma049174h.

[119] Y. Wang and E. Arruda, "Constitutive Modeling of a Thermoplastic Olefin Over a Broad Range of Strain Rates," *J. Eng. Mater. Technol.*, vol. 128, pp. 551–558, Oct. 2006, doi: 10.1115/1.2349501.

[120] S. C. Chou, K. D. Robertson, and J. H. Rainey, "The effect of strain rate and heat developed during deformation on the stress-strain curve of plastics," *Exp. Mech.*, vol. 13, no. 10, pp. 422–432, 1973, doi: 10.1007/BF02324886.

[121] B. J. Briscoe and I. M. Hutchings, "Impact yielding of high density polyethylene," *Polymer (Guildf).*, vol. 17, no. 12, pp. 1099–1102, 1976, doi: 10.1016/0032-3861(76)90013-6.

[122] S. N. Kukureka and I. M. Hutchings, "Measurement of the Mechanical Properties of Polymers at High Strain-Rates By Taylor Impact," in *International Conference on High Energy Rate Fabrication*, 1981, pp. 29–38.

[123] B. J. Briscoe and R. W. Nosker, "Flow stress of high density polyethylene at high rates of strain.," *Polym. Commun. Guildf.*, vol. 26, no. 10, pp. 307–308, 1985.

[124] B. J. Briscoe and R. W. Nosker, "The influence of interfacial friction on the deformation of high density polyethylene in a split hopkinson pressure bar," *Wear*, vol. 95, no. 3, pp. 241–262, 1984, doi: 10.1016/0043-1648(84)90140-6.

[125] C. R. Siviour, "High strain rate characterization of polymers," *AIP Conf. Proc.*, vol. 1793, no. January, 2017, doi: 10.1063/1.4971585.

[126] G. T. (Rusty) Gray III, "Classic Split-Hopkinson Pressure Bar Testing," *Mechanical Testing and Evaluation*. ASM International, pp. 462–476, Jan. 01, 2000, doi: 10.31399/asm.hb.v08.a0003296.

[127] G. T. (Rusty) Gray III and W. R. Blumenthal, "Split-Hopkinson Pressure Bar Testing of Soft Materials," in *Mechanical Testing and Evaluation*, vol. 8, ASM

International, 2000, pp. 488–496.

[128] W. Chen and B. Song, *Split Hopkinson (Kolsky) Bar: Design, Testing and Applications*. Springer Science & Business Media, 2010.

[129] C. R. Siviour, S. M. Walley, W. G. Proud, and J. E. Field, "The high strain rate compressive behaviour of polycarbonate and polyvinylidene difluoride," *Polymer (Guildf).*, vol. 46, no. 26, pp. 12546–12555, 2005, doi: 10.1016/j.polymer.2005.10.109.

[130] A. D. Mulliken and M. C. Boyce, "Mechanics of the rate-dependent elastic-plastic deformation of glassy polymers from low to high strain rates," *International Journal of Solids and Structures*, vol. 43, no. 5. pp. 1331–1356, 2006, doi: 10.1016/j.ijsolstr.2005.04.016.

[131] M. J. Kendall and C. R. Siviour, "Experimentally simulating high-rate behaviour: Rate and temperature effects in polycarbonate and PMMA," *Philos. Trans. R. Soc. A Math. Phys. Eng. Sci.*, vol. 372, no. 2015, 2014, doi: 10.1098/rsta.2013.0202.

[132] J. Richeton, S. Ahzi, K. S. Vecchio, F. C. Jiang, and R. R. Adharapurapu, "Influence of temperature and strain rate on the mechanical behavior of three amorphous polymers: Characterization and modeling of the compressive yield stress," *Int. J. Solids Struct.*, vol. 43, no. 7–8, pp. 2318–2335, 2006, doi: 10.1016/j.ijsolstr.2005.06.040.

[133] P. Song, A. R. Trivedi, and C. R. Siviour, "Mechanical response of four polycarbonates at a wide range of strain rates and temperatures," *Polym. Test.*, vol. 121, no. February, p. 107986, 2023, doi: 10.1016/j.polymertesting.2023.107986.

[134] C. M. Roland, "Mechanical Behavior of Rubber at High Strain Rates," *Rubber Chem. Technol.*, vol. 79, no. 3, pp. 429–459, Jul. 2006, doi: 10.5254/1.3547945.

[135] C. M. Roland, J. N. Twigg, Y. Vu, and P. H. Mott, "High strain rate mechanical behavior of polyurea," *Polymer (Guildf).*, vol. 48, no. 2, pp. 574–578, 2007, doi: 10.1016/j.polymer.2006.11.051.

[136] D. M. Williamson *et al.*, "Temperature–time response of a polymer bonded explosive in compression (EDC37)," *J. Phys. D. Appl. Phys.*, vol. 41, no. 8, p. 85404, 2008, doi: 10.1088/0022-3727/41/8/085404.

[137] J. Cai, S. M. Walley, R. J. A. Hunt, W. G. Proud, V. F. Nesterenko, and M. A. Meyers, "High-strain, high-strain-rate flow and failure in PTFE/Al/W granular composites," *Mater. Sci. Eng. A*, vol. 472, no. 1, pp. 308–315, 2008, doi: 10.1016/j.msea.2007.03.068.

[138] O. Ramon, S. Mizrahi, and J. Miltz, "Merits and limitations of the drop and shock tests in evaluating the dynamic properties of plastic foams," *Polym. Eng. Sci.*, vol. 34, no. 18, pp. 1406–1410, Sep. 1994, doi: 10.1002/pen.760341807.

[139] A. Trautmann, C. R. Siviour, S. M. Walley, and J. E. Field, "Lubrication of polycarbonate at cryogenic temperatures in the split Hopkinson pressure bar," *Int. J. Impact Eng.*, vol. 31, no. 5, pp. 523–544, 2005, doi: 10.1016/j.ijimpeng.2004.02.007.

[140] J. E. Balzer, C. R. Siviour, S. M. Walley, W. G. Proud, and J. E. Field, "Behaviour of ammonium perchlorate–based propellants and a polymer–bonded explosive under impact loading," *Proc. R. Soc. London. Ser. A Math. Phys. Eng. Sci.*, vol. 460, no. 2043, pp. 781–806, Mar. 2004, doi: 10.1098/rspa.2003.1188.

[141] P. Viot, F. Beani, and J.-L. Lataillade, "Polymeric foam behavior under dynamic compressive loading," *J. Mater. Sci.*, vol. 40, no. 22, pp. 5829–5837, 2005, doi: 10.1007/s10853-005-4998-5.

[142] J. S. Foot, R. W. Truss, I. M. Ward, and R. A. Duckett, "The yield behaviour of amorphous polyethylene terephthalate: An activated rate theory approach," *J. Mater. Sci.*, vol. 22, no. 4, pp. 1437–1442, 1987, doi: 10.1007/BF01233145.

[143] B. Song, C. J. Syn, C. L. Grupido, W. Chen, and W.-Y. Lu, "A Long Split Hopkinson Pressure Bar (LSHPB) for Intermediate-rate Characterization of Soft Materials," *Exp. Mech.*, vol. 48, no. 6, pp. 809–815, 2008, doi: 10.1007/s11340-007-9095-z.

[144] J. L. Jordan, C. R. Siviour, J. R. Foley, and E. N. Brown, "Compressive properties of extruded polytetrafluoroethylene," *Polymer (Guildf).*, vol. 48, no. 14, pp. 4184–4195, 2007, doi: 10.1016/j.polymer.2007.05.038.

[145] E. N. Brown *et al.*, "Influence of Molecular Conformation on the Constitutive Response of Polyethylene: A Comparison of HDPE, UHMWPE, and PEX," *Exp. Mech.*, vol. 47, no. 3, pp. 381–393, 2007, doi: 10.1007/s11340-007-9045-9.

[146] D. G. Thompson, R. Deluca, and G. W. Brown, "Time–Temperature Analysis, Tension and Compression in PBXs," *J. Energ. Mater.*, vol. 30, no. 4, pp. 299–323, Oct. 2012, doi: 10.1080/07370652.2011.569831.

[147] M. J. Kendall and C. R. Siviour, "Experimentally simulating adiabatic conditions: Approximating high rate polymer behavior using low rate experiments with temperature profiles," *Polymer (Guildf).*, vol. 54, no. 18, pp. 5058–5063, 2013, doi: 10.1016/j.polymer.2013.06.049.

[148] J. Wang, L. F. Peng, Y. J. Deng, X. M. Lai, M. W. Fu, and J. Ni, "A finite strain thermodynamically-based constitutive modeling and analysis of viscoelastic-viscoplastic deformation behavior of glassy polymers," *Int. J. Plast.*, vol. 122, pp. 135–163, 2019, doi: 10.1016/j.ijplas.2019.06.013.

[149] F. Liu and Q. M. Li, "International Journal of Impact Engineering Strain-rate effect of polymers and correction methodology in a SHPB test," vol. 161, no. December 2021, 2022, doi: 10.1016/j.ijimpeng.2021.104109.

[150] M. Uchida, R. Wakuda, and Y. Kaneko, "Evaluation and modeling of mechanical behaviors of thermosetting polymer under monotonic and cyclic tensile tests," *Polymer (Guildf).*, vol. 174, no. March, pp. 130–142, 2019, doi: 10.1016/j.polymer.2019.04.064.

[151] M. Uchida, K. Kamimura, T. Yoshida, and Y. Kaneko, "Viscoelastic-viscoplastic modeling of epoxy based on transient network theory," *Int. J. Plast.*, vol. 153, no. February, p. 103262, 2022, doi: 10.1016/j.ijplas.2022.103262.

[152] H. Jiang and C. Jiang, "Finite deformation constitutive model for macro-yield behavior of amorphous glassy polymers with a molecular entanglement-

based internal-state variable," *Int. J. Mech. Sci.*, vol. 161–162, no. August, p. 105064, 2019, doi: 10.1016/j.ijmecsci.2019.105064.

[153] C. Jiang, Z. Zhu, J. Zhang, Z. Yang, and H. Jiang, "Constitutive modeling of the rate- and temperature-dependent macro-yield behavior of amorphous glassy polymers," *Int. J. Mech. Sci.*, vol. 179, no. October 2019, p. 105653, 2020, doi: 10.1016/j.ijmecsci.2020.105653.

[154] P. Zhu, J. Lin, R. Xiao, and H. Zhou, "Unravelling physical origin of the Bauschinger effect in glassy polymers," *J. Mech. Phys. Solids*, vol. 168, no. April, p. 105046, 2022, doi: 10.1016/j.jmps.2022.105046.

[155] J. Lin, P. Zhu, C. Tian, H. Zhou, and R. Xiao, "Physically-based interpretation of abnormal stress relaxation response in glassy polymers," *Extrem. Mech. Lett.*, vol. 52, p. 101667, 2022, doi: 10.1016/j.eml.2022.101667.

[156] J. Lin, J. Qian, Y. Xie, J. Wang, and R. Xiao, "A mean-field shear transformation zone theory for amorphous polymers," *Int. J. Plast.*, vol. 163, no. February, p. 103556, 2023, doi: 10.1016/j.ijplas.2023.103556.

[157] L. Anand, N. M. Ames, V. Srivastava, and S. A. Chester, "A thermo-mechanically coupled theory for large deformations of amorphous polymers. Part I: Formulation," *Int. J. Plast.*, vol. 25, no. 8, pp. 1474–1494, 2009, doi: 10.1016/j.ijplas.2008.11.004.

[158] N. M. Ames, V. Srivastava, S. A. Chester, and L. Anand, "A thermo-mechanically coupled theory for large deformations of amorphous polymers. Part II: Applications," *Int. J. Plast.*, vol. 25, no. 8, pp. 1495–1539, 2009, doi: 10.1016/j.ijplas.2008.11.005.

[159] J. L. Bouvard, D. K. Francis, M. A. Tschopp, E. B. Marin, D. J. Bammann, and M. F. Horstemeyer, "An internal state variable material model for predicting the time, thermomechanical, and stress state dependence of amorphous glassy polymers under large deformation," *Int. J. Plast.*, vol. 42, pp. 168–193, 2013, doi: 10.1016/j.ijplas.2012.10.005.

[160] J. L. Bouvard, D. K. Ward, D. Hossain, E. B. Marin, D. J. Bammann, and M. F. Horstemeyer, "A general inelastic internal state variable model for

amorphous glassy polymers," *Acta Mech.*, vol. 213, no. 1–2, pp. 71–96, 2010, doi: 10.1007/s00707-010-0349-y.

[161] B. D. Coleman and M. E. Gurtin, "Thermodynamics with internal state variables," *J. Chem. Phys.*, vol. 47, no. 2, pp. 597–613, 1967, doi: 10.1063/1.1711937.

[162] T. Lan, Y. Jiang, and P. Wu, "A thermodynamically-based constitutive theory for amorphous glassy polymers at finite deformations," *Int. J. Plast.*, vol. 158, no. August, p. 103415, 2022, doi: 10.1016/j.ijplas.2022.103415.

[163] J. Richeton, S. Ahzi, L. Daridon, and Y. Re, "A formulation of the cooperative model for the yield stress of amorphous polymers for a wide range of strain rates and temperatures," *Polymer (Guildf).*, vol. 46, pp. 6035–6043, 2005, doi: 10.1016/j.polymer.2005.05.079.

[164] K. Cao, Y. Wang, and Y. Wang, "Effects of strain rate and temperature on the tension behavior of polycarbonate," *Mater. Des.*, vol. 38, pp. 53–58, 2012, doi: 10.1016/j.matdes.2012.02.007.

[165] D. Garcia-Gonzalez, A. Rusinek, A. Bendarma, R. Bernier, M. Klosak, and S. Bahi, "Material and structural behaviour of PMMA from low temperatures to over the glass transition: Quasi-static and dynamic loading," *Polym. Test.*, vol. 81, no. October 2019, p. 106263, 2020, doi: 10.1016/j.polymertesting.2019.106263.

[166] P. Song, A. Trivedi, and C. R. Siviour, "Tensile testing of polymers: Integration of digital image correlation, infrared thermography and finite element modelling," *J. Mech. Phys. Solids*, vol. 171, no. August 2022, p. 105161, 2023, doi: 10.1016/j.jmps.2022.105161.

[167] C. Bauwens-Crowet, J. C. Bauwens, and G. Homès, "The temperature dependence of yield of polycarbonate in uniaxial compression and tensile tests," *J. Mater. Sci.*, vol. 7, no. 2, pp. 176–183, 1972, doi: 10.1007/BF02403504.

[168] M. G. Wyzgoski and G. S. Yeh, "Relation between Free Volume and the Low-Temperature " Beta " Transition in Glassy Polycarbonate," vol. 4, no. l, pp.

29–34, 1973.

[169] R. Safari, Keivan H.;Zamani, Jamal; Ferreira, Fernando; Guedes, "Constitutive Modeling of Polycarbonate During High Strain Rate Deformation," *Polym. Eng. Sci.*, vol. 53, no. 4, pp. 679–904, 2013, doi: 10.1002/pen.

A. Appendices

A.1. Multi-Mode Version

In Section 3.2.5, it is stated that a multi-mode spectrum can be utilised to increase the accuracy in modelling close to yield. This has been utilised in previous versions of the OGR model, such as Wu et al. [67]. The multi-mode version is detailed below.

The rate of deformation tensor for the multi-mode case is defined as:

$$\bar{D} = \frac{\hat{S}_j^b}{2G_j^b} + \frac{S_j^b}{\mu_j} \text{ where, } \mu_j = 2G_j^b \tau_j$$

The objective rate of the bond-stretching and the bond-stretching stress becomes:

$$\hat{S}_j^b = \dot{S}_j^b - WS_j^b + S_j^b W$$

$$S^b = \sum_{j=1}^{M} v_j S_j^b, \sum_{j=1}^{M} v_j = 1$$

Such that v_j is the volume fraction associated with each mode.

Previous the relaxation time, τ_j, was introduced linked to each relaxation process, to account for polymers that show both the α-relaxation and the β-relaxations. In a multimode spectrum, more than two modes could be imagined such that:

$$\tau_j = a_T a_s a_\sigma \tau_{0,j}^*$$

The definitions for the shift factors would become:

$$a_{T,j} = \exp\left[\frac{\Delta H_j}{R}\left(\frac{1}{T} - \frac{1}{T^*}\right)\right]$$

$$a_s = \exp\left(\frac{C}{T_f - T_\infty} - \frac{C}{T_f^* - T_\infty}\right)$$

$$a_{\sigma,j} = \frac{V_{s,j}\tau_{oct}^{b}}{2RT} \frac{\exp\left(-\dfrac{V_{p,j}\sigma_m}{RT}\right)}{\sinh\left(\dfrac{V_{s,j}\tau_{oct}^{b}}{2RT}\right)} , \quad \tau_{oct} = \sqrt{\frac{1}{3}S_j^b : S_j^b}$$

Noting that if the multi-mode form is used for a case with multiple relaxation processes than the use of a single fictive temperature would need to be considered again.

It was decided to simplify the computational time of the model and focus on different complexities within this thesis rather than implement a multi-mode spectrum. However, the result of using a 12-mode spectrum is presented in Appendix A.

A.2. Yield Equation Origin

Following the work of Wu et al. [67], an equation for the yield stress in compression can be formulated, as was utilised in Chapter 3 and 4. The definition of 'yield' is described as the peak in the stress.

Firstly, the objective rate of the bond-stretching stress can be defined as:

$$\hat{S}^b = 2G^b \bar{D} - \frac{S^b}{\tau}$$

$$\hat{S}^b = \dot{S}^b - WS^b + S^b W$$

where, $\tau = a_\sigma a_s a_T \tau_0^*$ and the shift factors are defined as:

$$a_{T,j} = \exp\left[\frac{\Delta H_j}{R}\left(\frac{1}{T} - \frac{1}{T^*}\right)\right]$$

$$a_s = \exp\left(\frac{C}{T_f - T_\infty} - \frac{C}{T_f^* - T_\infty}\right)$$

$$a_{\sigma,j} = \frac{V_{s,j}\tau_{oct}^b}{2RT} \frac{\exp\left(-\dfrac{V_{p,j}\sigma_m}{RT}\right)}{\sinh\left(\dfrac{V_{s,j}\tau_{oct}^b}{2RT}\right)}$$

Secondly, substituting $\dot{S}^b = 0$ where $W = 0$ and $S^c = 0$:

$$S^b = 2G^b \bar{D} \tau$$

Applying that sinh, present in the stress shift factor equation, is large compared to unity and assessing the shear d_{oct} on the octahedral plane, the following can be defined:

$$\frac{V_s \tau_{oct}}{2RT} + \frac{V_p \sigma_m}{RT} = \ln d_{oct} + \ln \tau_{j,0} + \ln\left(\frac{\sqrt{2}G^b V_s}{RT}\right)$$

Finally, the conditions for this equation are considered, here a uniaxial compression test. Such that at yield, $\dot{\lambda} < 0$:

194

$$\tau_{oct} = \frac{\sqrt{2}}{3}\sigma_y$$

$$\sigma_m = \frac{-\sigma_y}{3}$$

With all the assumptions and definitions above, the yield stress in compression is given as:

$$\sigma_y = \frac{6RT}{\sqrt{2}V_s \pm 2V_p}\left[\ln\left|\frac{\dot{\lambda}}{\lambda}\right| + \ln\langle\tau_0\rangle + \ln\left(\frac{\sqrt{2}G^bV_s}{RT}\right)\right]$$

A.3. Alternative Conversion of Shear to Elastic Modulus

In Section 3.3.9, it is discussed that depending on the DMA test conducted, the results yield E^* or G^*. In in this case, it is necessary to convert the experimental results acquired from E^* to G^*. Three methods were explored before the method discussed in Section 3.3.9 was selected. The first method trialled was to use the exisiting elastic relations and assume this to be true for our loss and tangent modulus equivalents, such that:

$$G = \frac{E}{2(1+\nu)}$$

$$K = \frac{E}{3(1-2\nu)}$$

$$G = \frac{E}{3 - \left(\dfrac{E}{3K}\right)}, G' = \frac{E'}{3 - \left(\dfrac{E'}{3K}\right)}, G'' = \frac{E''}{3 - \left(\dfrac{E''}{3K}\right)}$$

However, this method produced a different loss tangent to that taken from experimental DMA.

The second method is to use the experimental $\tan \delta$ to calculate G'', such that:

$$G = \frac{E}{3 - \left(\dfrac{E}{3K}\right)}, G' = \frac{E'}{3 - \left(\dfrac{E'}{3K}\right)}$$

$$\tan \delta = \frac{G''}{G'}$$

It was found that the third method used in Section 3.3.9 is the most thorough.

A.4. High Strain Rate Energy Plots for Polycarbonate

In Section 4.5.4 the accumulated energy during an adiabatic test is simulated against the strain. It is seen that close to yield, all the energy is linked to the elastic strain energy as bond-stretching is occurring. As the test continues the conformational energy becomes a major contribution, exacerbated by the material in these tests, polycarbonate. With this interpretation of the energies in adiabatic heating during deformation the total of the dissipated energy and conformational energies contribute to temperature rise. In Figure A.1. the energy plots for the high strain rate case are shown.
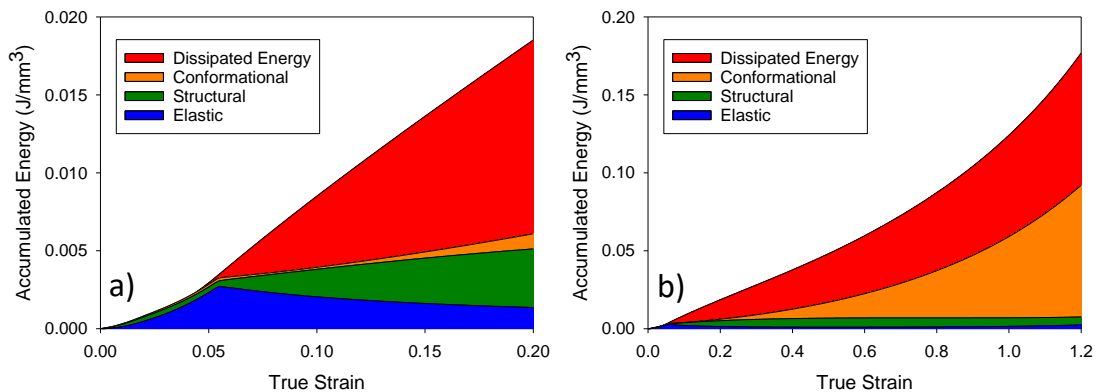
A1: Accumulated energies during the deformation of polycarbonate in a compression test at initial test temperature 22°C and strain rate $2800s^{-1}$ for a) a true strain of 0- 0.2 and b) for a true strain of 0-1.2

A.5. Multi-mode Spectrum Results

In Section 3.2.5 and Appendix 1 the use of a multiple-mode spectrum is introduced. As seen in Figure A.2. the model simulates a smaller yield strain than observed in the experimental responses. A 12-mode spectrum was simulated for a standard test of $20\,°C$ and $0.01\,s^{-1}$ and compared to the single mode version. Shown in Figure A.2, the multi-mode version does reduce the yield strain.
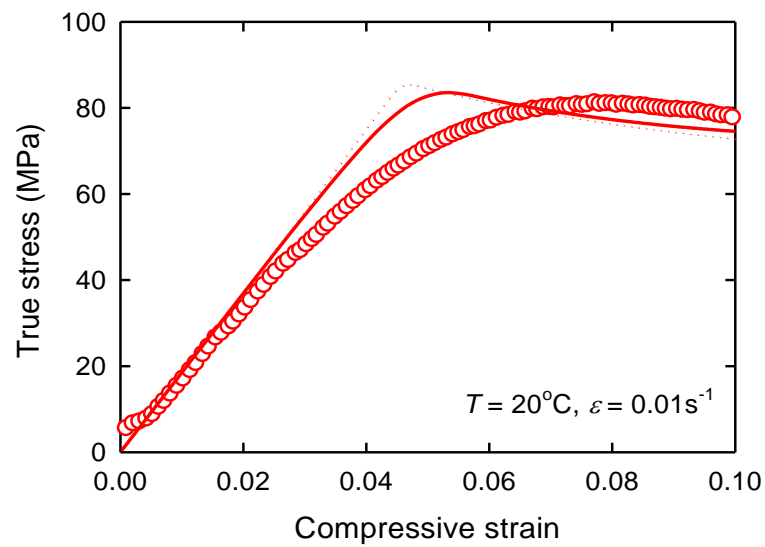
A2: Comparison of a single versus multimode viscoelastic spectrum